THREE-DIMENSIONAL VISUALISATION AND QUANTITATIVE CHARACTERISATION OF FOSSIL FUEL FLAMES USING TOMOGRAPHY AND DIGITAL IMAGING TECHNIQUES

A Thesis Submited to The University

of Kent

For The Degree Of DOCTOR OF PHILOSOPHY

In ELECTRONICS ENGINEERING

By

GUILLERMO, GILABERT-GARCIA

APRIL, 2010

THREE-DIMENSIONAL VISUALISATION AND QUANTITATIVE CHARACTERISATION OF FOSSIL FUEL FLAMES USING TOMOGRAPHY AND DIGITAL IMAGING TECHNIQUES

G. Gilabert-García, PhD 2010

ABSTRACT

This thesis describes the design, implementation and experimental evaluation of a prototype instrumentation system for the three-dimensional (3-D) visualisation and quantitative characterisation of fossil fuel flames.

A review of methodologies and technologies for the 3-D visualisation and characterisation of combustion flames is given, together with a discussion of main difficulties and technical requirements in their applications. A strategy incorporating optical sensing, digital image processing and tomographic reconstruction techniques is proposed. The strategy was directed towards the reconstruction of 3-D models of a flame and the subsequent quantification of its 3-D geometric, luminous and fluid dynamic parameters. Based on this strategy, a flame imaging system employing three identical synchronised RGB cameras has been developed. The three cameras, placed equidistantly and equiangular on a semicircle around the flame, captured six simultaneous images of the flame from six different directions. Dedicated computing algorithms, based on image processing and tomographic reconstruction techniques have been developed to reconstruct the 3-D models of a flame. A set of geometric, luminous and fluid dynamic parameters, including surface area, volume, length, circularity, luminosity and temperature are determined from the 3-D models generated.

Systematic design and experimental evaluation of the system on a gas-fired combustion rig are reported. The accuracy, resolution and validation of the system were also evaluated using purpose-designed templates including a high precision laboratory ruler, a colour flat panel and a tungsten lamp. The results obtained from the experimental evaluation are presented and the relationship between the measured parameters and the corresponding operational conditions are quantified.

Preliminary investigations were conducted on a coal-fired industry-scale combustion test facility. The multi-camera system was reconfigured to use only one camera due to the restrictions at the site facility. Therefore the property of rotational symmetry of the flame had to be assumed. Under such limited conditions, the imaging system proved to provide a good reconstruction of the internal structures and luminosity variations inside the flame. Suggestions for future development of the technology are also reported.

Aknowledgements

The author wishes to express grateful thanks to the following:

My supervisors, Prof. Yong Yan and Dr. Gang Lu for their expertise and academic support.

The British Coal Utilisation Research Organisation (BCURA) who provided funding for this project.

My loving wife Noelia for her care, emotional support, understanding, love and patience.

My family, parents, brother and sisters, aunties Leonor and Manuela for all the effort put in my persoal education.

John and Janet Higinbotham and David Cumming for all their help, academic support and altruist friendship since I first arrived in United Kingdom.

Dr. Benito Sanz-Izquierdo, Dr. Robert M. Carter and Dr. Jan Krabicka, members of the University of Kent for all long conversations and interesting contributions.

All my fellow postgraduate students and research assistants at the School of Engineering who made me laugh and enjoy while working long hours.

A number of academic, technical and secretary staff at the University of Kent that, in some way or another, contributed to the final fulfilment of this work.

Symbols and Nomenclature

Table 1: Symbols and nomenclature

	Symbols and nomenclature utilised in this thesis.
1-D	One-dimensional.
2-D	Two-dimensional.
3-D	Three-dimensional.
A	Cross-sectional area of the pipeline.
ART	Algorithm reconstruction technique.
ASCII	The American Standard Code for Information Interchange.
c	Speed of light.
C_1	Constant equivalent to $2\pi hc^2$.
C_2	Constant equivalent to hc/k.
CCD	Charged-coupled device.
D	Dyameter of the burner tube.
δ	Dirac delta function.
$\mathscr{E}(\lambda, T)$	Spectral emitted power of a black body.
$E(\lambda, T)$	Monochromatic exitance emitted from a blackbody.
ENN	Exposure enable synchronisation. A method in which the camera outputs a pulse that indicates the duration of the shutter, and can be used for controlling strobe illumination.

Continue ...

Table 1: (continued)

	Symbols and nomenclature utilised in this thesis.
f_j	jth element of vector solution in ART.
$f(x,y)$	Solution function in ART.
FBP	Filtered back-projection.
GIMP	the GNU image manipulation program; www.gimp.org
HD/VD	Horizontal Deflection/Vertical Deflection.
$\mathscr{G}$	Grey level from the output of the imaging system.
$\mathscr{G}(\lambda,T)$	Grey level proportional to the spectral emitted power.
ε_λ	Monochromatic emissivity of soot particles.
$g_R(x,y)$	Gradient function of a two-dimensional image.
h	Planck's constant.
$\mathscr{I}(\nu,T)$	Planck's law of spectral radiance of a black body.
k	Boltzman's constant.
$\mathscr{K}_o$	Instrument constant.
LCD	Liquid colour display.
λ	Wave length of radiance of a black body.
M	Total number of rays.
μ	Dynamic viscosity of a fluid.
ν	Frequency of radiance of a black body or ...
υ	Kinematic viscosity of a fluid.
p_i	ray-sum measured within the ith ray in ART.
$P_\theta(t)$	Projection from angle θ.
Q	Volumetric flow rate.
$Q_\theta(t)$	Filtered projection $P_\theta(t)$.
$\mathscr{R}$	Grey level ratio.

Continue ...

Table 1: (continued)

	Symbols and nomenclature utilised in this thesis.
$\mathscr{R}e$	Reynolds number.
$rect(t)$	Rectangular function.
ρ	Density of a fluid.
$\mathscr{S}_\lambda$	Spectral sensitivity of the imaging system.
$\mathscr{S}_\lambda$	Instrumentation factor.
$S_\theta(\omega)$	Fourier transform of projection $P_\theta(t)$.
T	Absolute temperature.
T_r	Radiance temperature.
V	Mean fluid velocity.
WEN	Write enable synchronisation. A method in which the camera writes data into the SDRAM memory of the system.
w_{ij}	contribution of the jth cell to the ith ray in ART.
XGA	Extended Graphics Array. It is the most common appellation of the 1024 × 768 pixels display.
X_k	Finite Fourier transform.
x_n	Inverse finite Fourier transform.

Contents

List of Figures

List of Tables

Chapter 1

Introduction

1.1 Introduction

Fossil fuel fired combustion systems are widely used in many industries to generate electrical power and thermal energy. Optimised operating conditions in such systems are required to enhance plant safety, improve combustion efficiency and reduce pollutant emissions. A flame is the central reaction zone of a combustion process and its geometrical, luminous and fluid-dynamics characteristics provide instantaneous information on the quality of the combustion process. The monitoring and characterisation of combustion flames have therefore become increasingly important to combustion engineers to provide an enhanced understanding and on-line optimisation of combustion conditions.

Several instrumentation systems operating on digital imaging and image processing techniques have recently been developed for the measurement of geometric, luminous and fluid-dynamic parameters of fossil fired flames (Lu et al., 1999; Huang and Yan, 2000; Bheemul, 2004; Brisley, 2006). Industrial trials of such systems have also been undertaken and results obtained have demonstrated their operability and effectiveness (Lu et al., 2001; Yan et al., 2002; Bheemul et al., 2003). However, these systems use a

single monochromatic Charge-Coupled Device (CCD) camera that allows a flame to be visualised from one direction only. The information obtained is therefore limited to two-dimensions. Brisley et al. (2004) used a similar system to implement the tomograhic reconstruction of a gaseous flame assuming axis-symmetrical properties of the flame. Bheemul (2004) extended the research to the three-dimensional (3-D) case using three monochromatic CCD cameras placed on a equiangular basis around a flame. However this study was limited to the geometric reconstruction of a flame using image processing techniques. The work presented in this thesis focuses on the 3-D tomographic reconstruction of a flame using three colour CCD cameras placed around a flame to perform a complete visualisation and characterisation of the geometric and fluid-dynamic properties of fossil fuel flames.

1.2 Three-dimensional Visualisation and Characterisation of a Flame

1.2.1 Significance

Advanced technologies for the monitoring and characterization of combustion flames have become increasingly important for improved understanding and subsequent optimization of combustion processes. With the advent of high-quality and low-cost digital imaging sensors, the application of digital capturing and subsequent image processing has become increasingly important. A significant range of measurements can be derived from digital images of the flame. The importance of these parameters depends upon the purpose of the study and the arrangement of cameras. The information obtained can provide substantial understanding of flame ignitability, internal variability, flame stability and other characteristics of complex combustion processes. Of particular importance is the flame temperature. According to CRF/BCURA (2004) as cited by Yan (2010), flame distribution provides fundamental information

on the combustion process, including coal devolatilisation, radiative heat transfer, pollutant formation, and the cause of combustion problems such as slagging and fouling. Digital imaging is an effective tool for the measurement of flame temperature and its distribution, which is very difficult to measure using other techniques (Yan, 2010).

A significant effort has been made previously to develop vision-based instrumentation systems for quantitative monitoring and characterization of combustion flames using digital imaging and image processing techniques however, most of this work has been carried out on a 2-D basis.

However as a flame is generally a 3-D flow field, to fully reveal its temperature distribution and obtain information about its pollutant formation and heat transfers, 3-D flame imaging techniques are desirable. These techniques can also provide complete geometrical and oscillation information to amply describe the stability and efficiency of a flame. In other words, 3-D flame imaging techniques are the key to reveal the important characteristics of the flame.

There have been increased activities in this particular area in recent years but the progress developed is still very limited. A comprehensive literature survey on existing visualisation techniques (see chapter 2) suggests that very limited work has previously been conducted to achieve a complete 3-D visualisation and quantitative characterisation of fossil fuel flames. To achieve a more reliable and accurate 3-D reconstruction of a flame and ultimately the 3-D measurement of flame parameters, a multi-projection sensing arrangement in conjunction with tomographic algorithms is necessary.

1.2.2 Requirements

An ideal instrumentation system for the 3-D visualisation and characterisation of fossil fuel flames necessitates a number of features. Firstly, an appropriate visualisation technique must be chosen to achieve the desired purpose of fully reconstructing a 3-D luminous and fluid dynamic model of the flame. In comparison with other techniques, a direct imaging technique using digital cameras offers more advantages than other techniques. These advantages include simpler set-ups, wider field of view, remote installations from furnaces for system protection and reasonable overall costs. Consequently, a technique based on direct imaging proves to be a potentially better technique for the 3-D visualisation and characterisation of fossil fuel flames. Therefore, a combination of direct imaging, digital processing and tomography would meet the requirements.

The second requirement for visualising and characterising a flame on a 3-D basis is that the flame should be viewed from several different locations using an imaging device such as a CCD sensor/camera. Identical CCD cameras should be employed to achieve 3-D reconstruction and visualisation of a flame. Each camera should be positioned equidistant and perhaps equiangular around the flame being monitored. In addition to the imaging device, it is important to synchronise the CCD cameras so that the flame images are captured simultaneously from the different locations. A system that is capable of generating such a synchronisation is therefore required.

Thirdly, an ideal instrumentation system should be capable of reconstructing 3-D mdels of a flame continuously from its instantaneous images. The CCD cameras provide 2-D information of the flame from different directions in the form of real-time continuous image transfer. Algorithms based on advanced image processing and tomographic techniques can combine the information of the flame images and

generate its corresponding 3-D reconstruction. Therefore, direct imaging in conjunction with CCD base sensing, image processing and tomographic techniques offers the most promising solution for continuous, on-line 3-D visualisation and quantitative characterisation of fossil fuel flames.

1.3 Major Technical Challenges

The development of a digital imaging based instrumentation system for the 3-D visualisation and quantitative characterisation of fossil fuel flames has a number of technical challenges due to the dynamic nature of a flame. The major technical challenges that have been identified include:

- **Multiple cameras adjustment and tuning:** Identical adjustment and tuning of camera lens, to ensure that the images of a flame captured by the multiple cameras have the same properties, remains one of the technical difficulties.

- **Fast system response:** The system should process a vast amount of image data to give a steady reading but it should also posses a fast dynamic response to react to any rapid change in the characteristics of the flame.

- **Variable operational conditions:** A furnace can operate under a wide range of conditions such as burner structure, type of fuel, fuel flow rates and furnace load. The instrumentation system should therefore be operational throughout a wide range of combustion conditions.

- **3-D reconstruction of an object with undefined shape:** Conventional methods for the 3-D reconstruction of an opaque object are inapplicable to the 3-D reconstruction of a flame because of the lack of required features, such as edges and textures in a flame image. An appropriate method is also required to integrate and analyse all the information obtained from all the 2-D contours to reconstruct the complete 3-D model of a flame.

- **Tomographic reconstruction using a limited number of projections:** Existing tomographic reconstruction algorithms require a significant number of projections to perform an accurate reconstruction. However a large number of projections yields to complicated set-ups in most of the cases. To overcome this complication, a more effective tomographic approach must be considered.

- **Multiple parameters:** The physical characteristics of a flame are represented in terms of number and parameters. Therefore the system to be developed must be capable of deriving all the parameters from the 3-D model of a flame. The development of suitable algorithms to extract these vital data remains one of the most difficult challenges.

1.4 Objectives of the Research Programme

The aim of the research programme is to develop an instrumentation system for the three-dimensional (3-D) visualisation and quantitative characterisation of fossil fuel flames. Unlike other existing flame monitoring systems, the new system would be the first of its kind and capable of reconstructing the complete 3-D model of a flame and characterising the flame in terms of its geometric, luminous and fluid dynamic properties. The specific objectives of the project are defined as follows:

- To design and implement a prototype instrumentation system for the 3-D visualisation and quantitative characterisation of a combustion flame in terms of its geometric, luminous and fluid dynamic parameters.

- To develop digital image processing and tomographic algorithms for the 3-D reconstruction of the model of a flame and subsequently the quantification of the 3-D geometric, luminous and fluid dynamic parameters of the flame.

- To developed a sophisticated software interface that, combining the latest programming technology oriented to the creation of user-friendly tools, allows the control of the observations and the examination of the reconstructions.
- To evaluate the performance of the system under a range of combustion conditions on a gas fired combustion test rig at the University of Kent and under industrial conditions.

1.5 Structure of Thesis

All relevant contents that are related to this research programme, including literature survey, system description, experiments, results and discussions are reported in this thesis. It is organised and presented in such a way that contributes to a logical flow towards the set of objectives. A brief summary of each chapter is given below:

Chapter 1 introduces the subject and states the significance and requirements of this research programme. It also specify the major technical challenges and the objectives. Finally describes the structure of this thesis.

Chapter 2 presents a comprehensive literature survey on flame visualisation techniques. Different 3-D flame visualisation systems that have been proposed and developed during the past decades are reviewed. The volume of research that has been covered based on the techniques has been referenced, digested and discussed. The *state-of-the-art* in the field is then defined to ensure the originality of the work.

Chapter 3 describes the foundations of two fundamental techniques utilised in this research programme: tomography and the two-colour method. Tomography is explained in detail indicating its importance to reconstruct the internal cross-section of objects. Two of the major tomographic techniques, the Filtered Back-Projection

(FBP) and the Algorithm Reconstruction Technique (ART) are described and compared. The two colour method is scrutinised and its utilisation to calculate the temperature of flames using data from two different wavelengths is explained.

Chapter 4 provides a detailed description of the design and implementation of the prototype system for the 3-D visualisation and quantitative characterisation of fossil fuel flames. The constituent elements of the system including CCD cameras, optical lenses, frame grabbers and system software are described. The geometrical, luminous and temperature calibration of the system is also presented.

Chapter 5 describes the measurement principles and computational algorithms that have been developed for the reconstruction of a complete 3-D model of flame. This description includes the description of a novel tomographic algorithm created specifically for this research programme. In addition, 3-D geometrical, luminous and fluid dynamic parameters are defined and their measurement procedures are elaborated.

Chapter 6 details the extensive experiments conducted on a laboratory combustion rig in the department instrumentation laboratory at the University of Kent. The experimental program was conducted to study and quantify the 3-D geometric, luminous and fluid dynamic characteristics of fossil fuel flames under various combustion conditions.

Chapter 7 gives the conclusions that have been drawn from this research programme as well as recommendations for future work in the field.

Chapter 2

Review of Techniques for the Three-dimensional Visualisation and Characterisation of Combustion Flames

2.1 Introduction

A complete literature review was conducted to examine all possible existing techniques which could be potentially capable to visualise, quantify and characterise combustion flames on a 3-D basis. The *state-of-the-art* in the field of study is defined following the analysis and reviews of all relevant references and materials obtained during the last few years. The literature survey not only was useful to acquire any necessary background knowledge that might contribute to this work but also guaranteed the genuine originality of the proposed research programme.

From the beginning of the review, it was evident that previous research in combustion visualisation and characterisation involved different areas of study and diverse

techniques to investigate flames and their industrial applications. The study of flame has been widely investigated. Hertz (1985) studied the two-dimension temperature distribution of an asymmetric diffusion flame using a Mach-Zehnder interferometer recording projections of the index of refraction of the flame from eight different directions. Zhao and Ladommatos (1998) described in detail the characteristics of the two-colour method for optical diagnosis and soot measurements for in-cylinder combustion processes in diesel engines. Okuno et al. (2006) performed a study of methane diffusion flames using imaging spectroscopy. Huang and Yan (2000) developed a novel instrumentation system for on-line continuous monitoring of a combustion flame. The system comprised of a CCD camera, special optical assembly and associated software and utilised the two-colour principle to calculate the temperature from the ratio of grey levels corresponding to pixels within two images. Wang et al. (2001) proposed some investigations on the flame temperature reconstruction developing the concept of optical sectioning proposed originally in (Agard and Sedat, 1983). Sbarbaro et al. (2003) described the characterization of combustion flames using principal component analysis (PCA) and generalized Hebbian learning to extract the meaningful components from flame images. Experimental results demonstrated that a flame can be characterised in terms of just a few components. But all of them were limited to the 2-D case.

For more than ten years, the Instrumentation Group at the University of Greenwich first and at the University of Kent more recently, has been developing cutting-edge research programmes for flame characterisation by combining direct imaging techniques with image processing and soft computing techniques. Lu (2000); Lu et al. (2004) proposed a novel intelligent vision system for the monitoring characterisation and control of fossil fuel fired flames. The system focused on the study of geometrical and luminous parameters including flame area, centroid, orientation, length, width, brightness, uniformity and luminosity distribution on a 2-D basis. Huang and Yan

(2000) developed a new system incorporating beam splitters to measure the 2-D temperature distribution and flickering frequency of gaseous flame using the two-colour pyrometry and spectral analysis. Huang (2001); Yan et al. (2002) performed extensive trials of such systems on both laboratory- and industrial-scale combustion test facilities and the results obtained demonstrated their effectiveness and operability under such conditions. Lu et al. (2006) monitored the oscillatory characteristics of pulverized coal flames using image processing and spectral analysis techniques. Lu et al. (2008) studied the flame stability and other characteristics of complex combustion processes such as co-firing biomass with coal. Carter et al. (2009) developed a system to measure the stability of a flame through advanced flame monitoring. The task was achieved by 'tapping' the signal from an existing flame eye and processing the resulting data as an analogue signal using a dedicated signal processing approach. Other researchers have also combined digital imaging and advanced computing processing to quantify and characterise flames in terms of their geometric, luminous, thermodynamic and aerodynamic parameters on a 2-D basis. Jiang et al. (2002) developed and tested a novel optical instrumentation system for flame characterization which was capable of providing temporal and spatial characterization of the combustion process. The system used the two-colour method to perform an on-line measurement of the temperature distribution. Very recently, Wang et al. (2010)presented a model for the simultaneous measuring of the temperature and particle concentration distribution in a coal flame. The calculations utilised a novel inverse method that utilises the radiative transfer measured from the original images of the flame using a digital camera.

However as a flame is a 3-D object, to fully reveal all the information and properties of the combustion process and achieve an in-depth understanding of the flame and subsequent optimisation of combustion conditions, a complete 3-D examination is necessary. Such an approach would also mean the acquisition of a wide range of instrumentation data that could be used to validate results produced in other im-

portant fields of investigations such as Computational Fluid Dynamics (CFD) which has been under developing by many research groups worldwide (Wang et al., 2005; Lautenberger et al., 2005; Yu et al., 2008).

A comprehensive survey on existing techniques for the 3-D flame monitoring and characterisation of fossil fuel flames had already been conducted by Bheemul (2004) and Brisley (2006). This research programme is a natural extension of these two projects. Further to these reviews, it has been recognised that 3-D flame reconstruction and particularly, 3-D mapping of temperature distribution involves two main areas: 3-D visualisation-reconstruction of a flame and the measurement of flame temperature. This review focused on all possible techniques that have been proposed and developed in these areas in recent years and their possible variations in configurations and hardware arrangements in search of real practicability combined with high efficiency. The benefits, limitations and inconvenient aspects will be indicated in each case.

2.2 Flame Visualisation Techniques

The most prominent aspect of a combustion flame is its luminosity (Fristrom, 1995) due to many chemical and thermal reactions. Common radicals and intermediates present in combustion processes are: oxygen (O), nitrogen (N), hydrogen (H), hydroxyl (OH), nitrogen oxide (NO), imidogen (NH), methyl (NH_3), formyl (HCO), formaldehyde (CH_2O), hydrogen peroxide (H_2O_2), hydroperoxo (HO_2). The visible region of a flame is the zone where many of these reactions take place. The flame colour depends on several factors, the most important typically being blackbody radiation and spectral band emission, with both spectral line emission and spectral line absorption playing smaller roles. Soot particles in a rich fuel flame with no premixed oxygen produce a yellowish diffusion combustion. CH and C_2 produce the bluish colour in a fully oxygen premixed flame with no soot particles in it. On the other

hand, other radicals like OH and CN emit radiation in the ultraviolet region and radicals like H_2O_2 and $C_2H_2O_2$ emit in the infrared region.

Flame visualisation techniques can be based on electrical or/and optical devices to observe the flame object and extract quantitative and qualitative information. With the advent of optical imaging and digital processing over the last two decades, the application of flame visualisation techniques has extended significantly. A comprehensive review of different flame visualisation methods is described in the following sections.

2.2.1 Deflection/Diffraction Photography

A common method to visualise the characteristics of flames is the so called deflection/diffraction photographic technique. This procedure detects the variation of the refractive indices of a flame induced by the changes of the density, pressure and temperature of the flame. There are three major categories of approaches that can be consider as a deflection/diffraction technique: Schlieren photography, shadowgraphy and interferometry. However, these categories are not rigidly separated and intermediate systems are often designed and utilised.

2.2.1.1 Schlieren Photography and Shadowgraphy

Schlieren photography was developed initially by Foucault and Toepler betwee 1859 and 1864 (Fiedler et al., 1985) and has been an important optical tool to perform studies of compressible flows and low speed flow involving temperature effects. To achieve this process, parallel light from a point light source is projected against a concave mirror, usually a spheric mirror but it could be parabolic. The test flow object is placed between the light source and this mirror. At the opposite site of the

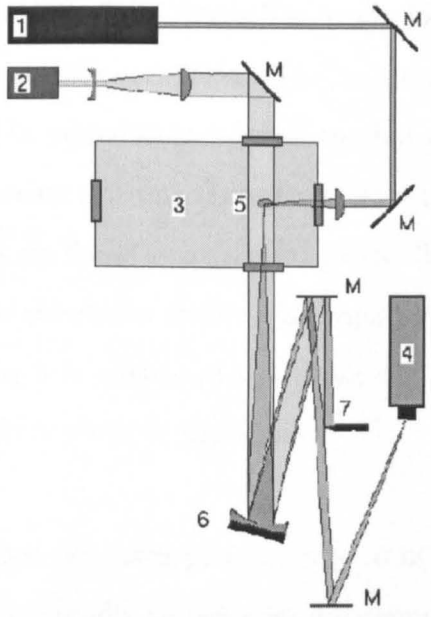

Figure 2.1: Experimental setup for Schlieren photography; 1: pulsed Nd:YAG laser for ignition; 2: flash lamp; 3: combustion chamber; 4: CCD camera; 5: focus of the Nd:YAG laser beam; 6: spherical mirror ($f = 660mm$); 7: knife edge or aperture; M: mirror. (Lackner et al., 2004).

concave mirror, a receptor is placed. This receptor could be another mirror to project the image onto photographic paper or a digital camera. If there are gradients in the density of the test flow, there will be local changes in its refractive index causing a deflection of the originally parallel light beam. As a result, an image with variable luminosity is obtained. This image allows the qualitative study of an entire flow field in an entire picture.

Wernekinck et al. (1987) designed a new optical apparatus where a light beam from a pulsed ruby laser was directed through a pinhole and then expanded to illuminate a circular area on a ground glass-plate. The ground glass is imaged by means of a lens onto a holographic plate where the light pulse creates a subjective speckle pattern. The experiment focused on the quantification of turbulent jet fields. Dobashi et al. (1992) utilised a newly developed 3-D high-speed Schlieren system that gives a view

from the direction normal to the flame front. The study focused on the disturbances in a flame induced by a weak pressure wave. The image obtained was considerable different to those obtained by preferential diffusion mechanisms. Dobashi et al. (1994) carried out similar experiments utilising the same system to analyse the effect of unburned mixture properties on flame front disturbances. The authors demonstrated that these disturbances are circular in shape. The apparatus, on the other hand, was incapable of reconstructing 3-D models of the flame either completely or partially and no flame parameters were given or determined.

Lackner et al. (2004) utilised Schlieren photography to investigate the effects of using a Nd:YAG laser as a potentially superior ignition source in internal combustion engines. The laser-induced ignition of stoichiometric to fuel-lean CH_4/air mixtures was studied experimentally in a thermostated constant-volume chamber with temperatures ranging from 300 to 473 K and with initial pressures between 1 and 25 *bar*. The chamber was equipped with four windows made of sapphire. Two of them are opposite each other in the lateral and transverse direction (along the axis and perpendicular to it). The Nd:YAG laser was deployed for igniting the combustible mixture inside the chamber. Perpendicularly to the igniting laser beam, a collimated light from a flash lamp was directed through the combustion chamber. The spherical mirror (6 in Figure 2.1) had two functions: (1) It focuses the unscattered part of the incoming parallel light in the distance of its focal length and (2) it images a real and an inverted picture of the scattering area on the CCD chip of the camera. The Schlieren photography was used to obtain visual information on the shock-wave formation and flame kernel development following the laser-induced breakdown.

Shadowgraphy is similar to Schlieren photography. As its name indicates, it utilises the shadow of flow objects to reveal non-uniformities in the transparent media. With this method, the shadow of a flame is projected by an uniform beam of light pass-

ing through the region of interest of the flame. The deflection of light induced is proportional to the steepness of the gradient of the flame's density (Settles, 2001). Parsinejad et al. (2007) developed a theoretical model based on geometrical optics to analyse the light intensity pattern of shadows of spherical flames. The theoretical results were compared with the experimental measurement of light intensity profiles across the flame front. Experimental results agreed very well with the theoretical predictions. Due to some problems like the complexity of the systems required and poor portability, shadowgraphy has not been extensively utilised in combustion research.

The potential use of deflection/diffraction photography as a tool to perform research in the combustion field is limited. There are several factors that contributed to this. First, the restricted availability of light sources. Secondly, the lack of ability of the existing 3-D visualisation systems to quantify meaningful parameters of flames. Thirdly the extensive complications encountered when implementing the set-up on an industrial furnace.

2.2.1.2 Interferometry

Interferometry is a technique that uses two or more superposed waves to study the pattern of the interferences originated after their superposition. This pattern may show some meaningful properties that can be utilised to diagnose the state of a sample object placed in the optical path of the waves. Interferometry was invented by Michelson and Morley (1887) with the intention of observing the relative motion of the Earth to the Ether.

More recently, this technique has been extensively utilised, in conjunction with holography, to visualise flows and combustion processes (Fristrom, 1995). Wakil (1975) outlined the theory and principles of operating a Mach-Zehnder interferometer and dis-

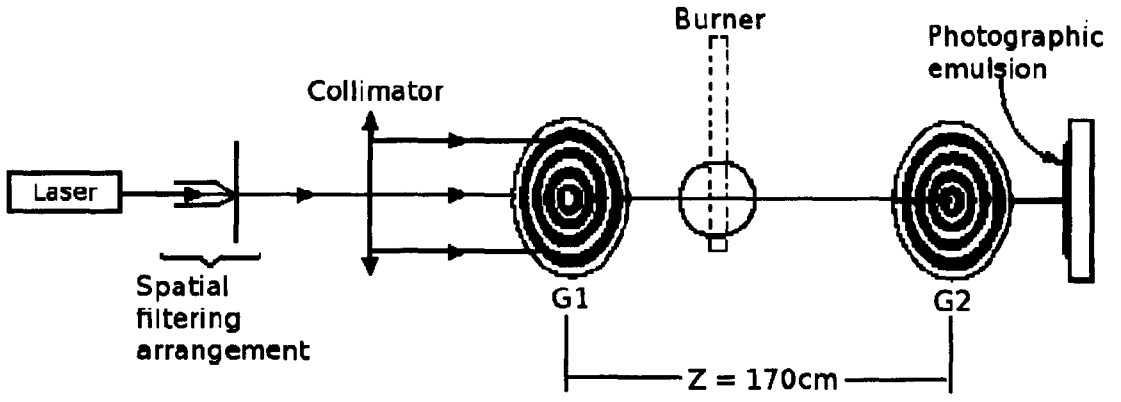

Figure 2.2: Schematic of a typical experimental set-up of interferometer with circular grating for temperature measurement for the axi-symmetric flame (shown by solid line) and the slot burner flame (shown by dotted line). (Shakher, 2009).

cussed the major aspects and applications of interferometry to study fames. Xudong et al. (2000) focused on the utility of laser interferometric holography as a tool to measure the refractive index and consequently infer the temperature of 2-D partially premixed Methane-air flames on a rectangular Wolfhard-Parker slot burner. Stella et al. (2000) used a (Carlomagno et al., 1987) interferometer to visualise reacting round jets of premixed and non-premixed flames. The discussion of the results was organized according to laminar, transitional and turbulent flows. Zhang and Zhou (2007) developed a systematic method to measure the temperatures and the mass concentrations of local species in a non-premixed ethylene-air flame. This new method could overcome the difficulty of having to know the concentrations of local species when measuring the temperature by using holographic interferometry. However, despite the extensive use of interferometry to investigate flames, limited success has been achieved in applying this technique for the 3-D visualisation of a flame.

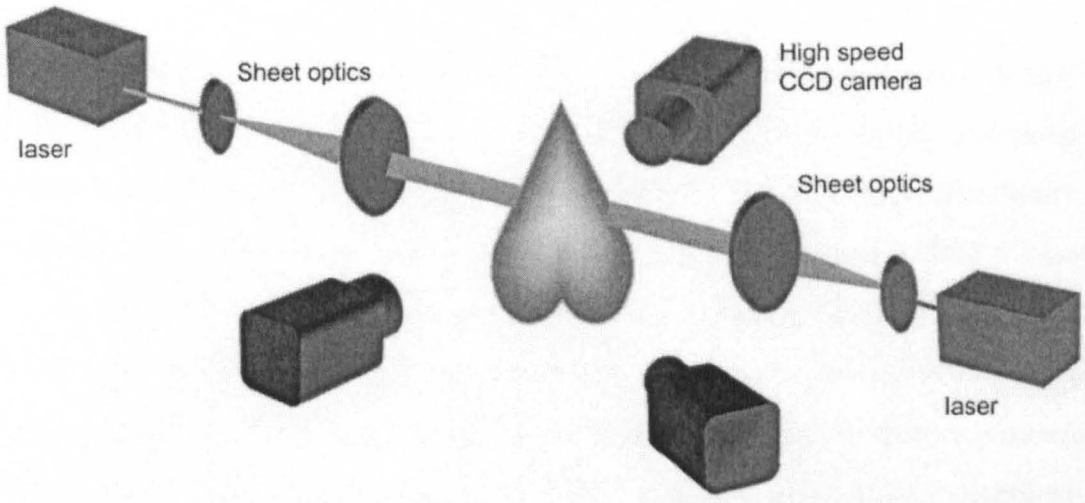

Figure 2.3: A PLIF system for flame visualisation. (Hult et al., 2004)

2.2.2 Light Scattering

Light scattering relies on a general physics process where different forms of radiation interact with molecules or moving particles of the test object and are forced to deviate or scatter. Normally in the case of research with flames, the light is the product of a laser source and illuminates a particular section of the flow. The scattered radiation is then collected and imaged onto an optical sensor. There are five techniques that are regarded as light scattering: fluorescence, incandescence, ramanography, Raleigh scattering and particulate scattering.

2.2.2.1 Fluorescence

A certain type of molecules, also called *fluorophores*, has the property of absorbing light at a specific wavelength and subsequently emit light with a larger (less energetic) wavelength. This happens when incident light excites a molecule of the material to a higher level of vibrational energy. When the molecule relaxes and returns the its original state, the fluorophore material emits a photon. The energy difference between the absorbed and emitted photons is dissipated in the fluorescent material.

One of the most common fluorescence technique utilised for flame diagnosis is the so called Planar Laser-Induced Fluorescence (PLIF). Nygren et al. (2002) performed a 3-D investigation of fuel distributions in a Homogeneous Charge Compression Ignition (HCCI) engine. The system utilised comprised a high-speed multiple Nd:YAG laser and detection system, in combination with a scanning mirror. In total eight images of the flame were collected with an equidistant separation of 0.5 *mm*. The images were analysed by identifying five intensity ranges corresponding to five increasing degrees of reaction progress. Hult et al. (2002) and Hult et al. (2004) described a new 3-D imaging system for studies of reactive and non-reactive flows that could be used to reveal the topology of turbulent structures and to extract quantities, such as concentration gradients. The measurements were performed using a high repetition rate laser and a detector system in combination with a scanning mirror. Bessler et al. (2003) gave a brief review of the wide variety of different excitation and detection strategies which are proposed in the literature and stated clear guidelines to use specific strategies for particular diagnostic situations. Chen and Bilger (2004) reported laser measurements of 3-D flame front structures for turbulent lean hydrogen/air premixed Bunsen flames and suggested, by comparison with previously published data for turbulent hydrocarbon/air premixed flames, that local flame orientation in 3-D space is close to an isotropic distribution, which is attributed to flame-surface wrinkling being strongly nonpassive. Roser et al. (1999) proposed a more sophisticated laser-based system to determine the time of the flame front propagation along a connecting pipe for cases where a dust or gas explosion can occur in a connected process vessel. They also reported measurements of data from large-scale explosion tests in industrially relevant processes. The PLIF approach has also been utilised in conjunction with other techniques such as holographic visualisation (Bryanston-Cross and Gardner, 1988) and Particle Image Velocimetry (see Section 2.2.3).

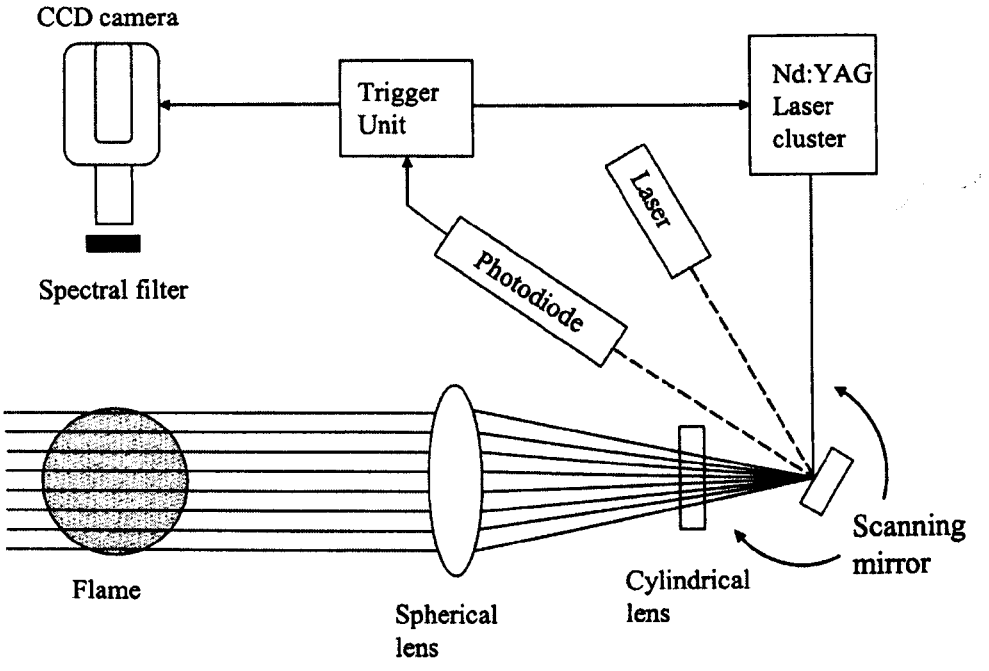

Figure 2.4: Experimental set-up of a LII based imaging system. (Hult et al., 2002)

2.2.2.2 Incandescence

The incandescence is defined as the emission of visible light from a hot body due its temperature. In combustion research, incandescence occurs when a laser beam encounters a soot particle, a body or micrometer carbon piece resulting from the incomplete combustion of a hydrocarbon. The soot particle absorbs the energy from the laser beam, its temperature increases subsequently and as a result the particle emits light. Systems based on the Laser Induced Incandescence (LII) technique have been extensively utilised to investigate properties like concentrations and profiles of soot particles in combustion processes.

In order to obtain quantitative soot concentration results in flames using LII, different correction and calibration procedures are needed. Vander Wal et al. (1996) designed a LII calibration technique via comparison of LII signal intensities with gravimetrically

determined soot volume fractions. Subsequently the spatial and temporal fluctuations of the soot field within a gravimetric chimney were characterised. Pastor et al. (2006) applied two different calibration methodologies to a laminar diffusion flame in order to obtain the most suitable calibration. First, based on a series of spatially resolved light extinction measurements and second, based on a one single-point light extinction. Finally they detailed an analysis of its applicability in real flames. Crua et al. (2003) applied the LII technique to investigate soot formation and distribution in a single cylinder rapid compression machine. The study concluded that the amount of soot produced was not significantly affected by changes in the in-cylinder pressure. Soot was observed distributed in definite clusters, which were linked to slugs of fuel caused by oscillations in the injector needle. Michelsen (2006) presented measurements of time-resolved LII from soot recorded on a picosecond (ps) time scale. A 532 nm output from a ps Nd:YAG laser was used to heat the soot, and a streak camera was used to record the LII signal. He found that under this set-up the excited state or states responsible for the fluorescence appear to be accessed via a two-photon transition and have an effective lifetime of 55 ps.

2.2.2.3 Rayleigh Scattering

Rayleigh scattering is the elastic scattering of light radiation by particles much smaller than the wavelength of the light. These particles may be individual atoms or molecules. The name of this phenomenon is derived from the English physicist Lord Rayleigh and it is the strongest molecular scattering process for normal molecules (Fristrom, 1995). It is indeed the main reason why the sky is blue. For cases where the particles are similar or even larger than the wavelength of the incident light, the Mie theory of scattering should be taken into account (Venkatesh and Prasad, 1983).

Barat et al. (1991) used pulsed laser Rayleigh scattering to obtain instantaneous flame temperatures in a turbulent flow combustor. The techniqe was based on polarisation

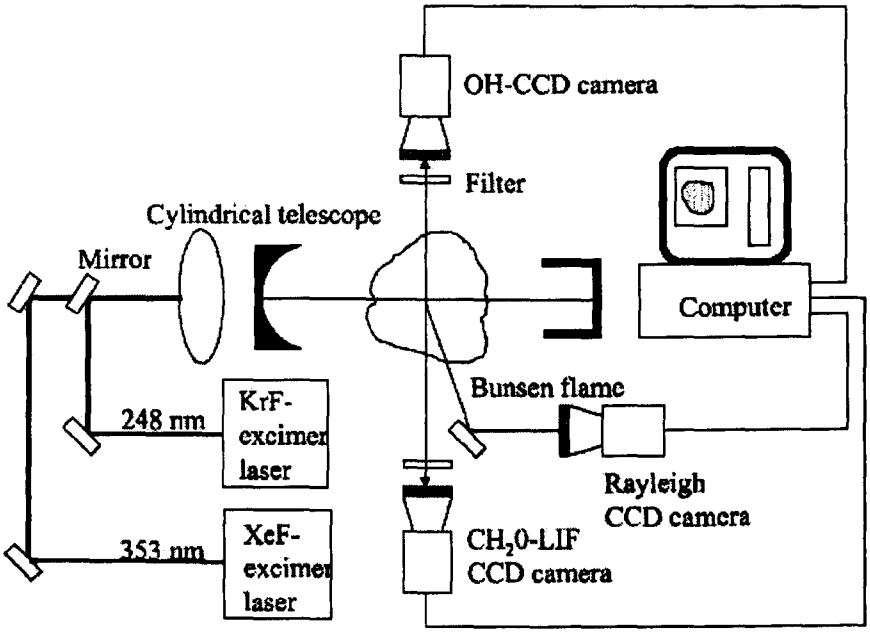

Figure 2.5: A Rayleigh scattering system for flame visualisation. (Scharr et al., 2000)

for the extraction of the Rayleigh scattering. As a result, probability density functions (PDF) of the fluctuating temperature were obtained for fuel lean ethylene-air combustion. Fielding et al. (2002) combined Rayleigh scattering with a simultaneous measurement of the fuel concentration and demonstrated that the fuel concentration can be obtained by measuring the polarised and depolarised components of the Rayleigh signal and taking their difference or a suitable linear combination. Scharr et al. (2000) developed an instrumentation apparatus combining a 248 nm KrF and a 353 nm XeF excimer laser to determine the flame position, structure, thickness and temperature of different sections of a Bunsen flame. Brummund and Scheel (2000) used a multi-dimensional imaging system to measure the temperature, OH and NO distribution in a diffusion flame emerging from a swirl burner. Bookey et al. (2006) reported the application of coherent Rayleigh scattering (CRS) to the measurement of temperature in a flame using a narrow bandwidth pump and probe fields. A 3% of uncertainty was found in the temperature utilising a CRS model that includes

scattering from a multicomponent gas for the first time. The model was validated at room temperature.

2.2.2.4 Mie Scattering

The Mie scattering, so called after the explanation given by the Mie theory, also called Lorentz-Mie theory or even Lorentz-Mie-Debye theory, can be explained analytically by a solution of the Maxwell's equation for the scattering of electromagnetic radiation by spherical particles. This phenomenon, it is responsible for the white appearance of vapour clouds in the sky. Mie scattering has been also used to the study of different properties of combustions processes.

Steeper et al. (1988) developed and use a particle sizer designed to measure relatively large individual particles in a combustion process. They documented the accuracy of the sizer using mono-disperse droplets of water and n-decane. They also examine the effect of combustion on particle sizer performance by comparing the results obtained for burning n-decane droplets with results of non-burning tests. (Stepowskia and Cabota, 1989) utilised the laser Mie scattering technique to measure the mean distributions of seed particles in a turbulent diffusion flame of a jet of hydrogen air issuing in a coflowing air stream. The data obtained was used to derive mean values of mixture fraction, density and temperature in the mixing flow. Ossler et al. (1995) recorded 2-D images of Mie scattered light from a water aerosol using streak camera with a time resolution of a few picoseconds. A laser pulse whose length was 35 ps was reflected and refocused on a probe volume. The pictures obtained in this way were separated in time by less than 3 nanoseconds (ns) and separated in space by fixed intervals and it was concluded that they could be used to compose a 3-D picture of the aerosol distribution.

Stamatov and Stamatova (2006) performed an experimental study of soot formation in precessing jet flames. The Mie diagnostic technique was implemented to provide qualitative visualisation of the zones of soot formation. To compete the experiment, a range of conditionally sampled experiments was carried out for several Reynolds (see Section 6.2.2) numbers. The data obtained reveals that soot is predominantly formed in sheets of varying thickness. However very little soot is observed in the region near burner's nozzle indicating that this is consistent with the idea that the formation of soot in appreciable quantities is kinetically limited. The experimental results supported the hypothesis that low strain in a diffusion flame promotes soot formation and high emissivity i.e., that soot formation correlates inversely with flame strain.

2.2.2.5 Raman Scattering

The Raman scattering also called Raman effect is the inelastic scattering of a photon. It was first discovered by Sir Chandrasekhara Wenkata Raman and it is considered the weakest of the scattering processes (Fristrom, 1995). Experimental systems based on this phenomenon have not been used extensively in the field of combustion.

Lapp et al. (1972) described the laser Raman scattering for nitrogen, oxygen, and water vapour from Hydrogen-air and Hydrogen-Oxygen flames. The experimens showed that the ground-state and upper-state vibrational bands exhibited strong asymmetrical broadening. The experimental spectral profiles were fitted theoretically to provide a new measurement technique for the determination of rotational and vibrational excitation temperatures. Lipp et al. (1992) implemented simultaneous space- and time-resolved measurements of CO_2, O_2, N_2, CH_4 and H_2O using spontaneous Raman scattering in a turbulent CH_4/N_2 diffusion flame and a narrowband 308 nm $XeCl$ excimer laser. An intensified multichannel camera was aslo used to give full information about the spectral background and the major species. The paper presented new

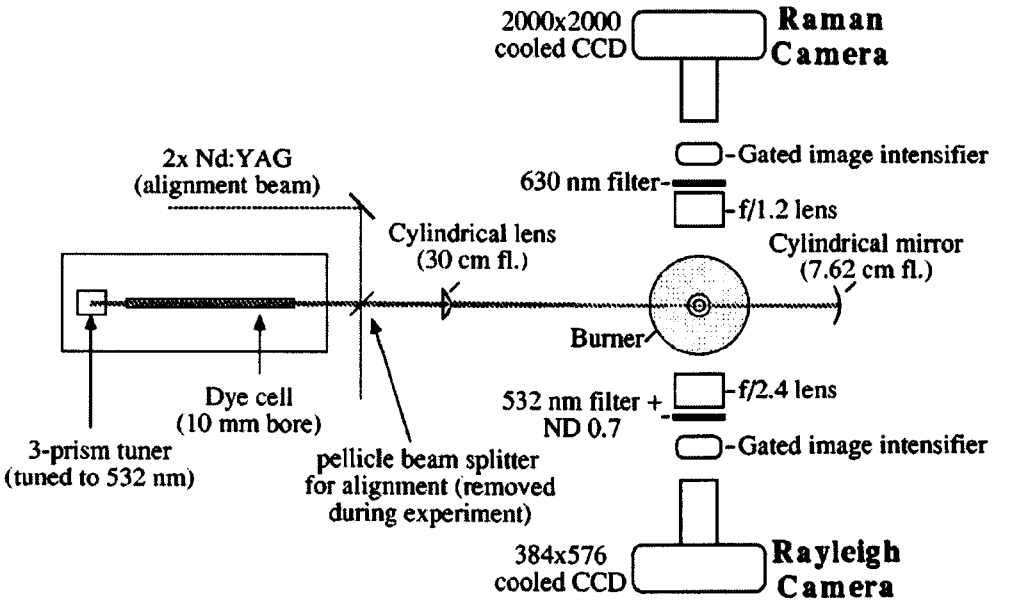

Figure 2.6: A Raman and Rayleigh scattering system for flame visualisation. (Marran et al., 1995)

experimental results containing concentration, temperatures and mixture-fractions. Fielding et al. (1998) employed this method to examine the fuel mass fraction and the 3-D distribution of temperature in non-premixed Methane flames. Meier and Keck (2002) performed a comparative study to quantify the signal-to-background ratio of Raman measurements in fuel-rich flames using pulsed laser radiation at 532, 489, 355 and 266 *nm*. The results showed the potential and limitations of concentration measurements by laser Raman scattering in fuel-rich flames indicating the importance of the decision of what laser system should be used for measurements in laboratory or practical flames.

In particulate scattering, the light scattered from particles in a flame is used to estimate regions in the flames. The particles utilised can either be naturally present in the flame or artificially introduced as a tracer. This technique is a potentially powerful diagnosis tool to investigate the velocity profiles of particles present in a

flame. However its application is mainly restricted to the 2-D case and only very limited work has been carried out for the 3-D case (Bheemul, 2004).

Despite the fact that light-scattering systems are commonly utilised in the field of combustion processes it is an invasive technique that has not been used to provide geometrical and luminous parameters of a flame. Moreover, scattering-based systems are very complex and subsequently expensive. Therefore, the use of light scattering is not advisable in this research programme.

2.2.3 Particle Image Velocimetry

Particle Image Velocimetry (PIV) is an optical technique of whole-flow-field visualisation. It is utilised to obtain instantaneous velocity measurements in a cross-section of a flow. The fluid is normally seeded with tracer particles which are supposed to follow accurately the laws of flow dynamics. The motion of these particles show information about the velocity of the flow being studied. In PIV, the measurements provide two components of the vector velocity. In other words, PIV produces a 2-D vector field only. When combined with other methods, such as holographics and stereoscopic (see Section 2.2.5), the complete 3-D vector field can be calculated. Instantaneous 3-D measurements of the whole cross-section is then achieved.

Han et al. (2000) applied stereoscopic PIV to investigate the velocity field of a complex 3-D structure of a lifted flame. It was found that the change of the index of refraction due to the presence of the flame, when compared to a non-reacting flow, can distort the PIV images. They indicated that the turbulent kinetic energy distribution showed a sudden reduction when the flow encountered the flame base, which is thought to be due to the stabilizing effect of heat release. They also investigated the change in refractive index due to the heat release from the flame. Stella et al. (2001)

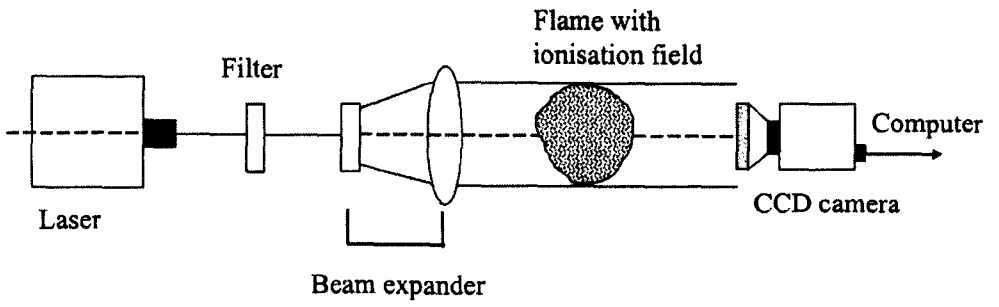

Figure 2.7: A holographic PIV system for flame visualisation. (Pan and Meng, 2005)

presented results of their analysis over turbulent premixed flames using stereoscopic PIV. This study explains how the availability of planar three component velocity fields significantly enhances the capability of inferring 3-D flows in a correct and detailed manner. In addition to PIV, topological information on the instantaneous reacting zones was claimed to be deduced by the observation of the seeding particle density in the recorded images. However, none of the geometric and luminous parameters was reported.

Palero and Ikeda (2002) utilised a droplet-size-classified stereoscopic PIV system to characterise the spray in a gun-type oil industrial burner. The combination of techniques were implemented in conjunction with a extremely complex mix of oil droplets, air and flow. The full 3-D velocity vector map were measured for different droplet sizes in non-reacting conditions with help of a technique called multi-intensity layer that provides the discrimination of particles according to their sizes. The paper concluded that different spatial structures are present depending on the droplet size. Similar differences were also the found for the swirl components. Pan and Meng (2005) presented a digital in-line holographic recording and reconstruction system for the measurement of the components of the velocity vector field in a 3-D space field with time history. The traditional holographic film was replaced by a CCD chip that

recorded instantaneously the interference fringes directly originating a new field experimental technique: The Digital Holographic Particle Image Velocimetry (DHPIV). The virtual image slices in different positions were reconstructed by computation using Fresnel-Kirchhoff integral method. Also a complex field signal filter was applied in image reconstruction to achieve a thin focus depth of image field. Finally the 3-D velocity field, 3-D streamline and 3-D vorticity fields, and the time evolution images were displayed.

Despite the fact that numerous techniques has been utilised alongside PIV methods to measure the velocity components of flames, no one has been able to develop a suitable combination capable of measuring not only the velocity components but mainly geometric, luminous and temperature parameters. Although PIV techniques have proved to be successful in partially reconstructing the 3-D characteristics of a flame, the approach has not been extended for the volumetric, luminous and temperature reconstruction of a flame.

2.2.4 Direct Photography/Imaging and Image Processing

All the techniques reviewed in previous sections are invasive methods that require the use of additional light sources or even injection of particles inside the flame. Direct photography, on the other hand, enables the direct capture of flame images by an imaging sensor without the necessity of altering the natural conditions of the flame. The understanding of the combustion processes can be improved by the combination of direct photography with image processing techniques. This understanding includes the analysis of physical, chemical and fluid-dynamic properties of the flame. For instance Lu (2000) utilised direct photography in combination with other techniques such as computing analysis, fuzzy logic and neural network to visualise and quantify a flame. Ruão et al. (1999) developed and tested an NO_x diagnostic system based on a

spectral ultraviolet/visible imaging device. The study was performed in a small-scale laboratory furnace fired by a propane and ethylene swirl burner. The measurements were obtained for a total of twenty three different operating conditions which quantify the effects of the gaseous fuel recirculation and heat losses. Lu et al. (2004) presented a novel complete imaging instrumentation system for the on-line monitoring and characterisation of fossil fuel fired flames on a 2-D basis. The system included dedicated software, digital image processing algorithms, two-colour pyrometry and power spectra analysis. The range of parameters that studied included: ignition point, area, spreading angle, brightness, non-uniformity, flicker and temperature. Xu et al. (2004) developed a novel approach for the on-line fuel identification using digital signal processing (DSP). The new system contained a detector with three photodiodes to derive multiple signals covering a wide spectrum of the flame. Advanced DSP were deployed to identify the dynamic fingerprints of the flame in both time and frequency domain. The series of experiments carried out demonstrated the viability of the approach to identify the type of coal being burnt under steady combustion conditions.

Xu et al. (2005) designed a flame detector system containing three photodiodes to derive multiple signals from a flame covering a wide spectrum of radiation from the infrared to ultraviolet regions through the visible band. Various flame features were extracted from the time and frequency domains utilising this approach, where a back-propagation neural network was deployed to map the flame features to an individual type of fuel. Huang and Zhang (2008) characterised the colour spectrum of methane flames under various burning conditions using colour models instead of resolving the real physical spectrum. The results demonstrated that each type of flame has its own characteristic colour distribution. Molcan et al. (2009) used flame imaging to investigate experimentally the co-firing of biomass with pulverised coal under a range of different co-firing conditions.

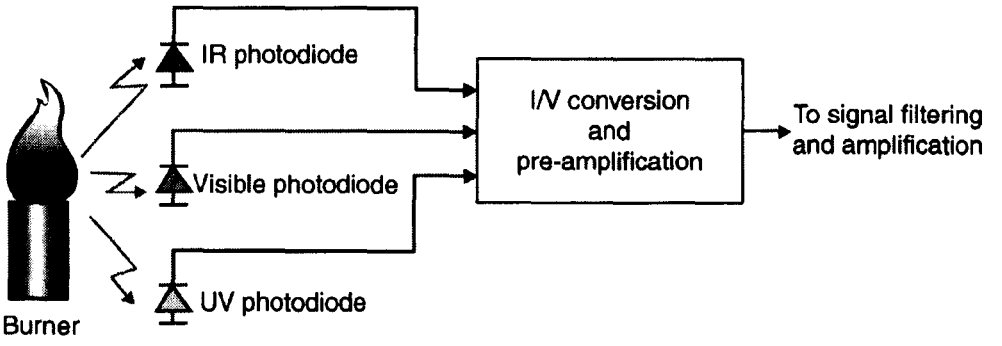

Figure 2.8: Basic sensing arrangement of the (Xu et al., 2005) fuel-tracking monitor

For the 3-D visualisation and characterisation of flames, very limited work using direct imaging techniques has been reported. Moratti et al. (1997) described a vision based system for the 3-D reconstruction of an industrial flame to determine the volume and area of the flame. Zhou et al. (2002) developed the numerical studies for the 3-D visualisation of the temperature distribution in a large-scale furnace via regularised reconstruction from radiative energy images. Eight CCD digital cameras were mounted around the furnace to capture the corresponding images inside the furnace and simulate the 3-D temperature distribution. A fast algorithm was proposed for pinhole imaging based on the Monte Carlo method. Zhou et al. (2005); Luo and Zhou (2007) carried out the experimental investigations on the visualisation of the 3-D temperature distribution in a large-scale pulverised-coal-fired boiler furnace. They accepted the assumption of grey radiation and used multiple colour flame detectors to capture approximately monochromatic radiation intensity images under the visible wavelengths of red, green and blue. A black body furnace was utilised to calibrate the colour images. A modified Tikhonov regularisation method (Tikhonov and Arsenin, 1977) was used to reconstruct the 3-D temperature distribution inside the furnace. However, this approach encounters a number of difficulties such as the utilisation of a significant number of cameras inside a furnace, synchronisation issues, adjustment and protections for each camera such as water jackets. Moreover, the

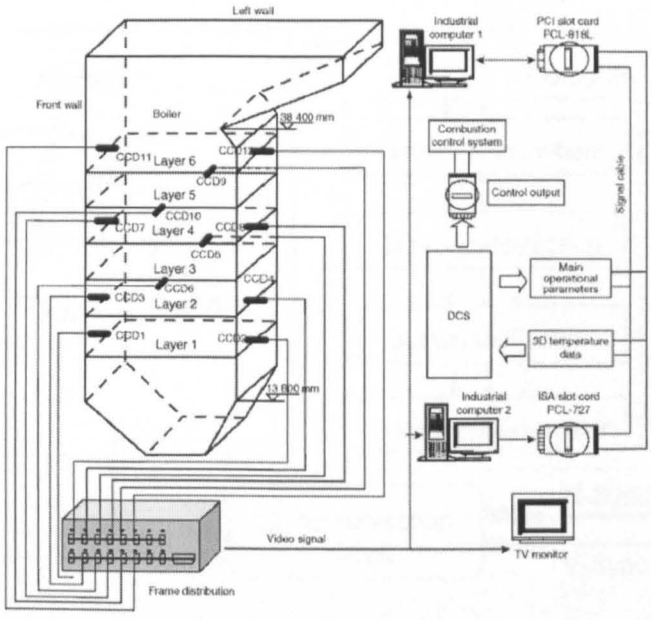

Figure 2.9: Installation of 12 CCD cameras mounted around a large-scale boiler furnace. (Luo and Zhou, 2007).

approach studies the distribution of temperature in a furnace, not the characteristics of the flame itself. Natterer et al. (1996) had previously proposed a similar study in large-combustion chambers placing specially designed cameras in two opposite corners of the camber where coal or waste were burnt.

Direct imaging has also been applied in other different approaches. Bheemul et al. (2002) presented a novel instrumentation system for the 3-D visualisation and quantitative characterisation of gaseous flames using three monocromatic CCD cameras. (See Figure 2.10) The system comprises three CCD cameras placed on an equiangular basis. The cameras were synchronised using an external circuit to ensure the simultaneous capture of images. The images were taken separated by 180° and the outer limits of every flame image extracted. These limits were utilised to obtain the real dimensions of the flames and reconstruct their geometrical models using mesh reconstruction techniques implemented in a computer.

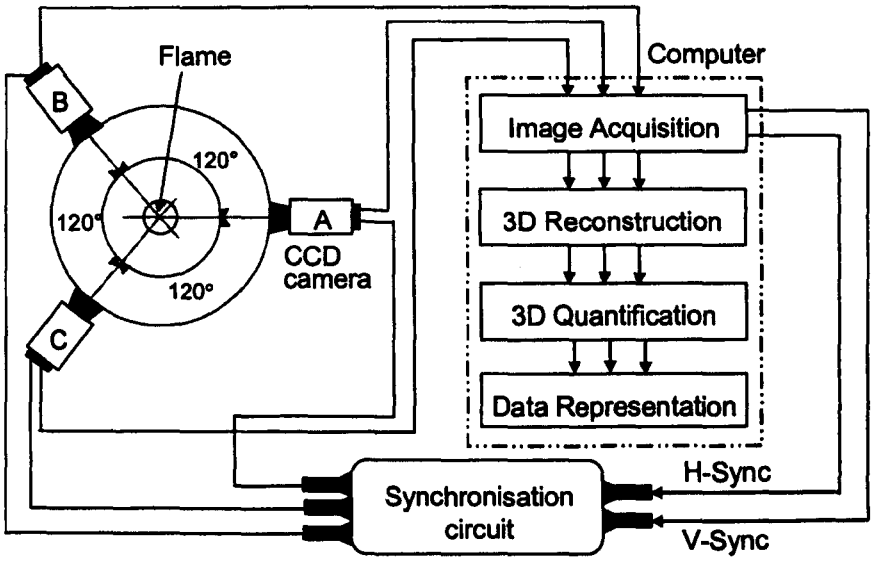

Figure 2.10: Schematic of a 3-D imaging system. (Bheemul, 2004).

Dedicated computing algorithms were developed and a set of geometrical parameters, including volume, surface area, orientation, length and circularity were defined to characterise the flames.

2.2.5 Stereovision

Stereovision, also known as stereoscopic vision or binocular vision, is a technique where two images of the same scene taken by two image sensors at different positions, are fused together into a single image. This technique is indeed a well known ability in many living species, like for instance, the human being where the two images captured from two different directions of the face are fused by the human brain. The fused or stereo-reconstructed image contains 3-D perception of the scene as contains embedded information about depth, width and an improved resolution.

A number of system configurations based on stereovision principles have been developed for the 3-D reconstructions of objects, but in the combustion sector, limited work

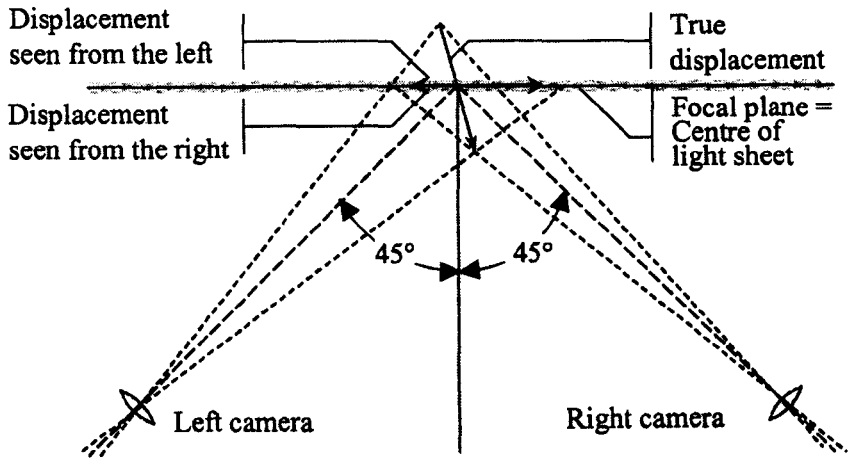

Figure 2.11: A stereovision system for flame visualisation. (Ng and Zhang, 2003).

has been performed using this approach. Ng and Zhang (2003); Ng et al. (2003); Ng and Zhang (2005) reconstructed the surface of turbulent impinging diffusion flames. The 3-D geometry was reconstructed from any pair of stereo images through digital image processing and computer vision. Only one camera was required to capture the pair of stereo images due to the use of a stereo adapter. Therefore the pair of images were captured on a single CCD chip. w The surface area of the flames and the corresponding attribute of the surface gradient were calculated. It is believed that this data can improve the understanding of flame and acoustic wave interaction. Cheung et al. (2005); Cheung and Zhang (2006) utilised a similar approach to track and measure the velocity of solid particles. The system was able to measure the position but also the shape and orientation of non-spherical particles. The system proved its potential for the quantitative 3-D measurement of multiphase flow.

Although stereovision is considered to be a well-established approach to reconstruct the 3-D model of a static object, there are aspects for which this technique has not been extensively used in the field of combustion processes. For instance, stereoscopic methods have been successful to detect geometrical parameters and some tempera-

ture information spatially distributed. On the other hand, stereoscopic systems have not been able to extend these achievements to complete a full 3-D temperature and geometrical model of a flame.

Therefore, at present, the implementation of stereoscopic vision for the 3-D complete reconstruction of a flame is not considered for this research programme.

2.2.6 Tomography

Tomography is the *art* of imaging an object reconstructing the complete 3-D model by sections. Typical fields where tomography is applied include radiology, archaeology, biology, geophysics, oceanography, etc. In the combustion field tomography has been applied for reconstructing cross-sections of flames from an array of data taken at various viewing angles. Tomographic images of a flame can be obtained using either electrical methods or optical methods.

Electrical tomography can be subdivided in different subcategories: passive electrical quantities namely resistance, inductance and capacitance (Bheemul, 2004). The most commonly used techniques are impedance (Waterfall et al., 1996) and capacitance tomography (Peyton et al., 1996; Yu et al., 1998). A typical electrical capacitance tomography (ECT) system for the 3-D flame visualisation consist of a capacitance sensor, capacitance measuring and unit control computer. The cross-section to be observed is surrounded by one or more circumferential sets of capacitance electrodes and the electrical capacitances between all combinations of electrodes within each set are measured. Burning fuel, produces a high concentration of ions. Therefore, the dielectric constant of the combustion volume is modified and overall, the conductivity of the volume increases significantly. This information is then used to reconstruct the cross-section of the flame.

The ECT technique is a popular tool in the field of combustion. Waterfall et al. (1996) extended the ECT technique to measure both the change in permittivity and the change in conductivity, yielding additional information on the flame composition. The authors successfully monitored the flame position. Waterfall et al. (1997) adapted the technique to characterise the combustion phenomena in a scaled model of an internal combustion engine. The method was able to locate flame position, measure flame size and monitor the effect of varied air/fuel ratio. Yan et al. (2001) proposed a new algorithm for ECT using multiple linear regression and regularisation. The authors claimed that the algorithm is numerically simple and computationally fast. Gomez et al. (2003) applied the ECT technique in conjunction with the Tikhonov regularisation (Tikhonov and Arsenin, 1977) and mesh generation to develop a mathematical model for the visualisation of combustion processes. The ECT has a series of drawbacks. It is recognised that the application of this approach on a real-time application would be very expensive. The spatial resolution of ECT is poor and the complexity of the systems is high. This technique is therefore regarded as unsuitable for the 3-D visualisation and quantification of flames.

Applications of optical tomography (OT) are more common in combustion applications. Most of the existing approaches utilised invasive methods as Schlieren shadowgraphy, interferometry and laser beam deflection. OT techniques have been a topical area of research over decades. Timmerman et al. (1999) utilised holographic interferometry tomography from quantitative phase maps recorded using a rapid-switching, double reference beam and double pulse laser system to study the behaviour of jet turbine flames. However, the system arrangement was too complex. Hertz and Faris (1988) described a simple experimental arrangement for the emission tomography of radicals in flames. The experiments determined 2-D spatially resolved distribution of excited-state CH in normal pressure Methane-Oxygen flames. The calibration

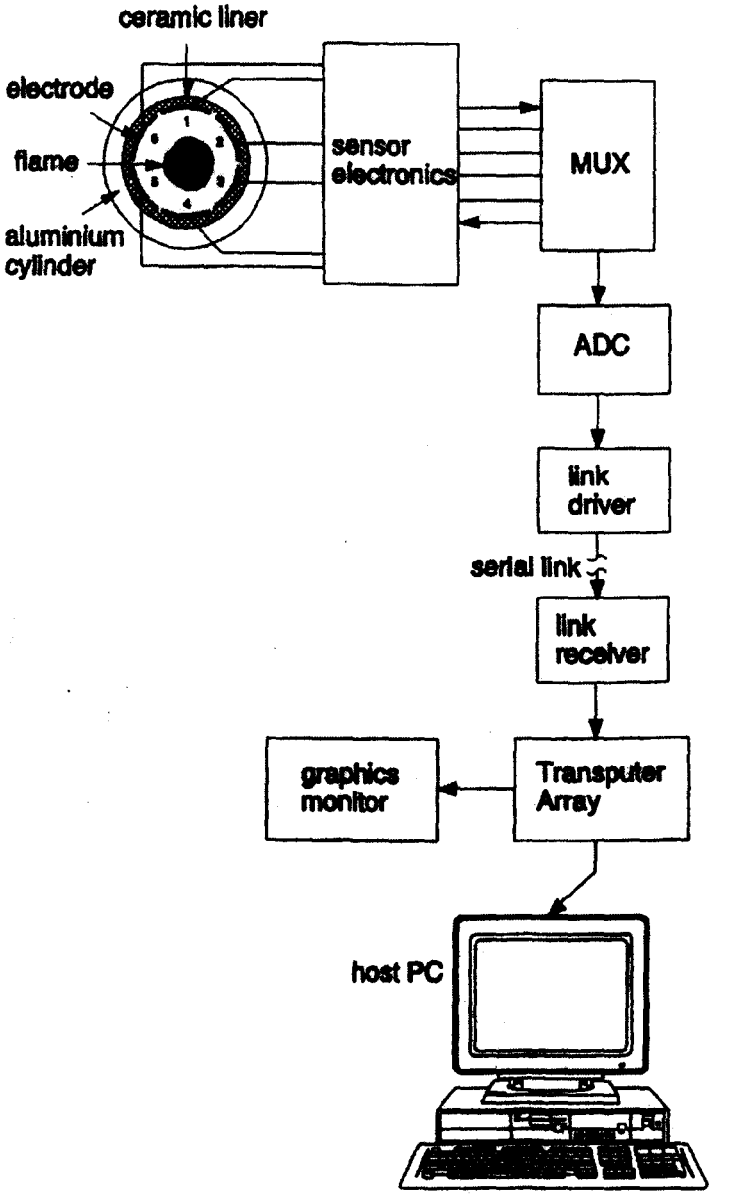

Figure 2.12: Transputer-based ECT system for flame measurement. (Waterfall et al., 1996)

of the system was performed by Rayleigh scattering techniques using an excimer-pumped dye laser. Fischer and Burkhardt (1990) performed the 3-D temperature measurement in flames by multi spectral tomograhic image analysis. The temperature measurements were performed after calibrating the system using a tungsten lamp and utilising the singular value decomposition (SVD) of the Abel transform as the reconstruction algorithm. Hall and Bonczyk (1990) presented the 3-D temperature reconstruction using the emission/absorption tomography of sooting ethylene flames. The experiment considered sets of parallel line-of-sight measurements and the Fourier transform tomography the perform the reconstruction. Burkhardt and Stoll (1995) applied also optical tomography and CCD arrays of sensors setting the so called Harburger System to capture the sequences of images to calculate the temperature distribution of flames using the SVD of the Abel transform. Leipertz et al. (1996) presented an experiment to control industrial combustion processes using ultra violet (UV) emission tomography. The measurements were performed in a 1 $MWth$ top-fired combustor cylinder with an inner diameter of 2 m. Brisley et al. (2004, 2005) proposed a new instrumentation system for the 3-D temperature measurement of combustion flames using a single monochromatic CCD camera. The system utilised the Filtered Back-Projection (FBP) algorithm and a Hamming window as the filter. However these investigations, to reduce the complexity of the systems, considered several assumptions like the rotational symmetry of the flame that affected the accuracy and reliability of the measurements.

Tomography is a powerful tool. It can be used for cross-sectional reconstruction of a flame and therefore the complete 3-D reconstruction of the whole combustion process. OT can be easy to implement and cost effective if performed with a reduced number of latest generation digital cameras.

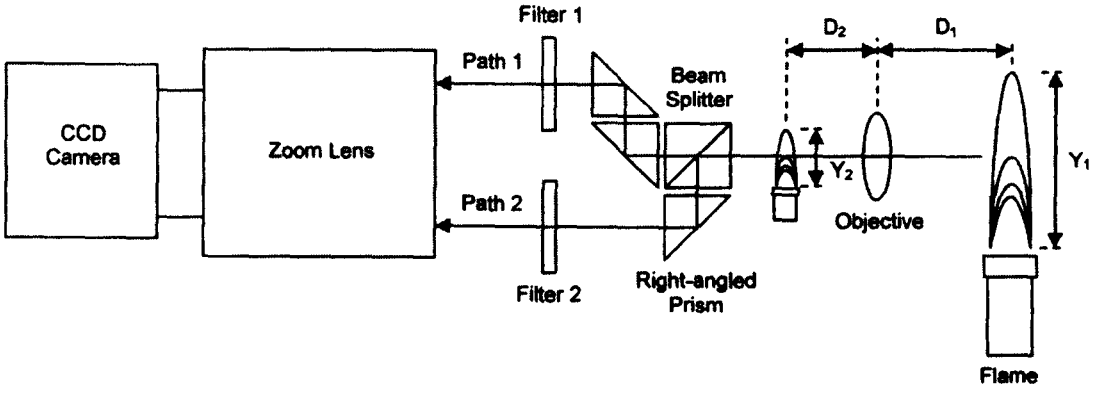

Figure 2.13: Optical transmission arrangement and constituent elements of the Brisley (2006) imaging system.

Moreover, advanced digital image processing techniques can be used in conjunction with traditional tomographic algorithms to boost the result and improve the information obtained to determine the geometrical, luminous and temperature characterisation of a flame on a 3-D basis. Due to the high interest that presents for this research programme, the following chapter explains in detail the two major algorithm used in tomographic approaches.

2.3 Summary

The review presented in this chapter has focused on a range of techniques that has been developed for the 3-D visualisation and quantitative examination of combustion flames. A wide range of flame visualisation techniques based on deflection/diffraction photography, light scattering, PIV, direct photography combined with digital image processing, stereovision and tomography have been previously used in certain industrial situations with several degrees of extension. These approaches have contributed to a fast and vast improvement of the knowledge and understanding of combustion processes in general but more particularly on micro-structures, velocity profiles and soot particles in flames. On the other hand, none of them have proved to be perfectly reliable in order to achieve a complete 3-D reconstruction of the entire flame.

Comparing all the above techniques, optical tomography offers a number of advantages. It is not an invasive technique and therefore it does not need to alter or modify the natural state of the flame. It can utilise the fast developing field of digital imaging with the genuine advantage of enjoying improved image quality and cost reduction almost every year. It can also be combined with all the functionality provided by modern digital image processing and can be versatile in terms of flexible set-ups.

The literature review has shown that, despite the significant progress achieved in the flame monitoring field, the success obtained in the 3-D visualisation of the flame has been very limited. None of the 3-D studies performed have been able to reconstruct a complete 3-D model of a flame. In particular there is not an efficient computing algorithm to performed an effective 3-D reconstruction using a simple and low cost system arrangement. Therefore, a new strategy based on OT is suggested to achieve an improved 3-D reconstruction of fossil fuel flames. To obtain a more reliable and accurate 3-D reconstruction of the flames and ultimately the 3-D measurement of flame parameters, a multi-projection sensing arrangement in conjunction with tomographic algorithms is presented. Subsequently, a number of geometric, luminous and temperature parameters of the flame will be derived from the reconstructed flame to improve the understanding and subsequent optimisation of combustion processes.

Chapter 3

Theoretical Foundations: Tomography and the Two-colour Method

3.1 Introduction

This chapter serves to review the theoretical foundations associated with the broad subjects of tomography, combustion, flames and the two-colour method to calculate the temperature of a flame. The understanding of these bases is of a capital importance as they are directly applied in the resolutions and implementations developed in this research study. The correct comprehension of the theory in the subject areas ensures the scientific correctness of the proposed research programme and the standard and quality of its technical implementation.

Tomography is the inverse problem method selected for this study due to its reliability, relatively easy implementation, computational effectiveness and feasible instrumentation. The two algorithms presented in this chapter are two of the most commonly used and well known, the Filtered Back-Projection algorithm (FBP) and

the Algorithm Reconstruction Technique (ART). Both are explained in detail with some necessary preliminary mathematical concepts.

The visible radiation spectra of a flame is the responsible of the luminosity observed and it is the characteristic that is measured by the camera sensors utilised in this research programme. This radiation comes from both, the gas and the soot particles existing in the flame. As it will be explained, most of the relevant radiation measured will be related to these particles and subsequently, the Plank's radiation law will be applied. This yields to the utilisation of the derived two-colour method which calculates the temperature of the soot particles surrounded by gas. A reliable equilibrium between the temperature of gas and particles guarantees the effectiveness of this method.

3.2 Tomographic Algorithms

3.2.1 Basic Concepts

3.2.1.1 Dirac Delta or Impulse Function

The Dirac Delta, also called, Impulse Function, it is a special function useful for explaining operations on functions (Schwartz and Shaw, 1975). It cannot be defined directly but it has to be defined as the limit of a sequence of functions. It is necessary to define a rectangular function or *rect* as follows:

$$rect(t) = \begin{cases} 1 & |t| < \frac{1}{2} \\ 0 & \text{elsewhere} \end{cases} \tag{3.1}$$

This is illustrated in Figure 3.1(a). It considers a sequence of functions of ever decreasing support on the t-axis as described by Equation 3.2.

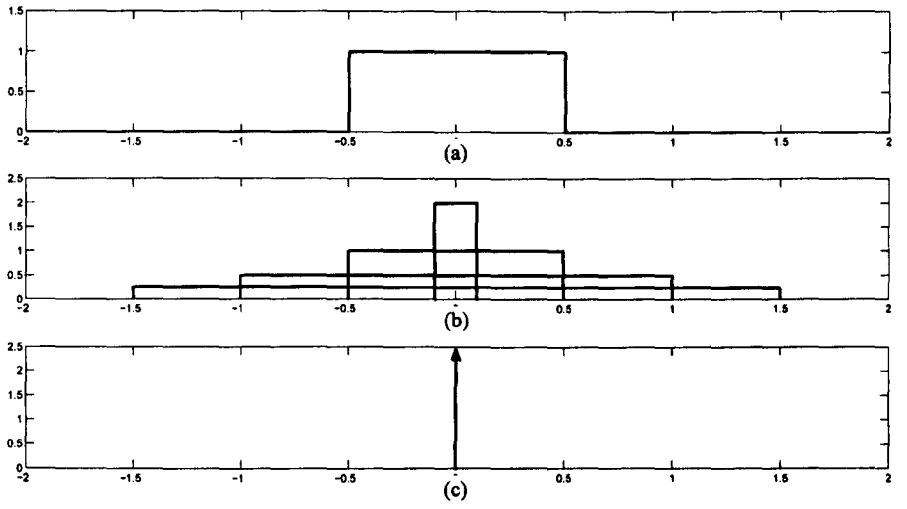

Figure 3.1: (a) A rectangle function as defined by Equation 3.1. (b) Rectangle function scaled in both height and width. (c) In the limit the result is the Dirac Delta function.

$$\delta_n(t) = n\,rect(nt) \tag{3.2}$$

In this sequence each function has the same area but has an increasing height which tends to infinity as $n \rightarrow \infty$ (Figure 3.1(b)). The limit case of this sequences of functions is a rectangle with infinite height but zero width (Figure 3.1(c)) and is usually denoted by $\delta(t)$ This explanation yields to the definition of the Dirac Delta function as follows:

$$\int_{-\infty}^{\infty} \delta(t)\,dt = 1 \tag{3.3}$$

The importance of the Dirac Delta function lies in its *sampling* property (McGillem and Cooper, 1974). Thus, taking into account that $\delta(t - t')$ is an impulse shifted to the location $t = t'$, the sampling property states that:

$$\int_{-\infty}^{\infty} x(t)\delta(t - t')\,dt = x(t') \tag{3.4}$$

That is, when the Dirac Delta enters into a product with an arbitrary signal $x(t)$ all the values of $x(t)$ outside the location $t = t'$ are disregarded.

3.2.1.2 Line Integrals and Projections

As the own name implies, a line integral represents the mathematical integral of some parameters of an object along a particular line or trajectory. In the case of a combustion flame and optical tomography, this property is the light coming from inside the flame as a product of all individual ignition processes produced by different reactions.

Figure 3.2 depicts a coordinate system that describes line integrals and projections. The object is represented mathematically by a bi-dimensional function $f(x, y)$ and each line integral by the parameters (θ, t). The equation of the line AB in Figure 3.2 (Kak, 1979) is:

$$x \cos\theta + y \sin\theta = t \tag{3.5}$$

This relation can be used to define the projection $P_\theta(t)$ as:

$$P_\theta(t) = \int_{(\theta,t)line} f(x, y)\, ds \tag{3.6}$$

Using the Dirac Delta function, the projection of an object can be re-defined as:

$$P_\theta(t) = \int_{-\infty}^{\infty}\int_{-\infty}^{\infty} f(x, y)\delta(x \cos\theta + y \sin\theta - t)\, dx\, dy \tag{3.7}$$

The function $P_\theta(t)$ is then known as the *Radon* transform of the function $f(x, y)$ A projection is therefore formed by the combination of a set of line integrals. The simplest projection and the type utilised in this study is a collection of parallel ray integrals as given by $P_\theta(t)$ and depicted in Figure 3.3 (Rosenfeld and Kak, 1982).

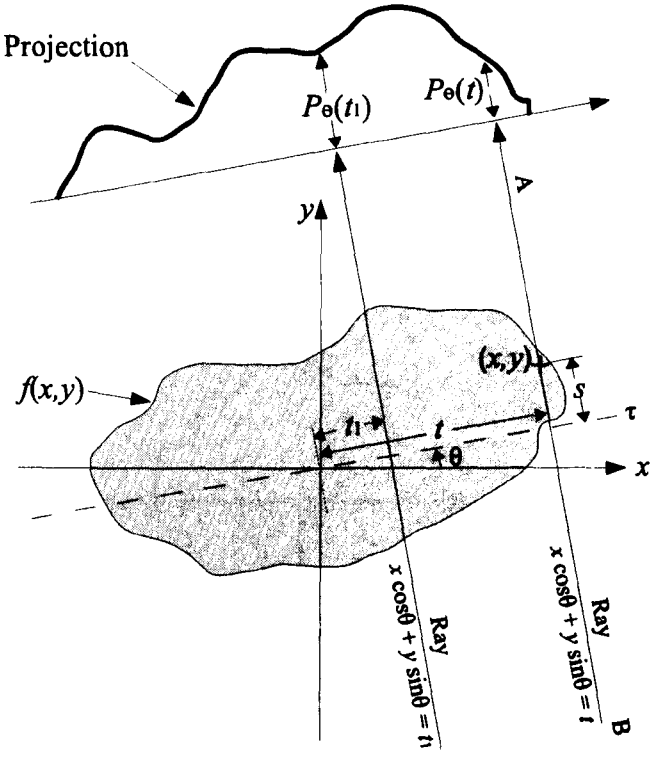

Figure 3.2: An object $f(x, y)$ and its projection $P_\theta(t_i)$ for an angle θ (Kak, 1979)

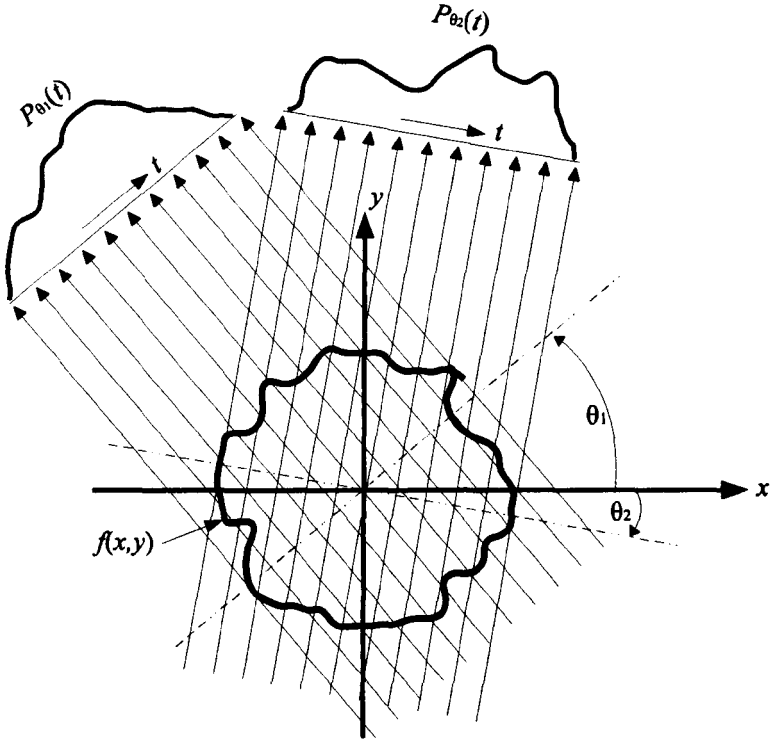

Figure 3.3: Parallel projections taken by measuring a set of parallel rays for a number of different angles (Rosenfeld and Kak, 1982)

3.2.1.3 Finite Fourier Transform

Although the Fourier Transform is a continuous transformation useful in many theoretical discussions, in practice, this transformation is implemented using computers utilising its finite version, the Finite Fourier Transform which is defined as:

$$X_k = \sum_{n=0}^{N-1} x_n e^{-\frac{2\pi i}{N}kn}, \quad k = 0, 1, 2, \cdots, N-1 \tag{3.8}$$

The different x_n are the discrete elements of the continuous function $x(t)$ sampled at regular intervals of τ in the time domain. Therefore, the sequence:

$$x_0, x_1, x_2, \cdots, x_{N-1} \tag{3.9}$$

is completely equivalent to the discrete function:

$$x(0), x(\tau), x(2\tau), \cdots, x((N-1)\tau) \tag{3.10}$$

The inverse finite Fourier transform is defined by:

$$x_n = \frac{1}{N} \sum_{k=0}^{N-1} X_k e^{\frac{2\pi i}{N}kn}, \quad n = 0, 1, 2, \cdots, N-1 \tag{3.11}$$

3.2.1.4 The Fourier Slice Theorem

To derive the Fourier Slice Theorem it is necessary to define the two dimensional Fourier Transform of an object function $f(x, y)$ as:

$$F(t, \theta) = \int_{-\infty}^{\infty} \int_{-\infty}^{\infty} f(x, y)\, e^{-2\pi i(tx+\theta y)} dx\, dy \tag{3.12}$$

Equally, for a projection of the object function $f(x, y)$ at an angle θ, $P_\theta(t)$ (see Figure 3.2), its Fourier transform is defined by:

$$S_\theta(\omega) = \int_{-\infty}^{\infty} P_\theta(t)\, e^{-2\pi i\omega t} dt \tag{3.13}$$

The simplest case of the Fourier slice theorem is presented for the projection at $\theta = 0$. The Fourier transform now simplifies to:

$$F(t, 0) = \int_{-\infty}^{\infty} \int_{-\infty}^{\infty} f(x, y)\, e^{-2\pi itx} dx\, dy \tag{3.14}$$

In this way, the integral can be split now in two factors:

$$F(t, 0) = \int_{-\infty}^{\infty} \left[\int_{-\infty}^{\infty} f(x, y) dy \right] e^{-2\pi itx} dx \tag{3.15}$$

For the given angle $\theta = 0$ the projection along lines of constant x is:

$$P_{\theta=0}(x) = \int_{-\infty}^{\infty} f(x, y) dy \tag{3.16}$$

Substitution of Equation 3.16 into Equation 3.15 gives the expression:

$$F(t, 0) = \int_{-\infty}^{\infty} P_{\theta=0}(x) e^{-2\pi itx} dx \tag{3.17}$$

The right hand side of the expression above is the one dimensional Fourier transform of the projection at $P_{\theta=0}$. Considering Equation 3.13 it is possible to write the following relationship:

$$F(t, 0) = S_{\theta=0}(t) \tag{3.18}$$

Clearly this result is independent of the orientation between the object and the co-ordinate system and results in the simplest form of the Fourier slice theorem which states (Kak, 1985):

> "The Fourier transform of a parallel projection of an image $f(x, y)$ taken at angle θ gives a slice of the 2-D transform, $F(t, \theta)$, subtending an angle θ with the t-axis."

In other words, The Fourier Slice Theorem relates the Fourier Transform of a projection to the Fourier transform of the object along a radial line (Pan and Kak, 1983) in such a way that the 1-D Fourier Transform of the projection is equivalent to a 2-D Fourier Transform of the object function.

3.2.2 Filtered Back-Projection Algorithm

The Fourier Slice Theorem relates the 2-D Fourier Transform of the projection of an object to a 1-D Fourier Transform of an object along a single radial line. This result sets conceptually the possibility of reconstructing an object from its projection. If there are enough projections of this object, they could be assembled to completely estimate the 2-D Fourier Transform of the whole object and then simply invert this transform to reach an estimate the real object. However, despite of this easy theoretical basis, practical implementations are more complex.

The Filtered Back-Projection algorithm (FBP) is one of the most utilised algorithms. It has proven to be highly accurate, fast and reliable and it is derived from the Fourier Slice algorithm. As Kak and Slaney (1988) states:

> "The derivation of this algorithm is perhaps one of the most illustrative examples of how we can obtain a radically different computer implementation by simply rewriting the fundamental expressions for the underlying theory."

3.2.2.1 Theoretical Approach to the FBP Algorithm

The FBP algorithm presents two major advantages. First, the reconstruction process can be started as soon as the first projection is measured. In this way, the reconstruction is accelerated and the amount of data that is necessary to store at any moment is reduced. Secondly, during the reconstruction process interpolation is often necessary. If so, it is more efficient to perform this interpolation in the space-domain provided by FBP than the frequency domain related to the Fourier Transform (Stark et al., 1981). As the name implies, the FBP algorithm contains two clearly defined parts: the filtering part and the back-projection part. The filtering consists of a simple weighting of each projection. This weighting is performed in the frequency domain. The simplest way to perform this weighting is to take the value of the Fourier Transform of the projection, $S_\theta(\omega)$ and multiply it by the 'width' of the projection at that frequency. Therefore, if there are K projections over 180° then at a given frequency ω each projection has a width $2\pi|\omega|/K$. On the other hand, the back-projection part is comparable to obtaining the elemental reconstruction corresponding to each projection.

The FBP algorithm can be completely described following these steps:

(a) Measure the projections $P_\theta(t)$ for the K angles between 0 and 180°.

(b) Find $S_\theta(\omega)$, the Fourier Transform of each $P_\theta(t)$.

(c) Multiply each $S_\theta(\omega)$ by the weighting factor $2\pi|\omega|/K$.

(d) Perform the back-projection process, i.e.: sum over the image plane the inverse Fourier Transforms of the filtered projections.

3.2.2.2 Mathematical Approach to the FBP Algorithm

Reconsidering the 2-D inverse Fourier transformation of the object function, $f(x,y)$ can be expressed in general terms as:

$$f(x,y) = \int_{-\infty}^{\infty}\int_{-\infty}^{\infty} F(u,v)e^{2\pi i(ux+vy)}du\,dv \tag{3.19}$$

Changing the Cartesian coordinates system in the frequency domain (u,v) for a polar coordinate system (ω,θ):

$$\begin{aligned} u &= \omega\cos\theta \\ v &= \omega\sin\theta \end{aligned} \tag{3.20}$$

the differential $du\,dv$ becomes:

$$du\,dv = \omega\,d\omega\,d\theta \tag{3.21}$$

By substituting Equation 3.20 and Equation 3.21 into Equation 3.19 the inverse Fourier Transform of the object function can be written in polar form as:

$$f(x,y) = \int_0^{2\pi}\int_0^{\infty} F(\omega,\theta)e^{i2\pi\omega(x\cos\theta+y\sin\theta)}\,\omega\,d\omega\,d\theta \tag{3.22}$$

The above integral can be split into two considering the two complementary ranges of θ from 0 to 180° and then from 180° to 360°:

$$\begin{aligned} f(x,y) &= \int_0^{\pi}\int_0^{\infty} F(\omega,\theta)e^{i2\pi\omega(x\cos\theta+y\sin\theta)}\,\omega\,d\omega\,d\theta \\ &= +\int_0^{\pi}\int_0^{\infty} F(\omega,\theta+180°)e^{i2\pi\omega[x\cos(\theta+180°)+y\sin(\theta+180°)]}\,\omega\,d\omega\,d\theta \end{aligned} \tag{3.23}$$

Considering the property:

$$F(\omega,\, \theta + 180°) = F(-\omega, \theta) \tag{3.24}$$

The expression of $f(x, y)$ indicated above in Equation 3.23 can be rewritten as:

$$f(x,y) = \int_0^{\pi} \left[\int_{-\infty}^{\infty} F(\omega,\theta)|\omega| e^{i2\pi\omega t}\, d\omega \right] d\theta \tag{3.25}$$

where the expression has been simplified by defining the substitution (Figure 3.2):

$$t \equiv x\cos\theta + y\sin\theta \tag{3.26}$$

Substituting the 2-D Fourier Transform $F(\omega, \theta)$ by the 1-D Fourier Transform of the projection $P_\theta(t)$ at an angle θ, $S_\theta(\omega)$, defined in Equation 3.13 (Fourier Slice theorem) the above equation can be expressed as:

$$f(x,y) = \int_0^{\pi} \left[\int_{-\infty}^{\infty} S_\theta(\omega)|\omega| e^{i2\pi\omega t}\, d\omega \right] d\theta \tag{3.27}$$

Finally, the integral in 3.27 can be simplified as:

$$f(x,y) = \int_0^{\pi} Q_\theta(t)\, d\theta \tag{3.28}$$

where:

$$Q_\theta(t) = \int_{-\infty}^{\infty} S_\theta(\omega)|\omega| e^{i2\pi\omega t}\, d\omega \tag{3.29}$$

Equation 3.28 estimates the object function $f(x, y)$ given the transforms of the projections $S_\theta(\omega)$. Equation 3.29 represents the filtering operation of the projection in the frequency domain where the frequency response of the filter is given by $|\omega|$. For this reason $Q_\theta(t)$ is called the *filtered projection.* These filtered projections are then 'back-projected', that is, added to form the estimate of $f(x, y)$.

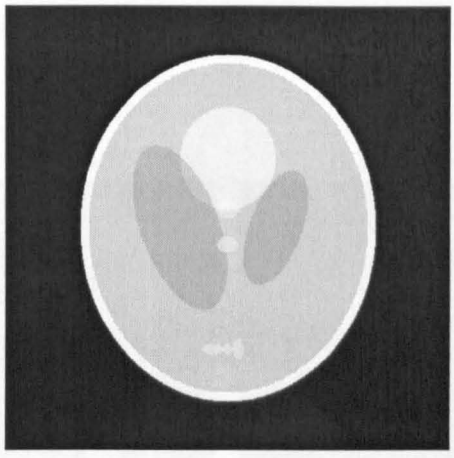

Figure 3.4: A created digital version of the Shepp-Logan head phantom.

In other words, every point (x, y) in the object (Figure 3.2) has associated a value of $t = x\cos\theta + y\sin\theta$ for a given value of θ, and the filtered projection $Q_\theta(t)$ contributes to the reconstruction at this value of t. The filtered projection, $Q_\theta(t)$, will make the same contribution to the reconstruction at all of these points. Therefore, it is possible to say that in the reconstruction process each filtered projection, $Q_\theta(t)$, is smeared back, or back-projected, over the image plane (Rosenfeld and Kak, 1982).

Equation 3.28 shows that the perfect estimation of the object function $f(x, y)$ is performed by using an integral operation. That is, to perfectly calculate $f(x, y)$ it would be necessary the addition of an infinitive number of projection separated by infinitesimally small angle. In practice this is impossible as only a finite number of projections is possible but Equation 3.28 still indicates that obtaining a higher number of projections will increase the quality of the reconstruction. This fact can be graphically described as it has been studied in this work. Figure 3.4 shows an *ex professo* digital version of the well known Shepp and Logan (1974) head phantom. Figure 3.5 shows the results of reconstructing this head phantom using the FBP algorithm. This was performed in the laboratory using bespoke software being the original template to reconstruct 256×256 pixels big. As it can be seen, the larger is

the number of projections taken, the better is the reconstruction using this algorithm as expected according to Equation 3.28.

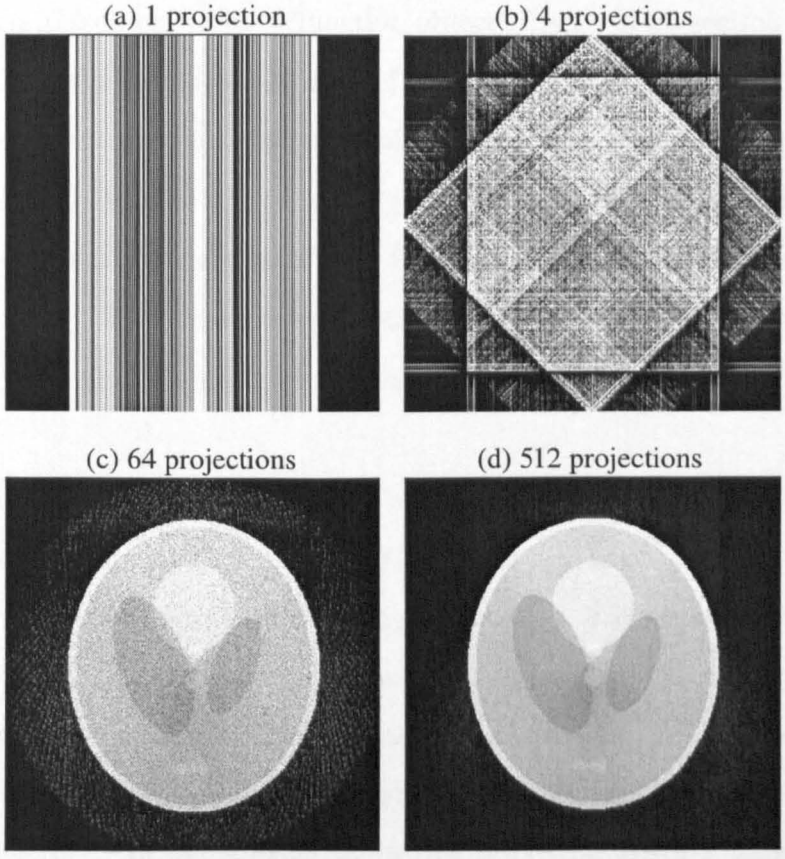

Figure 3.5: The result of reconstructing the Shepp and Logan head phantom in Figure 3.4 using the FBP algorithm is shown here. (a) Using 1 projection only. (b) Using 4 projections. (c) Using 64 projections and (d) Using a total of 512 projections. All the projections were taken on an equiangular basis from angles between 0 and 180°.

3.2.3 Algebraic Reconstruction Technique

The Algebraic Reconstruction Technique (ART) is a very different approach to FBP. ART considers the object to be a 'function object'. Every cross-section of this function object is considered to be an array of unknowns and ART sets up the required algebraic equations to find out the values of these unknowns. This is all done in terms of the measured data from a set of given projections. In this method, it is essential to know the 'ray paths' that connect the function object and the sensors utilised to measure the data. The provided equations are solved using the Kaczmarz method (Kaczmarz, 1937) first introduced in tomography by Gordon et al. (1970).

Figure 3.6 shows graphically the basics of the functioning of the ART. A grid is 'superimposed' over the object function $f(x, y)$. In this work, this grid consisted in reality of an array of computer double length variables. It is assumed that the value of $f(x, y)$ remains constant in each cell. Let us consider that f_j is this constant value inside the jth cell and let N be the total number of cells. In ART a ray path is defined as a line running through the (x, y)-plane with a non zero width whose value can be written as τ. In many cases, as in this work, the width τ is consider to be equal to the width of a cell. For instance, in this work τ was consider to be as wide as an image pixel. A line integral is now called a *ray-sum.*

Let p_i be the ray-sum measured within the ith ray (Figure 3.6). The equation relating f_j and p_i can be expressed as:

$$\sum_{j=0}^{N} w_{ij} f_j = p_i; \quad i = 1, 2, \cdots, M \tag{3.30}$$

where M is the total number of rays including all the projections and w_{ij} is the weighting factor that represents the contribution of the jth cell to the ith ray integral. There are different ways to calculate the values of the weighting factors w_{ij}. The

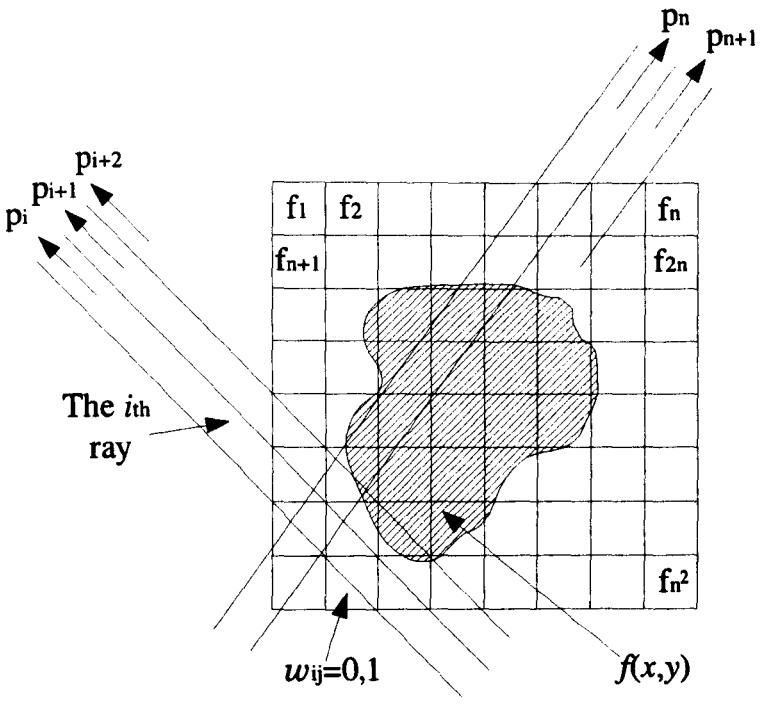

Figure 3.6: In the ART a square grid is superimposed over the object function $f(x, y)$. The image values are assumed to be constant within each cell of the grid (Rosenfeld and Kak, 1982).

simplest and utilised in this study is to consider its value either 0 or 1. The value is 1 if ray passes through the centre of the corresponding cell of the grid and 0 if it does not pass through. The Kaczmarz method, was also called *method of projections* by Tanabe (1971) who clarified the process in a more illustrative and clear way. The method can be explained rewriting the Equation 3.30 in an expanded form:

$$\begin{array}{ccccccccccc} w_{11}f_1 & + & w_{12}f_2 & + & w_{13}f_3 & + & \cdots & + & w_{1N}f_N & = & p_1 \\ w_{21}f_1 & + & w_{22}f_2 & + & w_{23}f_3 & + & \cdots & + & w_{2N}f_N & = & p_2 \\ \vdots & & & & & & & & & & \vdots \\ w_{M1}f_1 & + & w_{M2}f_2 & + & w_{M3}f_3 & + & \cdots & + & w_{MN}f_N & = & p_M \end{array} \tag{3.31}$$

When a total of N cells are given in the grid, the function object $f(x, y)$ may contain a maximum of N elements. Therefore, there are N degrees of freedom. A vector

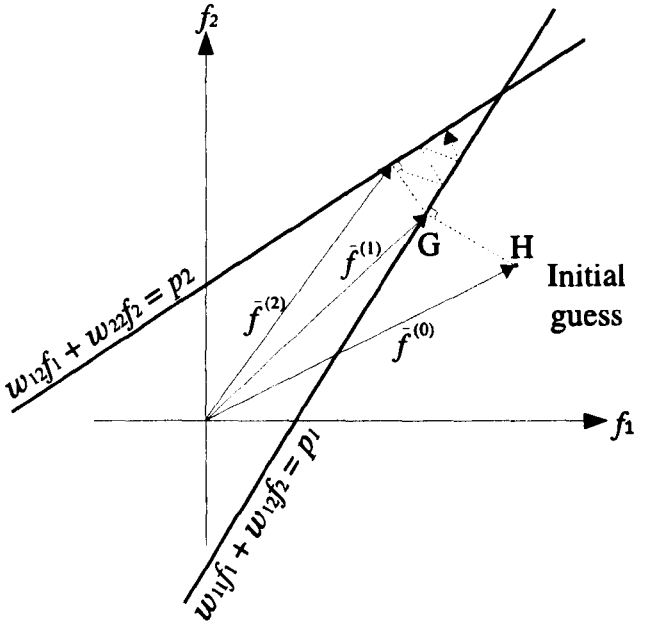

Figure 3.7: The Kaczmarz method of solving algebraic equations is illustrated for the case of two unknowns (Rosenfeld and Kak, 1982).

$(f_1, f_2, \cdots, f_N)$ representing the values of $f(x, y)$ may be considered a single point in an N-dimensional space in which, any of the above equations represent an *hyperplane*. If there is an unique solution, the intersection of all these hyperplanes is a single point in the space. This point gives the solution. Figure 3.7 depicts this concept where for simplicity purposes the total number of degrees of freedon, N, has been reduced to 2 and the values f_1 and f_2 satisfy the following expressions:

$$\begin{aligned} w_{11}f_1 + w_{12}f_2 &= p_1 \\ w_{21}f_1 + w_{22}f_2 &= p_2 \end{aligned} \tag{3.32}$$

As shown in Figure 3.7, the computational procedure consists of obtaining an initial guess solution point, H, and then project it onto the first hyperplane corresponding to the first equation. The resulting point is then projected onto the second hyperplane corresponding to the second equation and then projected back onto the first

hyperplane in a process that is repeated back and forth. If there is an unique solution the iterations will converge to the intersection point in the space.

To perform the computer implementation of the Kaczmarz method, an initial soluetion is guessed. This guess solution can be denoted by $f_1^{(0)}, f_2^{(0)}, \cdots f_N^{(0)}$ and represented in vector notation as $\vec{f}^{(0)}$ in N-dimensional space. In many cases, it is enough to assign the value of zero to all the elements f_i. Then, this initial guess is projected onto the first hyperplane represented by the first equation in 3.31 to obtain $\vec{f}^{(1)}$. Then, $\vec{f}^{(1)}$ is projected onto the second hyperplane represented by the second equation in 3.31 to obtain $\vec{f}^{(2)}$. This process is repeated for all the equations in 3.31. For the general case and the ith step, when the intermediate solution $\vec{f}^{(i-1)}$ is projected onto the hyperplane represented by the ith equation in 3.31 to obtain $\vec{f}^{(i)}$, the process can be mathematically described as:

$$\vec{f}^{(i)} = \vec{f}^{(i-1)} - \frac{(\vec{f}^{(i-1)} \cdot \vec{w}_1 - p_i)}{\vec{w}_1 \cdot \vec{w}_1} \vec{w}_1 \tag{3.33}$$

where $\vec{w}_i = (w_{i1}, w_{i2}, \cdots, w_{iN})$ and $\vec{w}_i \cdot \vec{w}_i$ is the dot product of $\vec{w}_i$ with itself.

3.2.4 A Comparison of FBP with ART

This section deals with the direct comparison of the two techniques described above: FBP and ART. This comparison was a genuine experiment performed as part of the work described in this thesis and aimed to study in detail which algorithm was more suitable to accomplish well under the required constraints. To achieve the task a bespoke computer program was created. This program was capable of utilising the two algorithms independently to reconstruct separately a digital template simulating a cross-section. The template utilised was the digital head phantom shown in Figure 3.4, a 256 × 256 pixels square with completely black background and a 'head' composed of ten grey ellipses with 8-bits grey levels ranging from 0 to 255. The pro-

gram was made with C language and the Matrox® MIL-Lite graphical library. The process of reconstructing the original template using both algorithms independently was repeated several times to study their performance under different conditions based on the total number of projections possibly measured. The cases studied were: 3, 6, 8, 16, 32, 64, 128 and 256 projections taken on an equiangular basis within the range from 0° to 180°. The complete process performed by the program can be summarised as follows:

(a) Load and display the digital head phantom template Figure 3.4.

(b) Select the number of projections requested.

(c) Rotate mathematically the original digital values of the template the necessary number of times the required angle to measure the requested number of projections.

(d) Measure the projections by simple addition of all the digital values of the rotated template along every parallel projection ray (see Figure 3.3).

(e) Store these projections in the computer memory.

(f) Perform either the FBP or ART reconstruction.

(g) Display the reconstructed template.

(h) Estimate the quality of the reconstruction by calculation of the correlation coefficient between the original and the reconstructed template and the mean absolute error.

(i) Display and save the data obtained.

Figure 3.8 depicts and compares graphically the reconstructions performed by FBP and ART respectively. It can be seen that for a reconstruction with a number of

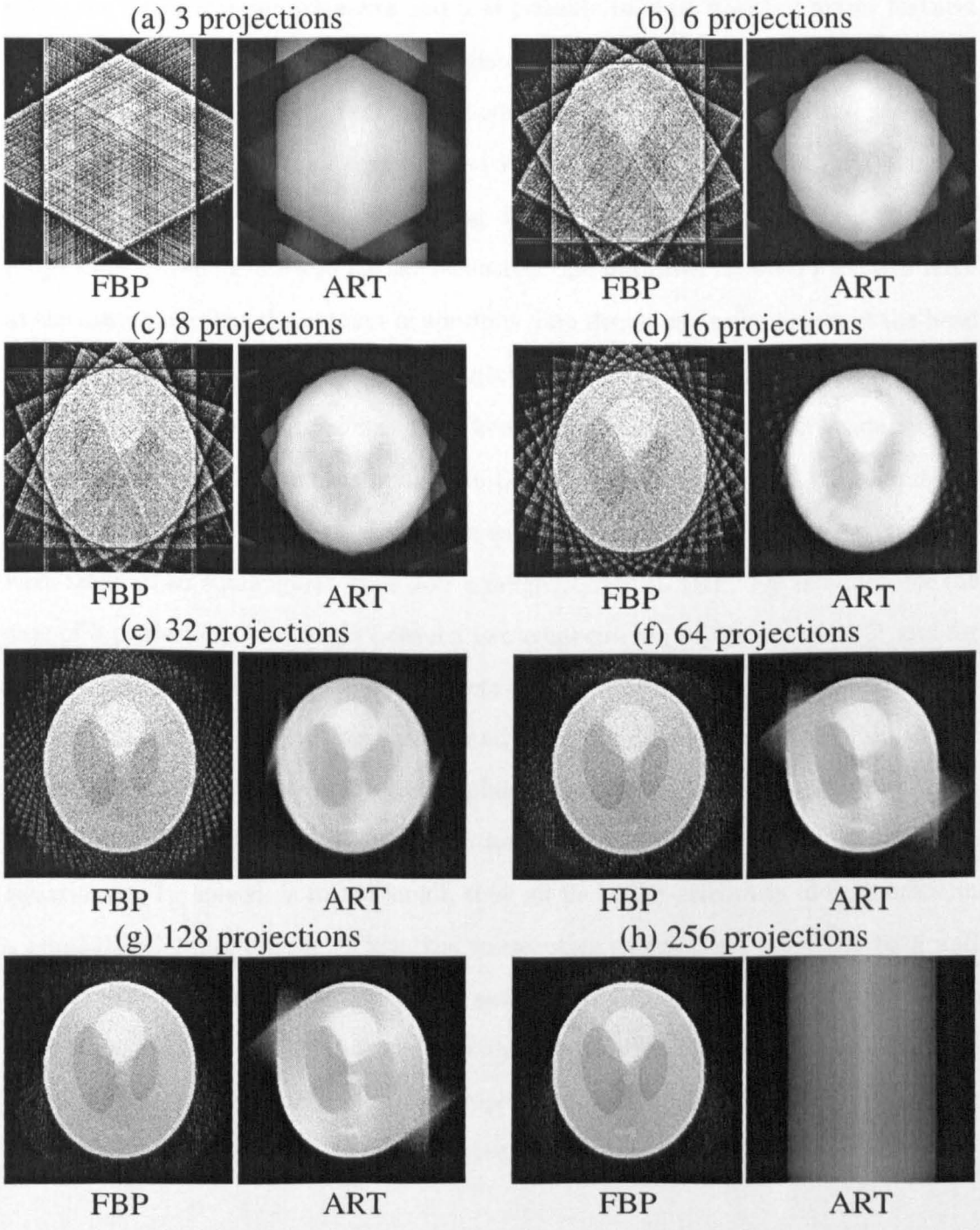

Figure 3.8: A comparison of FBP vs. ART using the digital head phantom as original template source (see Figure 3.4).

projections as low as 3, both FBP and ART perform poorly. For the case of 6 projections, the reconstruction improves and it is possible to start noticing major features of the Shepp-Logan heap phantom. Significant spurious reconstructed results can be observed in the outers of the template in positions placed outside the head phantom. FBP presents more *salt and pepper* noise and the spurious results in ART seem to be weaker and easier to remove by using digital image process. As the number of projections increases to 8 and 16, the reconstruction improves for both FBP and ART at the same time that the amount of spurious data decreases in the outers of the head phantom. For the cases of 32 and 64 projections, it is noticeable a divergence in the behaviour of the two algorithms. FBP keeps improving the reconstruction as it is expected theoretically from the integral in Equation 3.28. However, ART commences to yield poorer results. This is due to the way that the projections were taken. They were taken in an equiangular basis over a range from 0° to 180°. For instance, for the case of 3 projections, the angle between two consecutive projections was 50° and for the case of 6 projections, 30°. So, for the cases of 32 and 64 projections, the separation between consecutive projections is 5.6° and 2.8° respectively, rather small numbers. Paying attention to Figure 3.7, which explains graphically the actions taken by ART, it can be realised that when the separation between the hyperplanes, that is, the equations to be solved, is rather small, they all lie in the proximity of each other in a quasi-parallel distribution. Then, the consecutive calculations projected back and forth from one hyperplane to another do not 'advance' as fast as desirable and finally do not reach the unique. The final calculation ends up substantially far from the solution. For the cases of 128 and 256 projections, FBP maintains the improvements while ART keeps providing deteriorated reconstructions under the given conditions.

This graphical comparison can also be checked against a profound mathematical and numerical scrutiny of the two algorithms. Given that the grey values of the digital

Shepp-Logan template are known, they can be numerically compared one by one to those given by the algorithms.

The correlation coefficient in Figure 3.9 shows the statistical relation between the reconstructed images and the original head phantom template. The correlation coefficient gives the quality of the *least-square* fitting to the original data. The trend observed in the graph demonstrates the good behaviour of ART for a low number of projections, with correlation coefficient up to 0.93 for only 6 projections. FBP commences providing poor reconstructions for low numbers of projections but gradually improves its performance to overtake ART at the proximities of 50 projections. From this point, FPB continues enhancing its execution indefinitely but decelerated. On the other hand, the quality of the reconstruction provided by ART stabilises first to collapse subsequently. The mean absolute error in Figure 3.10 measures how close reconstructed data are to the original. The mean absolute error, as the name suggest, is the average of the absolute value of the difference measured pixel by pixel. As before, around the number of 50 projections there is a variety of *break-even* point. FBP overtakes ART providing minor errors regular and continuously as the inaccuracy of ART increases dramatically.

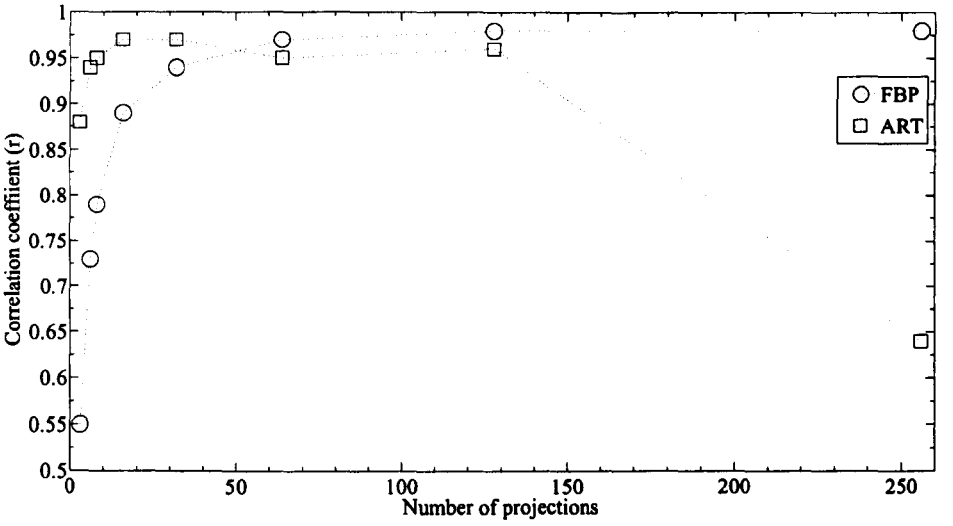

Figure 3.9: Correlation coefficient between reconstructed data from FBP and ART and the original digital Shepp-Logan head phantom. The correlation coefficient is measured in both cases against the number of projections taken on an equiangular basis over the range 0° and 180°.

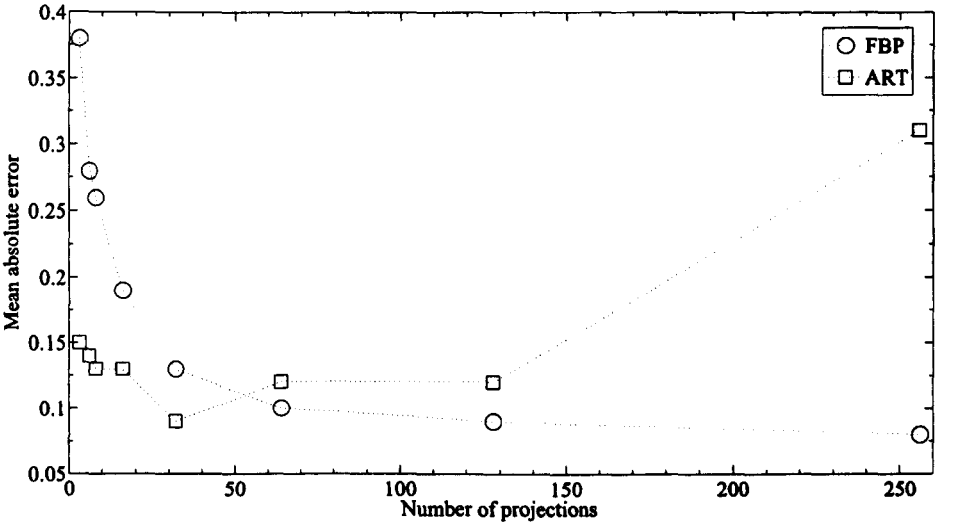

Figure 3.10: Mean absolute error between reconstructed data from FBP and ART and the original digital Shepp-Logan head phantom. The mean absolute error is measured in both cases against the number of projections taken on an equiangular basis over the range 0° and 180°.

3.3 Flame and the Two-colour Method

3.3.1 Radiation Spectra of a Flame

The spectral emissions from a flame consist essentially of banded spectra and continuous spectra (see Figure 3.11). The banded spectra are caused by electronics transitions and simultaneous changes in the internal vibrational and rotational energy of gas molecules such as CO_2 and H_2O and intermediate species like OH, CH, C_2 and CN formed in the primary combustion zone. Continuous spectra are due to the radiation from incandescent carbon particles, which are generated when a fuel-air mixture is heated under locally oxygen deficient conditions.

Gaydon (1974) presented the distribution of main banded spectra of a flame. The band spectra of CO_2 and H_2O lie in the infra-red region with band heads at $4.4\mu m$ and $2.8\mu m$ respectively. There are a number of other weak banded features due to CO_2 and H_2O. The band spectra in the visible region result mainly from the CH and C_2 radicals. CH bands have the band heads at 387.1 nm and 431.4 nm, while the C_2 bands at 473.7, 516.5 and 563.6 nm. Emission from OH radical lies in the ultra-violet region with the band heads of 260.8, 281.1, 306.6 and 342.8 nm. The continuous spectrum exists throughout the whole visible infra-red regions.

On the other hand, in order to calculate the temperature of a flame, it is possible to evaluate the continuous spectral properties of the soot particles inside the flame. The best known related technique implies the measuring of the radiation intensity emitted from the incandescent carbon particles at two different wavelengths and it is so called the *two-colour* method. Therefore, the temperature obtained by this procedure is actually the one of soot particles inside the flame rather than the one of gas molecules. The difference between them will be discussed in Section 3.3.3.

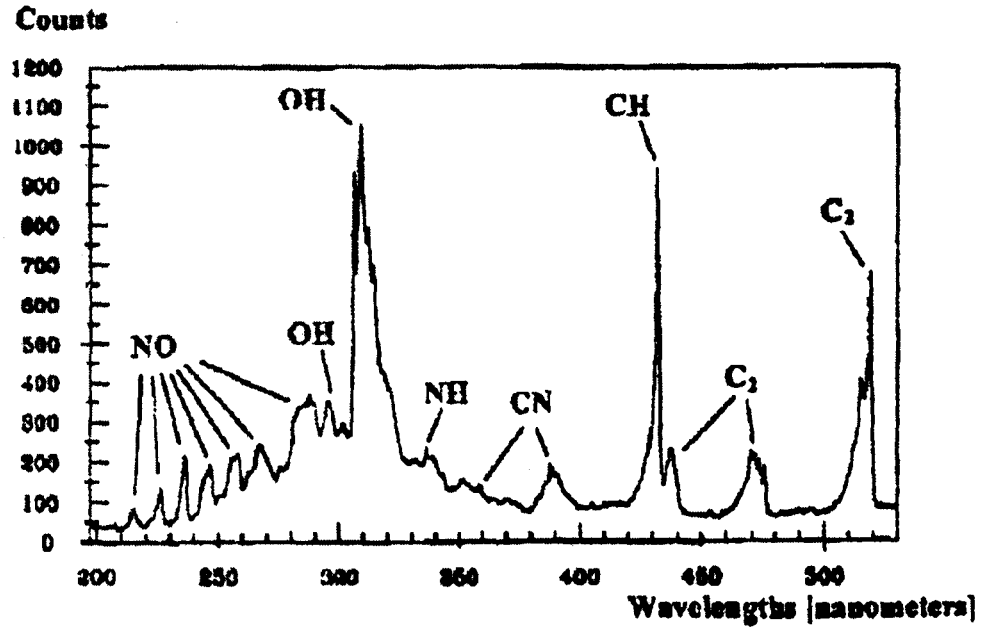

Figure 3.11: Emission spectrum of an ammonia-doped butane flame Leipertz et al. (1996).

The continuous radiation from a solid surface is related to the black-body radiation and governed by Plank's radiation law. Since the band radiation from gas molecules and free radicals do not fit the Plank's radiation law, the two-colour method ideally should avoid detecting the radiation from gas molecules and free radicals.

It is worth to mention that the radiation spectra of a flame depend also on the type of fuel. Figure 3.12 displays the radiation spectra for gas, oil and coal flames compared to blackbody radiation at 1650°C (Willson and Chappell, 1985; Jackson and Bulger, 1987). It can be seen from Figure 3.12 that gas flames exhibit a more distinctively banded structure, while the coal and oil flames have a better nature of continuous radiation.

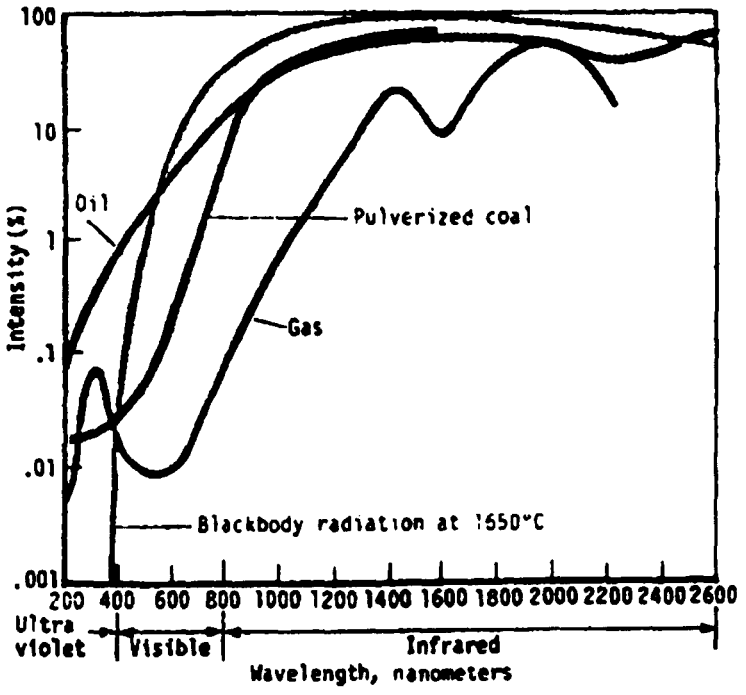

Figure 3.12: Radiation spectra for gas, oil and coal flames compared to blackbody radiation. (Willson and Chappell, 1985; Jackson and Bulger, 1987)

3.3.2 The Two-colour Method

Planck's law states that the spectral radiance of a black body as a function of frequency and temperature for all wavelengths is given by equation 3.34

$$\mathscr{I}(\nu, T) = \frac{2h\nu^3}{c^2} \frac{1}{e^{\frac{h\nu}{kT}} - 1} \tag{3.34}$$

where:

$\mathscr{I}(\nu, T)$ is the emitted power per unit area of emitting surface, per unit solid angle and per unit frequency.

ν is the frequency of the radiation (Hz).

T is absolute temperature of the black body (K).

h is the Planck's constant $(6.626\ 068\ 93(33) \times 10^{-34} J \cdot s)$.

c is the speed of light [299 792 458 $m \cdot s^{-1}$].

k is the Boltzman's constant, sometimes also referred to as k_B (1.380 650 4(24) $\times 10^{-23} J \cdot K^{-1}$).

As a function of wavelength λ, Planck's law is written as:

$$\mathscr{I} = (\lambda, T) = \frac{2hc^2}{\lambda^5} \frac{1}{e^{\frac{hc}{\lambda kT}} - 1} \tag{3.35}$$

Sometimes, Planck's law is written as $\mathscr{E}(\lambda, T) = \pi \cdot \mathscr{I}(\lambda, T)$ for the spectral emitted power integrated over all solid angles:

$$\mathscr{E}(\lambda, T) = \frac{C_1}{\lambda^5} \frac{1}{e^{\frac{C_2}{\lambda T}} - 1} \tag{3.36}$$

where:

$C_1 \equiv 2\pi hc^2$ [$3.742 \times 10^{-16} W \cdot m^2$].

$C_2 \equiv hc/k$ [$1.4385 \times 10^{-2} m \cdot K$].

Figure 3.13 depicts the spectral emitted power of a black body shown in equation 3.36 for a range of five different temperatures. The following general characteristics can be remarked:

(a) For a given temperature, the spectral emitted power reaches a single peak.

(b) As the temperature increases, the spectral emitted power rises for all wavelengths.

(c) The wavelength, at which the spectral emitted power peaks, decreases as temperature raises.

For a selected range of temperatures, 1000 - 3000 K, near the flame temperature bounds, Figure 3.14 illustrates spectral emitted power in the ultraviolet, visible and infrared regions. The power emitted increases with wavelength in the ultraviolet and

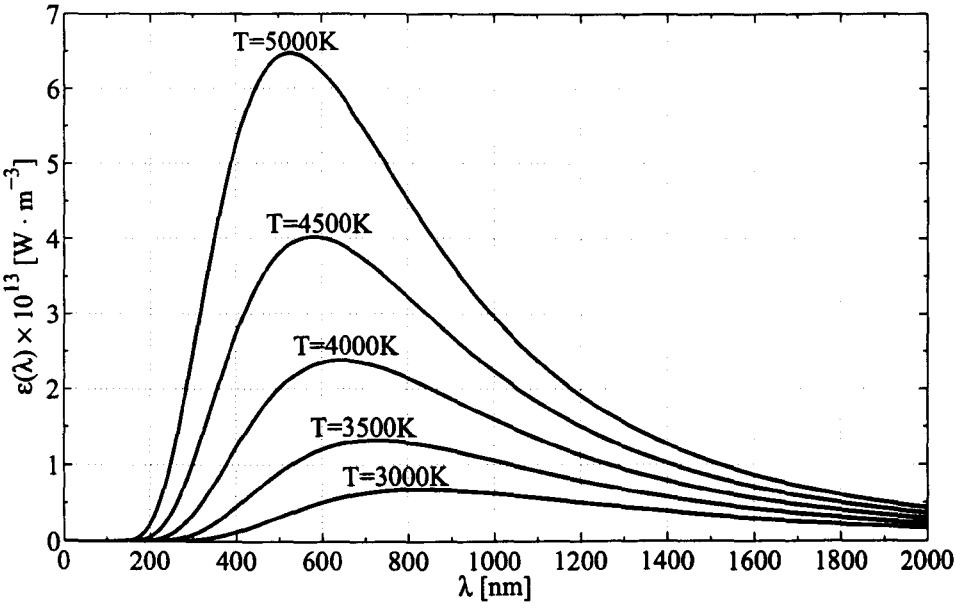

Figure 3.13: Spectral emitted power of a black body.

visible region, i.e., the rate $\partial\mathscr{E}/\partial\lambda$ is substantially higher in the ultraviolet and visible region than in the infrared region. The increment of power emitted with temperature, $\partial\mathscr{E}/\partial T$, is also significantly higher in the ultraviolet and visible regions than that in the infrared region.

For the range of selected temperatures, 1000 - 3000 K, and throughout the visible region, 380 - 750 nm, the exponential term in equation 3.36, $e^{C_2/\lambda T} \gg 1$. Therefore, equation 3.36 can be replaced by the Wien's approximation:

$$\mathscr{E}(\lambda, T) = \frac{C_1}{\lambda^5} e^{-C_2/\lambda T} \tag{3.37}$$

being,

$$\frac{1}{e^{C_2/\lambda T} - 1} \approx e^{-C_2/\lambda T} \tag{3.38}$$

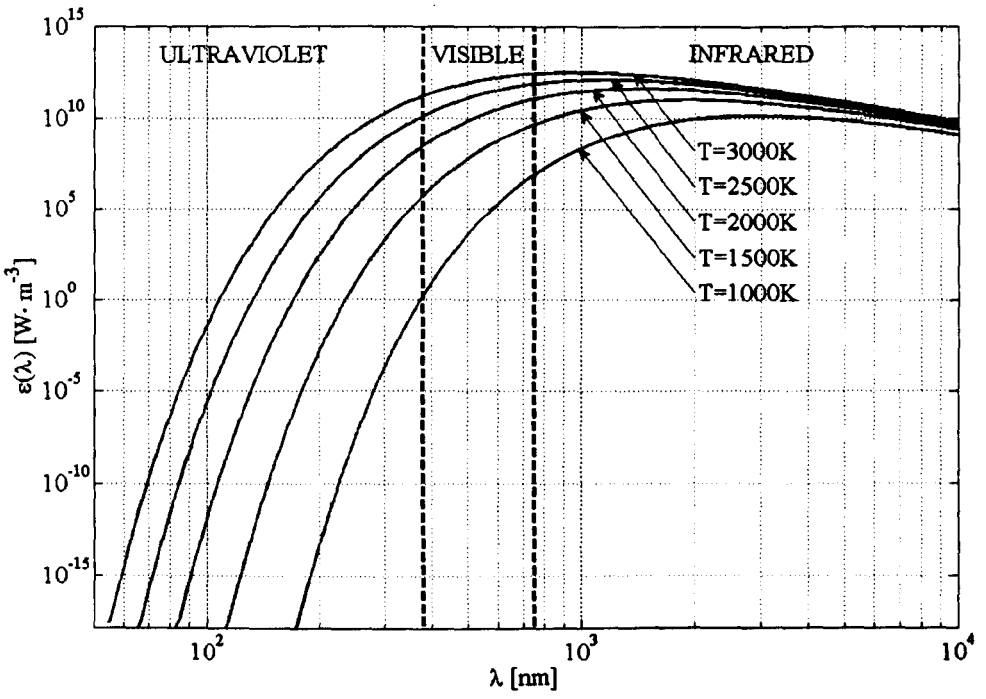

Figure 3.14: Spectral emitted power of a black body for a selected range of temperatures in the ultraviolet, visible and infrared regions. (Huang, 2001).

The radiation of a soot particle at an specific temperature in a flame is related to the radiation from a black body source at the same temperature. This relation is determined by the spectral emissivity of the soot particle. The size of soot particles inside a flame are usually diminutive with diameters often shorter than the wavelength of detected light. For this reason, the emissivity of soot particles tends to rise towards shorter wavelengths and their spectral emitted power can be expressed by:

$$\mathscr{E}(\lambda, T) = \varepsilon_\lambda \frac{C_1}{\lambda^5} e^{-C_2/\lambda T} \tag{3.39}$$

where ε_λ is the monochromatic emissivity of the soot particle.

The output of every camera of the imaging system is a colour image that is split into its three basic colour components, red, green and blue images. Each of these figures appears as a *black and white* picture being a quasi-monochromatic image. The corresponding grey-level, namely $\mathscr{G}(\lambda, T)$, is proportional to the spectral emitted power of the measured object and dependent on the spectral emissivity of the optical arrangement, namely $\mathscr{S}_\lambda$. Therefore:

$$\mathscr{G}(\lambda, T) = \mathscr{K}_o \cdot \mathscr{S}_\lambda \cdot \mathscr{E}(\lambda, T) \tag{3.40}$$

where $\mathscr{K}_o$ is called the *instrumentation constant* and is independent of wavelength. This constant includes the effects of various influential factors including the radiation attenuation due to absorption of optical components and existing air, length of optical path, camera characteristics and signal conversion. A detailed derivation of Equation 3.40 can be seen in Appendix B.

Since the grey level $\mathscr{G}(\lambda, T)$ is in fact caused by radiation spanning a spectral bandwidth $\Delta\lambda$ centred at λ , $\mathscr{G}(\lambda, T)$ can be expressed by substituting equation 3.39 into equation 3.40:

$$\mathscr{G}(\lambda, T) = \int_{\Delta\lambda} = \mathscr{K}_o \cdot \mathscr{S}_\lambda \cdot \varepsilon_\lambda \cdot \frac{C_1}{\lambda^5} e^{-C2/\lambda T} d\lambda \tag{3.41}$$

The ratio between grey levels at wavelengths λ_1 and λ_2 with bandwidths $\Delta\lambda_1$ and $\Delta\lambda_2$ respectively is given by:

$$\frac{\mathscr{G}(\lambda_1, T)}{\mathscr{G}(\lambda_2, T)} = \frac{\int_{\Delta\lambda_1} \mathscr{K}_o \cdot \mathscr{S}_{\lambda_1} \cdot \varepsilon_{\lambda_1} \cdot \frac{C_1}{\lambda_1^5} e^{-C_2/\lambda_1 T} d\lambda_1}{\int_{\Delta\lambda_2} \mathscr{K}_o \cdot \mathscr{S}_{\lambda_2} \cdot \varepsilon_{\lambda_2} \cdot \frac{C_1}{\lambda_2^5} e^{-C_2/\lambda_2 T} d\lambda_2} \tag{3.42}$$

When $\Delta\lambda_1$ and $\Delta\lambda_2$ sufficiently small, the ratio becomes:

$$\frac{\mathscr{G}(\lambda_1, T)}{\mathscr{G}(\lambda_2, T)} = \frac{\mathscr{S}_{\lambda_1} \cdot \varepsilon_{\lambda_1} \cdot \lambda_2^5 \cdot e^{-C_2/\lambda_1 T} \Delta\lambda_1}{\mathscr{S}_{\lambda_2} \cdot \varepsilon_{\lambda_2} \cdot \lambda_1^5 \cdot e^{-C_2/\lambda_2 T} \Delta\lambda_2} \tag{3.43}$$

Rearranging equation 3.43 yields to a crucial expression to determine the target temperature:

$$T = C_2 \cdot \left(\frac{1}{\lambda_2} - \frac{1}{\lambda_1}\right) \Big/ \left[ln\frac{\mathscr{G}(\lambda_1, T)}{\mathscr{G}(\lambda_2, T)} + ln\frac{\mathscr{S}_{\lambda_2}}{\mathscr{S}_{\lambda_1}} + ln\frac{\varepsilon_{\lambda_2}}{\varepsilon_{\lambda_1}} + ln\left(\frac{\lambda_1}{\lambda_2}\right)^5 + ln\frac{\Delta\lambda_2}{\Delta\lambda_1}\right] \quad (3.44)$$

The relation $\mathscr{G}(\lambda 1, T)/\mathscr{G}(\lambda 2, T)$ can be measured by the cameras of the system, λ_1, λ_2 $\Delta\lambda_1$ and $\Delta\lambda_2$ are known from the design of the system and shown in Figure 4.22. The ratio between the spectral emissivities, $\varepsilon_{\lambda_1}/\varepsilon_{\lambda_2}$, depends on the properties of the soot particles inside the flame which will be discussed in Section 3.3.3. The fraction between the spectral sensitivities, $\mathscr{S}_{\lambda_2}/\mathscr{S}_{\lambda_1}$, is called *instrument factor* for a particular wavelength pair. In principle, the instrument factor could be calculated if all technical details of the system's components were available. However, for practical purposes, the purely secure procedure to calculate the instrument factor value is by experimental calibration utilizing an well-known source of temperature, in this case, a tungsten lamp. More details concerning the calibration procedure will be stated in Section 4.3.3.2.

The importance of equation 3.44 lies in the fact that allows the measurement of temperature based on the signal ratios at two wavelengths. Therefore previous knowledge of the real radiance is not necessary. Equation 3.44 indicates that the three dimensional temperature of a flame can be calculated by taking simultaneous images corresponding to two different wavelengths, utilising those monochromatic images to determine the cross-sectional related values and finally evaluating the correlated grey ratios pixel by pixel.

All parameters in equation 3.44 can be determined easily except the ratio between the spectral emissivities, $\varepsilon_{\lambda_1}/\varepsilon_{\lambda_2}$, which cannot be determined unless some previous knowledge about the fuel and therefore the soot particles is obtained. However, this

problem can be by-passed when the two selected wavelengths λ_1 and λ_2 are close enough. In this case, only a small variation in the spectral emissivities is expected and the soot particles are supposed to behave as a grey body. Therefore $\varepsilon_{\lambda_1}/\varepsilon_{\lambda_2} \approx 1$ (Huang, 2001). This assumption would be true for both optical thick dust flames and thin optical flames if the size of soot particles is considerably larger than the selected wavelengths (Cashdollar, 1979). With all these considerations, equation 3.44 can be re-written as a new equation particularly suitable to calculate the temperature of coal fired flames:

$$T = C_2 \cdot \left(\frac{1}{\lambda_2} - \frac{1}{\lambda_1}\right) \Big/ \left[ln\frac{\mathscr{G}(\lambda_1, T)}{\mathscr{G}(\lambda_2, T)} + ln\frac{\mathscr{S}_{\lambda_2}}{\mathscr{S}_{\lambda_1}} + ln\left(\frac{\lambda_1}{\lambda_2}\right)^5 + ln\frac{\Delta\lambda_2}{\Delta\lambda_1}\right] \tag{3.45}$$

In the case of gaseous flames, the size of soot particles ranges from 0.005 to $0.1\mu m$ (Char and Yen, 1996) being much smaller than the wavelengths of observation. If it is assumed that soot particles in the flame are homogeneous, optically thin, isothermal along a horizontal plane through the flame and small compared to the used wavelength, it has been proved (Cashdollar, 1979; Flower, 1983, 1989; Timothy et al., 1986) that the spectral emissivity is inversely proportional to the selected wavelength, i.e. $\varepsilon_\lambda \propto 1/\lambda$. Therefore, equation 3.44 can be re-formulated by substituting $\varepsilon_{\lambda_2}/\varepsilon_{\lambda_1} = \lambda_1/\lambda_2$ to obtain a new formula applicable to gaseous flames and utilised in this study:

$$T = C_2 \cdot \left(\frac{1}{\lambda_2} - \frac{1}{\lambda_1}\right) \Big/ \left[ln\frac{\mathscr{G}(\lambda_1, T)}{\mathscr{G}(\lambda_2, T)} + ln\frac{\mathscr{S}_{\lambda_2}}{\mathscr{S}_{\lambda_1}} + ln\left(\frac{\lambda_1}{\lambda_2}\right)^6 + ln\frac{\Delta\lambda_2}{\Delta\lambda_1}\right] \tag{3.46}$$

Table 3.1: Estimated difference of temperature between soot particles and surrounding gas according to Ladommatos and Zhao (1994).

Particle diameter (μm)	Difference of temperature (K)
0.06	1
0.30	5
0.60	10
3.30	50

3.3.3 Thermal Equilibrium between Soot Particles and the Surrounding Gas

The two colour method, as based on the black body radiation, measures uniquely the temperature of soot particles but not the temperature of the surrounding gas which is, in principle, different. In general, soot particles will lose heat due to radiation. Theoretically their temperatures would fall below the temperature of the surrounding gas but the small size of these particles result in a rapid thermal equilibrium and consequently a similar temperature to that from the gas. Ladommatos and Zhao (1994) produced an estimation, using theoretical analysis, of the difference in temperature between the soot particles and the surrounding gas. The result of this study shows the estimated difference of temperature as a function of the particle size (see Table 3.1).

As shown previously the size of soot particles in gaseous flames ranges from 0.005 to $0.1 \mu m$ (Char and Yen, 1996). Therefore, according to Table 3.1 the difference of temperature in our case could be considered to be around 1 K or even lower.

Also, Matsui et al. (1979) showed that soot particles reach the equilibrium temperature to the surrounding gas with a time constant of the order of 10^{-9} seconds and therefore proved that the difference of temperature can be negligible. Matsui et al. (1979) also performed an estimation for the particles with a diameter of 0.5 μm in

a diesel engine in terms of heat equilibrium and concluded that the difference of temperature was as small as 0.3 K. Gaydon and Wolfhard (1979) accepted that the temperature of soot particles differ negligibly from that of the surrounding gas.

3.4 Summary

The theoretical foundations of the basic principles that are of a required application for the 3D visualisation and characterisation of fossil fuel flames have been presented. These principles have been described as divided in two major sections: one related to the basis of the two principal tomographic algorithms and another that explains the characteristics of combustion processes and a significant method to calculate the temperature of a flame.

The two tomographic algorithms explained, the FBP algorithm and ART have been selected because they are the two more important algorithms implemented in many different disciplines. They have been explained in detail, including their mathematical bases and computational implementation. More importantly, they have been compared for different situations in terms of numbers of projections and comparison has served to elucidate the feasibility of each one for this research programme.

Some characteristics of flames have been explained. The radiation spectra has been described indicating its dual nature. Radiation can be originated by electronic transition in different gas molecules but can also been created due to the spectral properties of soot particles inside the flame. The two-colour technique to calculate temperatures has been presented and its theoretical background and practical methodology have been stated indicating that can be utilised in the presence of radiation coming from soot particles. For that reason special care has been put to show the existing thermal equilibrium between the soot particles and the surrounding gas.

Chapter 4

Instrumentation System: Description, Configuration and Calibration

4.1 Introduction

This chapter presents a detailed description of the prototype instrumentation system utilised for the 3-D monitoring and characterisation of fossil fuel flames using digital imaging techniques. This system, containing the latest generation of CCD industrial cameras and sophisticated opto-mechanical hardware, should be suitable for operation in a scale laboratory and real industrial situations.

The instrumentation system comprises of two mayor units: an *imaging* unit and a *computing* unit. The imaging unit principally consists of an optical arrangement that is capable of visualising the flame from different angles totalling a widespread area corresponding to almost half side of the flames. The choice of the sensing arrangement is critical for the performance and practicality of the instrumentation system. A number of algorithmic and technical issues are discussed in this chapter to justify the selection of the sensing arrangement. The other components of the imaging are also outlined.

The computing unit mainly consists of three identical frame grabbers, personal computer and bespoke software. The frame grabbers provide real time transfer of the images to the host computer whereas the developed software manipulates the information provided by the flame images and generates the numerical and graphical outputs. The complete structure of the system software for the 3-D visualisation and quantitative characterisation of fossil fuel combustion flames is described in this chapter.

4.2 Description and Configuration

A schematic block diagram of the 3-D flame imaging system is shown in Figure 4.1. The system can be subdivided into two units, i.e., imaging unit and computing unit. The imaging unit consists of three identical sets of a colour RGB camera, and an optical transmission component consisting of mirrors and lenses. The computing unit comprises three identical frame grabbers and a personal computer with bespoke application software. The cameras have a compact RGB colour progressive 1/3 *in.* CCD sensor with square pixels and a primary mosaic filter and a frame rate of 25 frames per second. The cameras are arranged on one side of the burner with an angle of 60° between two adjacent cameras. In chapter 3 there is a detailed technical discussion that yields to this arrangement. The minimum number of projections that were found to give an acceptable definition of the cross-section was six and this number can be easily obtained using three cameras. It is interesting to remark that one of the aims of this project was to use the simplest possible set-up using the lowest number of cameras. Moreover, in all computational simulations, a separation of 30° degrees between two consecutive optical paths, produced optimal results. This fact was also compatible with the simplicity involved in having set-up of camera in only half side of the installation. Therefore, having three cameras placed in one side of

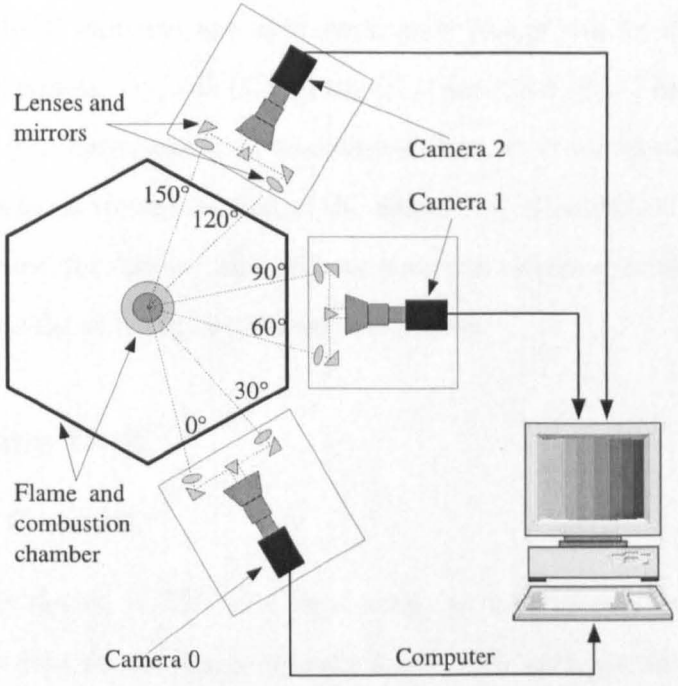

Figure 4.1: Schematic diagram of the system set-up.

the flame, obtaining six projections with a separation of 30° providing an optimal reconstruction complied with all the necessary requirements.

The optical transmission unit comprises a set of lenses and mirrors, forming two optical paths for each camera and enabling the transmission of the flame image from two different directions with an angle of 30° to the same CCD panel. With such an arrangement, the imaging system produces six flame images concurrently from six directions. The three frame grabbers, which are synchronized by the system software, acquire and digitise the image signals and convert them into 2-D matrices and transmit these data to the core of the personal computer.

To ensure that the system complied, to the highest possible exactitude, to the indications, measurements and magnitudes that it is supposed to obtain, a complete calibration process was performed. This calibration is explained completely in sec-

tion 4.3. Since RGB cameras are used here, each image can be disintegrated into three principal channels, i.e., red (R), green (G), and blue (B). The 3-D reconstruction of the flame luminosity can then be achieved for each color band. Any pair of the color-banded luminous reconstruction of the flame, i.e., R and G, R and B, or G and B, can thus be used for further analysis, such as the determination of temperature distribution of the flame using two-colour techniques.

4.2.1 Imaging Unit

4.2.1.1 CCD Cameras

A charged-couple device (CCD) is a light sensitive integrated circuit which stores and displays the data for an image in such a way that each picture element (pixel) in the image is converted into an electrical charge, the intensity of which is related to a colour in the colour spectrum. CCDs are commonly used for digital still and video cameras in security surveillance, machine vision, optical character recognition and satellite photographs. A good quality CCD can produce an image in extremely dim light, and its resolution does not deteriorate when the illumination intensity is low, as it is the case with conventional cameras.

The cameras utilised in this research study are the JAI® CV-M77 model, a compact colour camera designed for automated imaging applications. These cameras provide a RGB colour video signal with progressive scan mode (also known as non-interlaced scanning or P-Scan), a display system that scans the moving images in such a way that all the lines of each frame are drawn in sequence. This is in contrast to the interlaced scanning, used in traditional television systems, where only the odd lines, then the even lines of each frame are drawn alternately. The main features of this model are:

- New 1/3 *in.* full frame progressive scan interline transfer CCD. (Progressive scan is a method to capture images in which all the lines of each frame are drawn in sequence.)
- RGB Primary color mosaic filter(Bayer) and DSP for color reproduction.
- 1034 horizontal (h) × 779 vertical (v) 4.65 μm square pixels (1028 × 768 pixels read out) - XGA format.
- 25 full frames 1028 (h) × 770 (v) RGB video output per second.
- Fast frame readout of every third line in the full frame.
- 74 frames per second (fps) 1028 (h) × 242 (v) RGB video output.
- Internal, external HD/VD or random trigger synchronization.
- Edge pre-select and pulse width controlled external trigger modes.
- Programmable shutter speed.
- Long time exposure with external VD pulse interval.
- Frame delay readout for edge pre-select and pulse width controlled shutter.
- Exposure enable EEN, write enable WEN and pixel clock output.
- Short ASCII commands for fast mode setup via serial port.
- Setup by Windows 98/NT/2000/XP software via RS 232C.
- Lens mount of C-mount type.

Full technical specification of the cameras are listed in Appendix A. The characteristics of the cameras related to this work are further discussed in more detail.

4.2.1.2 Progressive Scan

The CCD cameras are 25 full fps progressive scan cameras offering superb image quality and high colour reproduction. Contrary to interlaced cameras used in Lu (2000); Bheemul (2004), these cameras provide a single complete frame rather than two separated fields separated by an interval of 1/50 seconds avoiding the corresponding degree of image distortion. Progressive scan offers other advantages. It provides higher vertical resolution than interlaced video with the same frame rate. Also, there are no visual artefacts associated with interlaced video of the same line rate, such as interline twitter. Therefore, frames have no interlace artefacts and can be used as still photos. Progressive scan offers much better results for scaling to higher resolutions than equivalent interlaced video images and there is no necessity to perform a anti-aliasing techniques to reduce interline twitter. On the other hand, progressive scan requires higher bandwidth than interlaced video with the same frame size and vertical refresh rate. But this disadvantage is not an important issue in this study.

4.2.1.3 Background Noise

Although the CCD arrays of the cameras have a low signal-to-noise (S/N) ratio, there still exist a certain amount of noise due to the radiative energy of heated semiconductor material of the electronic components, as well as optical components. This noise is determined by analysing the luminosity distribution of each pixel of an image captured with a fully closed iris. Theoretically, because there is no incident light, the output signal is expected to be zero. However this is not often the case. Figures 4.2-4.4 show the output of one of the cameras with the iris fully closed. These outputs were obtained after separating the original colour image (RGB) into its three major components, red, green and blue. The outputs of the other two cameras are similar and are not represented in this work.

A way to reduce the noise proposed in Lu (2000) consists of averaging a set of a large number of these type of images. This method, not only contributes to reduce the noise but also provides information about the natural threshold of the sensor on each channel, i.e. the minimum intensity (measured in 8 bits) transmited for a theoretical null background whose transmited value would hypothetically be zero. A bespoke computing program was created to average 1000 consecutive images. The result is ploted in Figures 4.5-4.7.

4.2.1.4 Camera Lens

The lens of a camera collects light from a source and refracts that light to form an usable image of the source. The source may produce light itself or may be an illuminated object. The most defining parameter of an optical lens is the focal length (f) which can be defined as the distance over which initially collimated rays are brought to a focus. There are other important parameters like the viewing angle (α) and in the case of digital imaging, the maximum sensor's size (d) that can be used with. These three parameters are closely related, being the viewing angle determined by the focal length and the size of the sensor ($\alpha \approx d/f$; except for wide angle lenses). Some 'mechanical' parts of a lens like the iris, controls the amount of light entering the lens. The iris can be manual or automatic. The lenses selected for the imaging system are Edmund Optics® 6× CCD C-mount lens with a manual iris. This lens allows the entire visualisation of the flame under laboratory conditions. Also, this type of lens provides clear flame images over a range of light intensities. A list of the lens specifications is given in Table A.7.

4.2.1.5 Optical Transmission Units

The optical transmission units play an important role in the system as they enable the transmission of the flame image from two different directions with an angle of 30° to the same CCD panel. Thanks to such an arrangement, the imaging is capable to

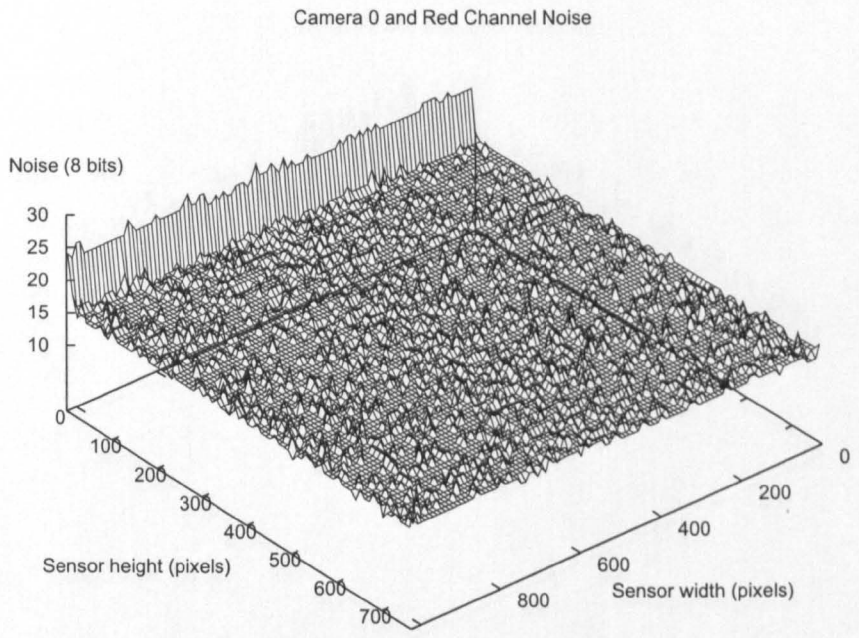

Figure 4.2: Noise distribution in an instantaneous image of the red channel.

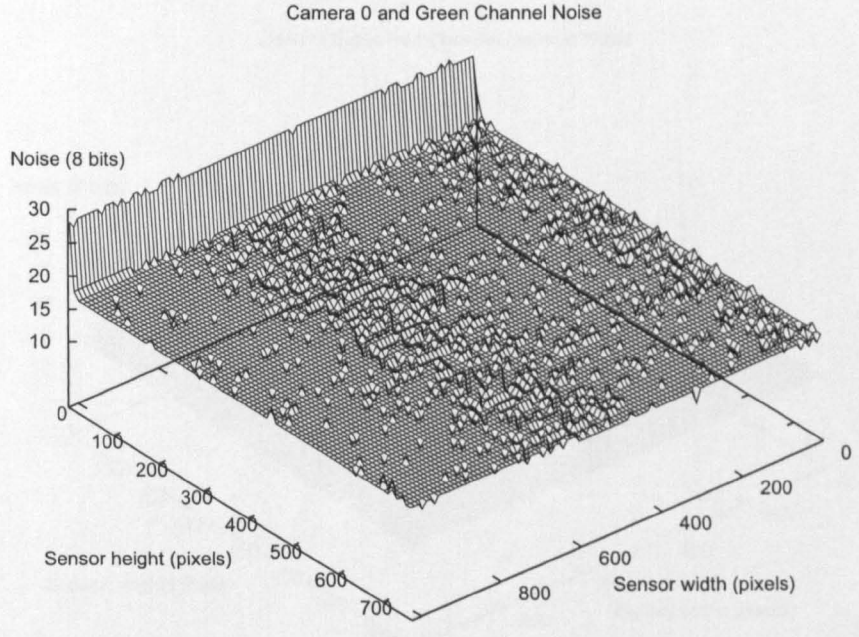

Figure 4.3: Noise distribution in an instantaneous image of the green channel.

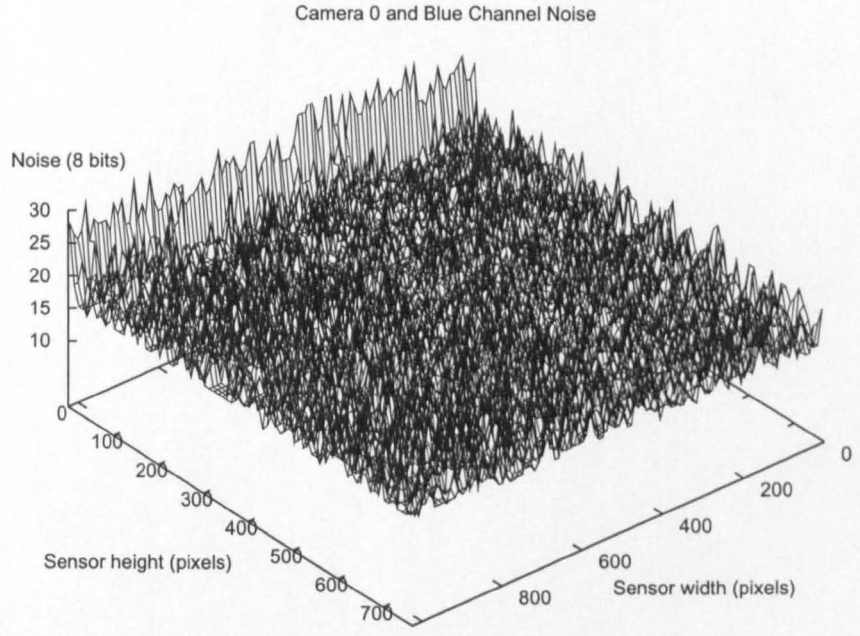

Figure 4.4: Noise distribution in an instantaneous image of the blue channel.

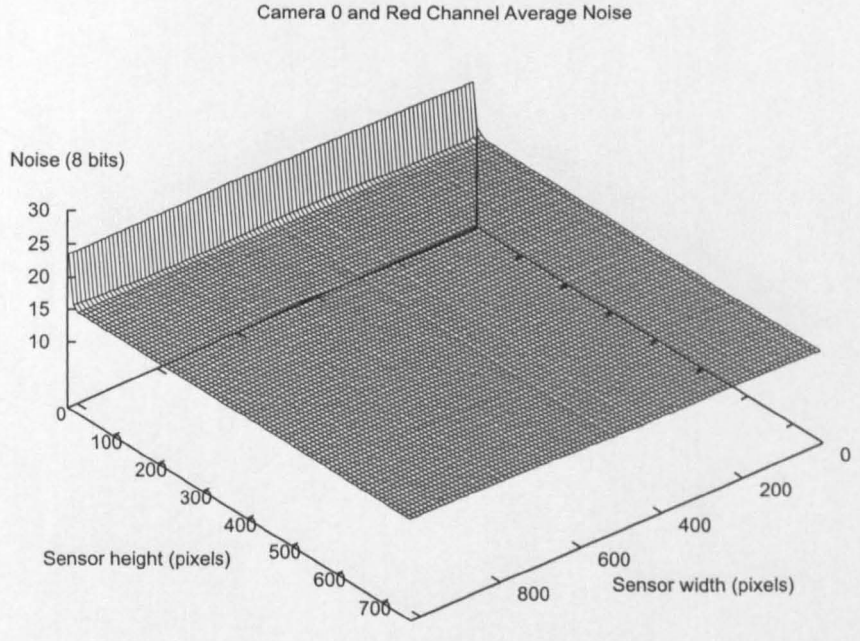

Figure 4.5: Noise distribution in an average image of the red channel.

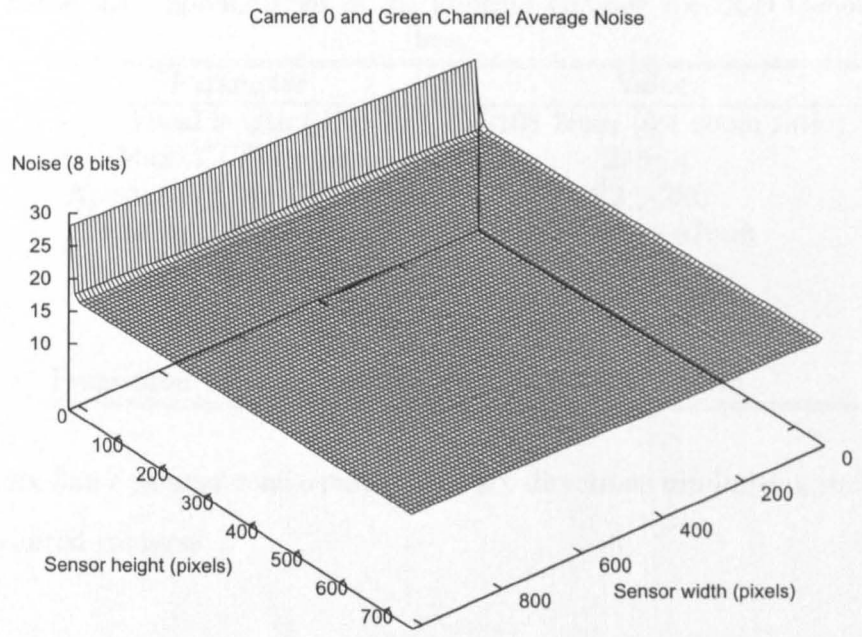

Figure 4.6: Noise distribution in an average image of the green channel.

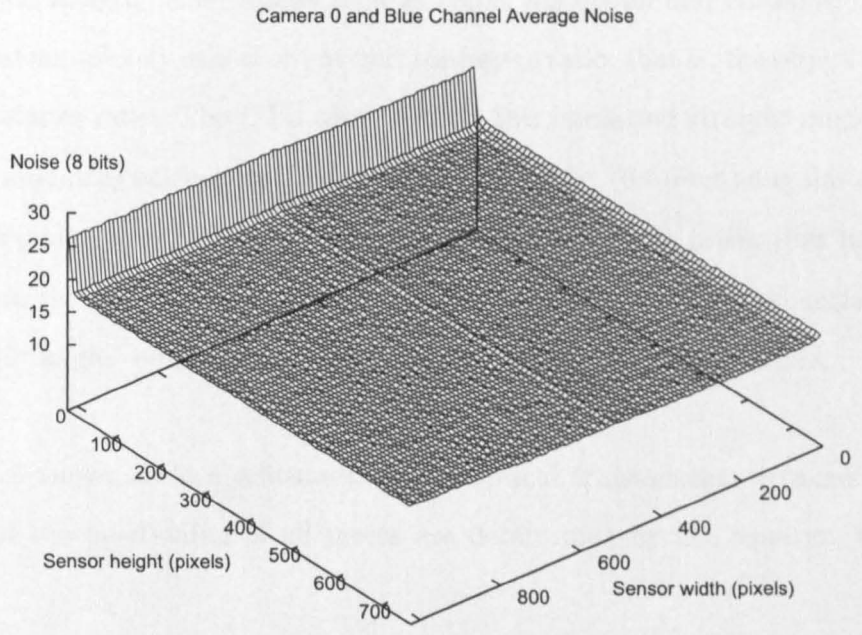

Figure 4.7: Noise distribution in an average image of the blue channel.

Table 4.1: Specifications of the Edmund Optics® 6× CCD C-mount lens.

Parameter	Value
Focal length (f)	18-108 $2mm$ (6:1 zoom ratio)
Max. CCD format	2/3 $in.$
Aperture ($f/\#$) C=closed	F2.5-28C
Total field of view range	$6.4mm - 97mm$
Working distance range	$140mm - \infty$
Max. dia. × L (mm)	62 × 159
Weight	540 g
Front filter size (dia.×pitch)	M52×0.75mm

produce six flame images concurrently from six directions minimising,such the number of required cameras.

Every optical transmission unit (OTU) comprises two bi-convex lenses of 30 mm of diameter and 30 mm of focal length. These lenses are manufactured with an identical convex surface on both sides. The lenses have positive focal length and form both real and virtual images. Aberrations such as coma, distortion and chromatic aberration are almost completely cancel out at unit conjugate ratio, that is, the object distance to image distance ratio. The OTU also contains two miniature straight mirrors offering a 1.0 $in.$ mounting surface and including fine resolution (64-pitch) angular adjustment screws. Finally, the OTU contains a Techspec® right angle prism that has a mirror coating on the two legs and an uncoated hypotenuse. The mirrored surfaces form a precise 90° angle. Full technical specifications are given in Appendix A.

Figure 4.8 shows a close schematic of the optical transmission arrangement. The focus and the positioning of all pieces are determined by the equation of the thin lens.

$$\frac{1}{S_1} + \frac{1}{S_2} = \frac{1}{f} \tag{4.1}$$

where $f = 30\ mm$ is the focal length of the bi-convex lens, $S_1 = 310.5\ mm$ is the

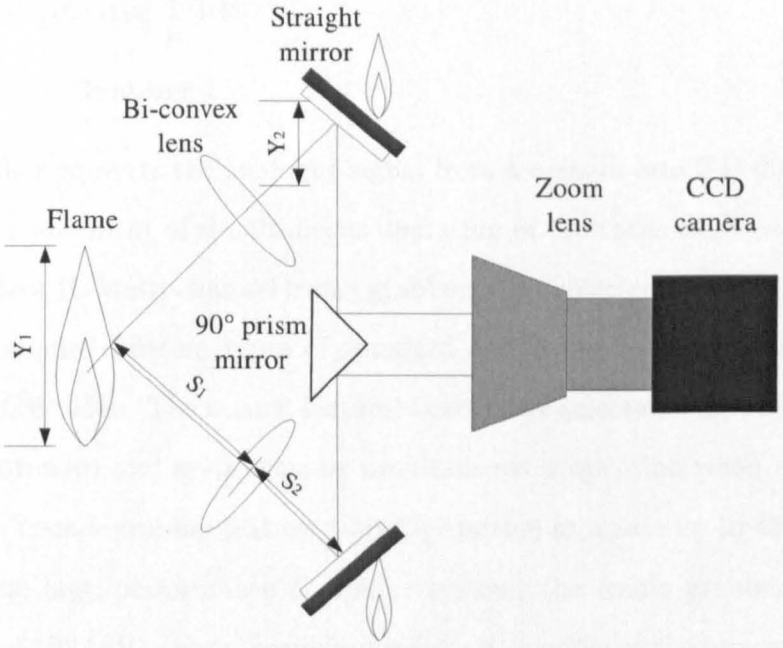

Figure 4.8: Schematic diagram of the optical transmission unit.

viewing distance and S_2 is the image distance. Therefore S_2 can be determined to be 33.2 mm.

Since the ratio of the object distance and the image distance (S_1/S_2) is equal to the ratio of the object size (Y_1) and the image size (Y_2):

$$\frac{S_1}{S_2} = \frac{Y_1}{Y_2} \tag{4.2}$$

for a fixed value of S_2 equal to the size of the straight mirror (25.4 mm), the maximum observable size of a flame is calculated to be 240 mm, a size that lies below the maximum height that flames reach with the outlet of the burner fully open under laboratory conditions.

4.2.2 Computing Unit

4.2.2.1 Frame Grabber

A frame grabber converts the analogue signal from a camera into 2-D digital images. To meet the requirement of simultaneous operation of the three CCD cameras, three Matrox® Meteor II/Multi-channel frame grabbers were selected. This model of frame grabber can acquire different types of standard and non-standard monocrhome and component RGB video. The boards feature six software selectable input channels and support synchronous and asynchronous simultaneous acquisition when using several cameras. The frames grabber feature 8-bit digitisation at a rate up to $45Mhz$. Combined with the high performance computer system, the frame grabbers support a transfer rate of $132MB/s$ each, providing real-time transfer of the images to the host computer memory.

To prevent loss of data during long bus-access latencies found in heavily loaded computer systems, the frame grabber features $4MB$ of SGRAM for temporary frame storage. Theoretically, up to 16 such frame grabbers can be installed in a computer for multiple simultaneous grabbing. The frame grabbers also generate several useful signals such as horizontal and vertical synchronisation (H-SYNCH and V-SYNCH) signals as well as the required voltage supply ($\pm 12V$). A full technical description of the Matrox Meteor-II frame grabber can be found in Appendix A.

An imaging library that comes with the frame grabbers, the Matrox® Imaging Library (MIL-Lite) provides an extensive list of commands to capture, process, analyse, transfer, display and archive images under C/C++ programming environment. The processing and analysis operation include spatial filtering, morphological operations, measurements, blob analysis and calibration.

4.2.2.2 Synchronisation of the Frame Grabbers

The MIL-Lite library was utilised to control the frame grabbers and synchronise the image adquisition. The command <MdigGrab> was used to capture the images. This command uses a specified digitiser to acquire the data from an individual CCD camera and stores the data in the destination image buffer. When acquiring data from a progressive scan camera, like the JAI® CV-M77 model, each line of the destination image buffer is either filled from top to bottom or a single line is grabbed, depending on synchronisation method utilised: Synchronous or asynchronous respectively.

Having three identical frame grabbers, the command <MdigGrab> must appear three times sequentially, starting the image acquisition in each case. If the synchronous mode is chosen, the application is synchronised with the end of a grab operation i.e. it waits until the capture finishes before returning from the grab order. Thus, a subsequent «MdigGrab»command will start the image acquisition from another camera only when the buffer corresponding to the previous one is completely filled.

However, in this study the asynchronous method was selected. With this option, the application is not synchronised with the end of a grab operation, but return immediately after initiating the start of the capture. Therefore, subsequent grabbing operations will start immediately after the previous one is started. Careful observation of images from fast moving flames taken following this procedure, corroborated the good synchronisation of the images with negligible time delays.

4.2.2.3 Software

A dedicated software system has been developed using C/C++ language under Microsoft® Visual .NET 2003 environment. Figure 4.9 depicts the user friendly graphic interface created. C/C++ offers all the features and traditional specifications to solve math-

ematical algorithms and compatibilities with modern graphic display libraries and the Active MIL Matrox® Imaging Library provided with the frame grabbers. The computing software consists of the following major features (more details about the internal routines and algorithm functioning can bee seen in Chapter 5):

- System operational management: including the user-interface to display the 3-D reconstruction of the flame. This reconstruction is shown in three different formats: geometric or mesh reconstruction, cross-sectional reconstruction of temperatures and 3-D point by point temperatures reconstruction.

- System configuration: including registration of the three cameras, adjustments, allocation of display buffers for each camera and image buffers, frame grabber control files, Active MIL controllers.

- Simultaneous image acquisition, display and storage: including grabbing the images from the three cameras simultaneously thanks to the asynchronous synchronisation provided by the Matrox library, separation of the images in their three colour components RGB, reading the 2-D digital images line by line, performing the reconstruction of the luminosity using the new algorithm (LFBP-ART), calculating the corresponding temperature map using the two colour method, storage of all this data into a three dimensional array, calculation of geometric and luminous parameters.

Figure 4.10 depicts a schematic of the software interface. The user is presented at a first stage the main window shown in Figure 4.9. This window enables the user to observe the six projections (red channel) of the flame taken by the three cameras, run the reconstruction process and observe the results. These results are displayed in three independent *tabs*. These tabs include respectively information about the geometry of the flame (a mesh reconstruction of its surface), internal temperature information by showing several cross-sectional temperature maps and finally completing

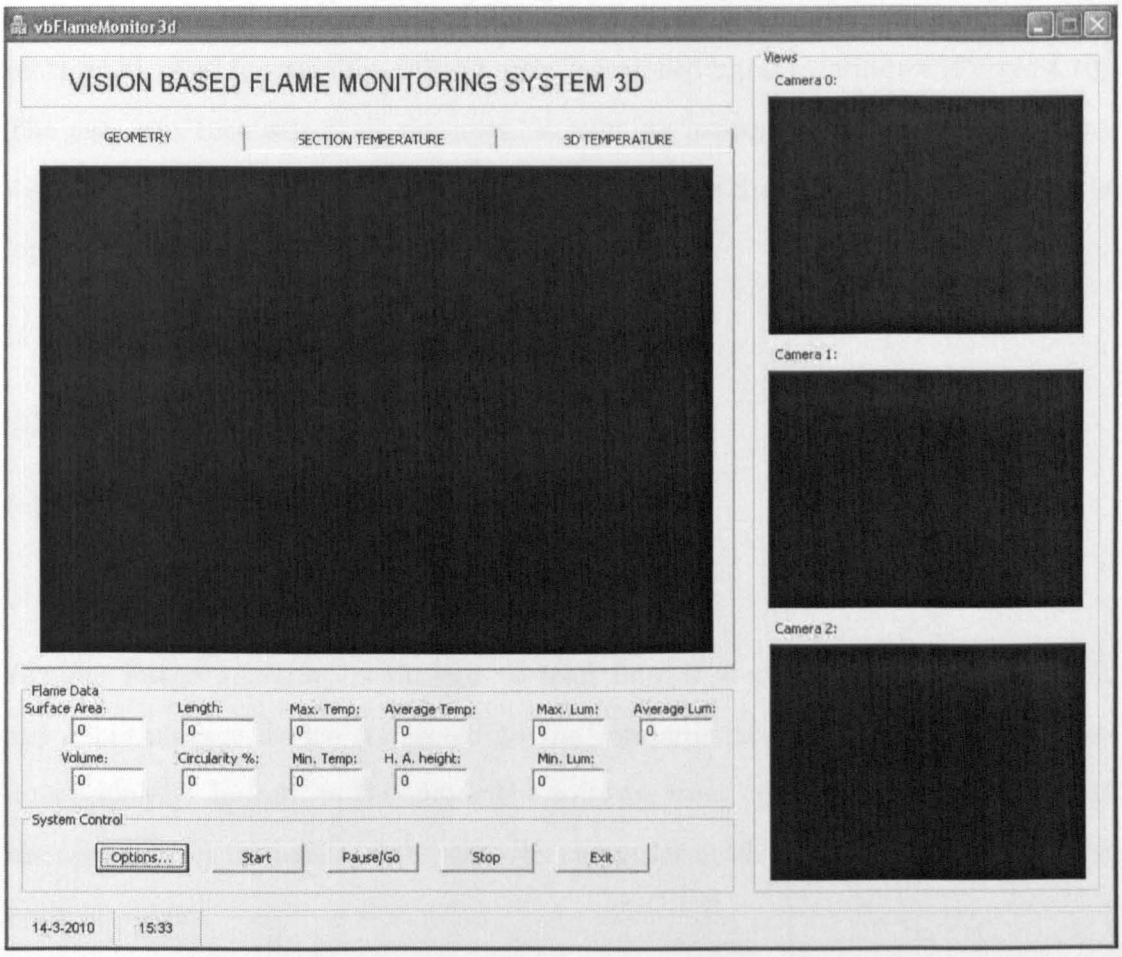

Figure 4.9: Bespoke software interface. On the right, three small windows display the grey images of the flame (red channel) captured by the system. On top and centre, three tabs and three corresponding windows display the geometry, cross-sectional and longitudinal information of the internal temperature map of the flame. At the bottom, the numerical information from the reconstructed model is displayed. Below: the user buttons, including the Options button that triggers the 'options' window (Figure 4.11).

a more in detail 3-D display showing a longitudinal-section of mapped temperature (corresponding to the centre of the images).

Figure 4.10 shows an schematic of the functioning of the software interface. The central hub of all functioning is the already mentioned interface window (Figure 4.10). The user can then select all the possible working modes popping up the 'options' window (see Figure 4.11). The most important feature that the user can select is the 'operational modes'. There are four types:

(a) Off-line image analysis

(b) Off-line data analysis

(c) On-line image analysis

(d) On-line image saving

Off-line image analysis is utilised to load images stored in the computer or in any other storage device connected to the computer and reconstruct them three-dimensionally. Indeed, in this mode the software does not need to be connected to the cameras but for technical reasons, the computer needs to have installed the three frame grabbers.

Off-line data analysis is used to load the already reconstructed data and stored in a <*.dat> file. This mode allows the re-visualisation or re-examination of a flame without the necessity of loading its images and perform its complete tomographic reconstruction. This allow a full revision of flames with the subsequent saving of time.

On-line image analysis is utilised for a full on-line process where a set of images of one instantaneous flame is grabbed simultaneously, displayed at the main window of the

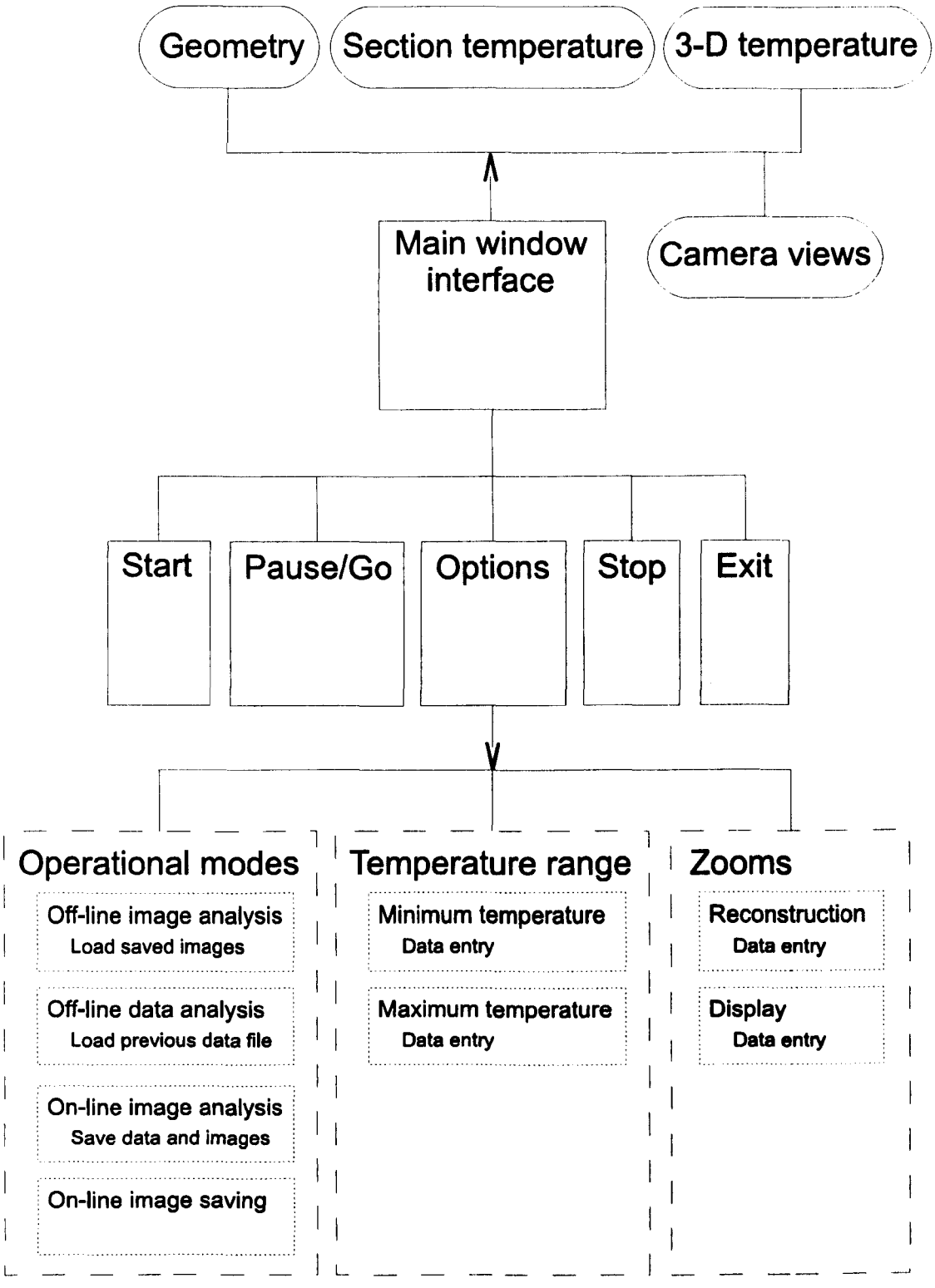

Figure 4.10: Software interface diagram.

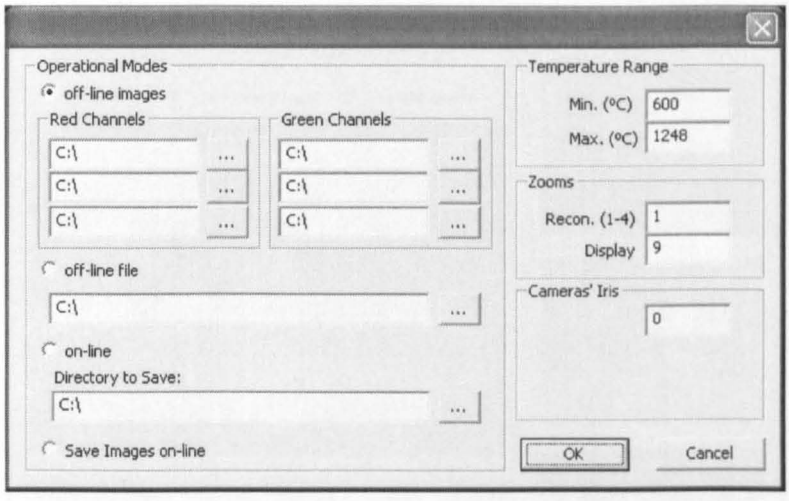

Figure 4.11: Options window availabe for the user to select all the working modes.

software interface and the full tomographic reconstruction is performed subsequently. As soon the reconstruction has finalised, the results are displayed numerically at the bottom of the main window and graphically at the three tabs mentioned above. Intermediately after, another set of images is captured and another reconstruction process begins. In the mean time, the user still can visualise the previous data and examine the graphical display.

On-line image saving is utilised to capture sets of images, six images from the red channel and six images from the green channel, and save them into the selected location without any extra calculation. The images are grabbed with an interval of one second between two consecutive images. These images can be subsequently reconstructed and study using the above off-line image analysis mode.

The user can also select or enter the temperature range that will be displayed graphically. This decision influences the colour mapping that will be utilised at the display and can be used for a more concise mapping if a narrow range of temperatures is to be studied. Zooms can also be altered in the options window. These zooms include

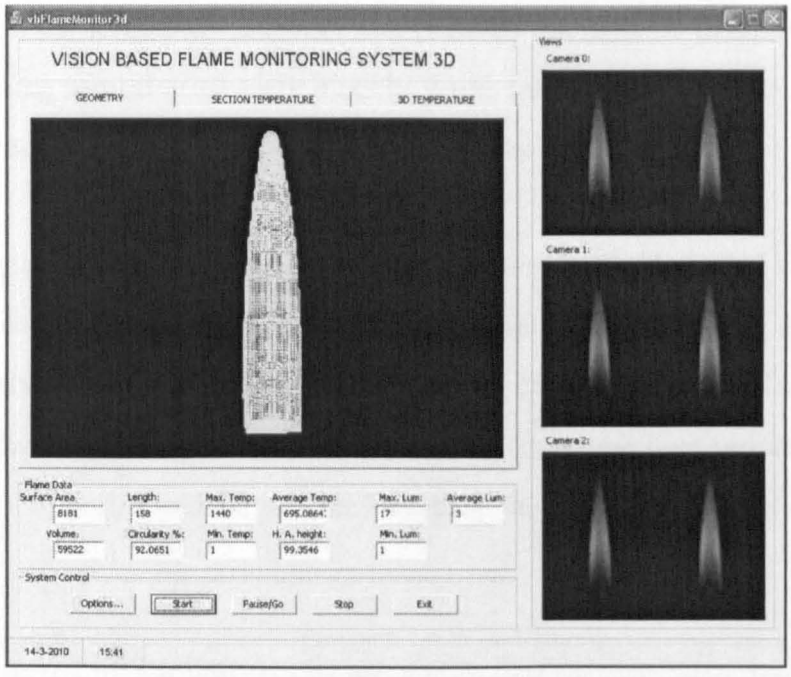

Figure 4.12: Software interface showing the flame images grabbed by the system and the geometrical reconstruction showed in the first tab.

the reconstruction and the display zoom. The reconstruction zoom is a feature that was included at a very initial stage but has not been utilised extensively in this research programme. It influences the size of the image grabbed by the system using the cameras in such a way that small flames could be zoomed in. The display zoom controls the initial size of the flame at the graphical displays corresponding to the three tabs mentioned above. This zoom can be modified as the user can zoom in and out the displays using the computer mouse.

When observing and examining the data, the user can visualise the grabbed images (see Figure 4.12) at the right hand side of the interface. By clicking the mouse on the first tab, the user can see the reconstruction of the flame geometry. This reconstruction is displayed by using a mesh that represents the surface of the flame (see also Figure 4.12).

By clicking on the second tab, the user can examine the internal mapping of temperatures observing several cross-section of the flame totalling ten of them. Figure 4.13 shows the graphical display of these temperature cross-sections.

By selecting the third tab, the user can observe a longitudinal map of temperatures. In this occasion, the central longitudinal slice of the flame (see Figure 4.14). This is achieved storing the data information of all the 2-D cross-sections forming a complete 3-D array which is subsequently showed partially (only one longitudinal section) in the tab. This feature could be modified altering the software code to display extra information.

As mentioned, the user has the possibility of zooming in and out the reconstructing information. This is true for the three tabs. Figure 4.15 shows this feature in the case of the cross-sectional examination of the internal map of temperatures of the flame. Figure 4.16 shows this feature in the case of the geometrical reconstruction of the flame. In all cases, the centre of coordinates is placed at the centre of the flame in such a way that the x-axis goes along the imaginary line corresponding to the left image of Camera 0 (see Figure 4.1) and the y-axis goes along the right image taken by Camera 1. Therefore, the z-axis coincides with the vertical line.

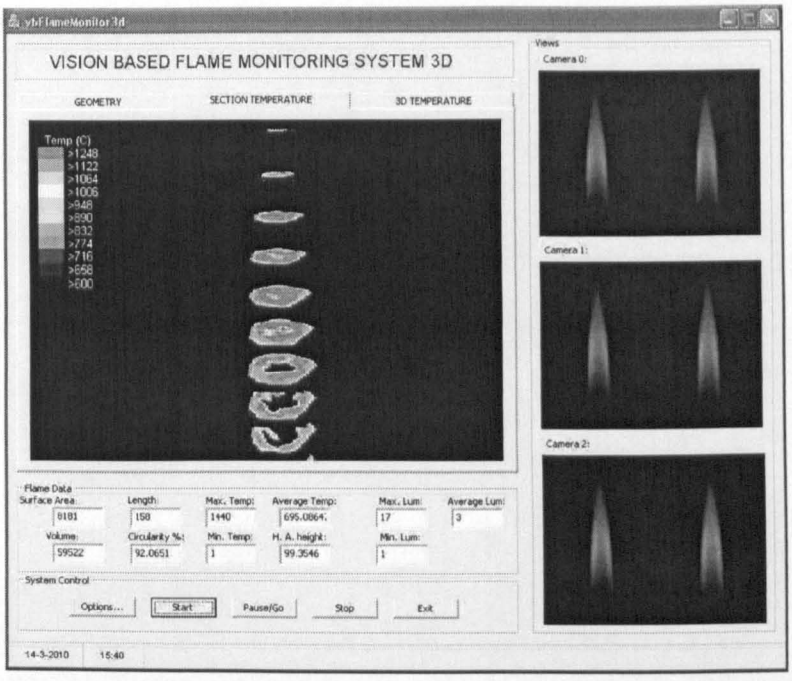

Figure 4.13: Software interface showing the second tab and the reconstructed cross-sections of temperatures.

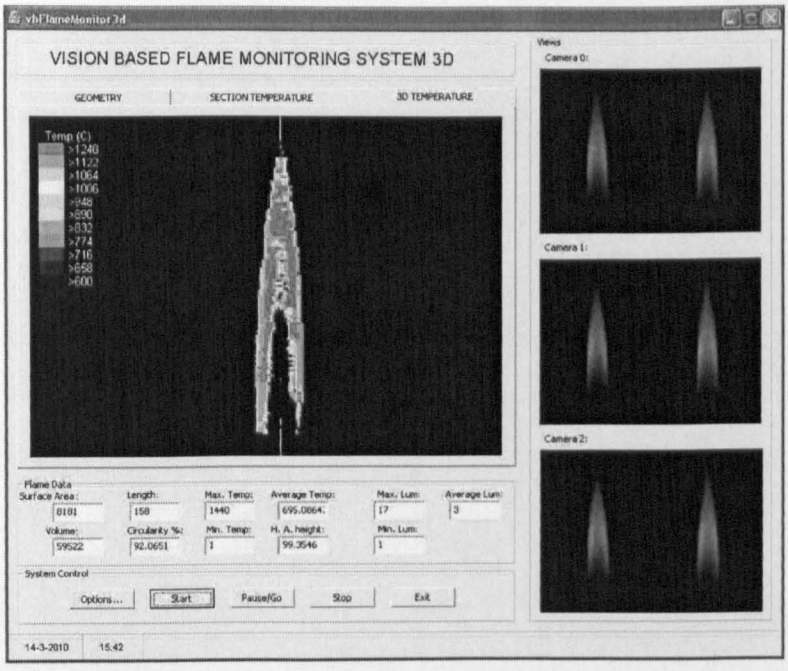

Figure 4.14: Software interface showing the third tab and the central reconstructed longitudinal section of temperatures.

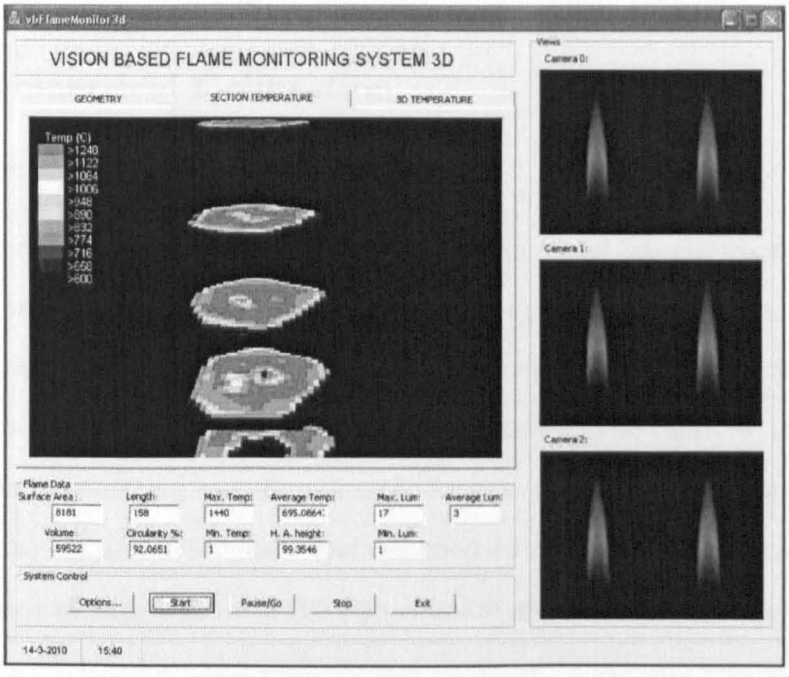

Figure 4.15: Zoom in applied to the cross-section view.

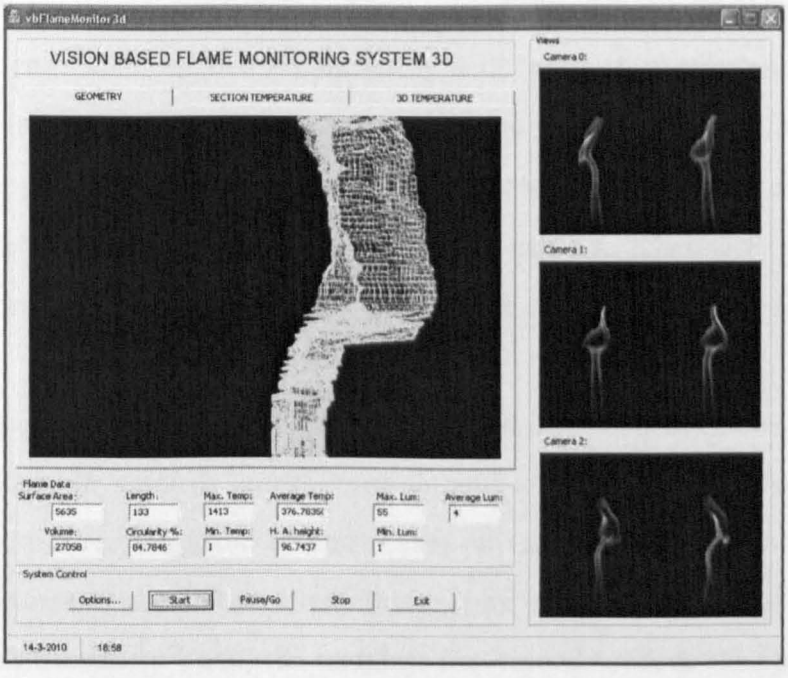

Figure 4.16: Zoom in applied to the geometrical or mesh view.

4.3 Calibration

4.3.1 Geometrical Calibration

4.3.1.1 Location Correction

The imaging system described above produces two different images from two different angles per camera. With no major adjustments at the imaging unit, it would be difficult to ensure that all the flame images are located at the correct and precise position. It would be possible that, due to deviations on the relative position of the lenses, mirrors, prisms and cameras, there had misalignments in the images. To avoid this, a bespoke computer program was designed to ensure, in conjunction with the precise mechanical adjustments of the transmission unit, a perfect location correction.

Figure 4.17 shows a photograph of this software during the location correction process. The picture displays the original image from one camera during the procedure. Both, the left hand side and the right hand side of the photograph show a template formed with concentric squares separated by a distance of 10 *mm* and specifically designed for image location corrections. On the top part of the figure, the template on the left appears perfectly and frontally positioned as it was located forming 90° with the optical path of the left hand side of the camera. Therefore, the template was out of location with respect to the optical path on the right hand side.

The software contains features as mobile horizontal and vertical colour lines. These lines are adjustable upwards and downwards and leftwards and rightwards respectively. The lines were adjusted to one square on the left hand side of one camera using the features of the software and this setting was recorded to be repeated as many times as necessary. Then, the template was turned towards the optical path of the right hand side until it was correctly located forming 90°. Rather than changing

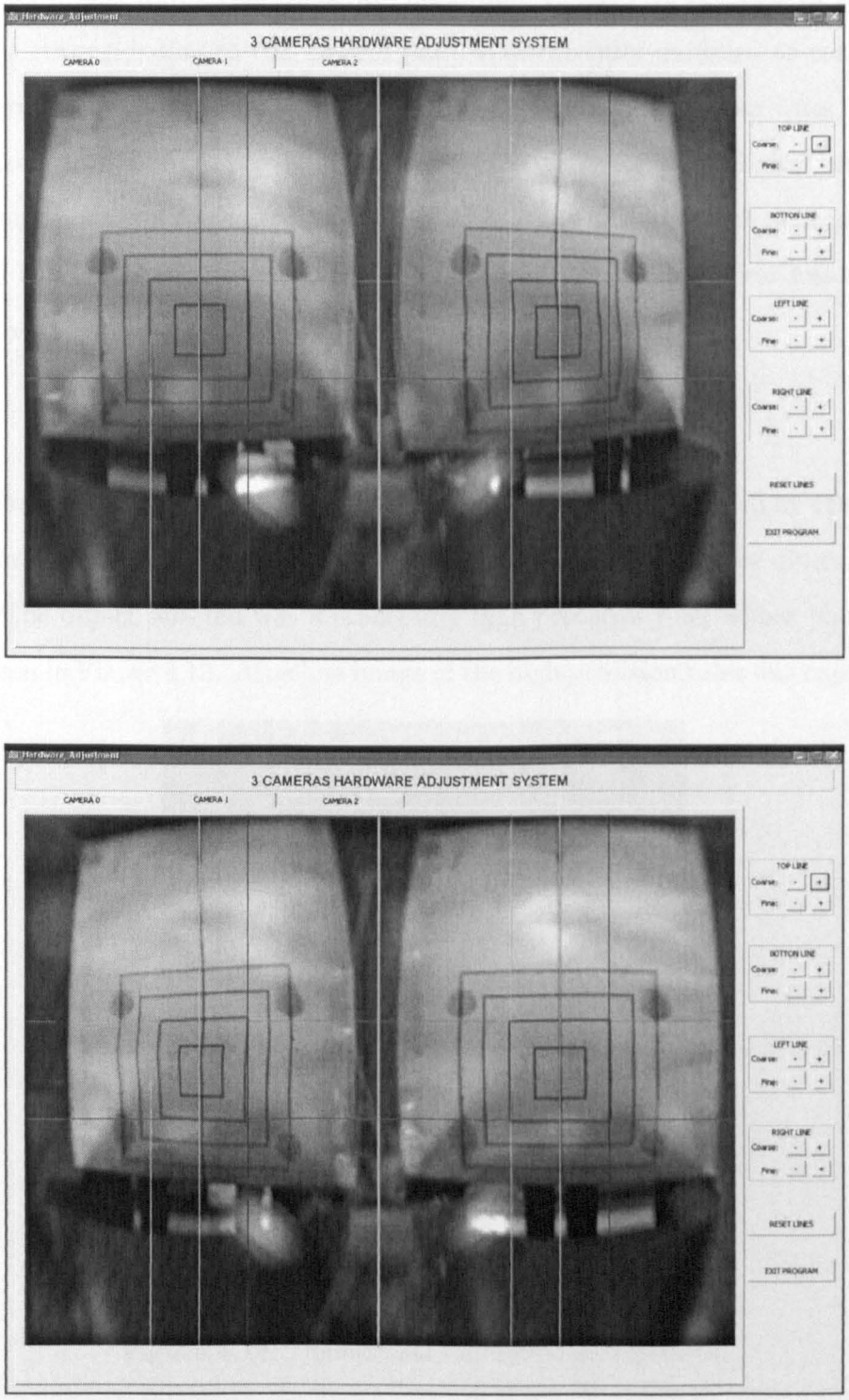

Figure 4.17: Location correction using bespoke software interface and mechanical adjustments.

the setting of the adjustable lines, the adaptable threads of the optical transmission units corresponding to this optical path were carefully modified to ensure that the squares of the template were correctly located within the colour lines. A close examination of the image provided by the bespoke software using digital image manipulation techniques provided by GIMP© proved that the maximum miss alignment obtained in any direction was two pixels or less than 1%. This process was repeated for the three cameras using the same setting of adjustable lines.

4.3.1.2 Dimension Calibration

The dimensional calibration of the multi-camera system was conducted by comparison of the number of pixels involved in the illustration of an object whose dimension was known. The object selected was a laboratory high precision ruler whose photograph can be seen in Figure 4.18. After the image of the high precision ruler was captured by

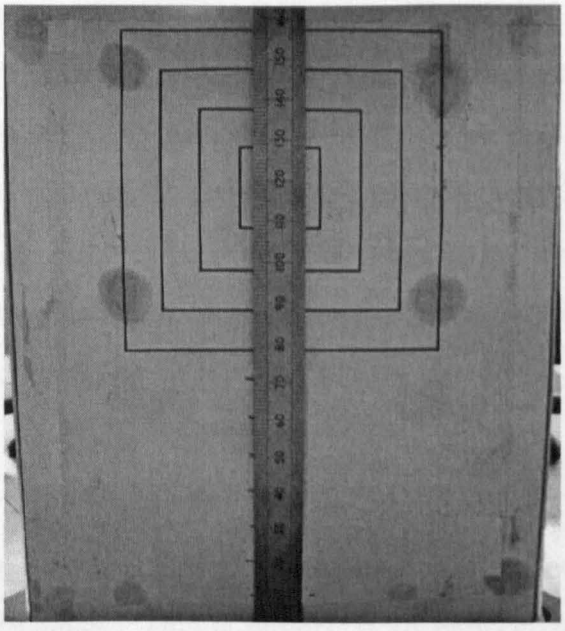

Figure 4.18: Dimensional calibration arrangement.

the imaging system, its length in the image was easily measured as so eight different points within its length. A diagonal straight line was plotted (Figure 4.19) by linear

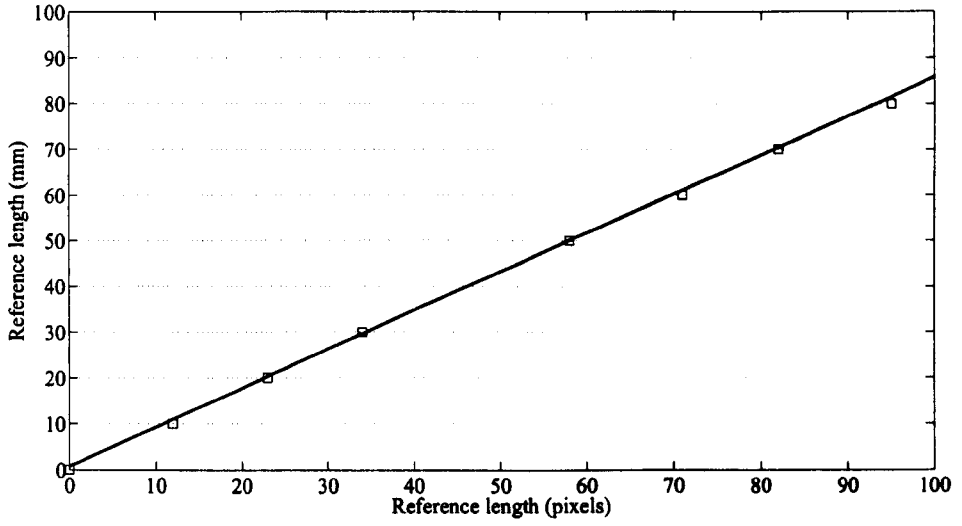

Figure 4.19: Direct comparison between the measurements in pixels and *mm*.

regression to give a direct comparison between the measured result in pixels and the reference values in *mm* and to obtain the spatial resolution of the system. The regression coefficient (r) obtained is 0.99 and the spatial resolution obtained by measuring mathematically the gradient of the straight line is 0.67 *mm*/pixel. The isotropy of the spatial resolution, the sphericity of the lens and its high quality construction with errors lower than 2% (see Appendix A), the high regression coefficient obtained and the stable conditions of the experimental laboratory guarantee the repeatability of the results and its extrapolation to any direction of the space.

4.3.2 Luminous Calibration

It is critical to ensure that the six images are captured instantly with the same intensity in all three channels. This is important to perform the three dimensional luminosity reconstruction of the flame but more critically to achieve an exact the equivalent temperature mapping as the calculation of temperature depends upon the exact ratio of luminosity under two different wavelengths (see Section 3.3.2). Having

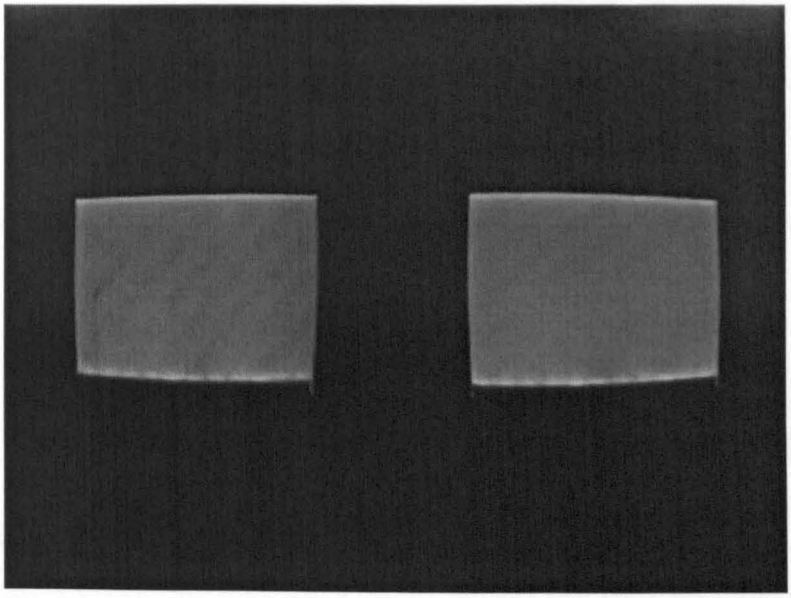

Figure 4.20: Colour LCD flat panel seen using the calibration software.

a total of six optical paths, it is possible to have some attenuation of intensities of light due to small imperfection in the materials of the transmission unit and small misalignment in the positioning of its different parts. Uneven absorption due to defects in the optical components is minimised by the high quality of the pieces utilised (see Appendix A for more details) and unequal attenuation due to differences in the length of the optical path is discarded by the accurate location correction explained in Section 4.3.1.1.

However, having three different cameras with dissimilar settings can produce a vast inconsistency in the measured luminosity. The cameras contain three gain potentiometers, one per colour channel, red, blue and green which is also the general or main potentiometer (see Appendix A). To avoid any disparity in the measured luminescence, another bespoke computer program was design to calibrate the three cameras by measuring. Figure 4.20 illustrates the colour LCD panel seen using the bespoke calibration software. The program captures the colour images, separates them into the three colour channels: R, G, B, measures the respective intensities at

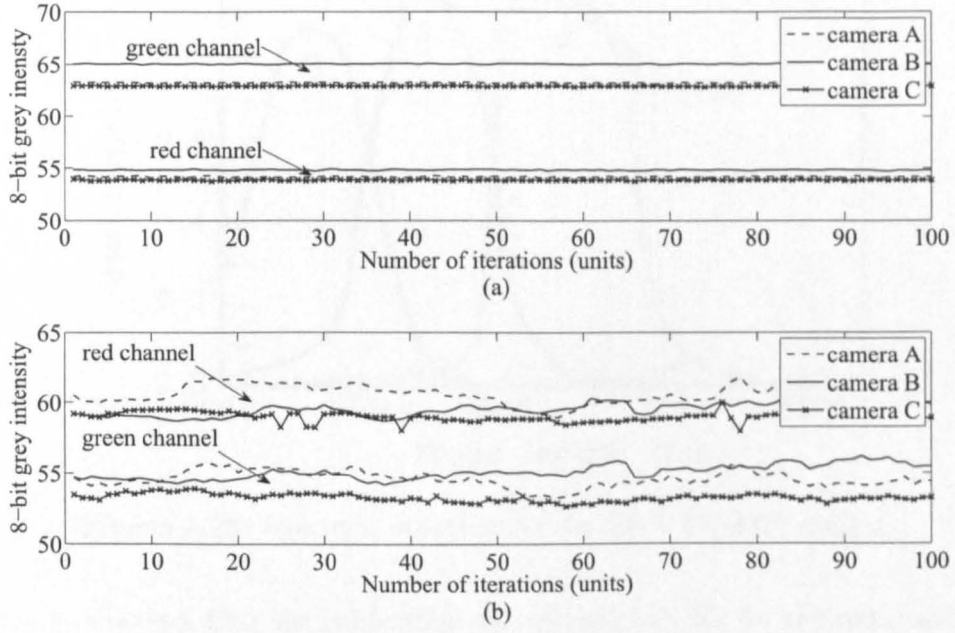

Figure 4.21: Comparison of the intensities captured by the three cameras after calibration. (a) 100 consecutive measurements of the light coming from the LCD panel after calibration. (b) 100 consecutive measurements of the light coming from candle-like gaseous flame after calibration.

the panel area pixel by pixel and calculates the average. Then it displays the three averaged values.

This operation was first performed for one camera retaining the values obtained as the point of reference. Then, the procedure was repeated for the other two cameras at the same time that the main potentiometers were manually adjusted, one time after another until the nearest results were obtained. Figure 4.21 shows the comparison of the light intensities measured by the three cameras (channels red and green) after the process of calibration. Figure 4.21(a) sketches 100 consecutive measurements of the light coming from the LCD panel. More concisely, it displays the light corresponding from the red and the green channel only as the blue channel was not determinant after all. This is explained in more detail at the following section. The maximum

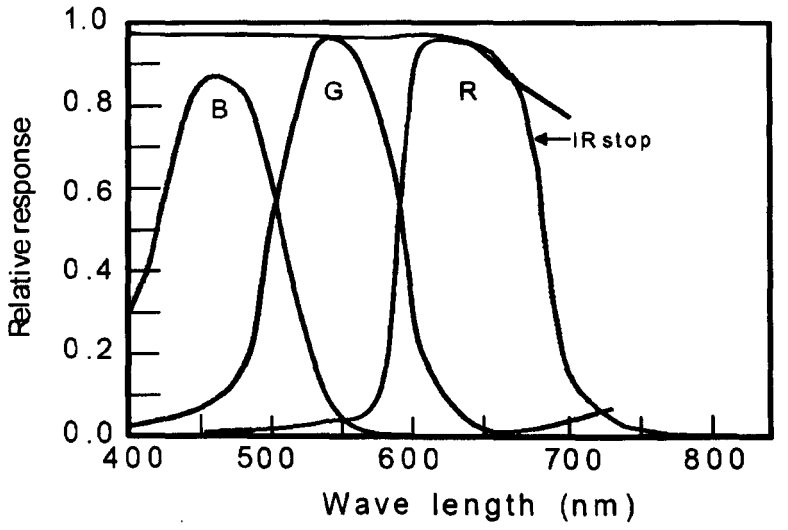

Figure 4.22: Spectrum sensitivity of the JAI® CV-M77 camera.

divergence observed after the calibration was of less than 2% for the red channel and 3% for the green channel. Figure 4.21(b) exhibits the divergences in the intensity measured of the light coming from a candle-like gaseous flame (see Figure 6.4).

4.3.3 Temperature Calibration

4.3.3.1 Choice of the Wavelengths

There are several factors that must be considered in the selection of the two wavelengths. Firstly, the wavelengths should be chosen to avoid any significant influence from the radiation coming from gas molecules and intermediate radicals in the flame (see Section 3.3.1).

Secondly, the wavelengths should be in a region where the outputs of the CCD camera can be expected to vary sufficiently in view of sensitivity and signal-to-noise. It can be found (Yan and Borman, 1988; Ladommatos and Zhao, 1994) from the radiation distribution of a blackbody (Figure 3.14), that the rate of change of spectral radiance with temperature, $\partial \mathscr{E}(\lambda, T)/\partial T$, in the visible region is higher than in the

infra-red region. Furthermore, the rate of change of spectral radiance with respect to wavelength, $\partial \mathscr{E}(\lambda, T)/\partial \lambda$, is also higher in the visible region for temperatures around 1000 - 3000 K. As a consequence, there will be a greater difference in signal output at the two wavelengths, resulting in reduced errors in the temperature calculation due to noise. In addition, the radiation from the refractory wall of a furnace distributes mainly in the infra-red region. The choice in the visible region helps to distinguish flame from the background. Therefore, visible wavelengths are preferred to achieve higher sensitivity and signal-to-noise ratio.

Thirdly, the two wavelengths are expected to be close to each other to reduce the error caused by the difference in spectral emissivity, especially when grey body behaviour of a flame is assumed. Moreover, a closer wavelength pair is also beneficial to reduce the effect of optical transmission. However, a closer wavelength pair will reduce the signal-to-noise ratio.

Finally, the bandwidths should be as narrow as possible to acquire the ideal single-wavelength radiation. However, it is difficult to obtain a clear flame image at a narrower bandwidth due to weakened radiation intensities. In theory, the bandwidths should be the narrowest bandwidths at which satisfactory flame images can be captured for the measured temperature range. Experiments have shown that the bandwidths must be greater than 40 *nm* for gas-fired flames in the combustion laboratory (Huang, 2001).

Following the points stated in this discussion, Huang (2001) selected the wavelengths of 701.2 and 598.7 *nm* with bandwidths of 40.4 and 43.1 *nm* respectively to perform a 2-D analysis of flames utilising a black and white camera and a transmission unit that created two different optical paths to obtain two images from the same flame. In this technical context, Huang (2001) utilised two band-pass filters, one per optical path,

to procure the selected wavelengths. However, in this study there are already two optical paths per camera (see Figure 4.1). To utilise the same solution would increase the optical paths per camera up to four, making it highly impractical and difficult to implement. However, as shown in Figure 4.22, having a colour RGB camera implies that every colour channel acts as a band-pass filter.

Therefore, the selection of the wavelengths was carried out selecting the wavelengths from the peak wavelengths of the colour channels. As seen in Figures 4.2 - 4.4 the blue channel has a substantially higher noise than the others. For this reason, the corresponding wavelength was discarded and the wavelengths 550 and 650 nm were selected. These wavelengths also accomplish the considerations stated above. Firstly, the wavelengths avoid any significant radiation from the molecules of gas. It is true that the wavelength of 550 nm is close to the C_2 bands at 516.5 and 563.5 nm (see Figure 3.11) but, as indicated in Figure 3.12, at this range of wavelengths, the radiation from gas is only 1% compared to that from a blackbody. Secondly, the selected wavelengths are in a region where the output of the CCD camera is expected to vary significantly. Thirdly, they are close to each other and finally the corresponding band-pass filters have bandwidths greater than 40 nm.

4.3.3.2 Calibration of the Instrumentation Factor

It can be seen in Figure 4.22 that the spectral sensitivity of the CCD sensor is different depending upon the wavelength. In addition, the optical components of the transmission unit (such as the lenses, mirrors and prisms) may have different spectral responses at the chosen wavelengths. The ratio between the spectral sensitivities at the two wavelengths, i.e. the instrumentation factor, $\mathscr{S}_{\lambda_2}/\mathscr{S}_{\lambda_1}$ in Equation 3.44 (in this section onwards $\mathscr{S}$) must be known for the correct calculation of the temperatures.

Table 4.2: Calibration of the tungsten lamp at 662.4 nm

Radiance Temperature ($°C$)	Current (A)	Radiance Temperature ($°C$)	Current (A)
700	3.241	1150	5.859
750	3.414	1200	6.298
800	3.611	1250	6.759
850	3.611	1250	6.759
900	4.092	1350	7.738
950	4.381	1400	8.251
1000	4.704	1450	8.778
1050	5.060	1500	9.320
1100	5.445		

A tungsten lamp manufactured by Engel and Gibbs Ltd. was used as a standard temperature source to calibrate the instrumentation factor ($\mathscr{S}$). Calibration using a tungsten lamp has been proven to be very reliable and accurate. Matsui et al. (1979, 1980) used both a blackbody and a tungsten lamp for calibration purposes and compared the results obtained from the two temperature sources. They found that the temperature obtained from the blackbody calculation was only around 10 K higher than that obtained from the tungsten lamp in the vicinity of 2000 K.

The tungsten lamp was pre-calibrated by the National Physics Laboratory (NPL) with regard to the spectral radiance temperature at the wavelength of 662.4 nm against the current of the power supply. The spectral radiance temperature of a surface at a given wavelength is defined as the temperature at which a blackbody radiator has the same spectral radiance at that wavelength. Details of the pre-calibration of the tungsten lamp can be found in the certificate of calibration (NPL, 1999). The overall uncertainty of the calibration is $\pm 3°C$ at $700°C$, $\pm 3°C$ at $1000°C$ and $\pm 4°C$ at $1500°C$. The crucial pre-calibrated data are reproduced in Table 4.2.

The true temperature of the tungsten lamp can be derived from its radiance temperature. In terms of the definition of the radiance temperature, the spectral radiance of an object $\mathscr{E}(\lambda, T)$ can be expressed as

$$\mathscr{E}(\lambda, T) = \varepsilon_\lambda E(\lambda, T) = E(\lambda, T_r) \tag{4.3}$$

where:

T is the true temperature of the object.

T_r is the radiance temperature of the object at wavelength λ.

$E(\lambda, T)$ is the monochromatic exitance emitted from a blackbody with temperature T.

$E(\lambda, T_r)$ is the monochromatic exitance emitted from a blackbody with temperature T_r

Replacing $E(\lambda, T)$ and $E(\lambda, T_r)$ with Wien's approximation (Equation 3.37) into Equation 4.3 and rearranging the new equation give rise to the expresion:

$$\frac{1}{T} = \frac{1}{T_r} + \frac{\lambda}{C_2} \ln(\varepsilon_\lambda) \tag{4.4}$$

This means that the true temperature of the tungsten lamp can be obtained if the emissivity ε_λ is known. The emissivity of tungsten is by its turn a function of the wavelength and of the true temperature T, according to the following equation proposed by Larrabee (1959):

$$\varepsilon_\lambda = 0.4655 + 0.01558\lambda + 0.2675 \times 10^{-4} - 0.7305 \times 10^{-4}\lambda T \tag{4.5}$$

where λ ranges from 450 - 680 nm and T is the true temperature of tungsten in K.

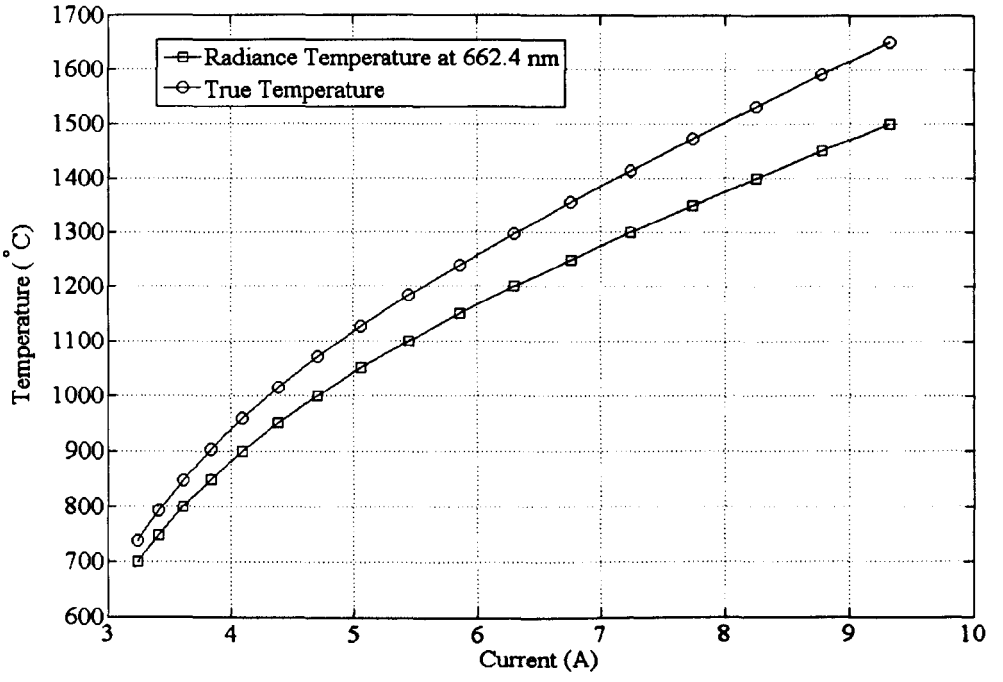

Figure 4.23: Tungsten lamp calibration curves.

Since there are two variables, T and λ, in equation 4.5, the following iterative process was executed to obtain the true temperature and the emissivity:

(a) The emissivity ε_λ is calculated from equation 4.5 using the radiance temperature T_r at 662.4 nm wavelength provided by calibration certificate.

(b) A value of T is obtained from equation 4.4.

(c) With this value T, a new value for ε_λ is calculated from Equation 4.5.

Steps (a) and (b) are repeated until the difference between two consecutive values is insignificant. A program written in C language was developed for this purpose. Figure 4.23 shows the curves of the radiance temperature and the computed true temperature of the tungsten lamp versus the current.

In order to light the tungsten lamp to reach the required temperature, a high stability and high capacity DC current supply (ISO-tech IPS 1810H) was connected directly to the lamp. The power supply is capable of providing up to 10 A DC current with an uncertainty of $\pm 0.13\%$.

The instrumentation factor ($\mathscr{S} \equiv \mathscr{S}_{\lambda_2}/\mathscr{S}_{\lambda_1}$) can be derived from Equation 3.44:

$$\mathscr{S} = \frac{e^{\frac{k_1}{T}}}{\mathscr{R} \cdot \frac{\varepsilon_{\lambda_1}}{\varepsilon_{\lambda_2}} \cdot k_2 \cdot \frac{\Delta\lambda_2}{\Delta\lambda_1}} \tag{4.6}$$

where $k_1 \equiv C_2\left(\frac{1}{\lambda_2} - \frac{1}{\lambda_1}\right)$ and $k_2 \equiv \left(\frac{\lambda_1}{\lambda_2}\right)^5$ are constant, $\mathscr{R} \equiv \frac{\mathscr{I}(\lambda_1,T)}{\mathscr{I}(\lambda_2,T)}$, $\lambda_1 = 650\ nm$ and $\lambda_2 = 550\ nm$ and the emissivities ε_{λ_2} and ε_{λ_1} can be calculated using Equation 4.5.

During the calibration process, the tungsten lamp was placed at the exact position of the burner outlet. Then, a colour image of the ignited filament was taken using a bespoke program and separated into its colour components, R, G, and B. The grey levels of the pixels over the tungsten filament on the selected channels, R and G, were averaged and utilised to create the corresponding R and G images. These images were inserted into the main system software and the reconstruction process was run. The ratio between the two average grey levels ($\mathscr{R}$) was tabulated against the instrumentation factor ($\mathscr{S}$). A detailed procedure of the calibration is as follows:

(a) The output current of the power supply was set to make the tungsten lamp at a given temperature T_j.

(b) The emissivities ε_{λ_1} and ε_{λ_2} at the two wavelengths (650 and 550 nm) were calculated from Equation 4.5. Accordingly, the ratio $\varepsilon_{\lambda_2}/\varepsilon_{\lambda_1}$ of the two emissivities was calculated.

(c) The bespoke software created to take images and obtain information from the tungsten lamp took 100 images of the incandescent filament and extract the 8-bit

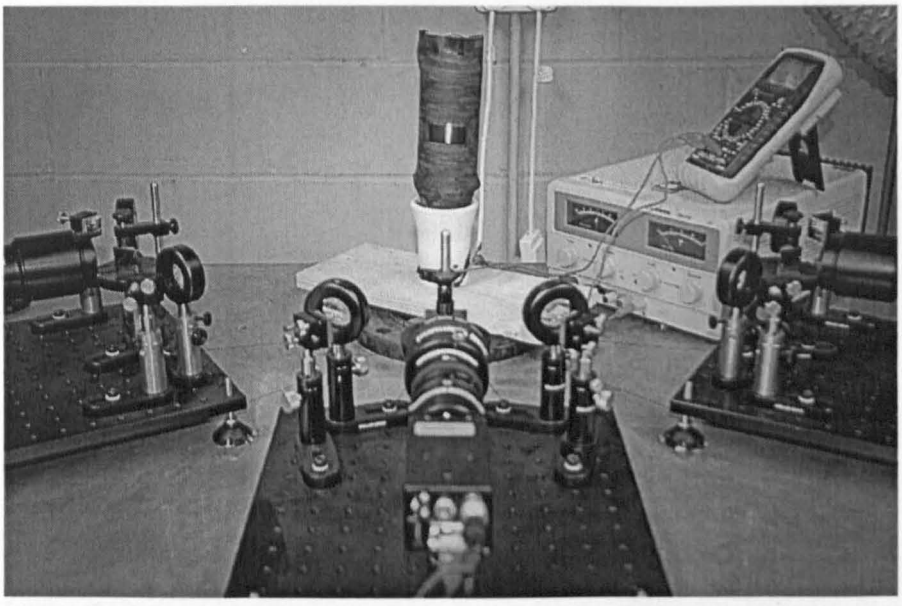

Figure 4.24: Tungsten lamp calibration set-up.

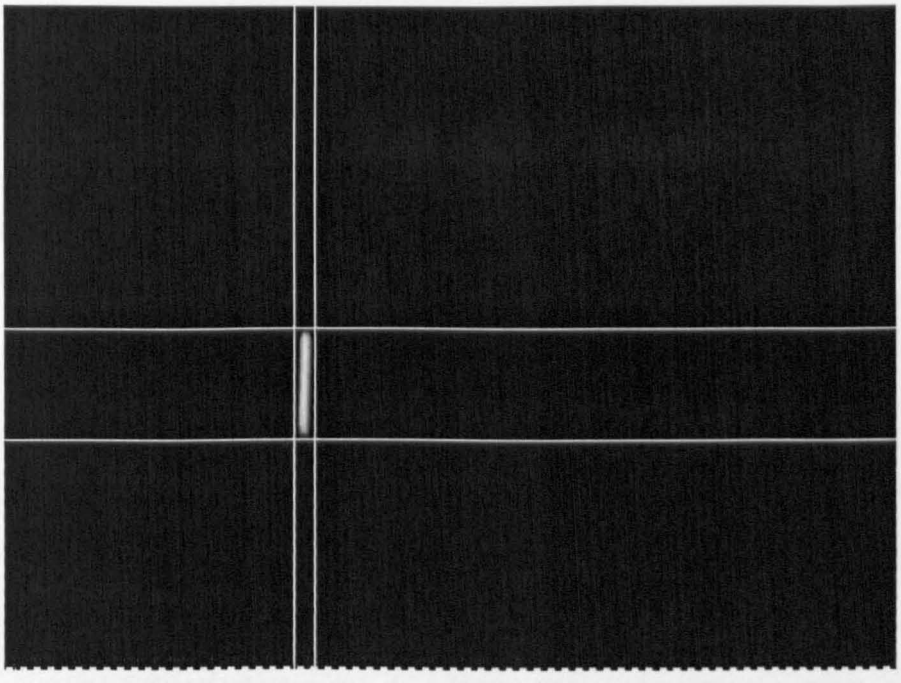

Figure 4.25: Tungsten lamp calibration images taken by the software and cameras.

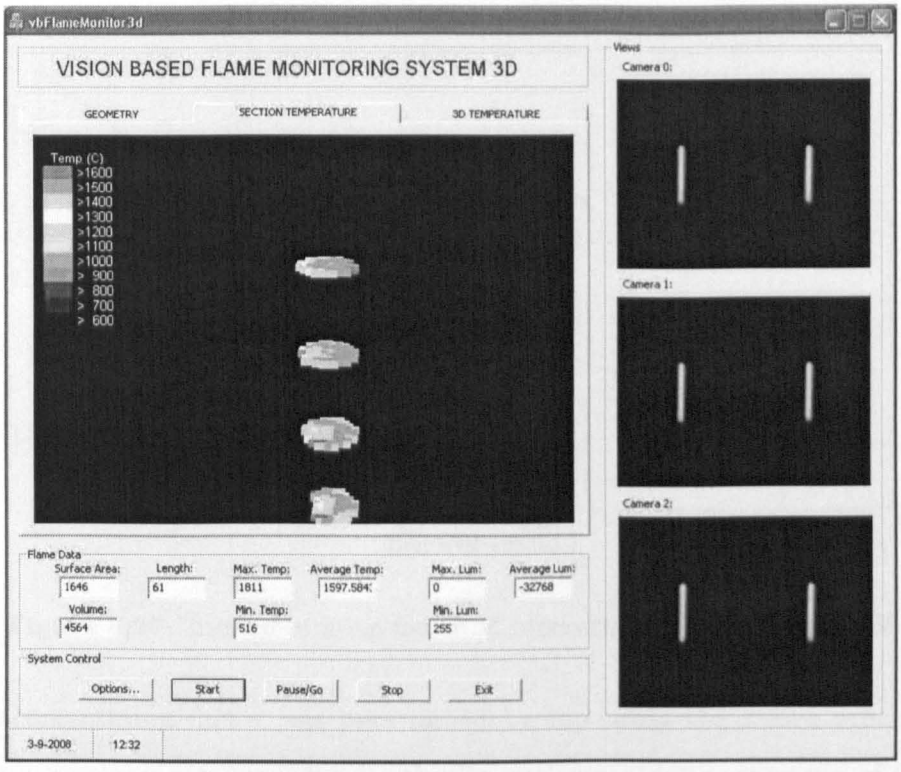

Figure 4.26: Calibration of the instrumentation factor using averaged tungsten filament images.

black and white images from R and G channels. The grey levels of the pixels over the tungsten filament were averaged for each channel. Then the average grey-levels of 100 images were averaged again. The results were the space-resolved average of the grey levels.

(d) The averaged images obtained at the point above were utilised with the main system bespoke software (see Figure 4.26) and a 3-D reconstruction of the filament was performed. In this reconstruction, the corresponding 3-D grey levels for channel R and G were calculated and consequently, the grey level ratio at the two wavelengths.

(e) The instrumentation factor for the given temperature T_j was finally obtained using Equation 4.6.

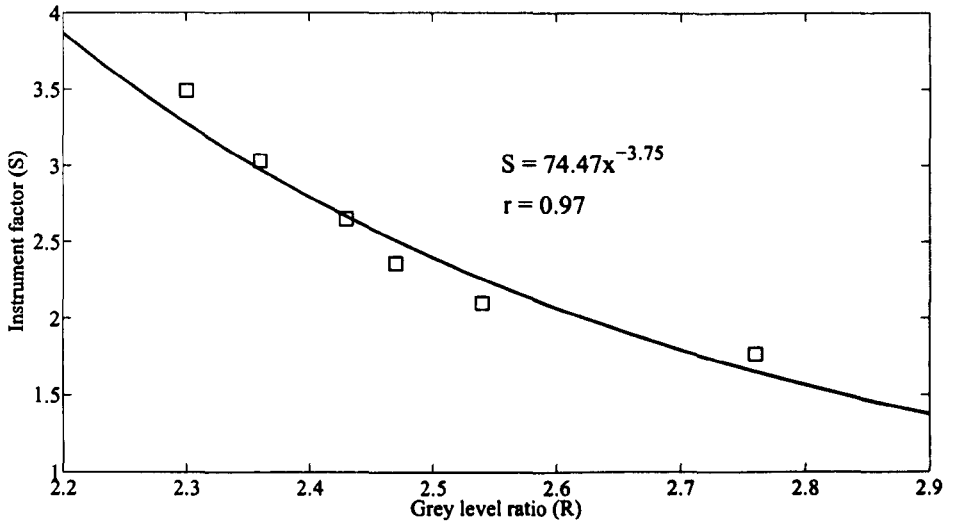

Figure 4.27: Instrumentation factor $\mathscr{S}$ versus the ratio of grey levels $\mathscr{R}$.

The instrumentation factor was determined by repeating the above procedure for several temperature settings. Due to the limitations in dynamic range of the CCD sensors, the temperatures utilised lied within the range 1399 - 1686 K. Below the range the luminosity of the filament was impossible to detect by the cameras and above this range, the images captured were completely saturated and therefore were useless. To cope with this issue, Huang (2001) varied the shutter speed of the cameras to ensure that images of the tungsten filament could be clearly collected over the whole temperature range. However, further research has proven that any change in settings, including the shutter speed can affect non-linearly the readings. In this study, a narrower range was selected as the instrumentation factor could be described accurately. The calibration results are shown in Figure 4.27, where the data points are marked with squares and the calibration equation is marked with a continuous line. The least square regression of the data points yields to the following exponential relationship:

$$\mathscr{S} = 74.47\mathscr{R}^{-3.75} \tag{4.7}$$
$$r = 0.97$$

where r is the correlation coefficient of the calibration result. Ideally the instrumentation factor should be constant. However the calibration results indicate that the instrumentation factor decreases almost exponentially with the ratio of the grey levels. This is due to the non-linearity characteristic of the imaging system.

4.4 Accuracy and Repeatability of the System

The repeatability of the system is guaranteed by the high quality of the materials utilised in its construction and the techniques used. The positioning of all optical components was completely secured after the geometrical calibration was carried out with relative errors lower than 1%. The luminosity calibration was accomplished with help of a highly stable back light panel and by modifying and fastening the gain potentiometers until the capture divergences were in the order of 2% and 3%. The temperature calculation was calibrated employing pre-calibrated tungsten lamp with relative errors lower than 3%.

The instrumentation factor obtained ($\mathscr{S}$) was implemented in the system's calculation to compute the temperature (T) within range of calibration of the tungsten lamp. These temperature results were compared to the original given by the lamp. This comparison is plotted in Figure 4.28 showing a maximum relative error of 4%.

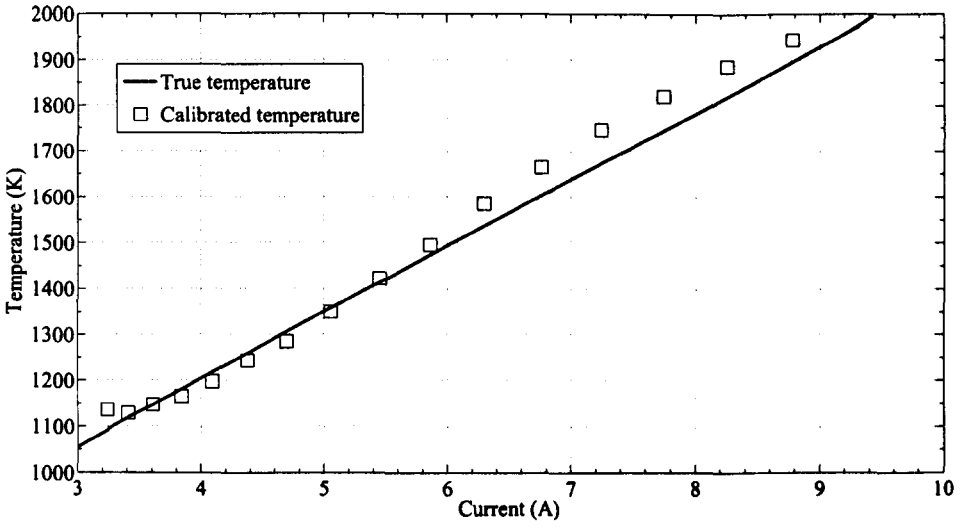

Figure 4.28: Temperature measurement accuracy of the system after calibration.

4.5 Summary

An instrumentation system for the 3-D visualisation and characterisation of fossil fuel flames has been designed and implemented by combining the latest optical sensing arrangement and the most novel digital image processing techniques in conjunction with the two colour principle. The different parts and components of the system have been described in detail explaining its characteristics and functionality. Different software has been specifically created and a stable reference sources has been utilised to ensure the stability, repeatability and superior accuracy of the system.

The two colour method and related factors have been analysed. Many other factors concerning instrumentation selection, including choice of the wavelength, noise of the system, instrumentation factor and processing of the measurement results have been discussed. A complete computer software has been developed, which integrates the system management, image acquisition and processing, temperature computation and result presentation to build up the complete instrumentation system. The

measurement accuracy of the prototype system has been verified by applying the system to measure the temperature of a standard tungsten lamp. The results have demonstrated that the system has a temperature relative measurement error lower than 4%.

Chapter 5

Three-Dimensional Reconstruction of a Fossil Fuel Flame and Measurements of its Luminous and Thermo Properties

5.1 Introduction

This chapter describes the algorithms utilised in this research programme for the complete 3-D reconstruction of a flame model and subsequent quantification of its luminous and fluid-dynamic parameters. This methodology is based on a number of image processing techniques, a new developed tomographic algorithm and computational graphical display tools.

The 3-D model of a flame is reconstructed from its corresponding set of 2-D images simultaneously captured from six equiangular images from three different CCD digital cameras. A set of 3-D geometric, luminous and thermal parameters are then computed from the flame model to provide instantaneous information from the flame

model. The 3-D models of the flames are reconstructed by the system in such a way that allows an all-round visualisation of its parameters and the visualisation system can be tuned to permit the visualisation of the parameters of the flame at each cross-section. The measurement of the temperature distribution is accomplished using the two-colour method.

5.2 Three-dimensional Reconstruction of an Object: A Brief Background

The 3-D visualisation of an object is achieved by reconstructing its 3-D model at different viewing angles. The technology for creating 3-D models of solid objects has exploded during the past decade and it is being applied to a wide range of applications such as medical imaging and multimedia. There is a wide variety of commercial rendering software including AutoCAD, Extreme 3D, Inspire 3D, Lightwave 3D, etc. that have been successfully applied to various situations and different applications where the appearance of an object had to be reconstructed naturally-looking (Bheemul, 2004). However, for a complete characterisation of an object including full reconstruction of its internal structure, software capable of integrating tomographic algorithms is required. Some tomographic-designed packages have been developed for applications with particular applications. For instance EM3D is a package developed at Stanford University for Electron microscopy tomography and the University of Chicago developed the GSECARS, a processing software for x-ray tomography.

For this research programme, an algorithm is therefore required for the on-line and continuous tomographic reconstruction of a flame three-dimensionally. Due to the unavailability of such commercial 3-D software, a custom-designed algorithm incorporating the most appropriated reconstruction technique had to be developed.

These 3-D reconstructing techniques can be mainly classified into two groups depending upon the method to perform the measurements (Zhang and Chen, 2001):

(a) Active method: using structured light or laser scanner, etc.

(b) Passive method: using images taken by one or several cameras.

As a flame is an illuminating object and multiple cameras are utilised in this research programme, only a brief introduction about the passive method is included. The 3-D reconstruction of a flame using the passive method is elaborated below:

(a) Image acquisition: The range of 2-D images covering the flame from six different positions are obtained using three CCD digital cameras and a set of mirrors and lenses as shown in Section 4.2. No external light is required to illuminate the flame as it produces enough light for the cameras to capture the object images. Some pre-processing operations are required. These include the separation of the colour images into its three basic components, R, G and B.

(b) Data extraction: the obtained black and white images corresponding to the channels red and green and wavelengths 550 and 650 *nm* respectively (see subsubsection 4.3.3.1) are selected. These images are 192 pixels high by 128 pixels wide. Pixel line by pixel line from top to bottom of the images, the points belonging to the background are separated of those belonging to the flame.

(c) Tomographic reconstruction: When one line of pixels is clean from background spurious data and the same operation has been completed for the equivalent lines of the remaining five images, these pixel lines are transformed into numerical data. This conversion is performed by the Matrox® MIL-Lite software graphical library. Every pixel of the line is mapped into an 8-bit number ranging from 0, corresponding to pure black, to 255 or pure white. Every number occupies one location in a 128 elements long one-dimensional software vector array in a *C*

language routine. These data are utilised and manipulated using a novel and *ex professo* tomographic algorithm.

(d) Quantification of temperature: when the tomographic reconstruction is completed, the six 1-D arrays are transformed into a 'reconstructed' 128 *by* 128 2-D array whose individual elements contain an 8-bit number or grey levels. In total, the system obtains two 2-D arrays, one for the wavelength of 550 *nm* and another one corresponding to the wavelength 650 *nm*. Then the two arrays are superimposed dividing the data in one element by the data in the equivalent element of the second 2-D array. This operation yields another 2-D array containing grey level ratios that are used to calculate the temperature of the 2-D array element by element. This operation is done by using the two-colour method (see Section 3.3.2). This elaborated distribution of temperatures is the real map of temperatures of the cross-section.

(e) Quantification of geometric parameters: the 2-D array of grey ratios is utilised to quantify the size of the cross-section by counting the total non-zero pixels. The elements of the contour of the cross-section are also quantified to calculate the perimeter of the flame at this section. When all the 192 cross-sections are piled up, these pixels are calculated to extract the volume and surface of the flame.

(f) Data display: all the data are gathered and displayed graphically when possible using the be-spoke interface created using Visual C++ .NET and OpenGL. Exclusively numerical data are also displayed.

Figure 5.1 shows an schematic of the elaborated passive reconstruction method described bove.

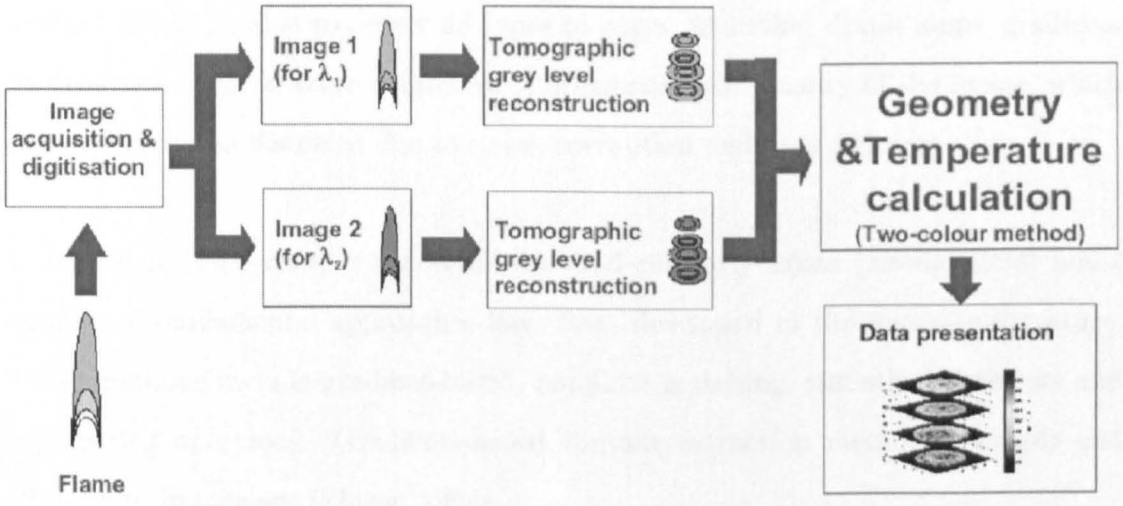

Figure 5.1: Schematic of the elaborated passive reconstruction method.

5.3 Identification of a Flame against the Background

A 3-D reconstruction of a flame is practically impossible without the identification of its virtual edges. It is imperative to initially identify the borders of the flame. This is accomplished by devising a generalised contour extraction method which is capable of extracting the contour of the flame irrespective or its combustion conditions.

5.3.1 Edge Extraction Methodology: a Brief Introduction

Contour extraction is an important and commonly used operation in image processing. It is performed to establish the boundary between two regions in an image. This operation depends on certain criteria such as image intensities of grey-levels. Common applications of contour extraction include the locating of biological cell walls and character recognition (Aramini, 1980). Each particular type of contour extraction method depends upon the criteria specified for the image under consideration and may differ depending on whether the located edges are intended for human visual interpretation of further machine interpretation. An ideal contour extraction

method would be able to detect all types of edges, including simple steps, gradients and changes of the texture regardless of orientation and quality of the image, which can commonly be distorted due to noise, corruption and poor lighting.

In reality, no such contour extraction method currently exists (Zheng, 1994) but a number of fundamental approaches have been developed in the scientific literature. These methods include gradient-based, template matching, statistical detectors and edge fitting operators. Gradients-based contour extraction method is simple and effective to implement (Zheng, 1994).

5.3.1.1 Gradient-based Method

Gradient based method work on the principle that edges in an image may be defined between areas of different intensities. The gradient value $g(x, y)$ of each 2-D image's grey-level pixel, which has a value relating to the grey-scale intensity of the image at that point, is related to the 2-D following differential equation (Dougherty and Giardina, 1987):

$$g_R(x, y) = \sqrt{\left(\frac{dg}{dx}\right)^2 + \left(\frac{dg}{dy}\right)^2} \tag{5.1}$$

where x and y are the positional values of each pixel.

The mathematical idea behind Equation 5.1 is normally applied by the use of a number of operators. Figure 5.2 shows the designation of image pixels in the local 'window' of an operator. This figure can be used to define the most frequent operators. For example, the frequently used Roberts operator g_{ROB} is defined as:

$$g_{ROB} = max(|A - E|, |B - D|) \tag{5.2}$$

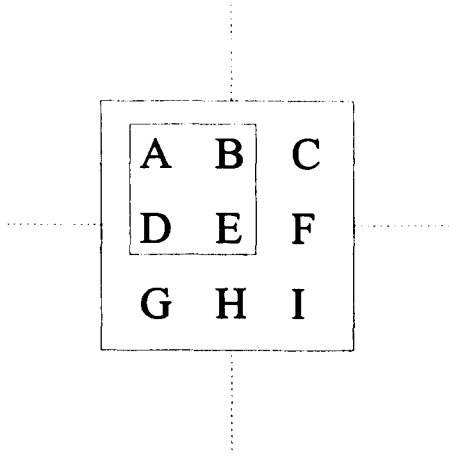

Figure 5.2: Designation of the image pixels in a 2 × 2 or 3 × 3 operator window. (Bheemul, 2004).

The Roberts gradient operates within a local 2 × 2 image window (Dougherty and Giardina, 1987). Without any prior low-pass filtering, intensity differences are produced in the directions of both diagonals. Therefore, this operator is expected to be particularly sensitive to noise presented in the image.

The equally common Sobel operator, g_{SOB}, is defined as (Bheemul, 2004):

$$g_{SOB} = |A + 2B + C| - |G + 2H + I| + |A + 2D + G| - |C + 2F + I| \qquad (5.3)$$

The Sobel operator within a 3 × 3 window is less sensitive to noise. However, the thickness of the generated contours is wider.

The absolute pseudo-Laplace operator is well-known for computing second-order differences from the intensity function and thus is very sensitive to the curvature of the function (Dougherty and Giardina, 1987). The absolute pseudo-Laplace operator, g_{APL} is defined as:

$$g_{APL} = |D - 2E + F| - |B - 2E + H| = |B + D + H + F - 4E| \qquad (5.4)$$

As for the pseudo-Laplace operator, the higher the order of the difference image the more sensitive the gradient operator to noise. This illustrates the limitations of other local gradient operators with noisy image signals.

Dougherty and Giardina (1987) adopted the following rule of thumb to choose the most appropriate gradient operator: to achieve a given noise robustness the stronger the noise superimposed on the image, the more extensive the operator window. However, larger processing windows involve higher computing times.

5.3.1.2 Threshold-based Method

Thresholding is the simplest method in image processing to detect edges in an image (Shapiro and Stockman, 2002). For an object brighter than the background, the threshold process is based on identifying individual pixels as 'object' pixels to discriminate them from the 'background' pixels. This convention is called *threshold above*. There are some thresholding methods that vary from this convention. These variations include *threshold below*, which is opposite of threshold above, *threshold inside* where a pixel is labelled 'object' if its value is between two thresholds and *threshold outside* which is the opposite of threshold inside.

The crucial point in the thresholding process is the choice of the threshold value. Figures 5.3 and 5.4 show an example of the implications that may have the selection of different levels of threshold. In Figure 5.4, after the thresholding, the 'object' pixels and the 'background' pixels have been painted white and black respectively. There are several different approaches to choose this value. One and simple possibility is to choose manually the threshold value but this requires prior knowledge of the subject. Another simple method consists of selecting the statistical *median* or the statistical *mean*. In the case of having a noiseless image with an uniform background, this approach is very effective, but unfortunately these ideal conditions are not usually

2	2	2	2	3	3	3	3
2	1	1	2	3	3	3	3
2	1	1	2	3	3	3	3
2	2	2	2	3	2	2	3
2	2	2	2	3	2	2	3
2	2	2	2	3	3	3	3
2	2	2	2	3	3	3	3
2	2	2	2	3	3	3	3

Figure 5.3: A $g(x, y)$ image with size 8×8 pixels and the following grey levels: $0 \equiv$ black; $1 \equiv$ dark grey; $2 \equiv$ light grey; $3 \equiv$ white.

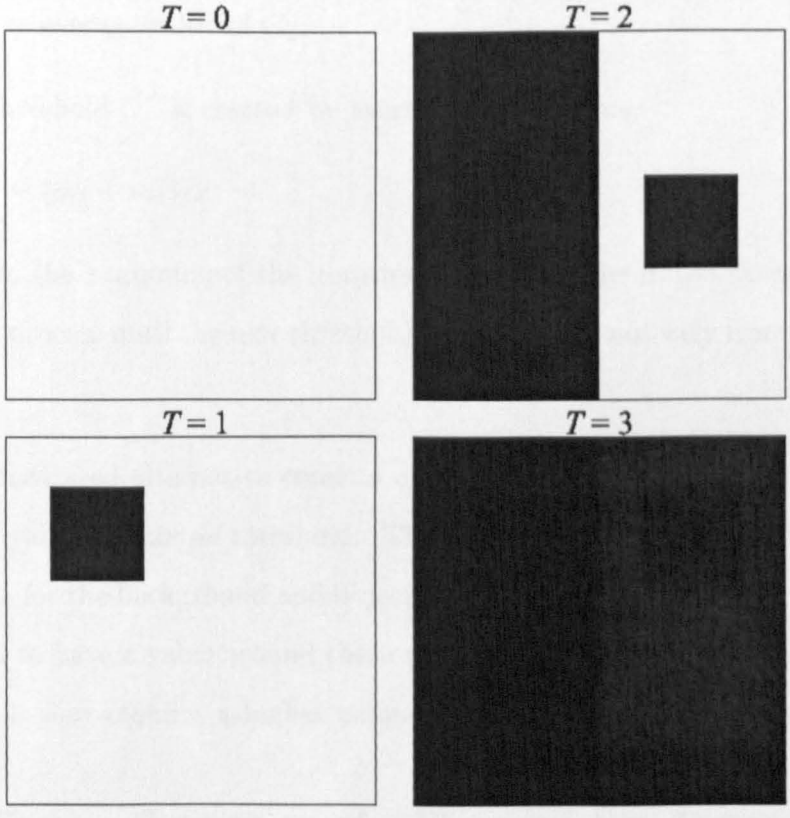

Figure 5.4: Thresholding Figure 5.3 can generate 4 different selections depending on the level of threshold $\mathscr{T}$. The operation perform is: IF $g(x_i, y_i) \leq \mathscr{T}$, $g(x_i, y_i) =$ black; ELSE, $g(x_i, y_i) =$ white.

achieved. Iterative methods can be simple, robust and do not require prior knowledge of the image. The following steps describe a thresholding iterative method that implements a special one-dimensional case of the *k-means clustering* (Bezdek, 1981).

(a) Choose an initial threshold $\mathscr{T}$.

(b) Two sets of pixels, objects and background, are created:

- $G_1 : \{\forall g(x,y) > \mathscr{T}\}$
- $G_2 : \{\forall g(x,y) \leq \mathscr{T}\}$

(c) The statistical average of each set is calculated:

- $m_1 \equiv$ average value of G_1.
- $m_2 \equiv$ average value of G_2.

(d) A new threshold $\mathscr{T}'$ is created by averaging m_1 and m_2.

- $\mathscr{T}' = (m_1 + m_2)/2$

(e) Return to the beginning of the iteration using T' as the initial threshold and repeat the process until the new threshold obtained does not vary from the previous one.

A more sophisticated alternative consists of creating a histogram of pixel intensities and use the valley points as threshold. This approach assumes that there is some average value for the background and object pixels. Therefore, the value of each pixel is considered to have a value around these average values. The main disadvantage of this method is that requires a higher number of computational operations.

5.3.2 Effective Extraction of a Flame and its Outer Contour

Theoretically, the luminous region of the flame is generated by the hot soot derived from the combustible, accompanying with intensive thermal reactions and heat ex-

changes (Fristrom, 1995). As the boundary of the luminous region is considered to be where the combustion has completed, the outer contour of a flame is defined as the boundary between the luminous region of a flame and its surroundings and corresponds to one fifth of the maximum heat released (Fristrom, 1995).

The above pages explain two common methods for the edge detection in image processing. Each of them has its own advantages and disadvantages. Gradient based methods have the advantage that do not require any prior knowledge about the subject and indeed it was the technique utilised by Bheemul (2004). However gradient based methods required a higher number of computational operations. For this reason, they were not considered for this programme research. Thresholding techniques are simple to implement and cheap computationally and can be implemented successfully (Moratti et al., 1997).

The easiest and cheapest option to implement a thresholding edge detector was to define an arbitrary but appropriate threshold. Figures 4.2-4.7 in pages 81-83 show the noise level for every channel. For the selected red and green channels, the noise is always randomly but clearly above of the value 15 in an 8-bits scale with numbers between 0 and 255. When averaged after 1,000 measurements, the noise seems flat and therefore constants, being 15 in the case of the red channel and 16 in the case of the green channel. These results make, at a first stage, any possible value under 15 completely unsuitable. Indeed, low values as 17 or 18 are too close to the noise and therefore, even they were considered as part of the flame, they would be terribly corrupted by the noise and could be classified as 'dirty' values. For this reason, a threshold with a value of 20 is considered. Figure 5.5 shows a zoomed flame image and the grey level values of representative pixels in diverse areas of the images. It can be seen that pixels belonging to the background have a value around 15 that increase slightly at the proximities of the flame. On the other hand pixels belonging

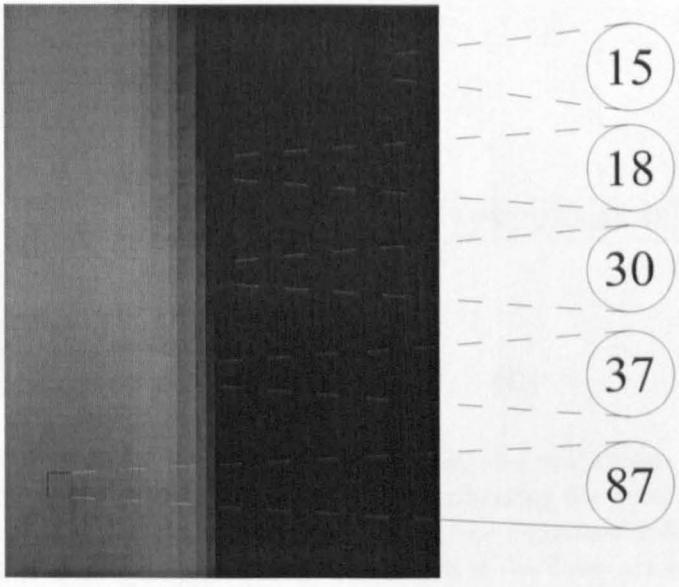

Figure 5.5: Zoomed details of a flame image taken by the system's cameras. The small squares indicate a selected pixel and the encircled numbers the corresponding grey value in an 8-bits scale with numbers ranging 0 (black) and 255 (white).

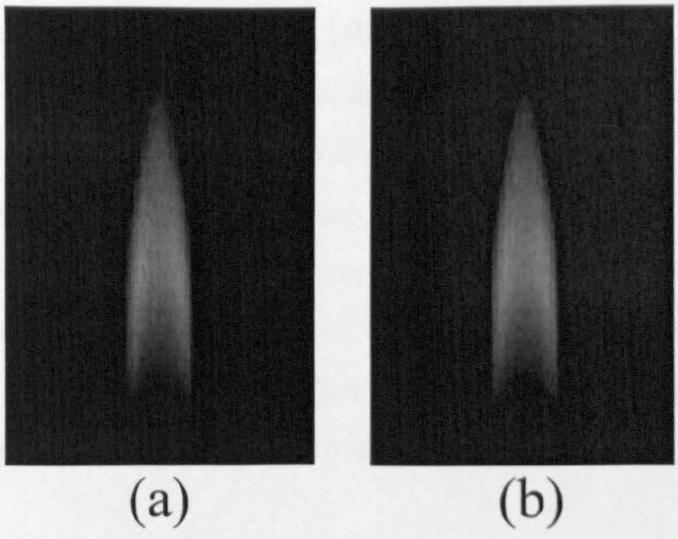

Figure 5.6: Thresholding a flame image using $\mathscr{T} = 20$. (a) Original image. (b) Thresholded image.

to clear and distinctly bright areas of the flame lay far above of the threshold's value of 20 and for brighter areas, 80, 90 and even more. Figure 5.6 shows the result of thresholdig a flame image using a threshold $\mathscr{T} = 20$.

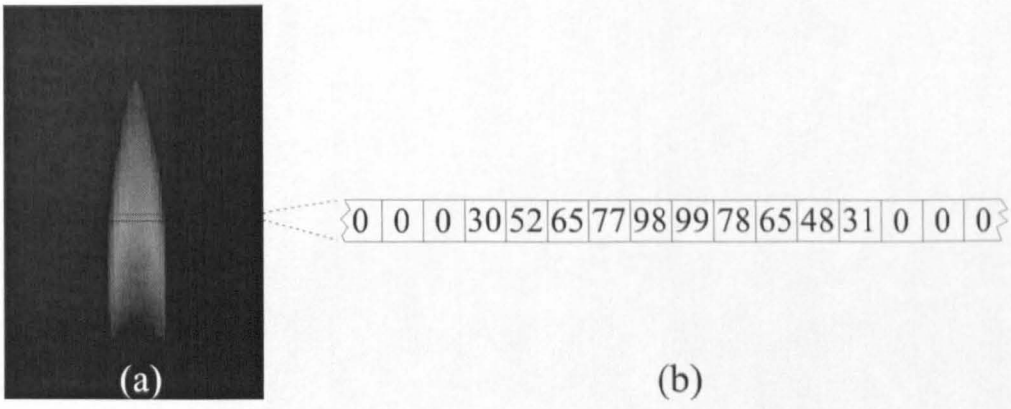

Figure 5.7: Digitalisation process to obtain the projections after the thresholding is completed. (a) Flame image indicating the pixel line to be digitalised. (b) Array of numbers containing the digitalised information; 'background' pixels outside the outer contours of the flame are assigned a value of 0.

Once the thresholding process has finalised the flame image is ready to be digitalised. This step is completed by the Matrox® MIL-Lite library. Every pixel line is transformed, as indicated in Figure 5.7, in an array of numbers ranging from 0 to 255. The 'background' pixels outside the identified flame are 'darken', i.e. assigned a value equal to zero to make them to have no noisy numerical influence in the reconstruction process of the cross-section of the flame. As the system obtains six different simultaneous images of the same flame, six different arrays containing digitalised information about the flame are extracted in total. Each of these arrays are utilised subsequently by the tomographic process as an individual projection.

5.4 A New Developed Tomographic Algorithm: LFBP-ART

In Section 3.2 the two main tomographic algorithms, the Filtered Back-Projection (FBP) and the Algorithm Reconstruction Technique (ART) have been explained in detail. In this research programme, a new tomographic algorithm, based on a suitable combination of ART and a derivation of FBP, has been developed for a more concise and precise tomographic reconstruction of flames using the hardware and configuration explained in Section 4.2.

Xu and Xu (1997) developed a derivation of the FBP, the Logical filtered back projection algorithm (LFBP). The authors proved that this derived algorithm can effectively restrain the blurring, which is normally encountered in the FBP. In real terms, the Equation 3.28, which is the theoretical base of the FBP to reconstruct the original object $f(x, y)$, has to be changed as it is impossible to obtain an infinitive number of projections of the object. Therefore, for a finite number of projections, denoted by M_p, Equation 3.28 is rewritten as:

$$f(x,y) \approx \frac{\pi}{M_p} \sum_{i=1}^{M_p} Q_{\theta_i} \left(x \cos\theta_i + y \sin\theta_i \right) \tag{5.5}$$

LFBP is a real-time two-value logical image algorithm and its major difference with FBP lies in the transformation of Equation 5.5 where the additive operation $\sum$ is substituted by a logical operator. Let us denote this logical operator as $\odot$. If A, B and C are $L \times L$ square matrices, the following operation is carried out by the logical operator $\odot$:

$$C = A \odot B; \quad c_{ij} = \begin{cases} 0, & \text{if } a_{ij} = 0 \cup b_{ij} = 0 \\ a_{ij}, & \text{if } a_{ij} = b_{ij} = 1 \end{cases} \tag{5.6}$$

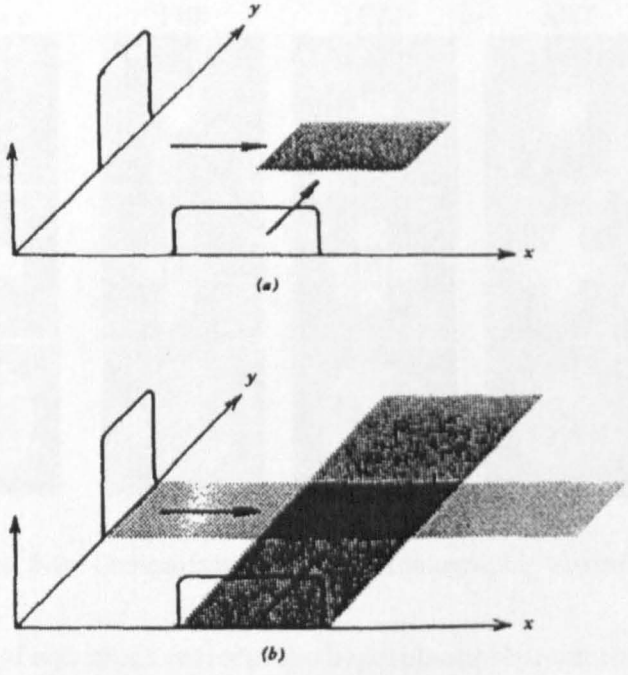

Figure 5.8: Difference between the logical operation $\odot$ and the additive operation $\sum$ in the back-projection. (a) Back-projection with the logical operation $\odot$. (b) Back-projection with the additive operation $\sum$ (Xu and Xu, 1997).

The difference between the logical operator $\odot$ and the additive operation $\sum$ is shown graphically in Figure 5.8. In this figure it can also been seen that LFBP not only smooths the blurring but also, and more importantly for this research programme, provides extra information about the situation and size of the cross-section to be reconstructed.

This extra information can be combined with ART in a novel algorithm in such a way that the total number of equations utilised is increased substantially. This new set of conditions affects ART as follows:

$$w_{ij} f_j = 0, \quad \text{if } c_{ij} = 0; \quad \{c_{ij} \in C\} \tag{5.7}$$

where $w_{ij} f_j$ are the elements in Equation 3.31 and C is the matrix in Equation 5.6.

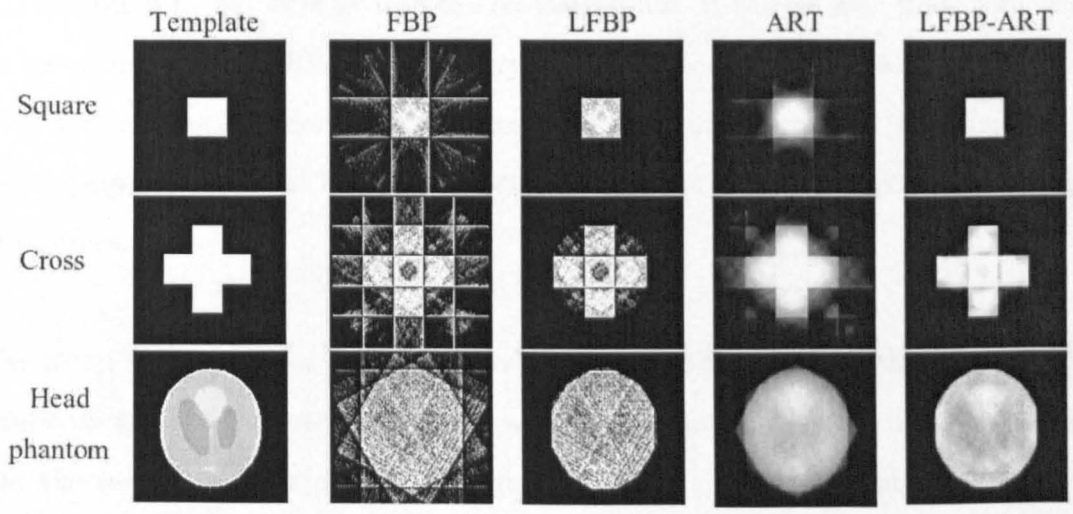

Figure 5.9: Comparison of the four tomographic algorithms.

This additional set of equations corrects the hyperplanes represented in Equation 3.30 resulting in a more accurate solution in performing the iterative operation described in Equation 3.33. In other words, the external contour obtained using the LFBP is utilized to determine which points have to be calculated using the ART. That is, if a particular point lies outside the contour, no unknowns are assigned and no calculations are performed. The value assigned to this point is set to be zero, indicating that there is no any possible luminosity at this position. It is in this way that no spurious values outside the external contour will be computed. This approach not only reduces significantly the number of required calculations but also improves the accuracy of the reconstruction.

To examine the effectiveness of the new algorithm developed, several simulations were carried out. The new algorithm, LFBP-ART was compared to FBP, LFBP and ART by reconstructing three different templates each of them playing the role of a flame cross-section. Figure 5.9 depicts the reconstructed results for different test templates (i.e., a square, a cross, and the head phantom) using the four algorithms. For each test template, six different 1-D projections that were taken on an equiangular basis

and separated by 30° were used in the reconstruction. It can be seen that, with only six projections, the LFBP gives the very similar reconstruction results as the FBP does but reduces considerably the blurring in the reconstruction. The simulation results proves that the LFBP-ART algorithm yields the best reconstruction in all the three cases.

The mean absolute error and the correlation coefficient between the original test templates and the reconstructed results were also computed for a further comparison, and the results are summarized in Figures 5.10-5.11. The mean absolute error is defined and calculated as follows: the original and the reconstructed templates are compared pixel by pixel. The difference in numerical value is measured and the corresponding absolute values is calculated. Finally, the arithmetic mean of all these values is obtained. It is evident that the LFBP-ART gives the smallest mean absolute error and highest correlation coefficient in all cases. This investigation has led to the conclusion that an LFBP-ART offers the best approach to the reconstruction problem.

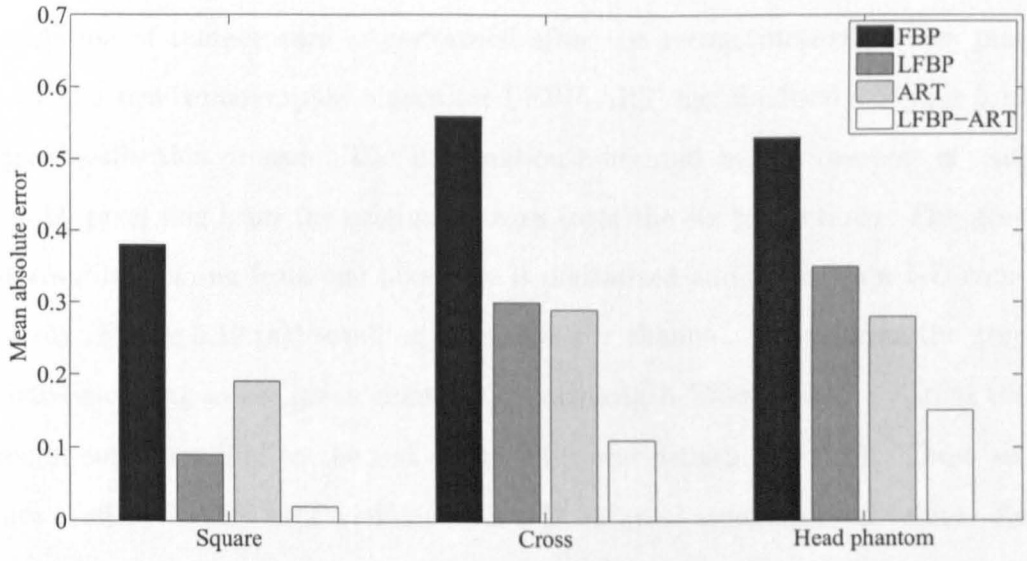

Figure 5.10: Mean absolute error of the comparison of the four tomographic algorithms.

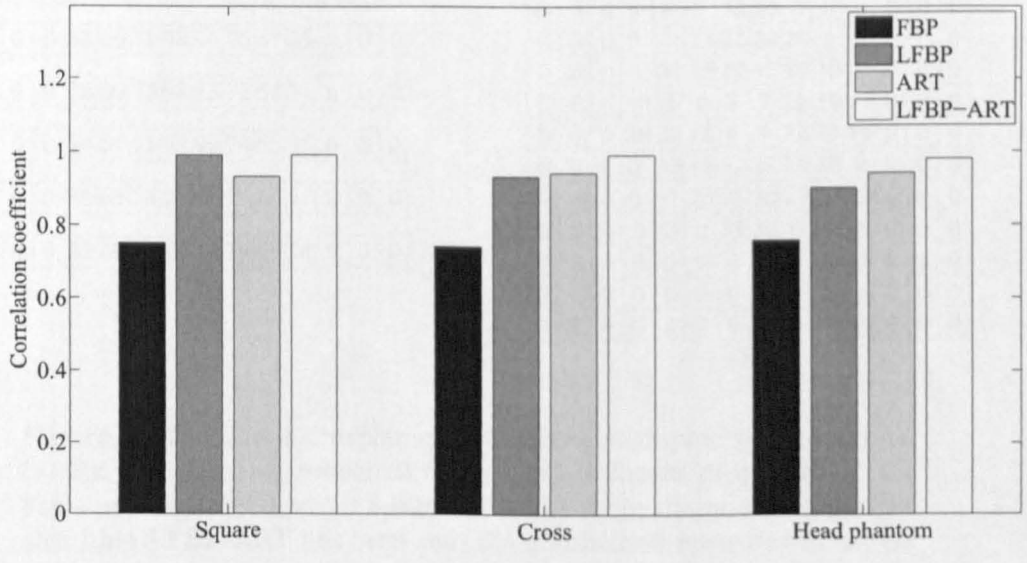

Figure 5.11: Correlation coefficient of the comparison of the four tomographic algorithms.

5.5 Quantification of Temperature

The calculation of temperature is performed after the reconstruction process performed by the new tomographic algorithm LFBP-ART has finalised. Figure 5.12 shows graphically this process. The information measured by the cameras is read pixel line by pixel line from the original images from the six projections. The grey level information coming from one pixel line is digitalised and stored in a 1-D computing array (Figure 5.12.(a)) totalling six arrays per channel. i.e. six from the grey images corresponding to the green channel (or wavelength 550 *nm*) and six from the grey images corresponding to the red channel (or wavelength 650 *nm*). These six arrays are used by LFBP-ART yielding to a 2-D array of reconstructed values. As the system obtains six 1-D arrays per channel, the final of the tomographic algorithm gives two different 2-D arrays.

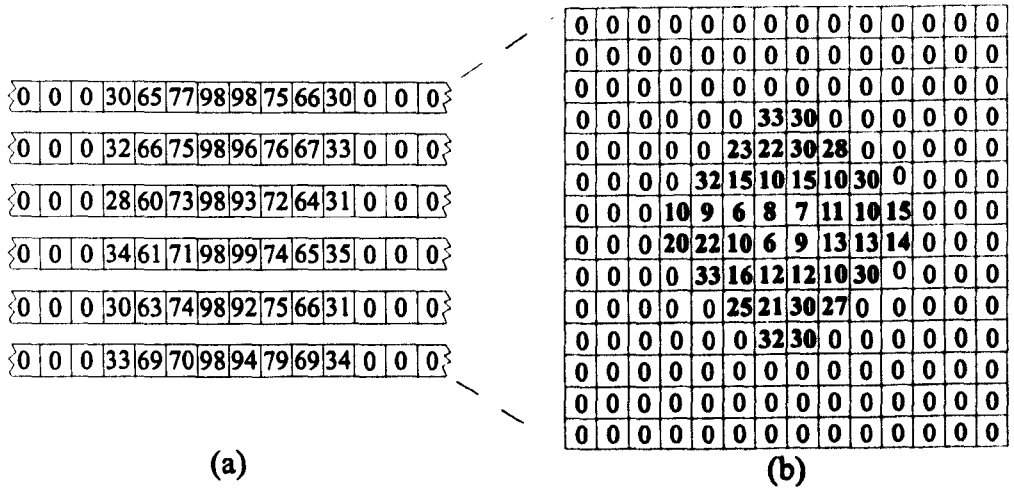

Figure 5.12: Graphic explanation of the tomographic reconstruction. (a) Six pixel lines are measured from the six different projections of the flame and digitalised on an 8-bits scale. (b) After the new tomographic algorithm LFBP-ART has been run, the information measured in the six arrays are transformed or 'reconstructed' in a 2-D array that represent the information of the equivalent and original cross-section of the flame.

These two 2-D arrays are compared dividing element by element in such a way that the element $R_{i,j}$ of the array corresponding to the red channel is divided only by the element $G_{i,j}$ of the array corresponding to the green channel. This operation produces a third array that contains ratios of grey values. Then, every ratio of this array is substituted into the element:

$$ln\frac{\mathscr{G}(\lambda_1, T)}{\mathscr{G}(\lambda_2, T)} \tag{5.8}$$

in the two-colour equation Equation 3.46. This process produces a total 2-D reconstruction of temperatures giving one unique value per element in the array. This reconstruction forms a complete map of the temperature distribution of an specific cross-section of the flame. When this full process is repeated for the 192 pixels lines that form the images of the flames from top to bottom, a complete 3-D map of temperature of the flame is achieved.

5.6 Mesh Generation for the 3-D Reconstruction of a Flame Geometry

Mesh generation, or also called meshing, is an attempt to define a set of elements in order to best describe a geometric domain, subject to various elements size and shape criteria. This geometric domain is most often composed of vertices, curves, surfaces and solids.

5.6.1 Mesh Generation: A Brief Introduction

Meshing can be defined as the process of breaking up a physical domain into smaller sub-domains or elements (Borouchaki and George, 2000). The concept of meshing is used in a wide range of different applications, including the numerical solution of partial differential equations. The major application of interest in the finite element

method is to reconstruct surface domains of various shapes i.e., triangular, tetrahedral, quadrilateral and hexahedral shapes (Li and Teng, 2001). The finite element method has become a powerful tool for the engineering design industry. Increasingly larger and complex designs are simulated using finite element methods. In some cases the mesh generation algorithms subdivide domains into thousands or millions of elements (Bheemul, 2004).

Mesh generation can be categorised into two categories: *structured* and *unstructured.* Triangular and tetrahedral meshes are classified as unstructured meshing, while structured meshing includes quadrilateral and hexagonal meshes. Unstructured meshing allows any number of elements to meet a single node, whereas structured meshing shows a simple structured grid of a finite difference network of vertex connectivity level. The main features which distinguish the two fields are the unique iterative smoothing algorithms employed by structured grid 'detectors' (Bheemul, 2004).

A 'top-to-bottom' mesh generation technique to generate quadrilateral meshes and reconstruct an outer wire-frame surface of a flame has been adopted in this research programme (see Section 5.6.3). The choice of quadrilateral meshes is backed up by the fact that a number of mesh generation algorithms have been successfully developed for the reconstruction of high quality arbitrarily shaped domains (Salem et al., 1997; Owen, 1998).

The procedure of quadrilateral mesh generation has two major steps: designation of the surface points in a cross-section and surface reconstruction using quadrilaterals to join the outer points.

5.6.2 Designation of the Surface Points in a Cross-section

Bheemul (2004) utilised directly the contour points obtained from three 2-D images to measure six points and generate the meshing interpolating extra points in between using a circular model. This method is effective and fast from a computational point of view. On the other hand, it is function dependant as the circular method to interpolate the additional points is not unique. In this research programme, the approach has been considerably different. The edge points measured from the six 2-D images have been utilised only to perform the tomographic reconstruction completed by the new algorithm LFBP-ART. When this process has finalised, a 2-D array of data containing the 2-D information about the cross-section of a flame (see Figure 5.12.(b)) has been obtained. Unlike Bheemul (2004) no interpolation of extra points has been performed but a direct extraction of the information from this 2-D array. A logical algorithm defined the internal points of the cross-section, i.e. the whole cross-section but the outer points, as those points surrounded completely by non-zero elements. The following pseudo code explains its performance:

```
IF ( e(i,j) != 0 )
  IF ( e(i-1,j) != 0; e(i+1,j) != 0; e(i,j-1) != 0; e(i,j+1) != 0 )
    THEN
      e(i,j) = 0
    ELSE
      CONTINUE
```

where e(i,j) is the (i^{th},j^{th}) element in the 2-D array shown in Figure 5.12.(b) in page 134 and the meaning of != is 'not equal to'. The implementation of this algorithm transforms this 2-D array into a new array (see Figure 5.13(a)) containing only the contour points of the cross-section up to the point that the shape and silhouette of the cross-section is naturally and precisely defined with no interpolation or extrapolation of points. Its original shape obtained from the tomographic reconstruction is outlined.

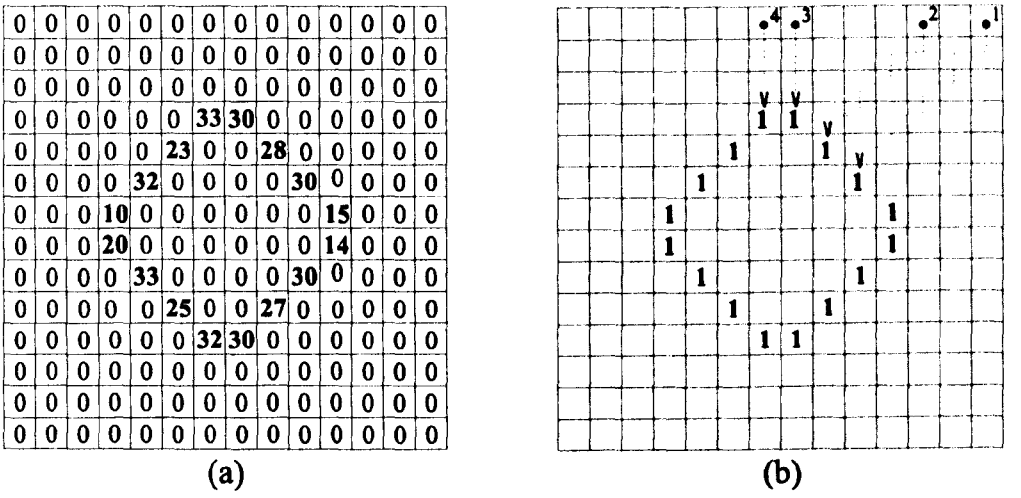

Figure 5.13: (a) 2-D cross-sectional array sketched in page 134 is transformed into another 2-D array containing only the original contour points of a cross-section of a flame. (b) Algorithm to determine the position and the order of the already defined contour points.

5.6.3 Surface Reconstruction

The 3-D geometry model of a flame is obtained by covering the entire contour arrangement with a meshed surface. During the designation of the points forming the surface of a cross-section, the silhouette of the cross-section becomes clearly defined. To represent this contour using the industrial standard OpenGL, it is necessary to draw polygon lines connecting these points in an increasing order to ensure that the polygon lines do not intersect incorrectly (Shreiner et al., 2006). To find the appropriate order on which, the points are to be joined using polygon lines, a new algorithm was developed. This algorithm is explained graphically in Figure 5.13(b). Starting from the top-right corner of the array, the algorithms search the first point progressing on a radial basis. When it finds it, the algorithm stops this search, assigns the first position to this point, and continues the search of new points on the same radial basis but commencing from a different cell placed at the top of the array.

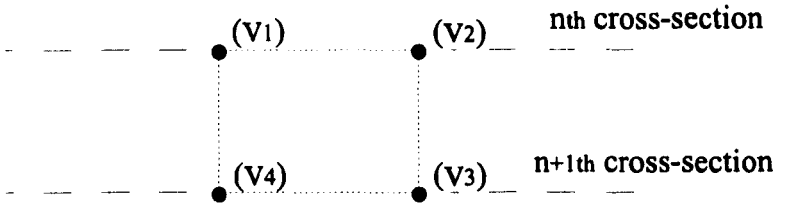

Figure 5.14: Schematic of how quadrilaterals are drawn in OpenGL using polygon lines.

This process is done for two consecutive cross-sections and repeated subsequently from top to bottom of the flame. When all the contour points are detected and assigned the correct position, the polygon lines are rendered to form quadrilaterals using four points, two from one projection and two from the consecutive projection as shown in Figure 5.14. The following lines present the OpenGL code required to draw the quadrilateral depicted in Figure 5.14. The order in which the points appear is essential to avoid errors like, for instance, joining point v1 and v3 directly.

```
glBegin(GL_POLGON);
  glVertex3f(v1);
  glVertex3f(v2);
  glVertex3f(v3);
  glVertex3f(v4);
glEnd();
```

Figures 5.15-5.16 shows the 3-D geometric model and silhouettes of a flame, reconstructed from its 2-D images using the meshing model explained above.

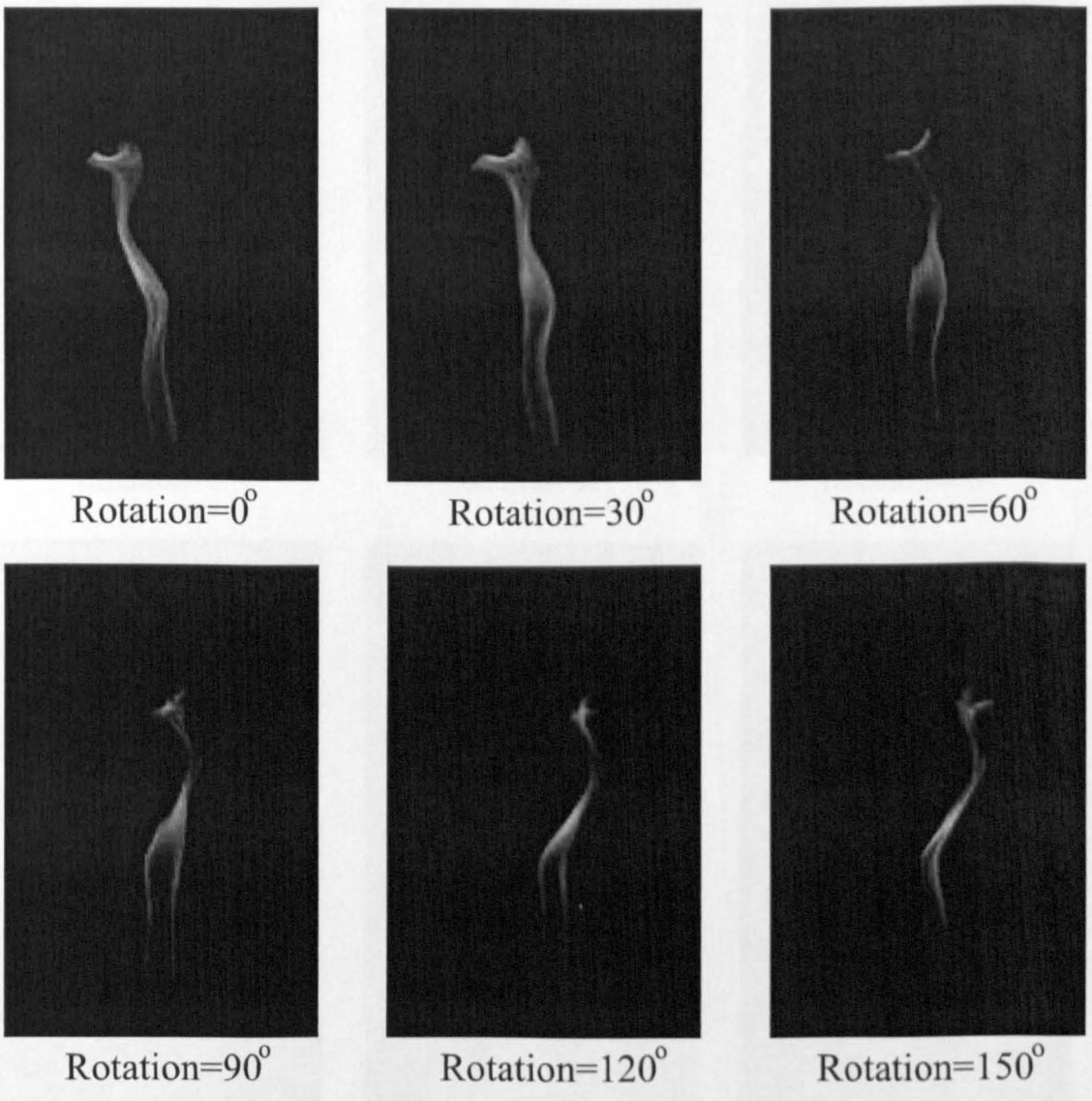

Figure 5.15: Original six images (red channel) of a gaseous flame reconstructed by the system.

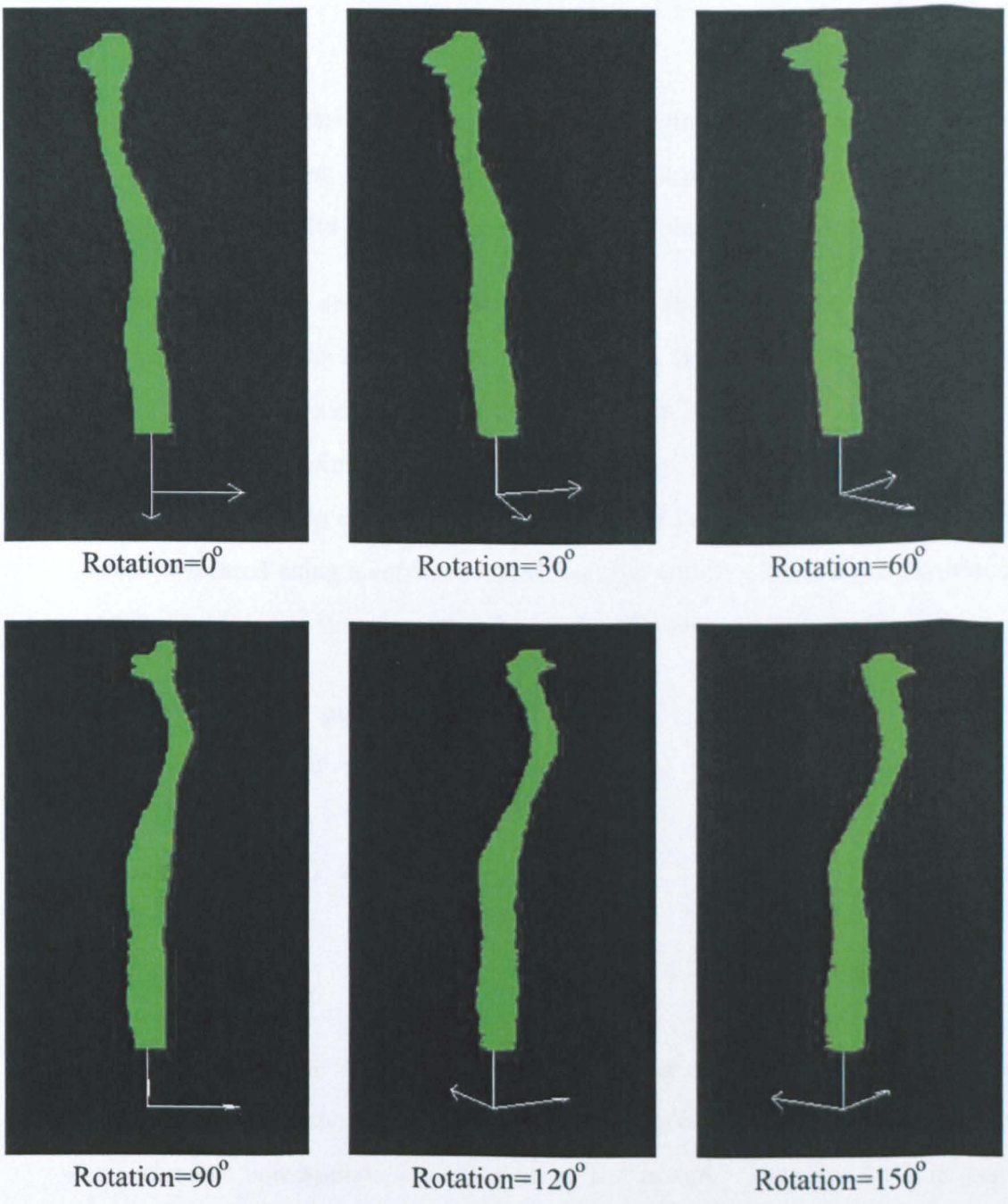

Figure 5.16: Reconstructed geometry of the flame shown in Figure 5.15. At this particular zoom, the silhouettes can be observed and compared to the original to realise the close look.

5.7 Definition and Quantification of Flame Parameters

Following the 3-D reconstruction of a flame and following the procedures described in detail previously, a set of geometric and luminous parameters are defined and determined. The principles of these parameters are explained as follows:

(a) Surface: The surface area of a flame is defined as the 3-D interface between the luminous region of the flame and its surroundings (Lu, 2000). The surface area of a flame is obtain counting the contour points in a cross-section. Figure 5.13 shows the contour points in a cross-sectional array. These points represent the numerical information of a flame in a particular cross-section. These points can be easily counted using a software algorithm that counts all the digits non-equal to zero. The logic of the procedure follows the following pseudo-code:

```
CHECKING = "outer point array"
VARIABLE COUNT = 0
BEGIN LOOP
IF ( e(i,j) != 0 ) THEN
  COUNT++
END LOOP
```

When the final value of COUNT is measured for all cross-sections, the total number of array elements forming the outer surface of the flame is known. Every array element corresponds to one pixel of the image. Section 4.3.1.2 in page 99 explained the dimensional calibration and gave the direct comparison of 67 *mm/pixel*. Counting the total number of counter pixels and applying this ratio gives the total surface of a flame.

(b) Volume: The volume of a flame is defined as the space occupied by the flame in the furnace. To calculate the volume, the resulting arrays after the tomographic reconstruction are considered directly without any external manipulation. Figure 5.12(b) shows a cross-sectional array after the reconstruction. The total number of elements and therefore pixels related to the volume of the flame is counted by the system software following a very similar algorithm as in the case of the surface:

```
CHECKING = "fully reconstructed array"
VARIABLE COUNT = 0
BEGIN LOOP
IF ( e(i,j) != 0 ) THEN
  COUNT++
END LOOP
```

Now, the variable COUNT takes into consideration of the pixels non-equal to zero of all cross-sections altogether and not only the contour elements. When the final value of COUNT is reached, the same relation 67 *mm/pixel* is considered to translate this information into standard measurement units.

(c) Maximum and average temperature: Section 5.5 in page 134 explains the process to obtain the temperature values in all the elements of a cross-sectional array. When this procedure has finished for all cross-sections, then the maximum and average value are calculated counting all the array elements non equal to zero:

```
CHECKING = "reconstructed temperature array"
VARIABLE LOCATION
VARIABLE AVERAGE = 0;
VARIABLE MAXTEMP = 0
VARIABLE COUNT = 0
```

```
BEGIN LOOP
IF ( e(i,j) != 0 ) THEN
  COUNT++
  AVERAGE = AVERAGE + e(i,j)
IF ( e(i,j) > MAXTEMP ) THEN
  MAXTEMP = e(i,j)
  LOCATION = j
END LOOP
AVERAGE = AVERAGE / COUNT
```

(d) Location of the hottest temperature: This parameter measures the height at which the maximum temperature is found. It is therefore calculated an extension of the maximum temperature algorithm. When a new local maximum temperature is found, the position or height of the cross-section is stored. This value is given again initially as a number in pixels. Subsequently this value is translated into *mm* as explained previously.

(e) Length: The length of the flame is defined as the height of the upper tip minus the height of the lower tip. The logic of the procedure follows the following pseudo-code:

```
VARIABLE LENGTH
BEGIN LOOP FROM TOP
IF ( e(i,j) != 0 ) THEN
  LENGTH = j
  BREAK
END LOOP
BEGIN LOOP FROM BOTTOM
IF ( e(i,j) != 0 ) THEN
```

```
    LENGTH = LENGTH - j
    BREAK
  END LOOP
```

Again, the initial value of length is measured in pixels and subsequently translated into *mm*.

(f) Circularity: A circumference is defined as a simple shape of geometry consisting of those points in a plane which are equidistant from a given point called the centre. The circularity of a flame is defined in this research programme following this axiom. Therefore, the cross-sectional arrays containing the contour points (see Figure 5.13) are scrutinised and the centre of 'gravity' of the contour points calculated. Then, the distance between this centre and every contour point is calculated point by point and counted up to be averaged later on. In the case of a perfect circumference, this averaged values should be equal to one. When multiplied by 100, this result is equal to the percentage of the circularity of the contour of the flame.

(g) Maximum and average luminosity: The procedure to find these values is identical to that explained at the maximum and average temperature point. The only difference is the array utilised. Rather than using the array containing the temperature information, the array containing the grey level values corresponding to the most luminous channel (the red channel) is considered.

5.8 Summary

A complete methodology for the 3-D reconstruction of a flame from a set of six simultaneously captured images per channel or wavelength has been described in this chapter. To obtain the most accurate reconstruction using such conditions a novel tomographic algorithm combining the location information provided by the Logical

Filtered Back-Projection (LFBP) and the computational reliability of the Algorithm Reconstruction Technique (ART) has been developed. This new algorithm has been tested and compared against FBP, LFBP and ART in the reconstruction of several cross-sectional templates. In all cases, LFBP-ART has proved to provide the most accurate reconstruction. The tomographic reconstruction process requires the help of accurate image processing manipulation to obtain and measure the appropriate information correctly. The theoretical background of several edge detection techniques has been explained and compared informing of the strengths and weaknesses of each one. Subsequently, the finally selected edge detector approach has been scrutinised indicating the advantages of using this procedure. The measurement of the reconstructed temperature on a 3-D basis has been studied in detail, including advanced discussion about the 2-D and 3-D numerical processing involved. The luminous and geometric parameters considered in this research programme have been defined and their calculation explained extensively using pseudo-code algorithm to make more accessible the understanding of the original C++ routines. The mesh generation capabilities of the newly designed system have been explained in detailed including some theoretical background for a better understanding. An in-depth technical description of the industrial standard OpenGL utilised by the novel system has been illustrated as a way to explain the complete meshing generation features. The 'fishnet' surface that the system creates, covers the entire flame structure and generates the geometric 3-D model of a flame. It is envisioned that the reconstruction of complete luminous and fluid-dynamic 3-D models of fossil fuel flames in conjunction with the measured flame parameters will enable combustion engineers to have a better understanding of the dynamic behaviour of flames under different operating conditions.

Chapter 6

Experimental Work

6.1 Introduction

Extensive experiments were conducted on a laboratory-scale combustion test rig in the university instrumentation laboratory. The objective of the experiments were to evaluate the performance and reliability of the prototype system in a laboratory environment and characterise gas fired butane flames in terms of their flow rate and 3-D parameters like the average temperature, maximum temperature, surface area of the flame's front, volume of the flame, height of the flame, location of highest temperature, circularity of the flame, maximum luminosity and average luminosity.

The original combustion rig in the university's laboratory was particularly designed for the evaluation of 2-D flame monitoring systems (Lu, 2000). However this rig is not appropriated for the installation of a sensing arrangement which is suitable to achieve the 3-D visualisation and characterisation of a flame. Bheemul (2004) adapted the original design for the 3-D visualisation and quantitative characterisation of combustion flames. However, the chamber, adapted to a particular camera positioning for a geometrical study, does not allow the utilisation of the tomographic algorithms proposed in this work. Therefore, the design of a new combustion rig which allows

the visualisation of the flame from the correct projections at the right angles from six different locations was a prerequisite for this research programme. This new rig also provides a steady, adjustable and repeatable camera installation.

The 3-D reconstruction of flames were accomplished under a range of combustion conditions. The geometric, luminous and tempcerature parameters of butane gas fired laminar diffusion flames were computed using the new developed system-rig under several flow rate conditions. The correlation between the flow rates and the geometric, luminous and temperature parameters of the laminar diffusion flames are quantified and discussed. Under the university laboratory stable conditions, external and unexpected disturbances can be easily minimised or even avoided. The newly designed chamber isolates the flames from room air currents. The black colour of all chamber and optical metal components minimise the background light and dismiss specular reflections. The quality of the CCD camera sensors stabilises and reduces the signal to noise ratio. It is therefore expected that due to this stability, the results obtained in the university laboratory demonstrate a clear relationship with the flame parameters and the processed data.

6.2 Experimental Conditions

6.2.1 Overview of the Combustion Rig

The general arrangement of the combustion rig is shown in Figure 6.1. The rig consists of an hexagonal chamber, each side 270 mm long. The chamber is 710 mm tall and contains a suction circular chimney at the top that connects it to the outside world in order to remove the exhaust gas from the chamber. Both, the interior and external walls of the chamber were painted black to provide a black background against which to record the images of the flame and to minimise any potential specular

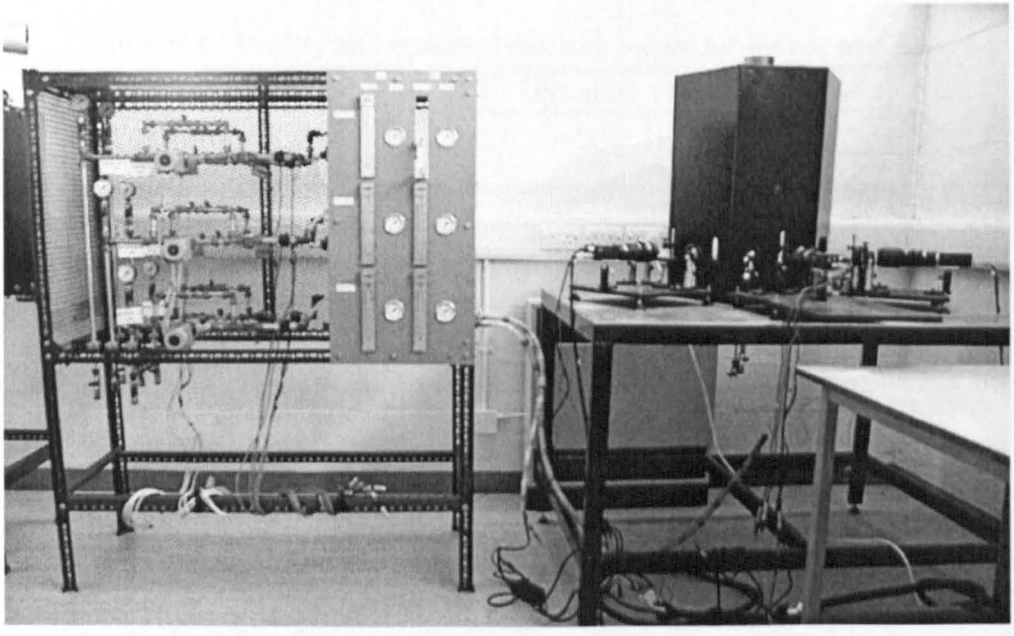

Figure 6.1: Laboratory combustion test rig.

light reflection. The three front sides of the chamber contain a view window which is 90 mm long by 165 mm wide and is placed at 115 mm from the base. These three windows were built to allow optical access to the flame. The rear side of the chamber contains a 100×100 mm window to easily ignite the combustion flame. The fuel is supplied through a pipeline with a 10 mm internal diameter. The fuel rate is measured by a laminar flow-meter (Key Instruments 1.0 $l/min.$) which is installed on the pipeline.

The design, physical properties and characteristics of the burner have been described in Lu (2000). The burner utilised was a Bunsen-type burner because it provides a similar performance to a single-port premixed gas burner in practical combustion systems (Borman and Ragland, 1998). The burner is positioned vertically in the centre of the base of the combustion chamber and consist of a cone-shaped nozzle from which the gaseous fuel is supplied. The burner tube has a length of 130 mm and could be changed to test different burner diameters. For the current study a single

Table 6.1: Density and dynamic viscosity values for butane and air.

	Density, $\rho(kg/m^3)$	Dynamic viscosity, $\mu(Pa \cdot s)$
Butane	2.520	7.5×10^{-6}
Air	1.293	18.1×10^{-8}

circular tube of internal diameter 20 mm was utilised. Only manually operated valves at the flow-meter were operated to control the fuel flow rate. The butane gas was supplied by a 15 kg (Calor Gas) bottle connected to the pipeline through a 6 $mbar$ regulator valve.

6.2.2 Nature of Combustion Flow

The characteristics of a flame, and therefore the flames utilised in this study, is affected fundamentally by the nature of its combustion flow. The different flow regimes are defined by using their corresponding values of the Reynolds number ($\mathscr{R}e$) (Fristrom, 1995; Rott, 1990), first proposed by Reynolds (1883). $\mathscr{R}e$ can be defined for a number of different situations where a fluid is in relative motion to a surface. These definitions generally include the fluid properties of density and viscosity, plus a velocity and a characteristic length or characteristic dimension. For a flow in a pipeline, the Reynolds number is generally defined as:

$$\mathscr{R}e = \frac{\rho V D}{\mu} = \frac{V D}{\upsilon} = \frac{Q D}{\upsilon A} \tag{6.1}$$

where:

V is the mean fluid velocity (m/s).

D is the diameter of the burner tube (m).

μ is the dynamic viscosity of the fluid $(Pa \cdot s$ or $N \cdot s \cdot m^2)$.

υ is the kinematic viscosity of the fluid, $\upsilon = \mu/\rho$ $(m^2 \cdot s)$.

ρ is the density of the fluid (kg/m^3).

Q is the volumetric flow rate (m^3/s).

A is the cross-sectional area of the pipeline (m^2).

The Reynolds number is therefore a dimensionless number that gives the measure of the ratio of inertial forces (ρV) to viscous forces (μ/D) and, consequently, quantifies the relative importance of these two types of forces for given flow conditions. In a straight constant area pipeline, for low values of $\mathscr{R}e$, as low and under 2000, where viscous forces are dominant, the flow is regarded as laminar and it is characterized by smooth, constant and fluid motion. For high values of $\mathscr{R}e$, 4000 and above, the inertial forces become dominant and the flow presents eddies, vortices and other fluctuations. Then, the flow is regarded as turbulent. For values of $\mathscr{R}e$ lying within 2000 and 4000, the flow is considered to be in a transitional state between laminar and turbulent (Brisley, 2006). The density and viscosity of the butane gas utilised in this study is listed in Table 6.1.

6.3 Preliminary Studies on the Reconstruction of the Luminosity of a Gaseous Laminar Flame

To evaluate the performance of the imaging system and the effectiveness of the developed algorithms, a series of experiments was conducted on a laboratory-scale gas-fired combustion rig. The system was used to capture multiple 2-D images of a butane flame concurrently from the six different directions under steady combustion conditions. The new developed algorithm, LFBP-ART, was integrated as part of the system software and implemented to reconstruct the grey-level sections of the flame using the images previously obtained. Figure 6.2 shows the set of six simultaneous images of the same flame from the six different equiangular position with a separation

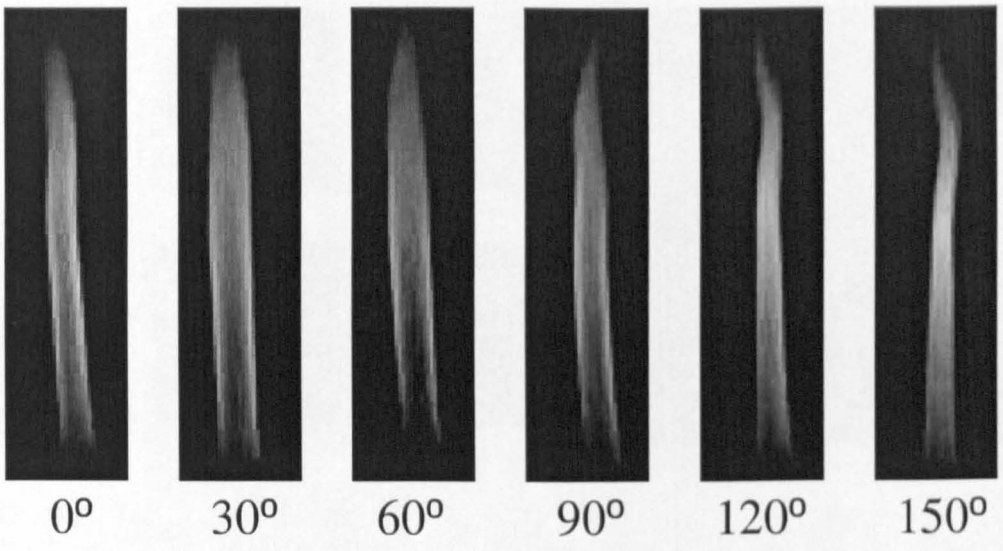

Figure 6.2: Six different images of the same flame from six different angles. Taken using the new developed system.

of 30 degrees between two consecutive images. Figure 6.3(a) shows the reconstructed luminous cross-sections of the flame using the LFBP-ART approach. Comparing the reconstructed cross-sections with the original images Figure 6.2 we can make several observations. For instance, cross-section i, is more circular as it is the nearest to the burner outlet. It also shows a sharp difference between the brighter outers and the darker inners. Moving upwards, we can observe that the circularity of the cross-sections deteriorates. This is also observed in different widths of the corresponding sections of the images captured from different angles (Figure 6.2). Additionally, the luminosity distribution of the upper cross-sections appears to be more homogeneous than the lower sections, as observed in Figure 6.2. The reconstruction of flame cross-sections can be computed repeatedly for every pixel row along the flame axis. Consequently, a large number of cross-sections are obtained and combined to form a complete 3-D reconstructed model of the flame. When this is accomplished, an exhaustive internal examination can also be performed by viewing the longitudinal sections of the flame. Figure 6.3(b) shows typical examples of reconstructed longitudinal-sections of the flame. It should be noted that the visual representation

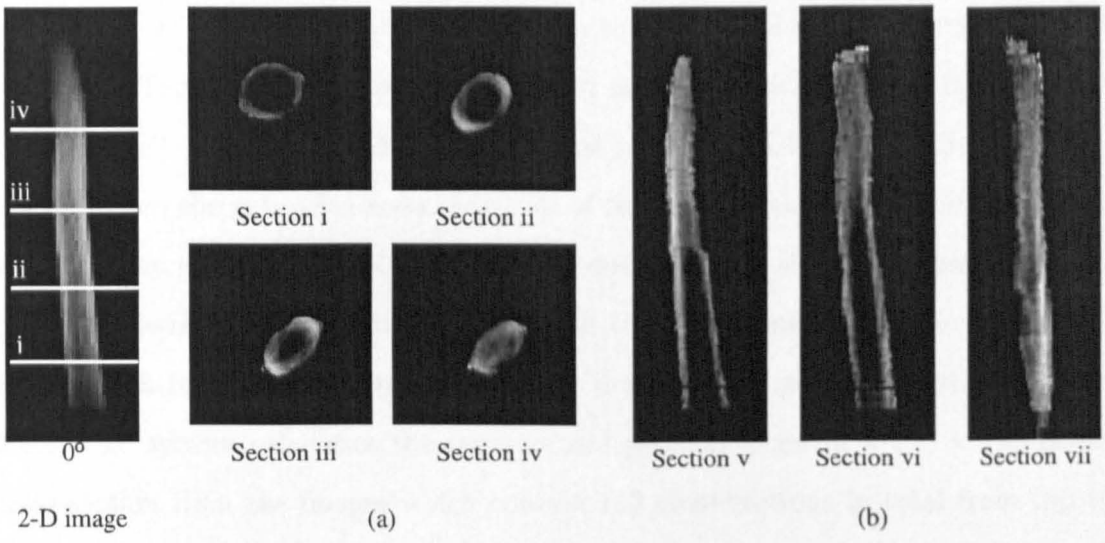

Figure 6.3: From left to right, a sample of the 2-D images utilised in the reconstruction, (a) Reconstructed cross-sections, (b) Reconstructed longitudinal sections

of the reconstructed longitudinal-sections depends on the point of view. The results presented in Figure 6.3(b) refer to the section viewed from the direction of 0° (refer to the reference image in Figure 6.2). Section *vi* depicts the longitudinal section along the burner axis whilst *v* and *vii* present the sections about 10 steps (pixels) back and forward the burner, respectively. Since the three segments are close to the burner axis they show similar luminous profiles. This result agrees well with the original 2-D images of the flame (Figure 6.2).

6.4 Experimental studies in laminar flames

The system developed in this study uses six equiangular 8-bit black and white images of the flame from six different projections, as described in Section 4.2, to achieve firstly the tomographic reconstruction of the flame grey-level cross-sections at the two different wavelengths 550 *nm* and 650 *nm* as stated. With such an arrangement, no assumption on the axis-symmetry of the flame is required. Therefore no details are lost due to this idealistic simplicity. The system reconstructs the cross-sectional grey

levels using an improved algorithms based on the combination of the Reconstruction Algorithm Technique (Kak and Slaney, 1988) and the Logical Filtered Back Projection (L-FBP) (Xu and Xu, 1997) as explained in Section 5.4 and in (Gilabert et al., 2007). When the grey level reconstruction of the cross-sections is performed for the two different wavelengths 550 *nm* and 650 *nm* using the six projections, the temperature distribution is calculated using the two-colour method (Huang and Yan, 2000) which reduces the problem of finding the temperature to solve the Equation 3.46. The system calculates the temperature pixel by pixel in a 128 × 128 pixels cross-section from the images which contain 192 cross-sections in total from top to bottom. The resulting values of temperature are stored into the computer temporal memory using a 3-D array of data. In this way, a complete 3-D reconstruction of the temperature profile is performed. The following section shows the comparison of the results obtained by the system developed in this study and multiple thermocouples.

6.4.1 Comparison of the results between thermocouples and the imaging system

Thermocouples have been utilised extensively to measure temperature. They are simple, relatively cheap, easy to use, reliable and do not require big installations or complicated set-ups. Tagawa and Ohta (1997) utilised two thermocouple probes of different diameters to carry out fluctuating temperature measurements of a diffusion flame formed in a 2-D wind tunnel. It also showed that thermocouples are successful even to study the characteristics of time-constant fluctuations in high temperature turbulent flows. McEnally et al. (1997) used the Thermocouple Particle Densiometry (TPD), firstly proposed by Eisner and Rosner (1985), to measure the absolute soot volume fraction in laminar non-premixed flames. The diagnostic relied on measuring the thermocouple's junction temperature history rapidly inserted into a soot con-

Table 6.2: Common types of thermocouples.

ANSI Code	Alloy Combination	Temperature Range ($°C$)	Stdandard - Special Errors (%)
J	Fe vs. Cu-Ni	0 to 750	0.75 - 0.4
K	Ni-Chr vs. Ni-Al	-200 to 1250	2.0 - 0.4
T	Cp vs. Cp-Ni	-250 to 400	1.5 - 0.4
E	Ni-Cr vs. Cp-Ni	-200 to 900	1.0 - 0.4
N	Ni-Cr-Si vs. Ni-Si	-270 to 1300	2.0 - 0.4
R	Pt(13%)-Rh vs. Pt	0 to 1700	0.25 - 0.1
S	Pt(10%)-Rh vs. Pt	0 to 1700	0.25 - 0.1
B	Pt(30%)-Rh vs. Pt(6%)-Rh	0 to 1800	0.5 - N/E

taining flame region. Caldeira-Pires and Heitor (1998) used digitally compensated thermocouples to characterise the time resolve behaviour of the temperature field in turbulent non-premixed jet flames for $\mathscr{R}e \geq 2 \times 10^4$. Santoni et al. (2002) utilised a double thermocouple probe to measure the fluctuating temperatures in a continuous flame spreading across a fuel bed for the validation of different existing models. These models were tested first with a clean diffusion flame of ethanol and secondly with a turbulent flame of a fire spreading across a bed of pines needles. Qi et al. (2008) calculated the temperature field of a premixed butane/air slot laminar flame jet by studying the interferogram of the flame using Mach-Zehnder Interferometry and compared the results with those provided by thermocouples.

Table 6.2 shows the most common types of thermocouples available indicating their major characteristics and functioning temperature range. McCaffrey (1979) and Audouin et al. (1995) reported similar results in temperature measurements of unbounded fire. The maximum values barely reached 900 $°C$ and minimum values were as low as 320 $°C$. Cox and Chitty (1980) performed a study in buoyant diffusion flames and obtained maximum values circa 900 $°C$ and temperatures between 340 and 550 $°C$ at the flame tips. Smith and Cox (1992) found peak values of temperature of 1150-1250 $°C$ for natural gas flames under several conditions. Shakher

et al. (1992) obtained maximum values of temperature slightly higher than 1200 $°C$ in gaseous flames. Gaydon and Wolfhard (1979) found a peak temperature of around 1400 $°C$ in a candle flame. Qi et al. (2008) calculated maximum temperatures of around 1400 and 1600 $°C$ in a butane/air laminar flame. Char and Yen (1996) calculated maximum temperatures lower than 1700 $°C$ in a propane flame using infrared techniques.

To ensure that the thermocouples were able to function in the potential range of temperature, only thermocouples with ANSI codes R, S and B could be utilised. Thermocouples of type S can be used in oxidising or inert atmospheres continuously. For high temperature measurements, insulators made from recrystallised alumina are generally used. On the negative side, continuous use at high temperatures can cause degradation, and there is the possibility of diffusion of Rhodium into the pure Platinum conductor leading to a reduction in output. Thermocouples of type R are similar to the type S. It has slightly higher output but the applications covered by both types are broadly identical. Thermocouples of type B are were invented more recently. In many respects the device resembles thermocouples of types S and R, although the output is lower, and therefore it is not normally used below 600 $°C$. Miller et al. (1993) measured the temperature in a laminar methane/air diffusion flame using a tunable diode-laser spectroscopy and compared the results with uncoated type S thermocouples founding an agreement to within an experimental error of ± 100 K between the temperatures measured with the thermocouples and those obtained with the tunable diode-laser spectroscopy.

Multiple unsheathed type S thermocouples were utilised to validate the temperature reconstruction performed by the system. The thermocouples, had a diameter of only 0.125 mm to allow a fast time response. The thermocouples were introduced in tubes of aluminia ceramic (Al_2O_3) insulators to protect them and facilitate their

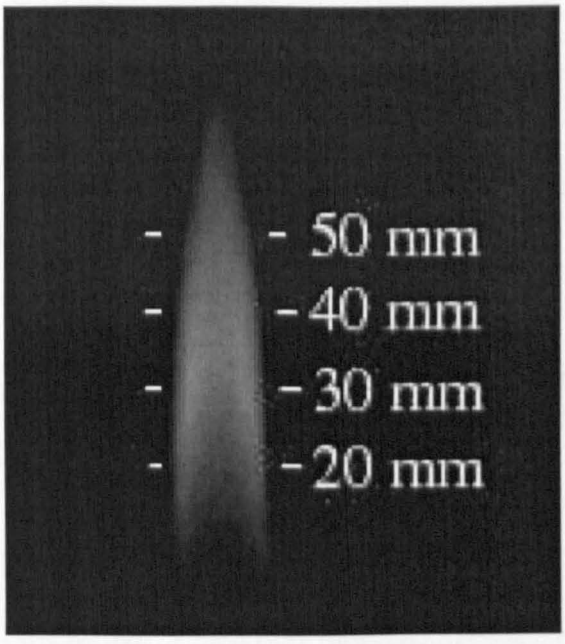

Figure 6.4: Averaged image of the non-premixed laminar butane flame.

manipulation and correct positioning. The two metal junctions were left outside of the two insulator tubes of 1.6 mm of external diameter. Both, thermocouples and the ceramic insulators were capable of measuring and coping with temperatures of 1760 $°C$ and 1900 $°C$ respectively. The thermocouples were connected to a four-channel hand-held data logger thermometer model Omega HH147. The thermometer accepts four different inputs and can display and save into a computer file (via RS232 interface) all four inputs at the same time. The temperature range accepted by the thermometer for a S-type thermocouple is 0 to 1700 $°C$. The accuracy measuring the temperature is $\pm 2°C$ at the given range. The thermocouples were connected to the data logger thermometer via extension grade Copper/Alloy#11 ANSI type RX and RS with insulation made of Neoflon PFA (perfluoroalkoxy) and four miniature SMPW type glass filled nylon connectors.

A highly stable ($\mathscr{R}e \approx 100$), with quasi candle flame appearance, non-premixed laminar flame was generated and imaged under steady combustion conditions. The

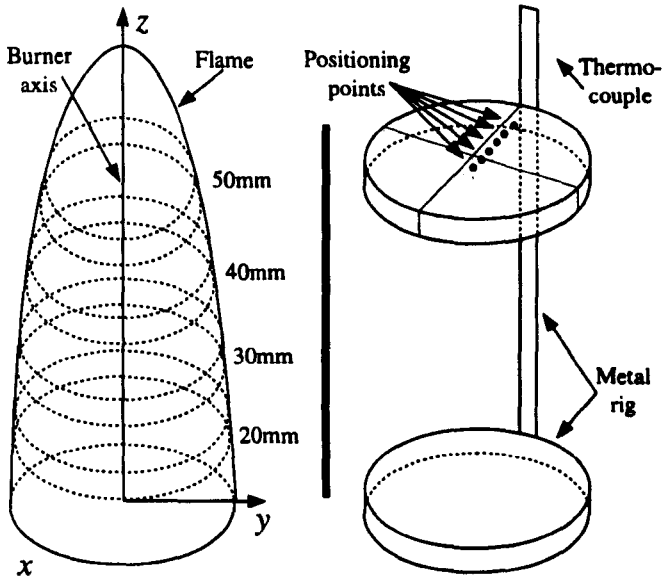

Figure 6.5: Schematic of metal rig and corresponding thermocouple positioning.

gaseous fuel used was butane (C_4H_{10}). To obtain an improved flame image and reduce the influence of small fluctuations, 100 images were taken with a time lapse of one second. These images were averaged using a process of 'superimpose and divide' algorithm implemented by bespoke software created specifically for this experiment. Simultaneously, the temperatures at each position were averaged over 100 runs and measured on a radial distance basis as described in Figure 6.5. Four principal cross-sections were selected to compare the temperature results measured from the thermocouples and from the system. The cross-sections, indicative of four different parts of the flame, were selected at corresponding heights of 20, 30, 40 and 50 *mm* measured from the burner outlet. Figure 6.4 depicts an averaged image of the non-premixed laminar flame and the four cross sections.

Figures 6.7 - 6.10 show the comparison of the results between the thermocouples and the imaging system. The specially designed positioning mechanism shown in Figure 6.6 enabled the traversing of the thermocouples from one side of the flame

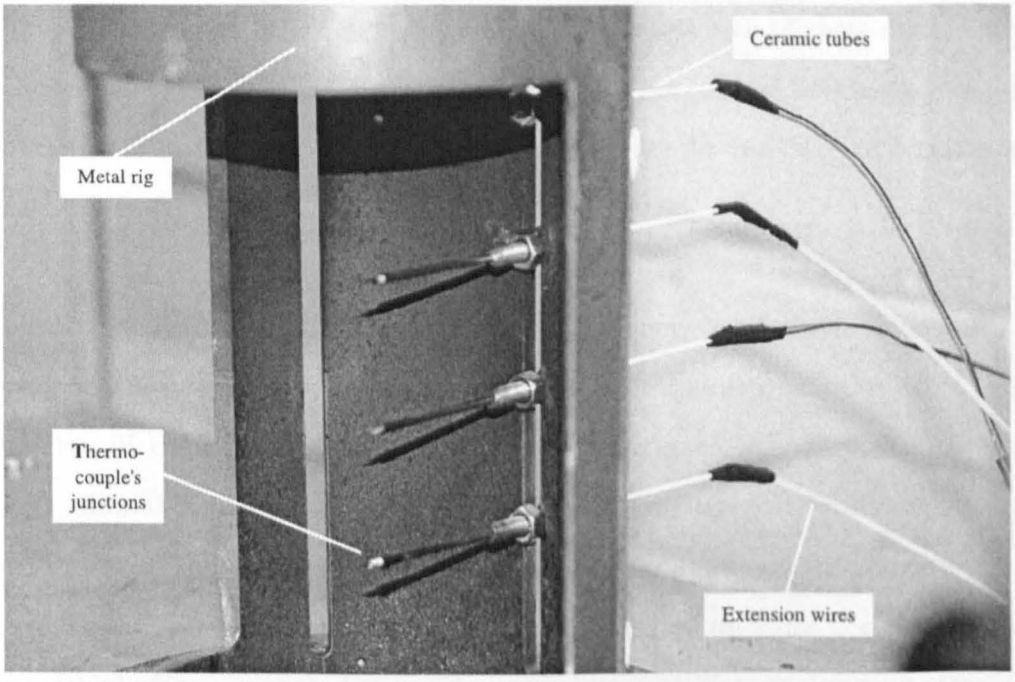

Figure 6.6: Metal rig and thermocouples positioning.

to the opposite side (Figure 6.5). The symmetric appearance of the thermocouple measurements in Figures 6.7 - 6.10 is partially an idealisation of a supposedly highly axis-symmetrical flame. The metal rig utilise for the positioning of the thermocouple allowed both an accurate positioning of the thermocouples and small interference with the combustion only in half side of the flame. The small size of the thermocouples and its careful positioning inside the flame ensured that the structure and characteristics of the flames did not change substantially.

A good agreement between the results from the system and from the thermocouples is observed in certain areas, those that were bright enough to be imaged by the cameras. The match between the results is particularly elevated in Figures 6.7 and 6.8, representing the 20 and 30 mm cross-sections in Figure 6.4, in the (-6, -4) and (4, 6) mm range. In this areas, the measured temperatures are almost identical in some points and in others, the difference does not exceed 100-200 $°C$ yielding to similar

results as measured by Miller et al. (1993). In the central area of these figures, within the range (-4, 4), the system provided irregular temperatures bellow the minimum temperature of calibration, 700 $^{\circ}C$ as these areas were far too dark to be imaged by the cameras making an effective comparison impossible.

Figures 6.9 and 6.10 show the temperature measurements from the thermocouples and the system. Both cases depict the same trend with temperatures 100 - 200 $^{\circ}C$ higher in the case of the developed system. These measurements reach values of around 1400 $^{\circ}C$, similar to the measurements obtained by Gaydon and Wolfhard (1979). It is worth noting that the system measures uniquely the temperature generated in one particular point of a flame. However, the thermocouples measure their tip temperatures reached after a supposed thermal equilibrium with the surrounding areas. This characteristic of the thermocouples might imply the variation of measurements due to thermal loses and that explains the lower temperature given by the thermocouple in the bright areas of the flame in Figures 6.9 and 6.10.

Figures 6.11 - 6.14 show the three dimensional temperature distribution of the four cross-sections indicated above (Figure 6.4). The colour distributions show the 3-D temperature mapping while the black meshes indicate the extended-idealised temperatures distribution as measured from the thermocouples. These figures emphasize the potential of the system developed and the complete information that can provide as a graphic constructor of the inner structure of a flame. The figures show the different parts of the flame and how they change as we move upwards. For instance, it is clearly visible how the dark zone decreases in size and disappear as we approach the luminous zone of the flame.

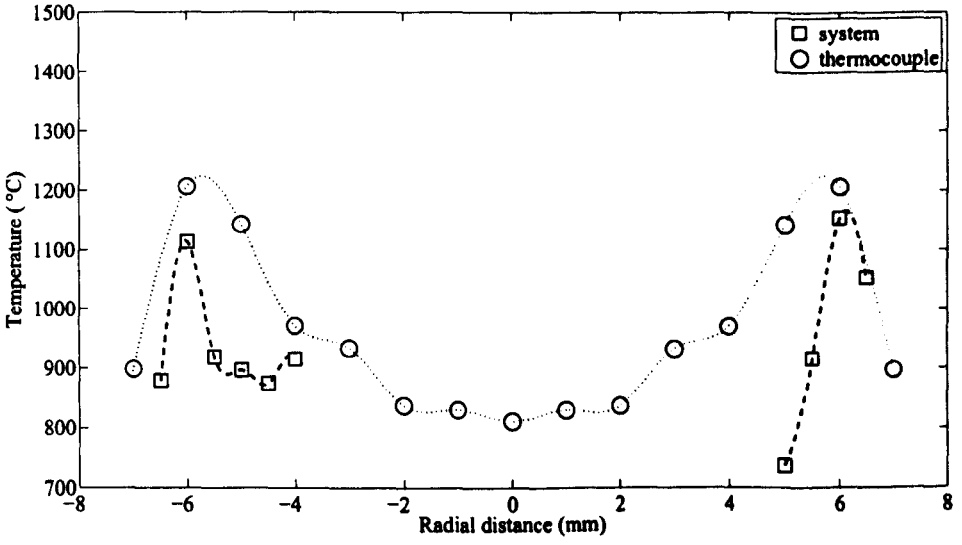

Figure 6.7: Cross-section at 20 mm. Comparison of the measurement results between the thermocouples and the imaging system.

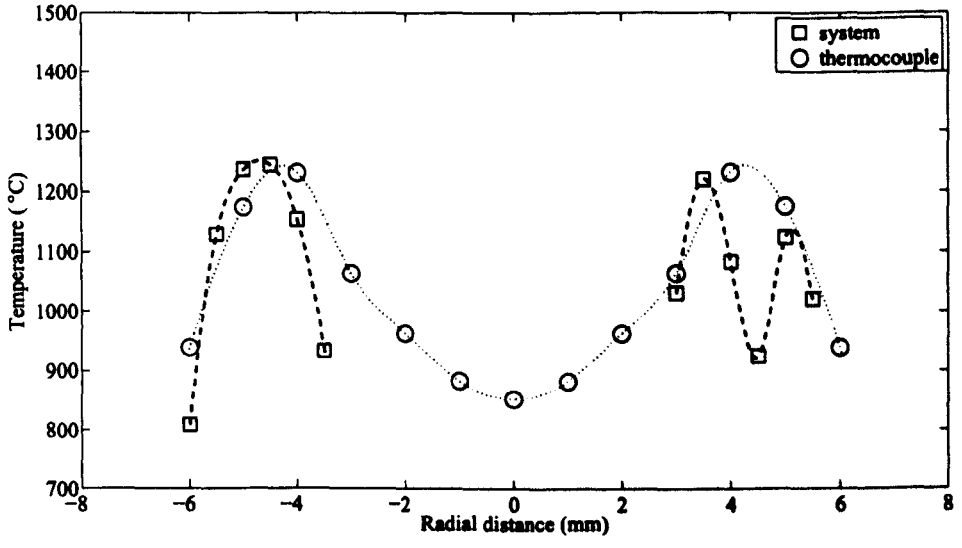

Figure 6.8: Cross-section at 30 mm. Comparison of the measurement results between the thermocouples and the imaging system.

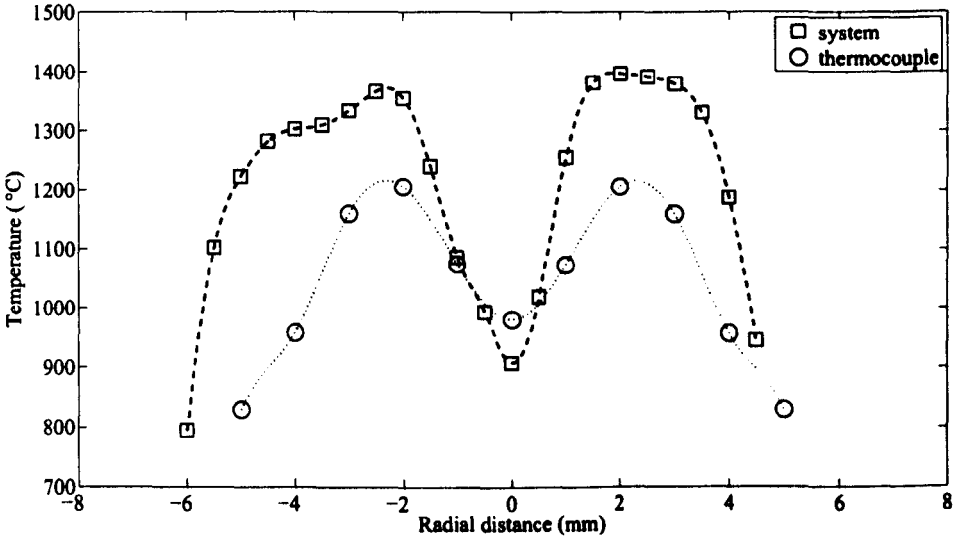

Figure 6.9: Cross-section at 40 mm. Comparison of the measurement results between the thermocouples and the imaging system.

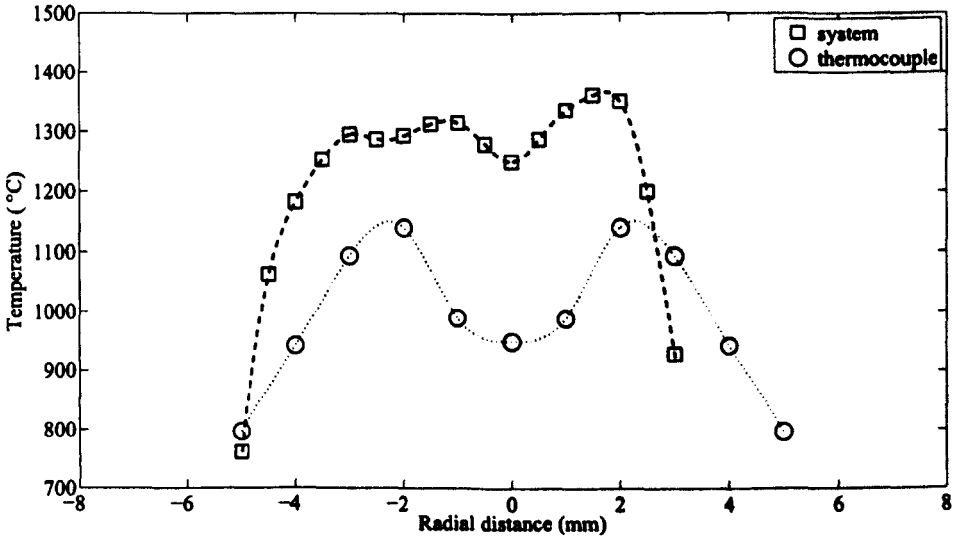

Figure 6.10: Cross-section at 50 mm. Comparison of the measurement results between the thermocouples and the imaging system.

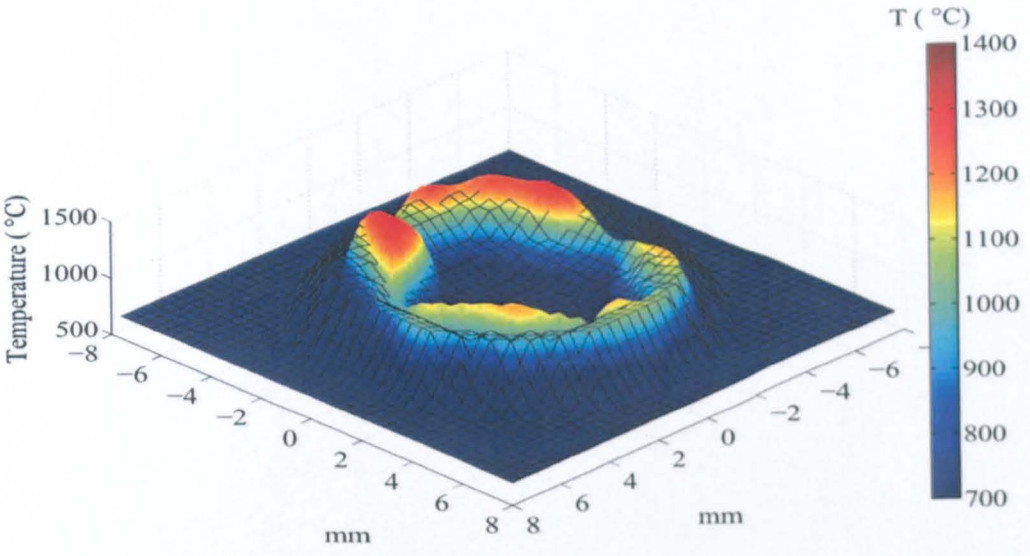

Figure 6.11: Three dimensional cross-section at 20 mm. Comparison of the measurement results between the thermocouples and the imaging system. The colour distribution shows the 3-D temperature mapping while the black meshes indicate the extended-idealised temperatures distribution as measured from the thermocouples.

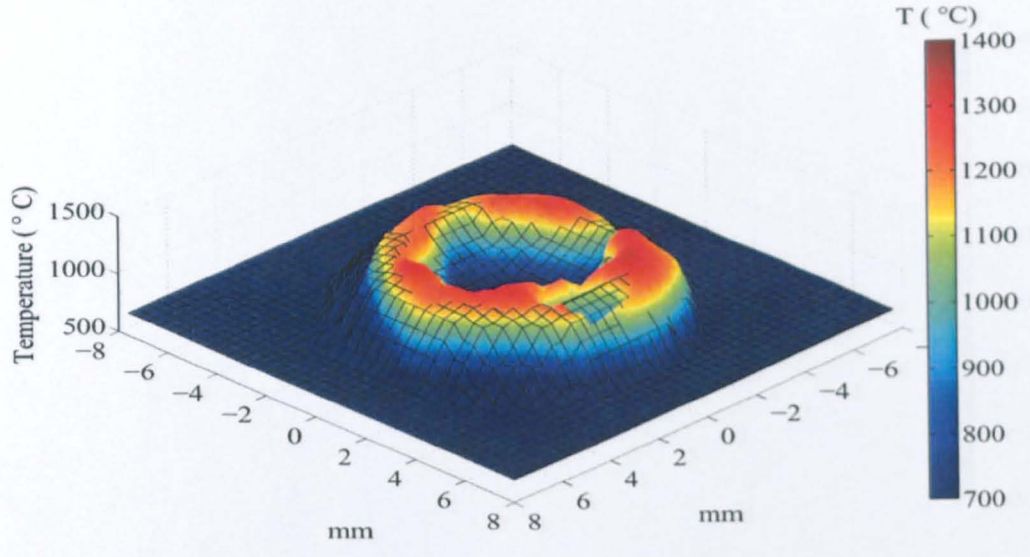

Figure 6.12: Three dimensional cross-section at 30 mm. Comparison of the measurement results between the thermocouples and the imaging system. The colour distribution shows the 3-D temperature mapping while the black meshes indicate the extended-idealised temperatures distribution as measured from the thermocouples.

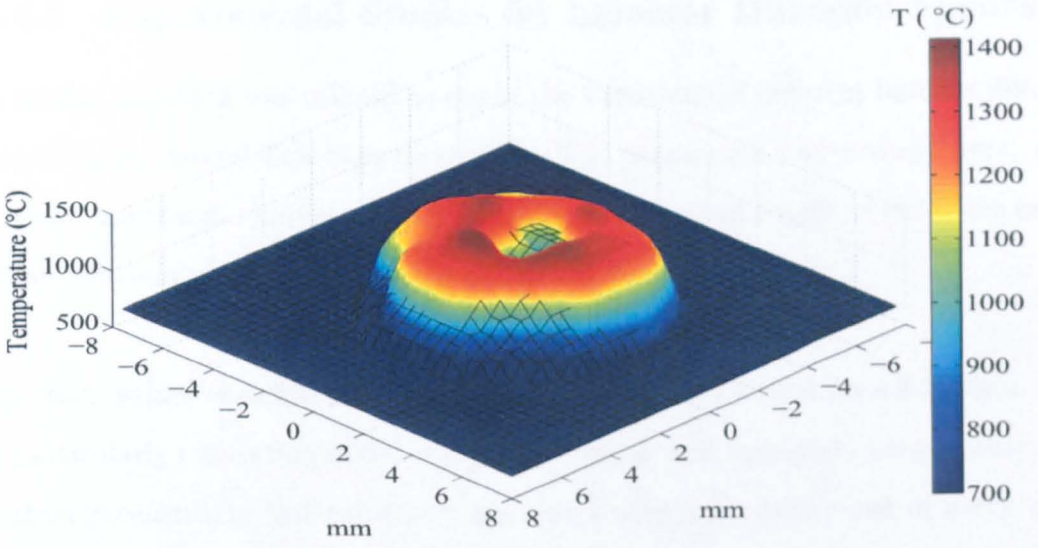

Figure 6.13: Three dimensional cross-section at 40 mm. Comparison of the measurement results between the thermocouples and the imaging system. The colour distribution shows the 3-D temperature mapping while the black meshes indicate the extended-idealised temperatures distribution as measured from the thermocouples.

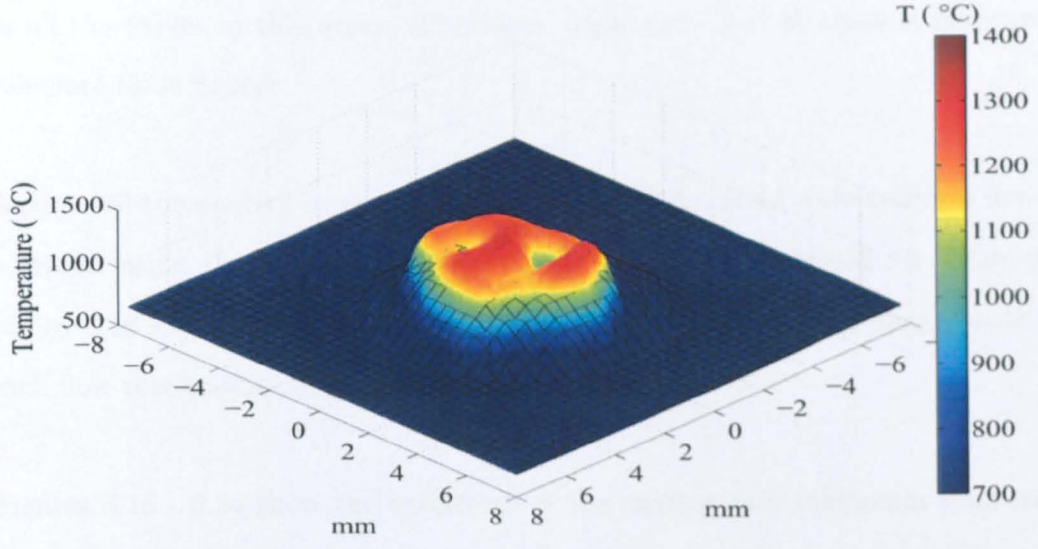

Figure 6.14: Three dimensional cross-section at 50 mm. Comparison of the measurement results between the thermocouples and the imaging system. The colour distribution shows the 3-D temperature mapping while the black meshes indicate the extended-idealised temperatures distribution as measured from the thermocouples.

6.4.2 Experimental Studies for Laminar Difussion Flames

A similar approach was utilised to study the variations of different laminar diffusion flames under several flow rate conditions. The parameters under study were: average and maximum temperature, surface area, volume and length of the flame and to finish, position of the hottest location inside the flame.

The final values obtained for these parameters were calculated on a 3-D basis. This is particularly interesting in the case of the average and maximum temperature. The system reconstructs and calculates numerical values for each pixel of every cross-section. Then, cross-section after cross-section, as the system analyses downwards every horizontal line of the digital flame images, the system repeats the process of reconstruction per pixel and, stores the data in a 3-D array and finalise the whole 3-D reconstruction of the original flame. When the process is complete and the 3-D array full of data, the system calculates the average and maximum temperatures counting in all the values in this array. Therefore, a complete 3-D analysis is performed to calculate these figures.

Again, 100 consecutive images with a time lapse of 1 second were taken in flow rate, averaged using the 'superimpose and divide' algorithm and used for examination. Figure 6.15 shows one projection of each of the final and averaged images utilised for each flow rate condition. In all cases, $\mathscr{R}e < 2000$.

Figures 6.16 - 6.24 show the variations of the average and maximum temperature, surface area, volume and length of the flame and to finish, position of the hottest location inside the flame against the change of fuel flow rate.

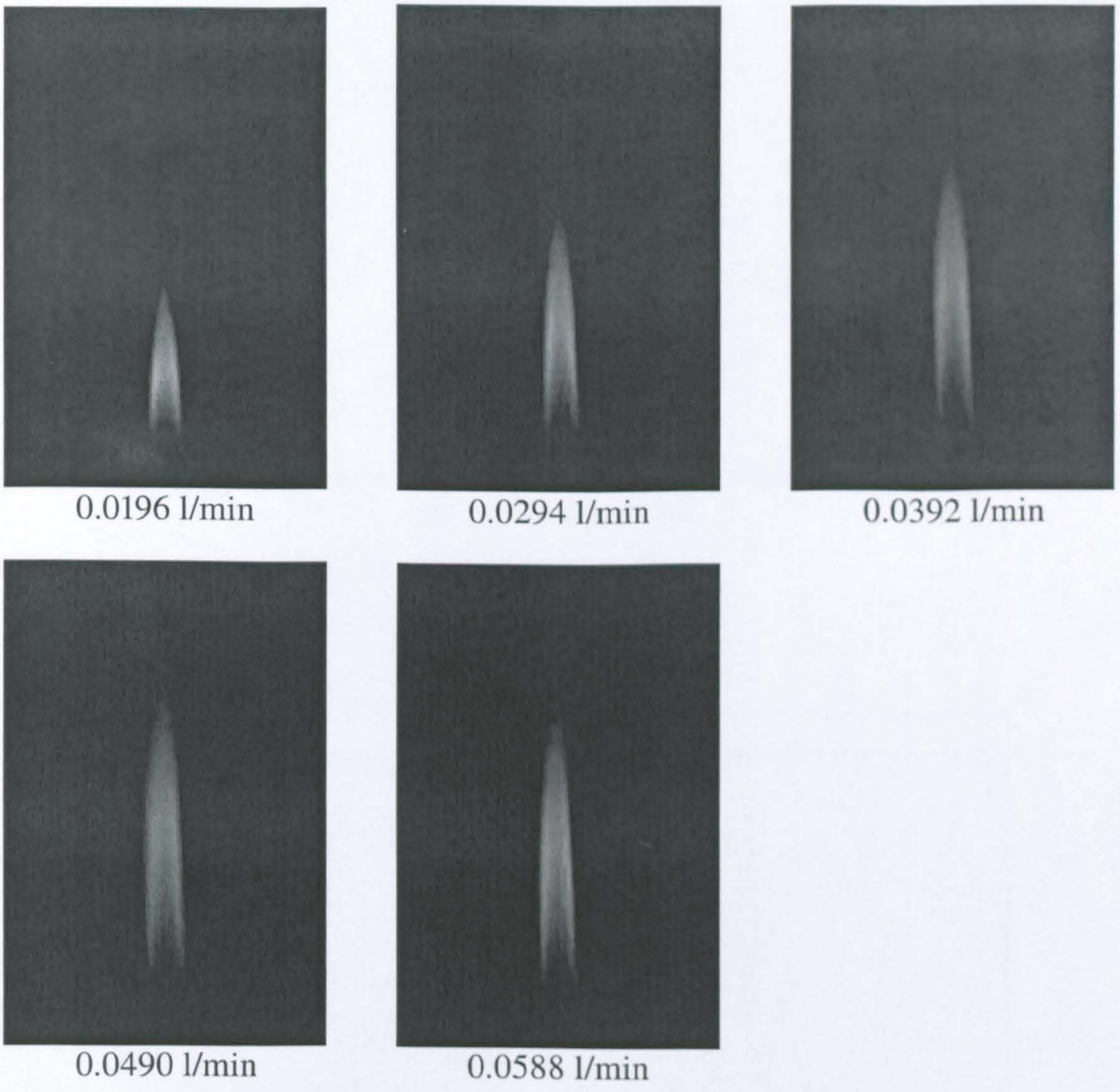

Figure 6.15: Averaged laminar difussion flames $\mathscr{R}e < 2000$.

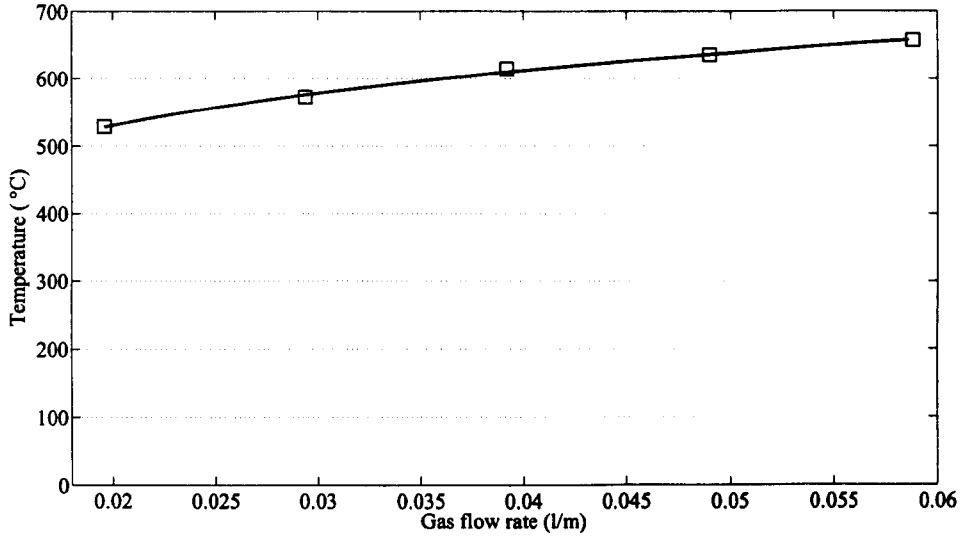

Figure 6.16: Variation of the 3-D average temperature of the flame for different fuel flow rates.

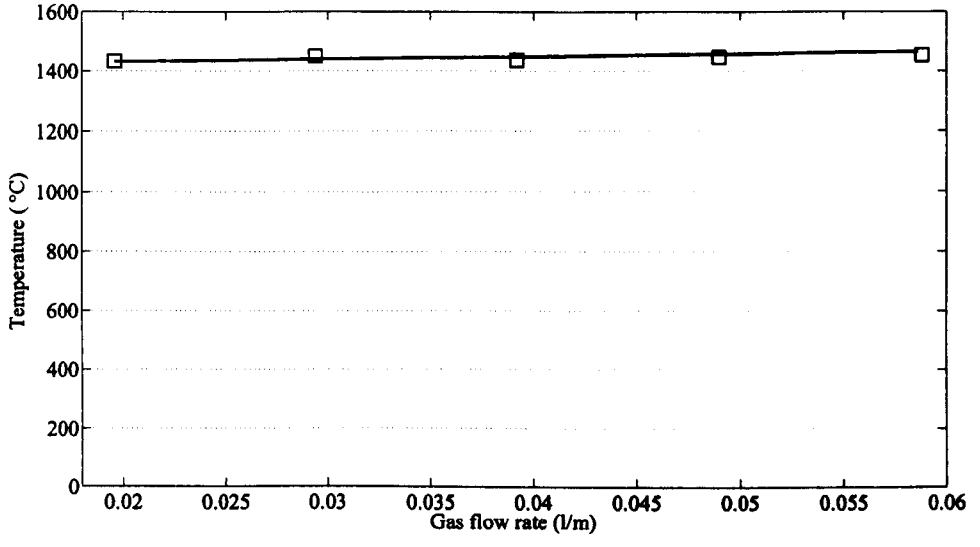

Figure 6.17: Variation of the 3-D maximum temperature of the flame for different fuel flow rates.

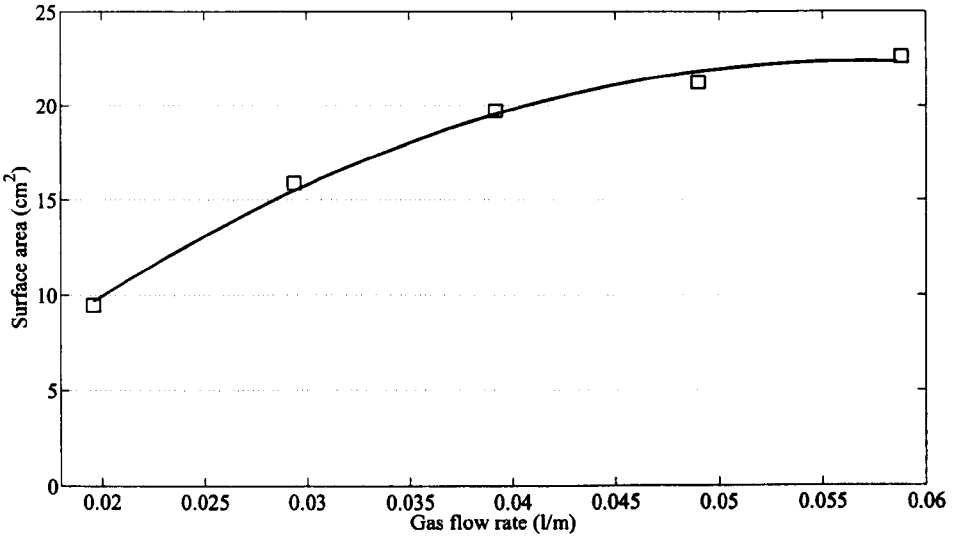

Figure 6.18: Variation of the surface area of the flame for different fuel flow rates.

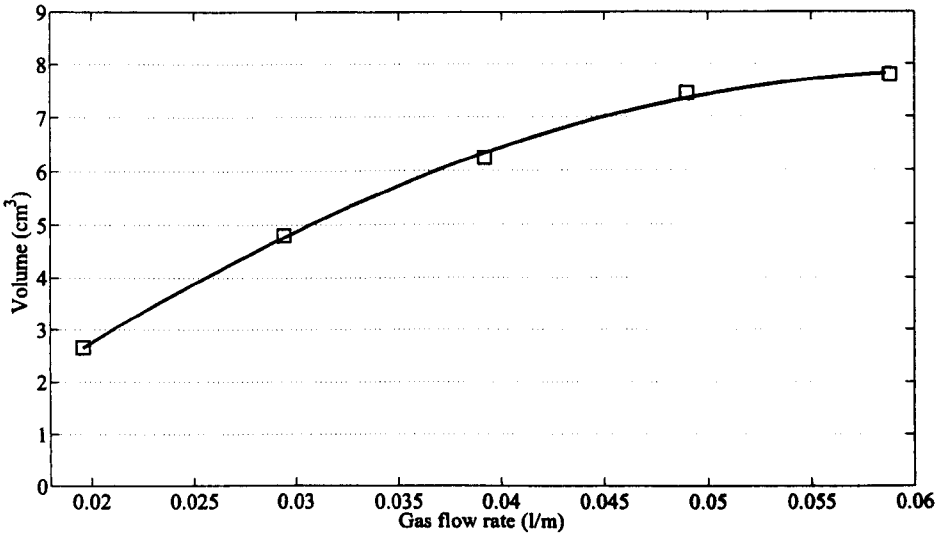

Figure 6.19: Variation of the volume of the flame for different fuel flow rates.

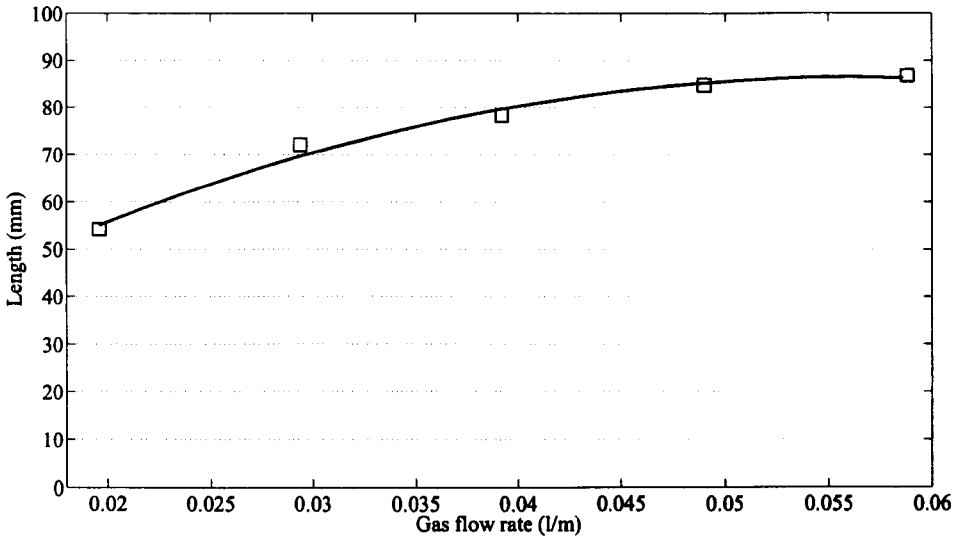

Figure 6.20: Variation of the length of the flame for different fuel flow rates.

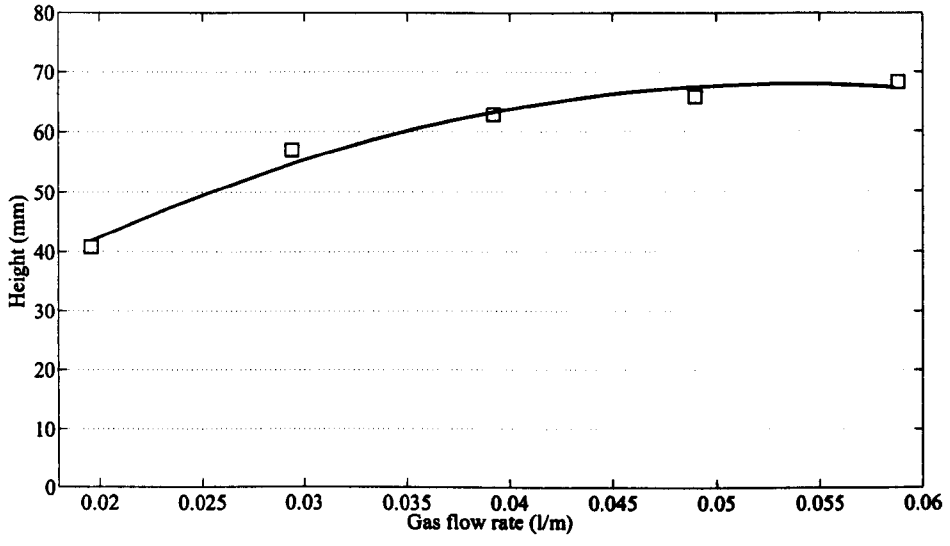

Figure 6.21: Variation of the location of the hottest spot inside the flame for different fuel flow rates.

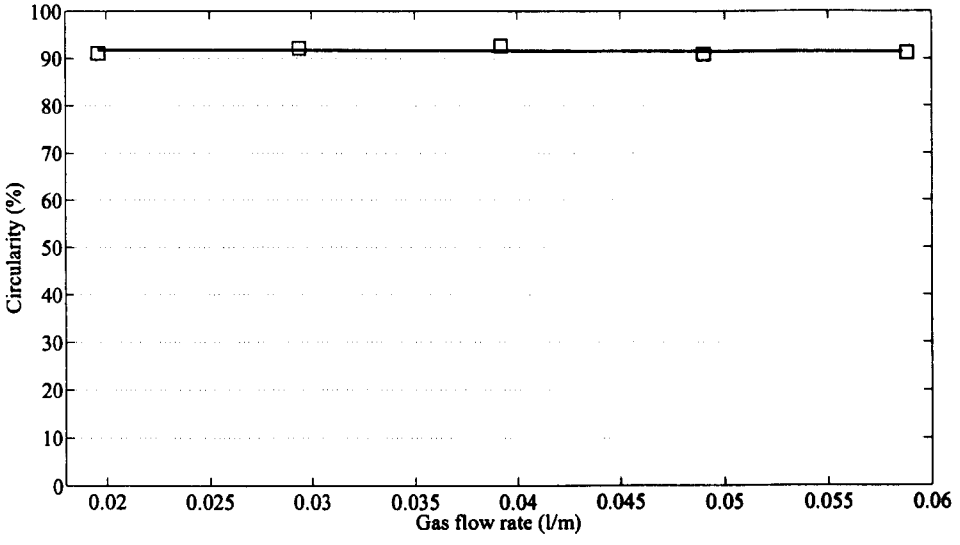

Figure 6.22: Variation of the circularity of the flame for different fuel flow rates.

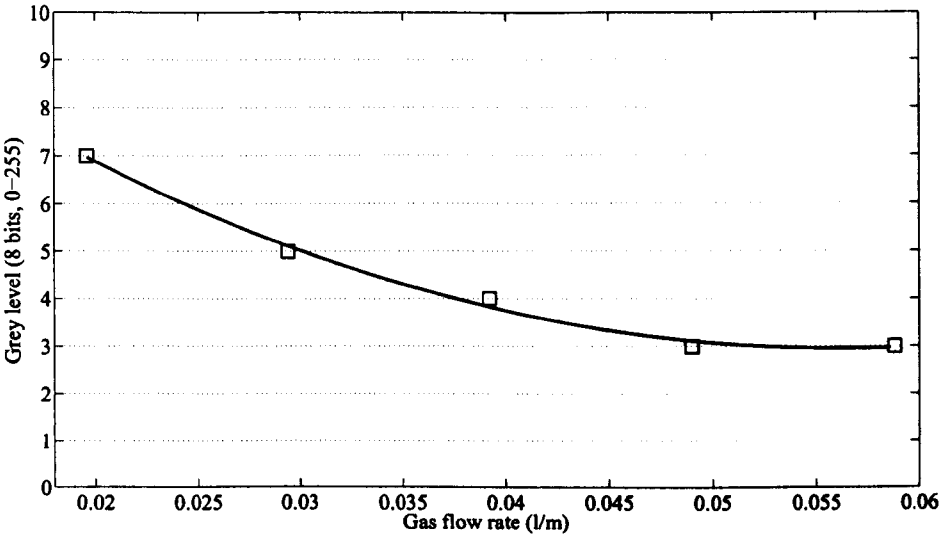

Figure 6.23: Variation of the average luminosity of the flame for different fuel flow rates.

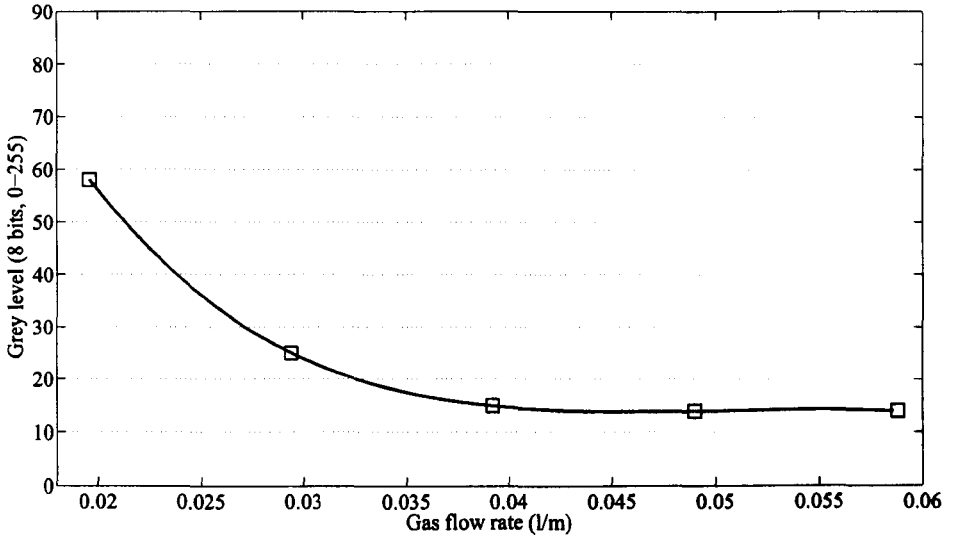

Figure 6.24: Variation of the maximum luminosity of the flame for different fuel flow rates.

The average temperature of the flames increases with the flow rate in an almost linear trend. If we considered the average temperature as the definitive parameter, we could conclude that laminar flames become 'hotter' as the flow rate increases. However the maximum temperatures remains almost unaltered, indicating not only that the maximum temperature is not a function of the flow rate but also suggesting that, for a particular type of chemical reaction, there is a well defined value which is the limit of temperature that cannot be trespassed. If we considered the maximum temperature as the definitive parameter, we would have to conclude that flames do not become 'hotter' as the flow rate increases.

Figure 6.17 clearly indicates that as the flow rate increases, the flame does not reach higher temperatures. Therefore, the increase in average temperature showed in Figure 6.16 is not due to the 'intuitive thought' that the flame becomes hotter. In fact, the same maximum temperature is reached. The increase in averaged temperature can be explained due to the fact that the luminous zone and more importantly, the

reaction zone increase in size. These areas contain the 'pixels' with higher temperatures. An increase in the size of these zones, will increment the total average obtained.

Figures 6.18 - 6.22 deal with the geometric parameters of the flame. The first two ones, Figure 6.18 and Figure 6.19 show the variations of the surface area and the volume of the flame. Both, surface and volume were calculated using the 3-D capabillities of the bespoke software developed. In the case of the surface, every cross-section contains a more or less compact set of pixels corresponding to the 'body' of the flame. These 'body' pixels are well differentiated from those corresponding to the air surrounding the flame. The existing 'contour' which acts as a border or frontier between these two specification of pixels is detected by the software by utilising an algorithm created *ex professo*. When counted in, these border pixels yields a number that define the length of the one-dimensional array of pixels or border line. When this process is repeated for every cross-section of the flame, the complete set of border lines builds up the surface of the flame and the total value of this surface, measured in square units, is counted by totalling the lengths of the border lines. The process to calculate the volume of the flame in conceptually very similar. In this case, every pixel corresponding to the 'body' of the flame, and not only the borders, in counted in, yielding to a number that total the 2-D 'flat' surface of a cross-section. When the process is repeated for every cross-section, the total number of 'body' pixels and therefore, the volume is calculated.

The figures of the variations indicate that both, surface and volume, change in a similar way, increasing with gas flow rates in a decreasing and almost parabolic trend. This is intuitively easy to understand after observing the pictures in Figure 6.15. It is evident that the flames become 'bigger' as the gas flow rate increases and that increment in size is reflected in the surface and the volume.

Figure 6.20 depicts the evolution of the length of the flame with flow rate. The trend is extremely similar to the figures reflecting the changes in surface and volume. This indicates that, under the experimentation conditions, the change in length is the principal factor that influence the changes in volume and surface. Therefore the variation in flow rate influences primarily the length of the flame, due to an increase in gas velocity, and subsequently, under high stable conditions with low $\mathscr{R}e$, the surface and the volume are effected by the geometric relations with the length.

Figure 6.22 depicts the variation of the circularity of the flames with the flow rate. The circularity is again measured by an algorithm created specifically as part of the system. As mentioned before, the 'border' pixels are detected and quantified. Then, the centre of mass of all of them is determined and the circularity is calculated considering the definition of circumference as the geometric object for which all the points are equidistant to a specific position, the centre. The algorithm is calibrated is such a way that for a perfect circle, the circularity would be 100%. The results shown in the graphic proofs that the circularity of the flame is not affected by the change in the gas flow rate. Again, features observed in Figure 6.15 corroborated technically in detail by the system. The high axis-symmetry featured observed initially is quantified correspondingly with circularities above 90%.

Figures 6.23 - 6.24 illustrate the variation in the average and maximum luminosity of the flames with the gas flow rate. Again, the plots indicate these variables in a 3-D basis. In the case of a 2-D photographic image of a flame, an observed luminosity of, let us say, 25 (in a grey scale of 8 bits) can be, for instance, measured by the cameras. From a tomographic point of view, this value of 25 measured from one particular position, is the result of adding consecutively the luminosities originated inside the cross-section of the flame and along the secant line to the measured spot. From a computational point of view, this means that this luminosity of 25 might correspond,

for instance, to the addition of five integers each of them with a value of five and lined up at the same secant line. These integer values are part of the numerical reconstruction of a cross-section and are represented by pixels in the graphic display. For this reason, it is possible to find in Figures 6.23 - 6.24 values as low as 2 or 3 when, from a 2-D flame image perspective, such low values would be impossible to observe.

In both cases, the luminosities decrease with the gas flow rate but more dramatically in the case of the maximum luminosity. In a diffusion flame, most of the combustion reactions occurs near the surface of the flame and therefore, the change in surface is the most influential cause to explain the change in luminosity. Figure 6.18 depicts a curve with positive gradient. This means that the surface of the flames increases faster than the gas flow rate and consequently the volume of gas coming out the burner outlet. Therefore, the concentration of gas reaching the surface decreases and so the accumulation of particles igniting at a given time. As the slope in Figure 6.18 diminishes, the increment in surface area measured against the volume of gas slows down, the amount of fuel burning at a given time becomes constant and the luminosities reach a minimum.

6.5 Industrial Trials

Experimental tests were also conducted on a coal-fired industry-scale combustion test facilities. More concisely on the biggest test facility in the world a Doosan Babcock's 90 $MWth$ coal combustion furnace located at the outskirts of Glasgow. Figure 6.25 shows the the test facility at Doosan Babcock. Due to the restriction of on-site installation, only a single camera was used to capture the flame images. Figure 6.26 shows the installation of the single-camera system utilised which was previously developed by Lu et al. (2004). In view of fact that the combustion condition is fairly steady during the test runs, the assumption on the rotational symmetry of the flame was applied here (Brisley et al., 2005), and thus the six projections required in the reconstruction are treated the same in this study. Figure 6.27(a) illustrates a typical instantaneous image of the coal-fired flame, whilst Figure 6.27(b) shows the luminosity reconstruction of the flame for four cross-sections. Figure 6.28(b) shows the same type of reconstruction but in this case the cross-sections are stored into the computer memory and the data is display in longitudinal-sections. A pseudo colour technique is used here for a better data presentation where red presents the highest grey-level and black the lowest. Near the base of the flame, a quasi-perfect circular blue area is observed. This corresponds to the zone of the flame near the ignition area where turbulences and imperfections have not affected yet the characteristics of the flame. In this situation, only the outer part of the flame is ignited. Bear in mind that, as the single-camera approach achieves the 3-D reconstruction of the flame from only one image assuming rotational symmetry of the flame, circular outer contours are clearly visible. It is clear, however, that the reconstructed cross-sections of the flame appear to give a good indication of the internal structures and variations in luminous properties of the flame along the burner axis and radial directions.

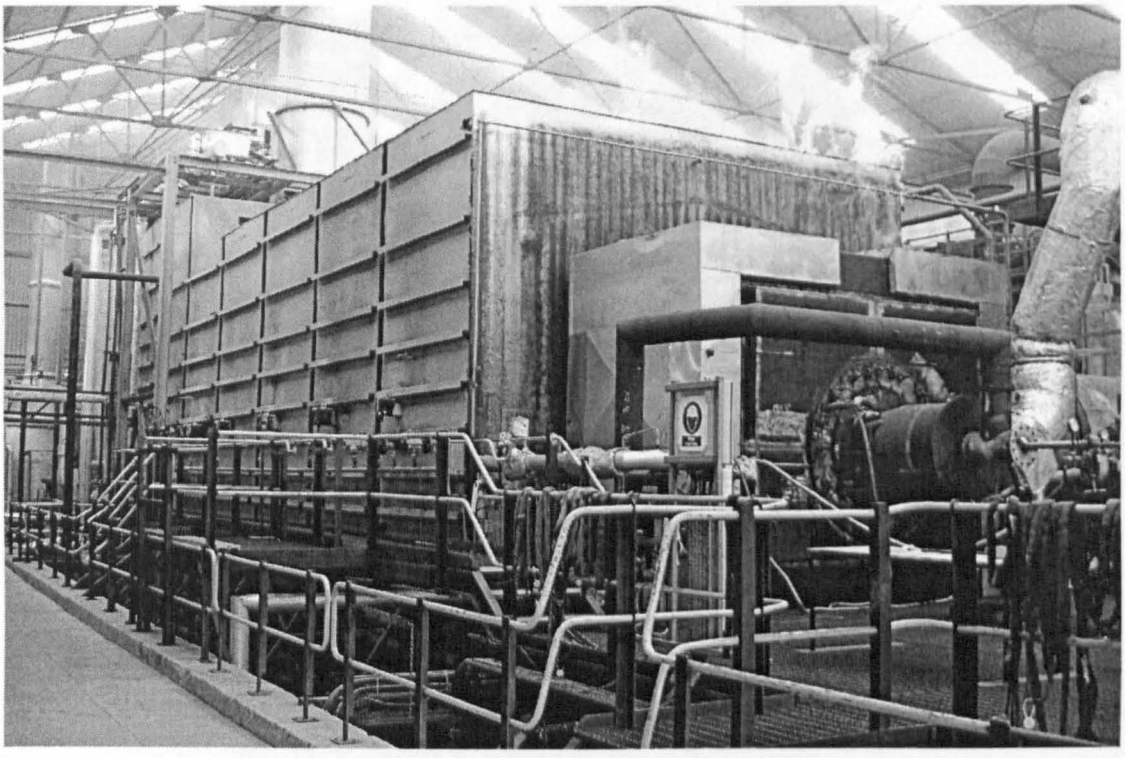

Figure 6.25: Doosan Babcock's 90 $MWth$ coal combustion test facily (Glasgow).

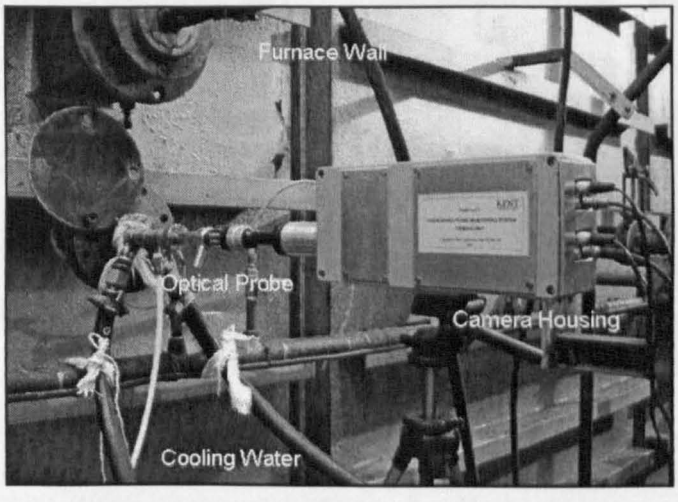

Figure 6.26: The single-camera system tested at Doosan Babcock's

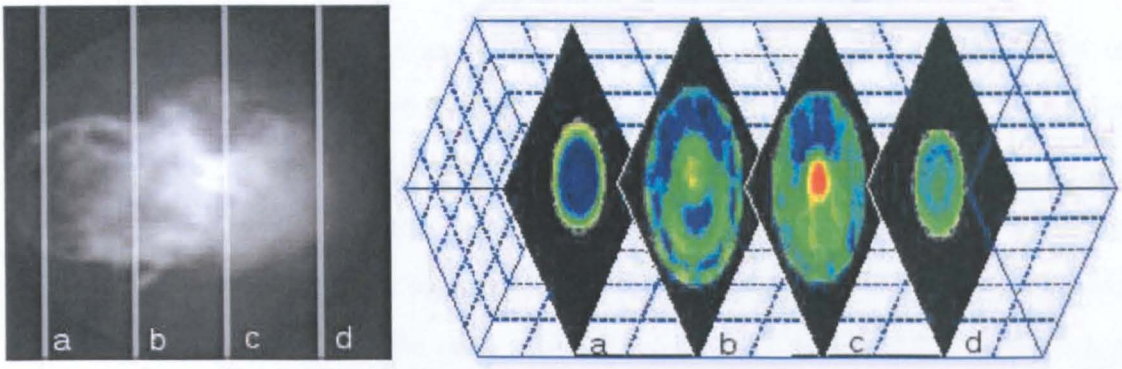

(a) (b)

Figure 6.27: Flame image obtained on a coal-fired industry-scale combustion test facility, (a) Original image, (b) Coloured luminosity reconstruction of some cross-sections.

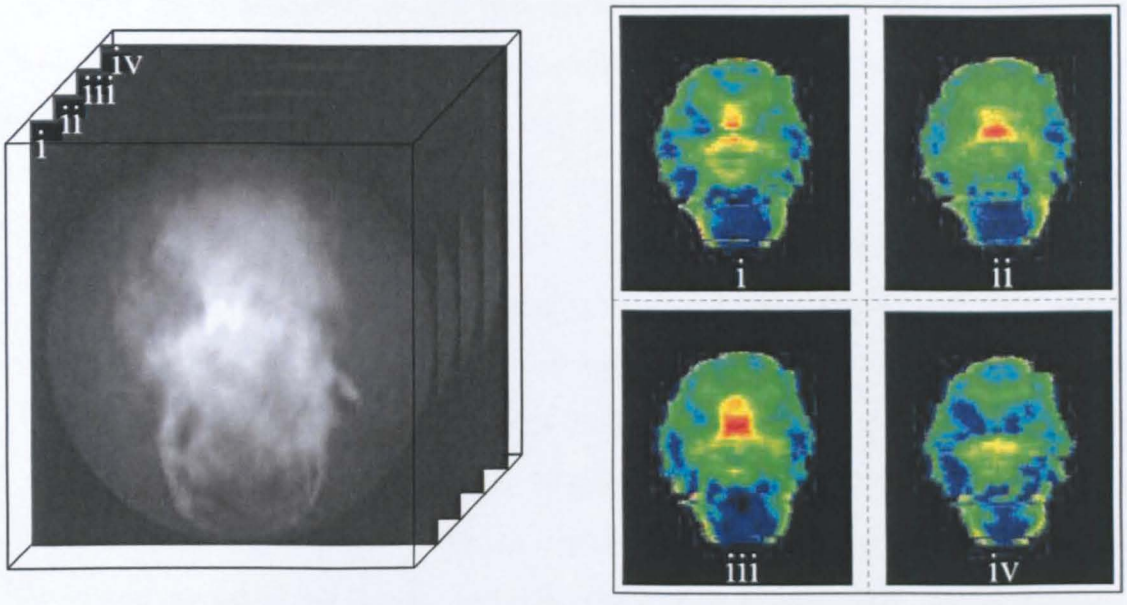

Figure 6.28: Longitudinal examination of the flame obtained at the industry-scale combustion test facility. (a) Original images. (b) Coloured luminosity reconstruction of some longitudinal-sections.

6.6 Summary

The experimental conditions and the gas laboratory combustion rig have been described in detail and so the *Reynolds* number and how it can be used to characterised the diversity of states of a flow and therefore a flame. The multi-camera based imaging system has been applied to the 3-D visualisation and characterisation of gaseous combustion flames. Its new tomographic approach utilising a novel algorithm have been tested to reconstruct the inner structure of gaseous flames under different conditions. The results obtained for a quasi candle shape flame were compared with the readings taken from reliable fast time response S-type thermocouples embedded in isolation ceramic tubes and highly accurately positioned by using a metal rig. Comparison proves the reliability of the new non-invasive technique developed and the 3-D temperature map reconstructed by the system as this map shows similar values and trends to those giving by the thermocouples. The system has been utilised to study and characterise diverse gaseous flames under different $\mathscr{R}e$ numbers. The results obtained on the gas laboratory combustion rig facility indicates that the system is also capable or reconstructing on a 3-D basis parameters like the average and maximum temperature, geometric parameters like the area of the surface and the volume of the flame, length, position of the hottest spot, circularity and also luminous parameters. The experimental studies were aimed to asses the operability of the system and it is envisioned that the system developed would provide and effective means for an in-depth understanding of the complete nature of combustion flames. The results presented in this chapter have demonstrated the potential of the digital imaging technology for advanced flame monitoring. Further work is needed to explore the full potential of the system for applications to fossil fuel combustion processes.

Chapter 7

Conclusions and Future Work

7.1 Introduction

The research work presented in this thesis is concerned with the development of a prototype instrumentation system for the three-dimensional (3-D) visualisation and quantitative characterisation of fossil fuel flames. The system operates on the latest optical sensing and digital image processing. Dedicated algorithms, incorporating contour extraction, mesh generation, tomographic reconstruction and luminous and fluid dynamic calculations have been developed for the reconstruction of 3-D models of flames based upon the information obtained from six different locations. A set of geometrical, luminous and fluid dynamic parameters were defined and computed from the 3-D flame reconstructions. The system was evaluated on a laboratory-scale combustion rig and then on a coal combustion test facility. Results obtained have demonstrated that the system is capable of reconstructing the flame from a complete 3-D cross-sectional reconstruction as well as quantifying the defined parameters.

This chapter presents the conclusions that have been drawn from the research programme conducted and makes recommendations for future work in the field.

7.2 Contributions to the Field

The work developed in this research programme has contributed to the design and fabrication of a full integrated system that is the first of its kind capable of reconstructing the complete 3-D model of a flame and characterising the flame in terms of its geometric, luminous and fluid dynamic properties. The specific contribution of this project can be stated as follows:

- Development of a new tomographic algorithm: the new approach has been specifically developed to improve the reconstruction under the limited experimental conditions related to this research programme. The new algorithm combines the location information provided by LFBP and the potential of ART in cases where a small number of projections is available. This novel combination reduces the number of unknowns to be solved and optimise the performance of the reconstruction.

- Design and fabrication of a new instrumentation system: the novel system combines the efficiency and simplicity of the latest generation of digital imaging cameras with the power of computational processing. The colour cameras not only capture the radiation from the flames but their characteristics also allow the utilisation of the two-colour technique to calculate ultimately the 3-D distribution of temperatures. The system also includes an original optical arrangement that maximise the efficiency of the tomographic reconstruction.

- Development of a high-end software interface: as part of the instrumentation system, the new software allows the control and examination of the observations and reconstruction. The software utilises the versatility of object oriented programming and the industrial standard graphical tool to create, for the first time, an integrated display to monitor and measure the geometric, luminous and fluid dynamic properties of fossil fuel flames on a 3-D basis.

- Evaluation of the performance of the new system under a wide range of combustion conditions on a gas fired combustion test rig and under industrial conditions to ensure and guarantee its performance, operability and potential under real industrial conditions.

7.3 Conclusions

7.3.1 The Instrumentation System

The prototype instrumentation system comprises three identical colour CCD cameras, three identical sets of lenses and mirrors, three identical frame grabbers and an advance personal computer with bespoke software. The choice of the CCD cameras has proven to be very suitable for the visualisation of a flame under various combustion conditions. The choice of lenses and mirrors were effectively used to multiply the number of images taken by the cameras and therefore improved the reconstruction results. The frame grabbers can handle the cameras simultaneously and have demonstrated a high performance in the digitalisation and processing of flame images. The bespoke software enables a full visualisation of the flame, ensure the synchronisation of the image acquisition and have proven to be a robust tool for the tomographic reconstruction and quantitative characterisation of flames. The software plays an important role in the entire system in terms of system performance, functionality and operability.

The contour of the flame was effectively detected from its red and green channels images using the devised edge detection technique. The complete luminosity information from the flame two-dimensional grey level images was subsequently extracted. Based on this information, a novel tomographic algorithm was utilised to reconstruct the complete 3-D model of the flame. The software interface displayed the model in

such a way that could be zoomed in and out and rotated to be seen from different directions. The models generated included 3-D temperature mapping and 3-D geometric reconstruction using mesh generation techniques. Luminous parameters were displayed numerically. These models have demonstrated that the system software, incorporating advanced image processing and tomographic techniques, was capable of reconstructing successfully the original 3-D flames from six two-dimensional projected images under various combustion conditions.

From the flame models, a set of luminous, geometrical and fluid dynamic parameters were determined to quantify the characteristics of the flame, including average and maximum temperature, surface area, volume, length, position of the hottest spot, circularity and average and maximum luminosity. Experimental results have demonstrated that the defined flame parameters are effective in quantifying the flame characteristics.

The calibration and performance evaluation of the system were carried out under laboratory conditions using purpose-designed templates and temperature source. The accuracy of the location correction performed by *ex professo* software found that the maximum miss alignment obtain was less than 1%. The dimension calibration was achieved by a linear regression line between pixels and *mm* yielding a regression coefficient of 0.99. The luminous calibration was performed to ensure that the three cameras measured the same intensities. A flat back light panel was utilised as a highly stable light source. The maximum observed after calibration was a 3% in the case of the green channel. To calibrate the system for temperature measurement, a tungsten lamp was used. The regression coefficient of this calibration was 0.97.

The temperature reconstruction was validated by comparing the results provided by the system with those provided by multiple unsheathed S-type thermocouples. A

highly stable flame ($\mathscr{R}e \approx 100$) with quasi candle flame appearance was utilised. The profiles obtained in the case of the system reconstruction were similar to those provided by the thermocouples indicating the reliability of the measurements obtained by the imaging system.

The prototype system was tested on a combustion rig facility at the University of Kent. Extensive investigations into the behaviours of laminar diffusion flames were carried out. The system performed satisfactory throughout the trials in terms of functionality, operability and reliability. Results obtained from the investigations have demonstrated that the instrumentation system is capable of reconstructing and characterising completely fossil fuel flames on a 3-D basis. The software has proven reliable and operational in different combustion environments. All parameters that were defined and measured have proven adequate and effective in the 3-D visualisation and quantitative characterisation of fossil fuel flames.

7.3.2 Trials on Laboratory-scale Combustion Rig

Extensive experiments were conducted on the laboratory-scale combustion rig for the three-dimensional visualisation and quantitative characterisation of fossil fuel flames over a range of combustion conditions such as variable fuel rates. The results have demonstrated that the system is capable of reconstructing complete 3-D models of a flame under different combustion condition. The results have also suggested that the flame's geometrical, luminous and fluid dynamic parameters obtained by the system have close correlation with the gas fuel rate. A constant increase of average temperature was observed with the increase of gas flow rate. However, the maximum temperature remains constant with no appreciable change with the increase of gas flow rate. An important augmentation of the length, surface and volume of flames is observed at initial increments of flow rates. Further increments in gas flow

rates are followed by a less steep variation in length, surface and volume. A similar behaviour is detected when the position of the hottest spot inside the flame is studied. The circularity of the flame is another parameter that does not change and remains constant at high levels. In the case of the luminous parameters, it is observed that decrease with gas flow rates.

7.3.3 Industrial trials

A experimental test was conducted on a 90 $MWth$ coal-fired industry-scale combustion test facility at Doosan Babcock in Glasgow. Due to the fact that only one camera was utilised, the property of rotational symmetry of the flame had to be assumed. Therefore, the six projections required by the tomographic reconstruction algorithm were considered to be the same. The test results have proven that the system is capable of providing a good reconstruction of the internal structures and luminosity variations inside the flame. Thus the system proved its potentials to be able to reconstruct the internal map of temperatures under these conditions.

7.4 Future Work

The work presented in this thesis has demonstrated the potential of a digital based instrumentation system capable of the three-dimensional visualisation and characterisation of fossil fuel flames. However, the prototype system is still at a development stage and some areas still require further investigations and improvements. This section outlines the areas that should be pursued over the next few years.

One of the main areas of research that seems encouraging is parallel programming. With the advent of new multi-core processors, new designs in the software routines could be implemented to take advantaged of this new hardware feature that allows the realisation of multiple computational operations simultaneously. Another type

of parallel programming is the utilisation of new technology known as CUDA, an NVIDIA computing architecture that enables substantial increases in computational performance by harnessing power from the Graphics Processing Unit (GPU). Indeed, several graphic cards can be installed in the same personal computer as supplementary processing cards. In this way, the system software can be further improved to achieve a faster three-dimensional visualisation of fossil fuel flames under different combustion conditions.

Another area of research is the development of new tomographic algorithms that can provide a better reconstruction under the given conditions of using only six projections per channel. The starting point of this improvement could be the utilisation of algorithms derived from ART, the Simultaneous Iterative Reconstruction Technique (SIRT) or the Simultaneous Algebraic Reconstruction Technique (SART) and further derivation of these two algorithms combining them with the LFBP algorithm.

The tomographic algorithm utilised in this research programme used six two-dimensional images of the flame under the principles of parallel projections and non-diffracting sources. Despite the fact that parallel projections is accepted to be accurate for the combustion conditions, the reconstruction algorithm could be further improved by considering additional computational operations that took into consideration alterations in the emission of radiation energy. These alterations to be considered include basic principles as diffraction/scattering of light and absorption of energy inside the own flame. Another improvement that could be implemented is the utilisation of more than six images. This suggestion is certainly challenging as implies an important redesign of the hardware of the system and therefore, if not implemented smartly, could result in an impractical set-up. To avoid this, micro-digital CCD cameras and optical fibre connections could be adapted.

Another area or research is the measurement of extra 3-D fluid dynamic parameters. The instrumentation system developed in this research programme is a multi-functional system capable of measuring not only geometrical and luminous parameters but also the 3-D temperature mapping of a flame. The system is able to provide simultaneous information of all these physical parameters. However, when fully developed, a new system could provide also information about oscillation frequency and soot concentration of a flame.

The current laboratory-scale furnace is designed for a single burner only. However, multiple burners are widely used in large industrial furnaces. Three-dimensional visualisation and characterisation of multiple flames present a more technically challenging problem due to the partial overlapping of some parts of the flame. The furnace structures make it too difficult to visualise an individual flame even if cameras with wide-angle lenses are utilised. The multi-camera sensing arrangement would need further re-configuration to enable visualisation of individual flames. Additionally, dedicated algorithms would need to be developed to identify the individual flames from the images captured from each camera to integrate the information related to each individual flame and reconstruct its 3-D model from the computed data.

Bibliography

[1] Agard, D. A. and Sedat, J. W. (1983), 'Three-dimensional architecture of a polytene nucleus', *Nature* **302**, 676–681.

[2] Aramini, M. J. (1980), Implementation of an improved contour plotting algorithm, Master's thesis, Stevens Institute of Technology.

[3] Audouin, L., Kolb, G., Torero, J. L. and Most, J. M. (1995), 'Average centreline temperatures of a buoyant pool fire obtained by image processing of video recordings', *Fire Safety Journal* **24**, 167–187.

[4] Barat, R. B., Longwell, J. P., Sarofim, A. F., Smith, S. P. and Bar-Ziv, E. (1991), 'Laser rayleigh scattering for flame thermometry in a toroidal jet stirred combustor', *Applied Optics* **30**(21), 3003–3010.

[5] Bessler, W. G., Schulz, C., Lee, T., Jeffries, J. B. and Hanson, R. K. (2003), 'Strategies for laser-induced fluorescence detection of nitric oxide in high-pressure flames. III. comparison of A-X excitation schemes', *Applied Optics* **42**(24), 4922–4936.

[6] Bezdek, J. C. (1981), *Pattern Recognition with Fuzzy Objective Function Algorithms (Advanced Applications in Pattern Recognition)*, Springer.

[7] Bheemul, H. C. (2004), Three-dimensional visualisation and quantitative characterisation of combustion flames, PhD thesis, University of Greenwich.

[8] Bheemul, H. C., Lu, G. and Yan, Y. (2002), 'Three-dimensional visualization and quantitative characterization of gaseous flames', *Meas. Sci. and Tech.* **13**, 1643–1650.

[9] Bheemul, H. C., Lu, G. and Yan, Y. (2003), Digital imaging based three-dimensional characterization of combustion flames, *in* 'IMTC Instrumentation and Measurement', IEEE.

[10] Bookey, H. T., Bishop, A. I., and Barker, P. F. (2006), 'Narrow-band coherent rayleigh scattering in a flame', *Optics Express* **14**(8), 3461–3466.

[11] Borman, G. L. and Ragland, K. W. (1998), *Combustion engineering*, McGraw-Hill.

[12] Borouchaki, H. and George, P. L. (2000), 'Quality mesh generation', *C.R. Acad. Sci. Paris* **328**, 505–518.

[13] Brisley, P. M. (2006), Three-dimensional temperature measurement of combustion flames usind digital imaging techniques, Master's thesis, University of Kent.

[14] Brisley, P. M., Lu, G., Yan, Y. and Cornwell, S. (2005), 'Three-dimensional temperature measurement of combustion flames using a single monochromatic ccd camera', *IEEE Transactions on Instrumentation and Measurement* **54**(4), 1417–1421.

[15] Brisley, P. M., Lu, G., Yand, Y. and Cornwell, S. (2004), Three dimensional temperature measurement of combustion flames using a single monochromatic CCD camera, *in* 'IMTC 2004 Instrumentation and Measurement Technology Conference', IEEE.

[16] Brummund, U. and Scheel, F. (2000), Simultaneous application of Rayleigh scattering and laser-induced fluorescence for compressible mixing layer analysis, *in* 'Ninth International Symposium of Flow Visualisation'.

[17] Bryanston-Cross, P. J. and Gardner, J. W. (1988), 'Holographic visualisation of a combustion flame', *Optics and Lasers in Engineering* **9**(2), 85–100.

[18] Burkhardt, H. and Stoll, E. (1995), *Process tomography: principles, techniques and applications*, Butterworth-Heinemann, Oxford, chapter 25 Application of optical tomography to visualize temperature distributions in flames.

[19] Caldeira-Pires, A. and Heitor, M. V. (1998), 'Temperature and related statistics in turbulent jet flames', *Experiments in Fluids* **24**, 118–129.

[20] Carlomagno, G. M., Luca, L. D. and Rapillo, A. (1987), A new type of interferometer for gas dynamics studies, *in* 'Proc. 12th Int. Cong. on Instrumentation in Aerospace Simulation Facilities', IEEE Aerospace Electronic Syst. Soc., pp. 221–226.

[21] Carter, R. M., Krabicka, J., Yan, Y. and Cornwell, S. (2009), An integrated instrumentation system for combustion plant optimisation, *in* 'Proceedings of International Instrumentation and Measurement Technology Conference', IEEE, pp. 780–784.

[22] Cashdollar, K. L. (1979), 'Three-wavelength pyrometer for measuring flame temperature', *Applied Optics* **18**, 1595–1597.

[23] Char, J. M. and Yen, J. H. (1996), 'The measurement of open propane flame temperature using infrared technique', *J. Quant. Spectrosc. Radist. Transfer* **56**(1), 133–144.

[24] Chen, Y.-C. and Bilger, R. W. (2004), 'Experimental investigation of three-dimensional flame-front structure in premixed turbulent combustion: II. Lean hydrogen/air Bunsen flames', *Combustion and Flame* **138**, 155–174.

[25] Cheung, K., Ng, W. B. and Zhang, Y. (2005), 'Three dimensional tracking of

particles and their local orientations', *Flow Measurement and Instrumentation* **16**(5), 295–302.

[26] Cheung, K. Y. and Zhang, Y. (2006), 'Stereo imaging and analysis of combustion process in a gas turbine combustor', *Measurement Science and Technology* **17**(12), 3221–3228.

[27] Cox, G. and Chitty, R. (1980), 'A study of the deterministic properties of unbounded fire plumes', *Comnustion and Flame* **39**(2).

[28] CRF/BCURA (2004), *in* 'Coal research needs in the UK', Coal Research Forum/British Coal Utilisation Research Association, Cheltenham, UK.

[29] Crua, C., Kennaird, D. A. and Heikal, M. R. (2003), 'Laser-induced incandescence study of diesel soot formation in a rapid compression machine at elevated pressures', *Combustion and Flame* **135**(4), 475–488.

[30] Dobashi, R., Hirano, T. and Tsuruda, T. (1992), 'Detailed structure of flame front disturbance', *Combustion Science and Technology* **96**, 155–167.

[31] Dobashi, R., Hirano, T. and Tsuruda, T. (1994), Flame front disturbance induced by a weak pressure wave, *in* 'Twenty-Fifth Symposium (International) on Combustion', Vol. 25, The Combustion Institute, pp. 1415–1422.

[32] Dougherty, E. R. and Giardina, C. R. (1987), *Image processing - continuous to discrete: Geometric, transform and statistical methods*, Vol. 1, Prentice-Hall, Englewood Cliffs, NJ.

[33] Eisner, A. D. and Rosner, D. E. (1985), 'Experimental studies of soot particle thermocouples in nonisothermal combustion gases using thermocouple response techniques', *Combustion and Flame* **61**(2), 153–166.

[34] Fiedler, H., Nottmeyer, K., Wegener, P. P. and Raghu, S. (1985), 'Schlieren photography of water flow', *Experiments in Fluids* **3**, 145–151.

[35] Fielding, J., Frank, J. H., Kaiser, S. A., Smooke, M. D. and Long, M. B. (2002), 'Polarized/depolarized Rayleigh scattering for determining fuel concentrations in flames', *Proceedings of the Combustion Institute* **29**, 2703–2709.

[36] Fielding, J., Schaffer, A. M. and Long, M. B. (1998), Three-scalar imaging of turbulent non-premixed flames in methane, *in* 'Twenty-Seventh Symposium on Combustion.', The Combustion Institute, pp. 1007–1014.

[37] Fischer, W. and Burkhardt, H. (1990), Three-dimensional temperature measurement in flames by multispectral tomographic image analysis, *in* 'Applications of Digital Image Precessing XIII', SPIE.

[38] Flower, W. L. (1983), 'Optical measurement of soot formation in premixed flames', *Combustion Science and Technology* **33**, 17–33.

[39] Flower, W. L. (1989), 'Soot particle temperatures in axisymmetric laminar ethylene-air diffusion flames at preasures up to 0.7MPa', *Combustion Flame* **77**, 279–293.

[40] Fristrom, R. M. (1995), *Flame structure and processes*, Oxford University Press.

[41] Gaydon, A. G. (1974), *The spectroscopy of flames*, Chapman and Hall.

[42] Gaydon, A. G. and Wolfhard, H. G. (1979), *Flames their structure. Radiation and Temperature*, Chapman and Hall.

[43] Gilabert, G., Lu, G. and Yan, Y. (2007), 'Three-dimensional tomographic reconstruction of the luminosity distribution of a combustion flame', *IEEE Transactions on Instrumentation and Measurement* **56**(4), 1300–1306.

[44] Gomez, S., Ono, M., Gamio, C. and Fraguela, A. (2003), 'Reconstruction of capacitance tomography images of simulated two-phase flow regimes', *Applied Numerical Mathematics* **46**(2), 197–208.

[45] Gordon, R., Bender, R. and Herman, G. T. (1970), 'Algebraic reconstruction techniques (ART) for threedimensional electron microscopy and X-ray photography', *Journal of Theoretical Biology* **35**, 471–481.

[46] Hall, R. J. and Bonczyk, P. A. (1990), 'Sooting flame thermometry using emission/absorption tomography', *Applied Optics* **29**(31), 4590–4598.

[47] Han, D., Su, L. K., Menon, R. K. and Mungal, M. G. (2000), Study of a lifted-jet flame using a stereoscopic PIV system, *in* 'Tenth International Symposium of Applications of Laser Techniques to Fluid Mechanics', Calouste Gulbenkian Foundation.

[48] Hertz, H. M. (1985), 'Experimental determination of 2-D flame temperature fields by interferometric tomography', *Optics Communications* **54**, 131–136.

[49] Hertz, H. M. and Faris, G. W. (1988), 'Emission tomography of flame radicals', *Optics Letters* **13**(5).

[50] Huang, H.-W. and Zhang, Y. (2008), 'Flame colour characterization in the visible and infrared spectrum using a digital camera and image processing', *Measurement Science and Technology* **19**(8), 085406.

[51] Huang, Y. (2001), Measurement of flicker and temperature of fossil fuel fired flames, PhD thesis, The University of Greenwich.

[52] Huang, Y. and Yan, Y. (2000), 'Transcient two-dimensional temperature measurement of open flames by dual-spectral image analysis', *Transactions of the Institute of Measurement and Control* **22**(5), 371–384.

[53] Hult, J., Harvey, A. and Kaminski, C. F. (2004), Combined high repetition-rate OH PLIF and stereoscopic PIV for studies of turbulence/chemistry interactions, *in* 'Laser Applications to Chemical and Environmental Analysis (Ninth Topical Meeting and Tabletop Exhibit)', Optical Society of America.

[54] Hult, J., Omrane, A., Nygren, J., Kaminski, C. F., Axelsson, B., Collin, R., Bengtsson, P. E. and Ald'en, M. (2002), 'Quantitative three-dimensional imaging of soot volume fraction in turbulent non-premixed flames', *Experiments in Fluids* **33**(2), 265–269.

[55] Jackson, P. and Bulger, J. (1987), 'Enhancing techniques for flame monitoring', *Control and Instrumentation* **19**, 73–75.

[56] Jiang, F., Liu, S., Lu, G., Yan, Y., Wang, H., Song, Y., Ma, R. and Pan, Z. (2002), 'Experimental study on measurement of flame temperature distribution using the two-color method', *Journal of Thermal Science* **11**(4), 378–382.

[57] Kaczmarz, S. (1937), 'Angenäherte auflösung von systemen linearer gleichungen', *Bulletin International de l'Academie Polonaise des Sciences et des Lettres, series A* **35**, 335–357.

[58] Kak, A. C. (1979), 'Computerized tomography using X-rays and ultrasound', *Proceedings IEEE* **67**, 1245–1272.

[59] Kak, A. C. (1985), Tomographic imaging with diffracting and non-diffracting sources, *in* 'Array Signal Processing', Prentice-Hall, Englewood Cliffs, NJ.

[60] Kak, A. C. and Slaney, M. (1988), *Principles of Computerized Tomographic Imaging*, IEEE Press.

[61] Lackner, M., Charareh, S., Winter, F., Iskra, K. F., Rüdisser, D., Neger, T., Kopecek, H. and Wintner, E. (2004), 'Investigation of the early stages in laser-induced ignition by Schlieren photography and laser induced fluorescence spectroscopy', *Optics Express* **12**(19), 4546–4557. Optical Society of America.

[62] Ladommatos, N. and Zhao, H. (1994), A guide to measurement of flame temperature and soot concentration in diesel engines using the two-color method. Part 1: Principles, Technical report, Society of Automotive Engineers.

[63] Lapp, M., Goldman, L. M. and Penney, C. M. (1972), 'Raman scattering from flames', *Science* **175**(4026), 1112–1115.

[64] Larrabee, R. D. (1959), 'Spectral emissivity of tungsten', *Journal of the Optical Society of America* **49**(6), 619–625.

[65] Lautenberger, C. W., de Ris, J. L., Dembsey, N. A., Barnett, J. R. and Baum, H. R. (2005), 'A simplified model for soot formation and oxidation in CFD simulation of non-premixed hydrocarbon flames', *Fire Safety Journal* **40**(2), 141–176.

[66] Leipertz, A., Obertacke, R. and Wintrich, F. (1996), Industrial combustion control using UV emission tomography, *in* 'Twenty-Sixth Symposium (International) on Combustion', The Combustion Institute, pp. 2869–2875.

[67] Li, X.-Y. and Teng, S.-H. (2001), 'Generating well-shaped Delaunay meshes in 3D'.

[68] Lipp, F., Hartick, J., Hassel, E. P. and Janicka, J. (1992), 'Comparison of UV Raman scattering measurements in a turbulent diffusion flame with Reynolds-stress model predictions', *Symposium (International) on Combustion* **24**(1), 287–294.

[69] Lu, G. (2000), Advanced monitoring, characterisation and evaluation of fossil fuel fired flames, PhD thesis, University of Greenwich.

[70] Lu, G., Yan, Y. and Bheemul, H. C. (2001), Concurrent measurements of temperature and soot concentration of pulverised coal flames, *in* 'Proceedings of IMTC 2001', IEEE, pp. 1221–1225.

[71] Lu, G., Yan, Y. and Colechin, M. (2004), 'A digital imaging based multifunctional flame monitoring system', *IEEE Transaction on Instrumentation and measurement* **35**(4), 1152–1158.

[72] Lu, G., Yan, Y., Colechin, M. and Hill, R. (2006), 'Monitoring of oscillatory characteristics of pulverised coal flames through image processing and spectral analysis', *IEEE Transactions on Instrumentation and Measurement* **55**, 226–231.

[73] Lu, G., Yan, Y., Cornwell, S., Whitehouse, M. and Riley, G. (2008), 'Impact of co-firing coal and biomass on flame characteristics and stability', *Fuel* **87**(7), 1133–1140.

[74] Lu, G., Yan, Y. and Reed, A. R. (1999), 'An intelligent vision system for monitoring and control of combustion flames', *Measurement and Control* **32**, 164–168.

[75] Luo, Z. X. and Zhou, H. C. (2007), 'A combustion-monitoring system with 3-D temperature reconstruction based on flame-image processing technique', *IEEE Transactions on Instrumentation and Measurement* **56**, 1877–1882.

[76] Marran, D. F., Frank, J. H., Long, M. B., Stårner, S. H. and Bilger, R. W. (1995), 'Intracavity technique for improved Raman/Rayleigh imaging in flames', *Optics Letters* **20**(7), 791–793.

[77] Matsui, Y., Kamimoto, T. and Matsuoka, S. (1979), A study on the time and space resolved measurement of flame temperature and soot concentration in a D. I. diesel engine by the two-colour method, Technical report, Society of Automotive Engineers.

[78] Matsui, Y., Kamimoto, T. and Matsuoka, S. (1980), Study on the application of the two-colour method to the measurement of flame temperature and soot concentration in diesel engines, Technical report, Society of Automotive Engineers.

[79] McCaffrey, B. J. (1979), Purely buoyant difussion flames: some experimental results, Technical report, Center for Fire Research, National Engineering Laboratory, Natioanal Bureau of Standards, Washington DC.

[80] McEnally, C. S., Köylü, Ü. Ö., Pfefferle, L. D. and Rosner, D. E. (1997), 'Soot volume fraction and temperature measurements in laminar nonpremixed flames using thermocouples', *Combustion and Flame* **109**, 701–720.

[81] McGillem, C. D. and Cooper, G. R. (1974), *Continuous and discrete signal and system analysis*, Holt, Rinehart and Wiston, New York, NY, USA.

[82] Meier, W. and Keck, O. (2002), 'Laser Raman scattering in fuel-rich flames: background levels at different excitation wavelengths', *Meas. Sci. Techno.* **13**, 741–749.

[83] Michelsen, H. A. (2006), 'Laser-induced incandescence of flame-generated soot on a picosecond time scale', *Appl. Phys. B* **83**, 443–448.

[84] Michelson, A. A. and Morley, E. W. (1887), 'On the relative motion of the Earth and the luminiferous Ether', *The American Journal of Science* **34**(203), 333–345.

[85] Miller, J. H., Elreedy, S., Ahvazi, B., Woldu, F. and Hassanzadeh, P. (1993), 'Tunable diode-laser measurement of carbon monoxide concentration and temperature in a laminar methane-air diffusion flame', *Applied Optics* **32**(30), 6082–6089.

[86] Molcan, P., Lu, G., Bris, T. L., andBenoît Taupin, Y. Y. and Caillata, S. (2009), 'Characterisation of biomass and coal co-firing on a 3 MWth Combustion Test Facility using flame imaging and gas/ash sampling techniques', *Fuel* **88**(12), 2328–234.

[87] Moratti, F., Annunzotia, M. and Giammartini, S. (1997), An artificial vision system for the 3D reconstruction and the dynamical characterisation of industrial flames, Technical report, ENEA-CRE Casaccia, Rome, Italy.

[88] Natterer, F., Setzepfandt, B. and Wübbeling, F. (1996), Tomography of flames in combustion chambers. Pages 105–108.

[89] Ng, W. B., Salem, A. F. and Zhang, Y. (2003), 'Three-dimensional visualization of diffusion flame shapes under acoustic excitation using stereoscopic imaging and reconstruction technique', *Journal of Visualization* **6**(4), 329–336.

[90] Ng, W. B. and Zhang, Y. (2003), 'Stereoscopic imaging and reconstruction of the 3D geometry of flame surfaces', *Experiments in Fluids* **34**(4).

[91] Ng, W. B. and Zhang, Y. (2005), 'Stereoscopic imaging and computer vision of impinging fires by a single camera with a stereo adapter', *International Journal of Imaging Systems and Technology* **15**(2), 114–122.

[92] Nygren, J., Hult, J., Richter, M., Aldén, M., Christensen, M., Hultqvist, M. and Johansson, B. (2002), 'Three-dimensional laser induced fluorescence of fuel distributions in an HCCI engine', *Proceedings of the Combustion Institute* **29**(1), 679–685.

[93] Okuno, K., Sano, T., Saitoh, H., Yoshikawa, N. and Hayashi, S. (2006), 'Measurement of temperature and concentration of nitrogen monoxide in flames by using LIF imaging spectroscopy with standard addition method', *Transactions of the Japan Society of Mechanical Engineers Part B* **18**(11), 2733–2740.

[94] Ossler, F., Agrup, S. and Aldén, M. (1995), 'Three-dimensional flow visualization with picosecond Mie scattering and streak-camera detection', *Applied Optics* **34**(3), 537–540.

[95] Owen, S. J. (1998), A survey of unstructured mesh generation technology, *in* 'International Meshing Roundtable', pp. 239–267.

[96] Palero, V. R. and Ikeda, Y. (2002), 'Droplet-size-classified stereoscopic PIV for spray characterization', *Meas. Sci. Technol.* **13**, 1050–1057.

[97] Pan, G. and Meng, H. (2005), 'Digital holography particle image velocimetry for the measurement of 3Dt-3c flows', *Optics and Lasers in Engineering* **43**(10), 1039–1055.

[98] Pan, S. X. and Kak, A. C. (1983), 'A computational study of reconstruction algorithms for diffraction tomography: Interpolation vs. filtered-backpropagation', *IEEE Trans. Acoust. Speech Signal Processing* **31**, 1262–1275.

[99] Parsinejad, F., Keck, J. C. and Metghalchi, H. (2007), 'On the location of flame edge in shadowgraph pictures of spherical flames: a theoretical and experimental study', *Experiments in Fluids* **43**(6), 887–894.

[100] Pastor, J. V., García, J. M., Pastor, J. M. and Buitrago, J. E. (2006), 'Analysis of calibration techniques for laser-induced incandescence measurements in flames', *Meas. Sci. Technol* **17**, 3279–3288.

[101] Peyton, A. J., Yu, Z. Z., Lyon, G., Al-Zeibak, S., Ferreira, J., Velez, J., Linhares, F., Borges, A. R., Xiong, H. L., Saunders, N. H., and Beck, M. S. (1996), 'An overview of electromagnetic inductance tomography: description of three different systems', *Meas. Sci. Technol.* **7**, 261–271.

[102] Qi, J. A., Wong, W. O., Leung, C. W. and Yuen, D. W. (2008), 'Temperature field measurement of a premixed butane/air slot laminar flame jet with Mach-Zehnder interferometry', *Applied Thermal Engineering* **28**, 1806–1812.

[103] Reynolds, O. (1883), 'An experimental investigation of the circumstances which determine whether the motion of water shall be direct or sinuous, and of the law of resistance in parallel channels', *Philosophical Transactions of the Royal Society* **174**, 935–982.

[104] Rosenfeld, A. and Kak, A. C. (1982), *Digital picture processing*, Academic Press, New York, NY, USA.

[105] Roser, M., Vogl, A., Radandt, S., Malalasekera, W. and Parkin, R. (1999), 'Investigations of flame front propagation between interconnected process vessels. development of a new flame front propagation time prediction model', *Journal of Loss Prevention in the Process Industries* **12**(5), 421–436.

[106] Rott, N. (1990), 'Note on the history of the reynolds number', *Annual Review of Fluid Mechanics* **22**, 1–11.

[107] Ruão, M., Costa, M. and Carvalho, M. G. (1999), 'A NO_x diagnostic system based on a spectral ultraviolet/visible imaging device', *Fuel* **78**, 1283–1292.

[108] Salem, A. Z. I., Canann, A. S. and Sunil, S. (1997), 'Robust distortion metric for quadratic triangular 2D finite elements', *Trends in Unstructured Mesh Generation* **220**, 73–80.

[109] Santoni, P.-A., Marcelli, T. and Leoni, E. (2002), 'Measurement of fluctuating temperatures in a continuous flame spreading across a fuel bed using a double thermocouple probe', *Combustion and Flame* **131**, 47–58.

[110] Sbarbaro, D., Farias, O. and Zawadsky, A. (2003), 'Real-time monitoring and characterization of flames by principal-component analysis', *Combustion and Flame* **132**(3), 591–595.

[111] Scharr, H., Jähne, B., Böckle, S., Kazenwadel, J., Kunzelmann, T. and Schulz, C. (2000), Flame front analysis in turbulent combustion, *in* 'DAGM-Symposium', pp. 325–332.

[112] Schwartz, M. and Shaw, L. (1975), *Signal processing: Discrete spectral analysis, detection and estimation*, McGraw-Hill, New York, NY, USA.

[113] Settles, G. S. (2001), *Schlieren and shadowgraph techniques: visualizing phenomena in transparent media*, Springer.

[114] Shakher, C. (2009), Interferometric methods to measure temperature and temperature profile of gaseous flames, *in* 'ICOP 2009 International Conference on Optics and Photonics', CSIO, Chandigarh, India.

[115] Shakher, C., Nirala, A. K., Pramila, J. and Verma, S. K. (1992), 'Use of Speckle technique for temperature measurement in gaseous flame', *J. Optics* **23**(2), 35–39.

[116] Shapiro, L. G. and Stockman, G. C. (2002), *Computer vision*, Prentice Hall.

[117] Shepp, L. A. and Logan, B. F. (1974), 'The Fourier reconstruction of a head section', *IEEE trans. Nucl. Sci*, **21**, 21–43.

[118] Shreiner, D., Woo, M., Neider, J. and Davis, T. (2006), *OpenGL Programming Guide, the Official Guide to Learnig OpenGL, Version 2*, Addison-Wesley.

[119] Smith, D. A. and Cox, G. (1992), 'Major chemical species in buoyant turbulent diffusion flames', *Combustion and Flame* **91**, 226–238.

[120] Stamatov, V. and Stamatova, L. (2006), 'A Mie scattering investigation of the effect of strain rate on soot formation in precessing jet flames', *Flow, Turbulence and Combustion* **76**(3), 279–289.

[121] Stark, H., Woods, J. W., Paul, I. and Hingorani, R. (1981), 'Direct Fourier reconstruction in computer tomography', *IEEE Trans. Acoust. Speech Signal Processing* **29**, 237–244.

[122] Steeper, R. R., Jensen, P. A. and Dunn-Rankin, D. (1988), 'Using Mie scattering for measuring size changes of individual particles', *J. Phys. E: Sci. Instrum* **21**, 378–383.

[123] Stella, A., Guj, G., Kompenhans, J., Richard, H. and Raffel, M. (2001), 'Three-components Particle Image Velocimetry measurements in premixed flames.

Stereoskopische PIV-messungen in flammen', *Aerospace Science and Technology* **5**(5), 357–364.

[124] Stella, A., Guj, G. and Mataloni, A. (2000), 'Interferometric visualization of jet flames', *Journal of Visualization* **3**(1), 37–50.

[125] Stepowskia, D. and Cabota, G. (1989), 'Laser Mie scattering measurement of mean mixture fraction density and temperature by conditional seeding in a turbulent diffusion flame', *Symposium (International) on Combustion* **22**(1), 619–625.

[126] Tagawa, M. and Ohta, Y. (1997), 'Two-thermocouple probe for fluctuating temperature measurement in combustion - rational estimation of mean and fluctuating time constants', *Combustion and Flame* **109**, 549–560.

[127] Tanabe, K. (1971), 'Projection method for solving a singular system', *Numer. Math.* **17**, 203–214.

[128] Tikhonov, A. N. and Arsenin, V. Y. (1977), *Solutions of Ill-posed Problems (Scripta series in mathematics)*, John Wiley & Sons Inc.

[129] Timmerman, B. H., Watt, D. W. and Bryanston-Cross, P. J. (1999), 'Quantitative visualization of high-speed 3d turbulent flow structures using holographic interferometric tomography', *Optics and laser technology* **31**(1), 53–65.

[130] Timothy, L. D., Froelich, D., Sarofin, A. F. and Beer, J. M. (1986), Soot formation and burnout during the combustion of dispersed pulverised coal particles, *in* 'Twenty-first Symposium (International) on Combustion', The Combustion Institute, pp. 1141–1148.

[131] Vander Wal, R. L., Zhou, Z. and Choi, M. Y. (1996), 'Laser-induced incandescence calibration via gravimetric sampling', *Combustion and Flame* **105**(4), 462–470.

[132] Venkatesh, P. and Prasad, C. R. (1983), 'Corrections for Mie theory given in the scattering of light and other electromagnetic radiation', *Appl. Opt.* **22**, 645–645.

[133] Wakil, M. M. E. (1975), Interferometric flame temperature measurements, *in* 'Combustion measurements: Modern techniques and instrumentation; Proceedings of the SQUID Workshop', Purdue University, pp. 225–244.

[134] Wang, F., Yan, J., Cen, K., Huang, Q., Liu, D., Chi, Y. and Ni, M. (2010), 'Simultaneous measurements of two-dimensional temperature and particle concentration distribution from the image of the pulverized-coal flame', *Fuel* **89**(1), 202–211.

[135] Wang, J. (1990), Modern metrology and measurement technology, Technical report, China Metrology Publications.

[136] Wang, L., Haworth, D. C., Turns, S. R. and Modest, M. F. (2005), 'Interactions among soot, thermal radiation, and NO_x emissions in oxygen-enriched turbulent nonpremixed flames: a computational fluid dynamics modeling study', *Combustion and Flame* **141**(1–2), 170–179.

[137] Wang, S., Cheng, X., Wang, F. and Xu, Y. (2001), The measurement of 3-dimensional temperature distribution in flame, *in* 'The Third International Symposium on Measurement Techniques for Multiphase Flow', The Japanese Society for Multiphase Flow, Fukui, Japan.

[138] Waterfall, R. C., He, R. and Beck, C. M. (1997), 'Visualizing combustion using electrical impedance tomography', *Chemical Engineering Science* **52**(13), 2129–2138.

[139] Waterfall, R. C., He, R., White, N. B. and Beck, C. M. (1996), 'Combustion imaging from electrical impedance measurements', *Meas. Sci. Technol.* **7**, 369–374.

[140] Wernekinck, U., Merzkirch, W. and Fomin, N. A. (1987), 'Measurement of light deflection in a turbulent density field', *Experiments in Fluids* **5**(6), 422–424.

[141] Willson, P. M. and Chappell, T. E. (1985), 'Pulverised fuel flame monitoring in utility boiler', *Measured and Control* **18**, 66–72.

[142] Xu, L.-J. and Xu, L.-A. (1997), 'Ultrasound tomography sustem used for monitoring bubbly gas/liquid two-phase flow', *IEEE Transactions on Ultrasounds, Ferroelectrics and Frequency Control* **44**(1), 67–75.

[143] Xu, L., Yan, Y., Cornwell, S. and Riley, G. (2004), 'On-line fuel identification using digital signal processing and fuzzy interference techniques', *IEEE Transactions on Instrumentation and Measurement* **53**(4), 1316–1320.

[144] Xu, L., Yan, Y., Cornwell, S. and Riley, G. (2005), 'Online fuel tracking by combining principal component analysis and neural network techniques', *IEEE Transactions on Instrumentation and Measurement* **54**(4), 1640–1645.

[145] Xudong, X., Choi, C. W. and Puri, I. K. (2000), 'Temperature measurements in steady two-dimensional partially premixed flames using laser interferometric holography', *Combustion and flame* **120**(3), 318–332.

[146] Yan, H., Liu, L. J., Xu, H. and Shao, F. Q. (2001), 'Image reconstruction in electrical capacitance tomography using multiple linear regression and regularization', *Meas. Sci. and Tech.* **12**(12), 575–581.

[147] Yan, J. and Borman, G. L. (1988), Analysis and in-cylinder measurement of particulate radiant emissions and temperature in a direct injection diesel engine, Technical report, Engine Research Center, University of Wisconsin, Madison, WI, USA.

[148] Yan, Y. (2010), *Advanced monitoring and process control technology for coal-fired power plants*, Woodhead Publishing, chapter 10, pp. 264–288.

[149] Yan, Y., Lu, G. and Colechin, M. (2002), 'Monitoring and characterisation of pulverised coal flames using digital imaging techniques', *Fuel* **81**(5), 647–656.

[150] Yu, M., Lin, J. and Chan, T. (2008), 'Numerical simulation of nanoparticle synthesis in diffusion flame reactor', *Powder Technology* **181**(1), 9–20.

[151] Yu, Z. Z., Peyton, A. J., Xu, L. A. and Beck, M. S. (1998), 'Electromagnetic inductance tomography (EMT) sensor, electronics and image reconstruction algorithm for a system with a rotatable parallel excitation field', *IEE Proc. Sci. Meas. Technol.* **145**(1), 20–25.

[152] Zhang, C. and Chen, T. (2001), Efficient feature extraction for 2D/3D objects in mesh representation, *in* 'in Mesh Representation, ICIP 2001', pp. 935–938.

[153] Zhang, D.-Y. and Zhou, H.-C. (2007), 'Temperature measurement by holographic interferometry for non-premixed ethylene-air flame with a series of state relationships', *Fuel* **86**(10–11), 1552–1559.

[154] Zhao, H. and Ladommatos, N. (1998), 'Optical diagnostics for soot and temperature measurement in diesel engines', *Progress in Energy and Combustion Science* **24**, 221–255.

[155] Zheng, J. Y. (1994), 'Acquiring 3-D models from sequences of contours', *IEEE Trans. Pattern Anal. Mach. Intell.* **16**(2), 163–178.

[156] Zhou, H.-C., Han, S.-D., Sheng, F. and Zheng, C.-G. (2002), 'Visualization of three-dimensional temperature distributions in a large-scale furnace via regularized reconstruction from radiative energy images: numerical studies', *Journal of Quantitative Spectroscopy & Radiative Transfer* **72**, 361–383.

[157] Zhou, H.-C., Lou, C., Cheng, Q., Jiang, Z., He, J., Huang, B., Pei, Z. and Lu, C. (2005), 'Experimental investigations on visualization of three-dimensional

temperature distributions in a large-scale pulverized-coal-fired boiler furnace', *Proceedings of the Combustion Institute* **30**, 1699–1706.

Fundamental Constants

Constant	Symbol	Value	Units
Boltzman's Constant	k, k_B	1.380 650 4(24)	$10^{-23} J \cdot K^{-1}$
Planck's Constant	h	6.626 068 96(33)	$10^{-34} J \cdot s$
	C_1	$2\pi hc^2$	$J \cdot m^2 \cdot s^{-1}$
	C_2	hc/k	$m \cdot K$
$h/2\pi$	$\hbar$	1.054 571 628(53)	$10^{-34} J \cdot s$
Speed of Light	c	299 792 458	$m \cdot s^{-1}$

Publications and Disseminations

The following research papers were published during the course of the work leading to the preparation of this thesis. The publications marked as (†) are including here:

(1) Gilabert G., Lu G. and Yan Y. (2009), Three-dimensional monitoring of combustion flames using digital imaging and tomographic reconstruction techniques, *in* 'What Where When Multi-Dimensional Advances for Industrial Process Monitoring', Leeds, UK.

(2) Gilabert G., Lu G. and Yan Y. (2007), 'Three-dimensional tomographic reconstruction of the luminosity distribution of a combustion flame', *IEEE Transactions on Instrumentation and Measurement*, **56**(4), 1300-1306. (†)

(3) Gilabert G., Lu G. and Yan Y. (2007), 3D visualization of flames, *in* 'One day meeting on Current Research in Combustion: A Forum for Research Students and Early Career Researchers', Loughborough University, Loughborough, UK.

(4) Lu G., Yan Y., Gilabert G. and Cameron S. (2007), Imaging based quantitative characterisation of coal fired flames on a 90 MWth combustion test facility, *in* 'International Conference on Coal Science and Technology', the University of Nottingham, Nottingham, UK, pp. 28-31.

(5) Gilabert G. (2007), 3D monitoring and characterisation of fossil fuel flames with digital imaging techniques, *in* 'Annual Cross Channel Doctoral Conference', University of Kent, Canterbury, UK, pp. 24-25.

(6) Lu G., Yan Y. and Gilabert G. (2006), Digital imaging based monitoring and diagnosis of combustion flames, *in* 'British Flame Workshop on Combustion Diagnostics, The Route Map to Increased Efficiency, Lower Emissions and Improved Product Quality', Swinden House Conference Centre, Rotherham, UK.

(7) Gilabert G., Lu G., Yan Y. and Cornwell S. (2006), Three-dimensional measurement of flame temperature through optical process tomography. *in* 'Sixth European Conference on Coal Research and its Applications', Canterbury, UK, p. 57.

(8) Gilabert G., Lu G., Shao J. and Yan Y. (2006), Tomographic reconstruction of the luminosity distribution of a combustion flame. *in* 'Proceedings of IEEE Instrumentation and Measurement Technology Conference', Sorrento, Italy, pp. 147-150.

(9) Gilabert G., Lu G. and Yan Y. (2005), Three-dimensional visualisation and reconstruction of the luminosity distribution of a flame using digital imaging techniques, *in* 'Conference Series; Sensors & their Applications', Vol.15, University of Greenwich at Medway, Kent, UK, pp. 167-171.

(10) Lu G., Gilabert G. and Yan Y. (2005), Vision-based monitoring and characterisation of combustion flames a review, *in* 'Journal of Physics: Conference Series; Sensors & their Applications', Vol. 15, University of Greenwich at Medway, Kent, UK, pp. 194-200.

(11) Gilabert G., Lu G. and Yan Y. (2005), 3D visualization and quantitative characterization of fossil fuel flames using digital imaging techniques. *in* 'British Coal Utilisation Research Association (BCURA)', Peterborough, UK.

Appendix A

System Configuration

A.1 Technical Specification of the CCD Cameras

The main features of the utilised cameras, the JAI® CV-M77 model, are given in Section 4.2.1.1. The full technical specifications of the camera are listed bellow:

Table A.1: Technical specification of the CCD camera, JAI® CV-M77 model.

Specifications	Value
Scanning system	Progressive 792 lines, 24.8 frames/sec.
Pixel clock	25.000 MHz
Line frequency	19.685 kHz (1270 clock/line)
Frame rate	24.8 frames per second (fps) (792 lines/frame). Normal 74 $fps.$ (264 lines/frame). High frame rate
CCD sensor	1/3 $in.$ RGB primary colur IT CCD. Type Sony ICX-204AK
Sensing area	4.8 (h) × 3.6 (v) mm
Efective pixels	1034 (h) × 779 (v)

Continue ...

Table A.1: (continued)

Specifications	Value
Pixels in video output	1028 (h) × 770 (v). 25 *fps*. Continuous mode 1016 (h) × 770 (v). Triggered modes 1028 (h) × 242 (v). Continuous high frame rate 1016 (h) × 242 (v). Triggered high frame rate
Cell size	4.65 (h) × 4.65 (v) μm
Sensitivity on sensor	1.5 Lux (Max. gain, 50% video)
S/N ratio	> 50 *dB*
Video output	RGB video signal, 0.7 Vpp, 75 Ω Composite sync. on G, 0.3 Vpp (selectable)
Gamma	1.0 - 0.6 - 0.45
Gain	Manual - Automatic
Gain range	-3 to +15 *dB*
Synchronization	Int. X-tal. Ext. HD/VD or random trigger
HD sync. input / output	4 V ±2 V, 75 Ω
Trigger input	4 V ±2 V, 75 Ω
WEN output (write enable)	4 V ±2 V, 75 Ω
EEN output (exposure enable)	4 V ±2 V, 75 Ω
Pixel clock output	4 V ±2 V, 75 Ω

Continue ...

Table A.1: (continued)

Specifications	Value
Composite sync. output	4 V ±2 V, 75 Ω
Trigger modes	Continuous, Edge pre-select, Pulse width control (HD non-reset)
Trigger input (edge pre-select)	> 1 H
Shutter	1/25, 1/50, 1/125, 1/250, 1/500, 1/750, 1/1000, 1/1500, 1/2000, 1/3000, 1/4000, 1/10,000 seconds
Programmable exposure	1.5 H to 791 H
Pulse width control	1.5 H to 2000 H
Long time exposure	2 frames to ∞
Frame delay readout	1 H to 2000 H. Time from trigger input to ext. VD input. For Edge pre-select and Pulse width control
Functions controlled by DIP switch on rear	Shutter speed, Trigger mode. Readout mode, Gamma, Gain, Control
Functions controlled by internal DIP switches	VD input/output, HD input/output. HD, VD and Trigger 75 Ĩľ termination on/off. WEN polarity, Sync. on G, White balance
Functions controlled by RS 232C	Shutter speed, Trigger mode. Readout mode, WEN polarity, Sync on G. Programmable exposure, Gain levels. White clip, Setup, Gamma, White balance

Continue ...

Table A.1: (continued)

Specifications	Value
Communication Baud rate	9600 *bps*
Operating temperature	$-5°C$ to $+45°C$
Humidity	$20 - 80\%$ non-condensing
Storage temp./humidity	$-25°C$ to $+60°C$ / $20 - 80\%$
Power	12V DC $\pm$ 10%, 5.5 W
Lens mount	C-mount
Dimensions	40 $\times$ 50 $\times$ 90 *mm* (H $\times$ W $\times$ D)
Weight	270 *g*

A.2 Camera Schematic and Functions

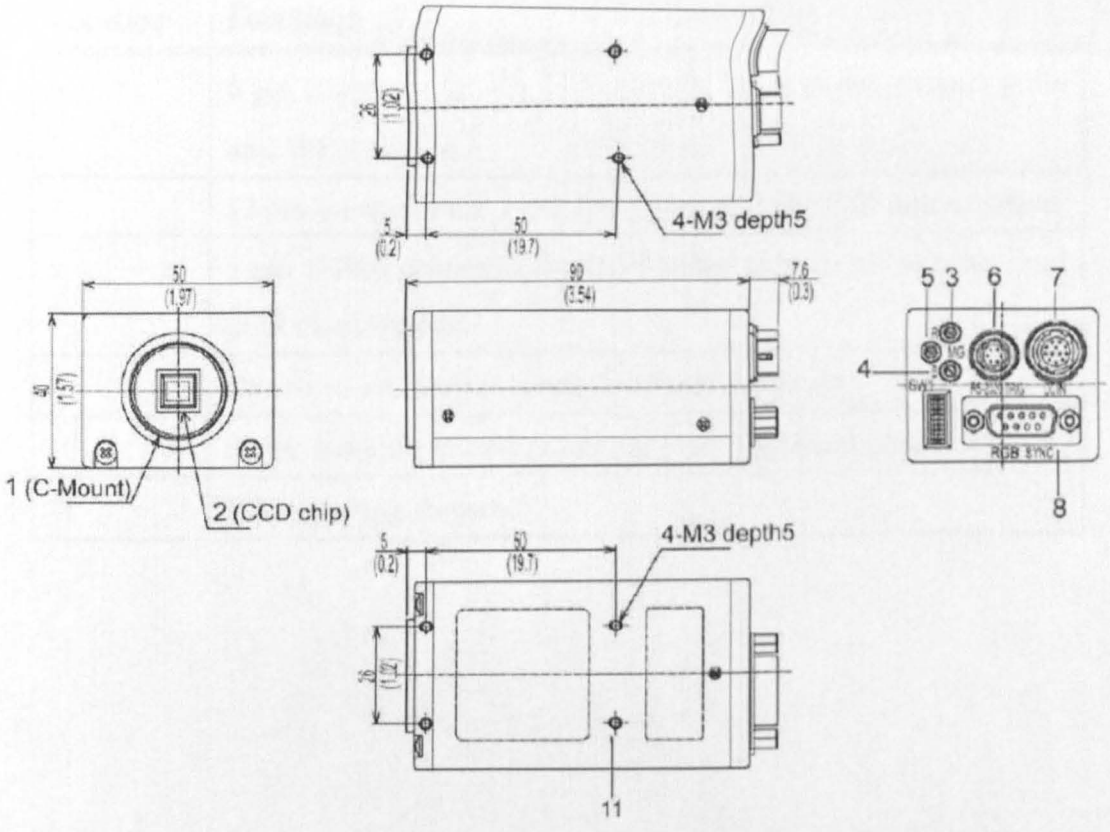

Figure A.1: JAI® CV-M77 schematic and locations.

Table A.2: Locations and functions.

Location	Functions
1	Lens mount of C-mount type.
2	1/3 *in.* CCD sensor with primary color mosaic filter. (Bayer filter).
3	R Gain Potentiometer. To adjust Red gain level manually.
4	B Gain Potentiometer. To adjust Blue gain level manually.
5	MG Gain Potentiometer. To adjust Master gain level manually.

Continue ...

Table A.2: (continued)

Location	Functions
6	6 pin connector for RS 232C signals, input of ext. trigger pulse and WEN output.
7	12 pin connector for +12V DC power and HD/VD input/output.
8	9 pin D-Sub connector for RGB video output, video sync. and pixel clock output.
9	Switch to set shutter speed and function mode.
10	Screw holes for tripod mounting plate (optional plate).
11	M3 mounting threads.

A.3 12-pin Multi-connector (DC-IN/Trigger)

Figure A.2 shows the 12-pin multi-connector seen from the rear of camera.

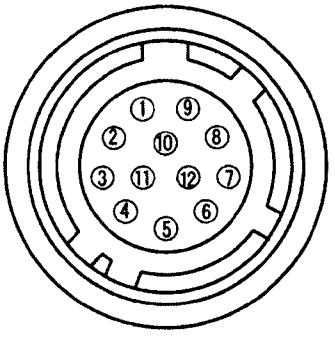

Figure A.2: CV-M77's 12-pin connector.

Table A.3: 12-pin multi-connector pin-out chart.

Pin No.	Signal
1	GND
2	+12 V DC input
3	GND
4	Iris video output
5	GND
6	HD input/output
7	VD input/output
8	GND
9	NC/Pclk out
10	GND/NC/WEN out
11	Trigger input /NC/+12V
12	GND

A.4 9-pin D-sub connector (RGB/SYNC)

Figure A.3 shows the 9-pin multi-connector seen from the rear of camera.

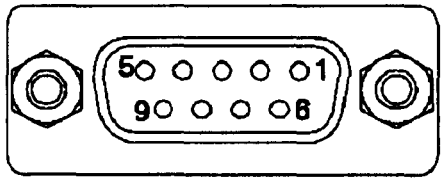

Figure A.3: CV-M77's 9-pin connector.

Table A.4: 9-pin multi-connector pin-out chart.

Pin No.	Signal
1	NC/VD in
2	GND
3	R output
4	G output /Sync on G
5	B output
6	HD input /HD output
7	Sync output /WEN output
8	GND
9	NC/Pclk

A.5 HD/DB-44 Male/Female Connectors

The cameras are connected to the frame grabbers using a cable with a a HD-44 male connector on one end and both BNC and open-ended wire part on the other. The video input connector on the frame grabber is therefore a DB-44 female connector depicted in Figure A.4.

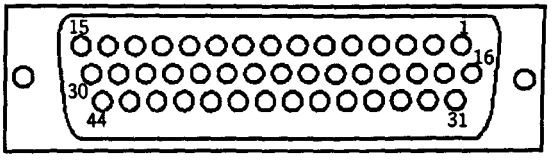

Figure A.4: Matrox Meteor-II/Multi-Channel's DB-44 female connector.

Table A.5: Compact DB-44 multi-connector pin-out chart.

Pin No.	Signal
15	RED analog video input (channel 1)
44	GREEN analog video input (channel 1)
13	BLUE analog video input (channel 1)
43	Analog video input (SYNC)
11	RED analog video input (channel 2)
41	GREEN analog video input (channel 2)
40	BLUE analog video input (channel 2)
1, 16	DC POWER; +12 V OR +5 V Power Supply.
7, 37	Not connected.
3-4, 14, 17-18, 25-31, 42	GND

A.6 Matrox Meteor-II/Multi-Channel Frame Grabber

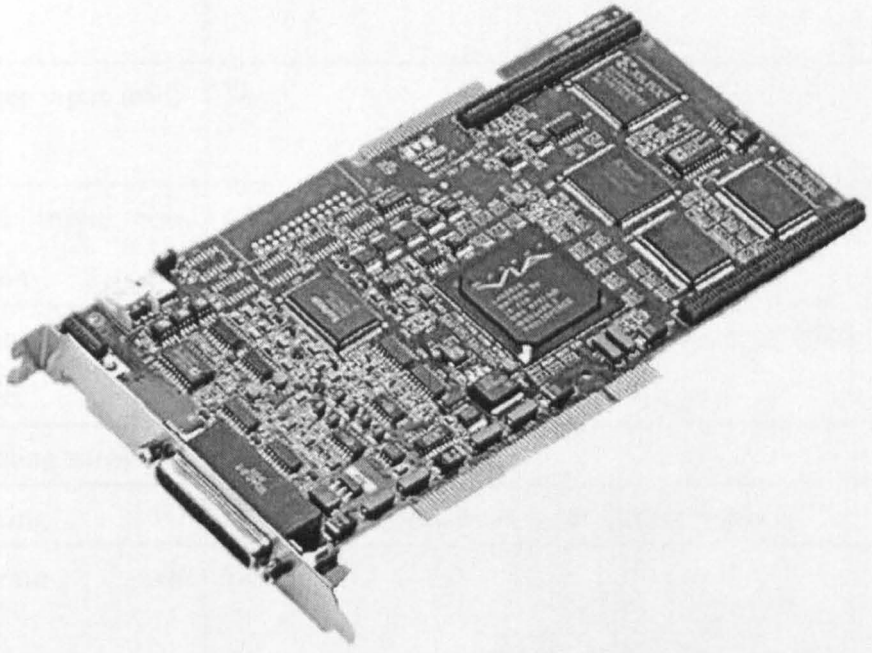

Figure A.5: Matrox® Meteor II/Multi-channel frame grabber.

Table A.6: Matrox® Meteor II/Multi-channel frame grabber specifications.

Specifications	Value
Real time capture rates	Up to 130 $MB/second$
Display	VGA
Capture methods	Standard analog composite (CVBS) or Y/C NTCS/PAL

Continue ...

Table A.6: (continued)

Location	Functions
Pixel format	CCIR 601
Progamable gamma correction	Yes
Trigger input available	Yes
Video input connection	4 CVBS, 2 CVBS and 1 Y/C or 2 Y/C
Acquisition supported	Interlaced and progressive scan component RGB. Single or two channel monochrome cameras.
Sampling rates	Up to 30 MHz
Filtering	10 MHz los-pass filter to eliminate aliasing
Separate pixel clock	Yes

A.7 Optical Transmission Unit

A.7.1 Bi-convex lens

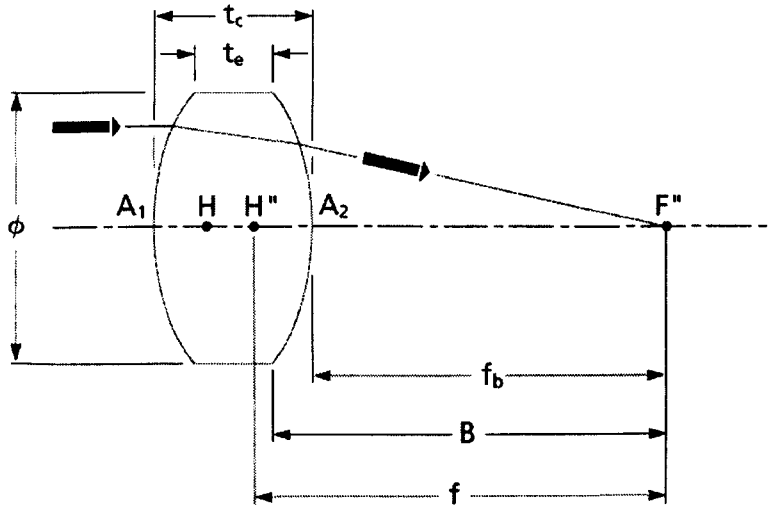

Figure A.6: Schematic of a bi-convex lens 30 *mm* diameter and 30 *mm* focal length.

Table A.7: Bi-convex lens 30 *mm* diameter and 30 *mm* focal length specifications.

Specifications	Value
Paraxial focal length	$30mm \pm 2\%$
Clear aperture (CA)	90% of central diameter
Optical material	BK7
Central thickness	$10.3mm \pm 0.2mm$
Centration	≤ 3 arc minutes
Diameter	$30 \pm 0.1mm$
Surface quality	Pitch polished 60-40 scratch and dig
Edge characteristics	0.25-0.50 *mm* bevel

A.7.2 Miniature Straight Mirror

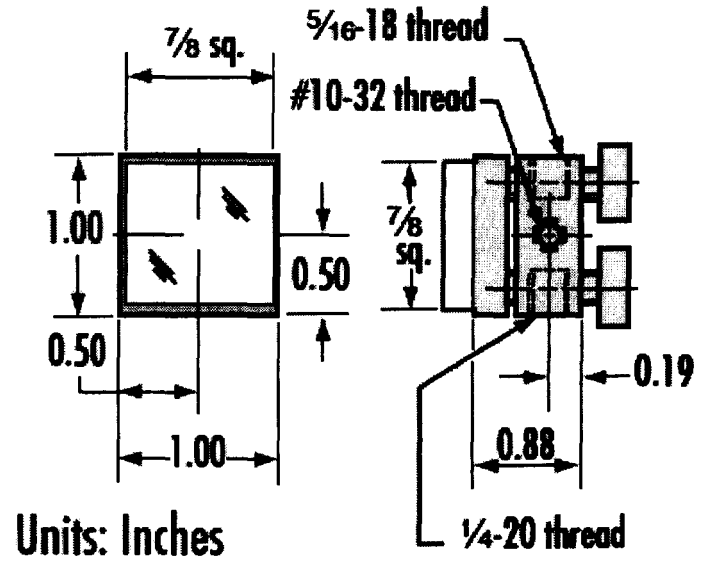

Figure A.7: Schematic of a 1.0 *in.* miniature straight mirror.

Table A.8: A 1.0 *in.* miniature straight mirror specifications.

Specifications	Value
Construction	Aluminium-stainless steel
Finish	Black anodized
Resolution	0.015 *in.*/turn
Weight	0.1 *lb.*
Range	15°

A.7.3 Right-Angle Prism

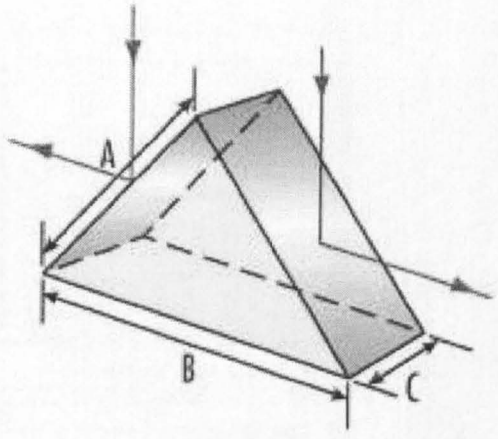

Figure A.8: Schematic of a right angle prism 90° mirror.

Table A.9: Right angle prism 90° mirror specifications.

Specifications	Value
Substrate	N-BK7
Dimensional tolerance	$\pm 0.1mm$
Angle tolerance	± 2 arc minute
Surface accuracy	$1/8\ \lambda$
Bevel	$0.3mm \times 45°$
Coating	Enhanced aluminium

A.7.4 White Backlight Panel

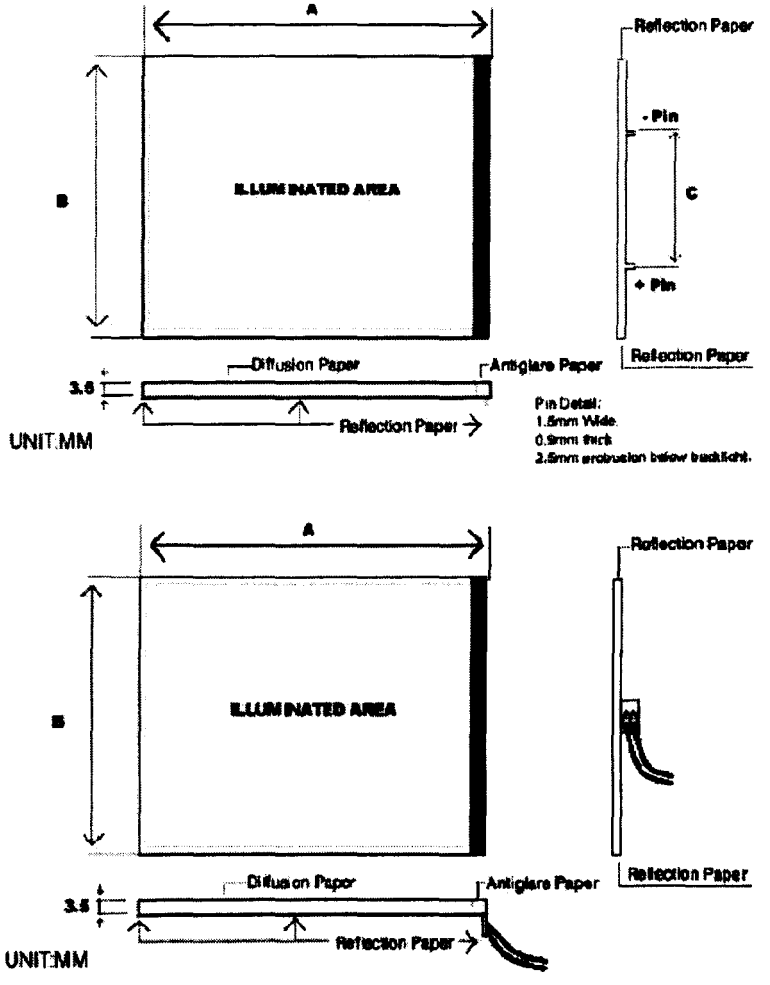

Figure A.9: LCD White backlight panel utilised in the system calibration.

Table A.10: LCD White backlight panel utilised in the system calibration.

Specifications	Value
A, B and C	111, 86 and 42 *mm*
Number of LEDs	8

Continue ...

Table A.10: (continued)

Location	Functions
Reverse Voltage	5 V
Power Dissipation	8 mW
Electric Static Discharge Threshold	1000 V
D.C forward current per LED	20 mA
Pulse current per LED	100 mA
Operating temperature range	$-25°C$ to $+85°C$
Storage temperature range	$-40°C$ to $+100°C$
Lead soldering temperature	$+260°C$ for 5 secs.

Appendix B

Derivation of Equation 3.40

Because the image of an object obtained by the CCD camera is a two-dimensional projection of the object, each pixel of the image corresponds to a particular point or area of the object. That is, the spectral emitted power $\mathscr{E}_i(\lambda, T)$ of the ith point, assuming that the temperature of the object is T, corresponds to the grey level $\mathscr{G}_i(\lambda, T)$ of the ith pixel. The spectral irradiance incident on the lens of the imaging system $\mathscr{H}_i(\lambda, T)$, emitted by the point, can be expressed as (135):

$$\mathscr{H}_i(\lambda, T) = \frac{\mathscr{E}_i(\lambda, T) \cdot \tau_a}{D_1^2} \tag{B.1}$$

where D_1 is the distance between the object and the lens and τ_a is the transmisivity of air.

If the attenuation due to the image distance is ignored, the radiation energy $\psi_i(\lambda, T)$ incident on the ith pixel of the CCD sensor is given by:

$$\psi_i(\lambda, T) = \mathscr{H}_i(\lambda, T) \cdot \tau_l \cdot A_l \tag{B.2}$$

where τ_l is the tansimitivity of the optical lens, A_l is the area of the lens. Substituting

$A_l = \frac{\pi}{a} \cdot D_1^2$ and Equation B.1 into Equation B.2 yields:

$$\psi_i(\lambda, T) = \frac{\mathscr{E}_i(\lambda, T) \cdot \tau_a \cdot \tau_l \cdot D_l^2}{4 \cdot D_1^2} \tag{B.3}$$

where D_l is the diameter of the optical lens.

The output grey level of the imaging system is proportional to the incident light intensity, i.e.,

$$\mathscr{G}_i(\lambda, T) = C_0 \cdot \mathscr{S}_\lambda \cdot \psi_i(\lambda, T) \tag{B.4}$$

where $\mathscr{S}_\lambda$ is the spectral sensitivity of the CCD sensor and C_0 is a proportional constant depending on the resolution of the analogue-digital conversion.

Substitution of Equation B.3 into Equation B.4 yields:

$$\mathscr{G}_i(\lambda, T) = \frac{\mathscr{S}_\lambda \cdot C_0 \cdot \tau_a \cdot \tau_l \cdot D_l^2}{4 \cdot D_1^2} \cdot \mathscr{E}_i(\lambda, T) \tag{B.5}$$

Renaming $K_0 \equiv \frac{C_0 \cdot \tau_a \cdot \tau_l \cdot D_l^2}{4 \cdot D_1^2}$, Equation B.5 can be converted into:

$$\mathscr{G}_i(\lambda, T) = \mathscr{S}_\lambda \cdot \mathscr{K}_0 \cdot \mathscr{E}_i(\lambda, T) \tag{B.6}$$

It is evident that $\mathscr{K}_0$ can be considered as an instrumentation constant as depends on the detection distance, the diameter of the lenses, the digitalisation process, and reflects the radiation attenuation due to the atmosphere and the optical system. Since the transmissivities of the optical lenses and the air are not related to the wavelength, $\mathscr{K}_0$ is therefore independent of wavelength.

Appendix C

Software for the Three-dimensional Visualisation and Quantitative Characterisation of Fossil Fuel Flames

C.1 Programme Structure

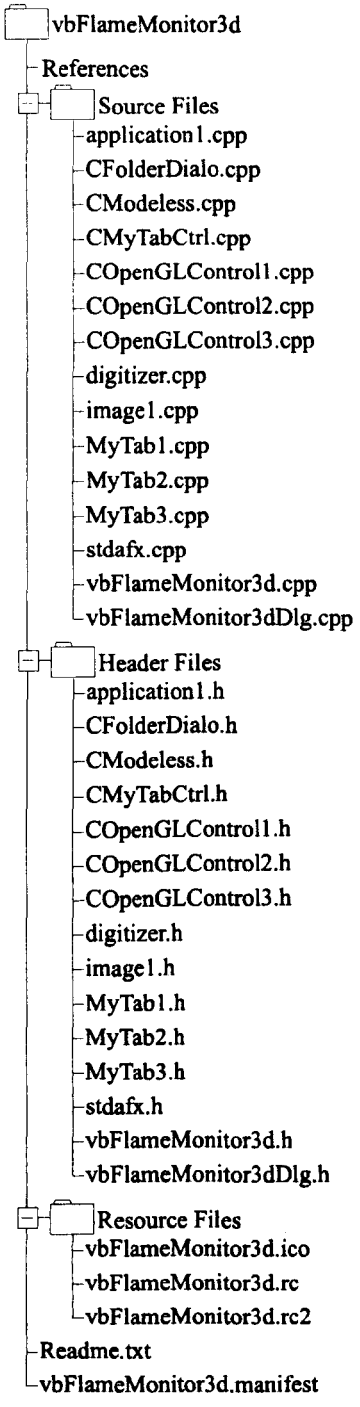

Figure C.1: Tree indicating the software interface structure.

C.2 Main File: vbFlameMonitor3d.cpp

```
// vbFlameMonitor3d.cpp : Defines the class behaviors for the application.
//

#include "stdafx.h"
#include "vbFlameMonitor3d.h"
#include "vbFlameMonitor3dDlg.h"
#include ".\vbflamemonitor3d.h"

#ifdef _DEBUG
#define new DEBUG_NEW
#endif


// CvbFlameMonitor3dApp

BEGIN_MESSAGE_MAP(CvbFlameMonitor3dApp, CWinApp)
ON_COMMAND(ID_HELP, CWinApp::OnHelp)
END_MESSAGE_MAP()


// CvbFlameMonitor3dApp construction

CvbFlameMonitor3dApp::CvbFlameMonitor3dApp()
: actvTab1(true)
, actvTab2(false)
, actvTab3(false)
```

```
, dispcolour(false)
, start(false)
, grab(false)
, go(false)
, opGl(false)
, building(false)
, copingdata1(false)
, copingdata2(false)
, copingdata3(false)
, rangetpt2(false)
, rangetpt3(false)
, stop(false)
, status(-1)
, rawtime(0)
, modes(0)
, redcam0(_T("C:\\"))
, redcam1(_T("C:\\"))
, redcam2(_T("C:\\"))
, greencam0(_T("C:\\"))
, greencam1(_T("C:\\"))
, greencam2(_T("C:\\"))
, datafile(_T("C:\\"))
, path(_T("C:\\"))
, mintpt(COLD_TEMP)
, maxtpt(HOT_TEMP)
, zoomrec(1)
, zoomdisp(9)
, zoom_factor(1)
```

```
, limit(DISPLAY_HEIGHT)
, readfile(false)
, cycles(0)
, camera_iris(0)
{
// TODO: add construction code here,
// Place all significant initialization in InitInstance
}


// The one and only CvbFlameMonitor3dApp object

CvbFlameMonitor3dApp theApp;


// CvbFlameMonitor3dApp initialization

BOOL CvbFlameMonitor3dApp::InitInstance()
{
// InitCommonControls() is required on Windows XP if an application
// manifest specifies use of ComCtl32.dll version 6 or later to enable
// visual styles.  Otherwise, any window creation will fail.
InitCommonControls();

CWinApp::InitInstance();

AfxEnableControlContainer();
```

```
// Standard initialization
// If you are not using these features and wish to reduce the size
// of your final executable, you should remove from the following
// the specific initialization routines you do not need
// Change the registry key under which our settings are stored
// TODO: You should modify this string to be something appropriate
// such as the name of your company or organization
SetRegistryKey(_T("Local AppWizard-Generated Applications"));

CvbFlameMonitor3dDlg dlg;
m_pMainWnd = &dlg;
INT_PTR nResponse = dlg.DoModal();
if (nResponse == IDOK)
{
// TODO: Place code here to handle when the dialog is
//  dismissed with OK
}
else if (nResponse == IDCANCEL)
{
// TODO: Place code here to handle when the dialog is
//  dismissed with Cancel
}

// Since the dialog has been closed, return FALSE so that we exit the
//  application, rather than start the application's message pump.
return FALSE;
}
```

```
void CvbFlameMonitor3dApp::GetDateTime(CString * myDate, CString * myTime,
bool secs, bool doub)
{
// Notes:
// theApp.rawtime is the raw time.
// If secs == true, the function will pass to *myTime information about second
// If doub == true, the format for time output will include ":"
// if doub == false the format for time output will include "."
// Either myDate or myTime can be NULL.

// Locals
char str[8];
char add[8];
int var;

// Current time
struct tm * infotime;
struct tm currenttime;

// Get raw time
time(&theApp.rawtime);

// Translate into local time
infotime = localtime(&rawtime);

// Copy information about time to be accessed
currenttime = *infotime;
```

```
// Avoid date calculations if not date parameter used
if (myDate == NULL)
goto time;

// GET CURRENT DATE...

// Get day of the month
var = currenttime.tm_mday;

// Change int to char
sprintf(str,"%d",var);

// Copy day into CString
*myDate = str;
*myDate += "-";

// Get month
var = 1 + currenttime.tm_mon;

// Change int to char
sprintf(str,"%d",var);

// Copy month into CString
*myDate += str;
*myDate += "-";

// Get year (from 1900)
var = 1900 + currenttime.tm_year;
```

```
// Change int to char
sprintf(str,"%d",var);

// Copy year into CString
*myDate += str;

// Time jump
time:

// Avoid date calculations if not date parameter used
if (myTime == NULL)
return;

// TIME CALCULATIONS...

// Get current hour
var = currenttime.tm_hour;

// Change int to char
sprintf(str,"%d",var);

// Copy hour into CString
*myTime = str;
if (!doub)
*myTime += ".";
else
*myTime += ":";
```

```
// Get minutes after the hour
var = currenttime.tm_min;

// Change int to char
if (var > 9)
sprintf(str,"%d",var);
else {
sprintf(str,"0");
sprintf(add,"%d",var);
strcat(str, add);
}

// Copy
    *myTime += str;

// Only obtain seconds if indicated
if (!secs)
return;

// Update format
if (!doub)
*myTime += ".";
else
*myTime += ":";

// Get seconds after the minute
var = currenttime.tm_sec;
```

```
// Change int to char
sprintf(str,"%d",var);

// Copy seconds into CString
*myTime += str;
}
```

Appendix D

Publications

Three-Dimensional Tomographic Reconstruction of the Luminosity Distribution of a Combustion Flame

Guillermo Gilabert, Gang Lu, *Senior Member, IEEE*, and Yong Yan, *Senior Member, IEEE*

***Abstract*—This paper presents the design, implementation, and evaluation of a 3-D imaging system for the reconstruction of the luminosity distribution of a combustion flame. Three identical red–green–blue charge-coupled device cameras together with appropriate optical transmission units are used to capture concurrently six equiangular 2-D images of a flame. A new tomographic approach that combines the logical filtered back-projection and the algebraic reconstruction technique is proposed to reconstruct flame sections from the images. A direct comparison between the proposed approach and other tomographic algorithms is performed through computer simulation for different test templates and number of projections. Experimental tests were undertaken using both gas- and coal-fired flames in order to evaluate the effectiveness of the system. This research has led to the establishment of an effective tool for the reconstruction of the luminosity distribution of flame sections and, ultimately, the quantitative characterization of the interstructures of a combustion flame.**

***Index Terms*—Combustion flame, flame monitoring, luminosity distribution, tomography, 3-D visualization.**

I. Introduction

ADVANCED technologies for the monitoring and characterization of combustion flames have become increasingly important for improved understanding and subsequent optimization of combustion processes. A significant effort has been made previously to develop vision-based instrumentation systems for quantitative monitoring and characterization of combustion flames using digital imaging and image processing techniques [1]–[3]. These systems use single charge-coupled device (CCD) cameras and are designed to measure the physical parameters of a flame such as size, location, brightness, uniformity, temperature, and oscillation frequency on a 2-D basis. However, a flame is generally a 3-D object. To fully reveal the characteristics of the flame, 3-D techniques are desirable. There have been increased activities in this particular area in recent years. Waterfall *et al.* [4] described an electrical capacitance tomographic system for visualizing and characterizing combustion phenomena in a scaled model of an internal combustion engine. Schwarz [5] proposed a Schlieren imaging-based multitomographic technique for the 3-D visualization of a gaseous flame. Moratti *et al.* [6] described a vision-based technique for the 3-D reconstruction of an industrial flame to determine the volume and surface area of the flame. Zhou *et al.* [7], [8] performed numerical and experimental investigations into the 3-D temperature distribution inside a large-scale coal-fired furnace using up to eight CCD cameras. Bheemul *et al.* [9] proposed a multicamera system for 3-D visualization and quantitative characterization of gas-fired flames, where the geometrical model reconstruction of a flame from its 2-D images was undertaken. Fisher and Burkhardt [10] reported a preliminary study on 3-D temperature measurement of a candle flame using multispectral tomographic imaging techniques. Brisley *et al.* [11] also demonstrated a single camera system for the 3-D temperature measurement of flames based on the cross-sectional reconstruction of a gaseous flame. The single-camera approach operates on the assumption that the flame is axisymmetric in its shape and structure. This approach is simple, robust, and low cost, which is particularly attractive for practical use, though it may not offer a satisfactory solution for an unsteady flame.

To achieve more reliable and accurate 3-D reconstruction of a flame and ultimately the 3-D measurement of flame parameters, a multiprojection sensing arrangement in conjunction with tomographic algorithms is necessary. This paper presents a new 3-D imaging system for the reconstruction of the luminosity distribution of a combustion flame. The system comprises three identical sets of red–green–blue (RGB) CCD cameras and purpose-designed optical transmission units. The system is capable of capturing flame images concurrently from six equiangular directions. Computing algorithms based on optical tomographic theory are developed to reconstruct the luminous sections of the flame from a limited number of 2-D projections (images). Different tomographic algorithms, including the filtered back-projection (FBP), logical filtered back-projection (LFBP), algebraic reconstruction technique (ART), and the combination of LFBP and ART (LFBP–ART), are described. Simulation results are presented for a direct comparison between the four algorithms for several test templates and a different number of projections. Experimental evaluations of the system were undertaken on both gas- and coal-fired combustion rigs.

II. System Description

A schematic of the 3-D flame imaging system is shown in Fig. 1. The system consists of three identical sets of an RGB camera, an optical transmission unit, and a frame grabber, in addition to a personal computer with bespoke application

Manuscript received June 30, 2006; revised March 22, 2007. This work was supported by a grant-in-aid from the British Coal Utilisation Research Association and the U.K. Department of Trade and Industry.

The authors are with the Department of Electronics, University of Kent, CT2 7NT Canterbury, U.K. (e-mail: gg35@kent.ac.uk; g.lu@kent.ac.uk; y.yan@kent.ac.uk).

Color versions of one or more of the figures in this paper are available online at http://ieeexplore.ieee.org.

Digital Object Identifier 10.1109/TIM.2007.900161

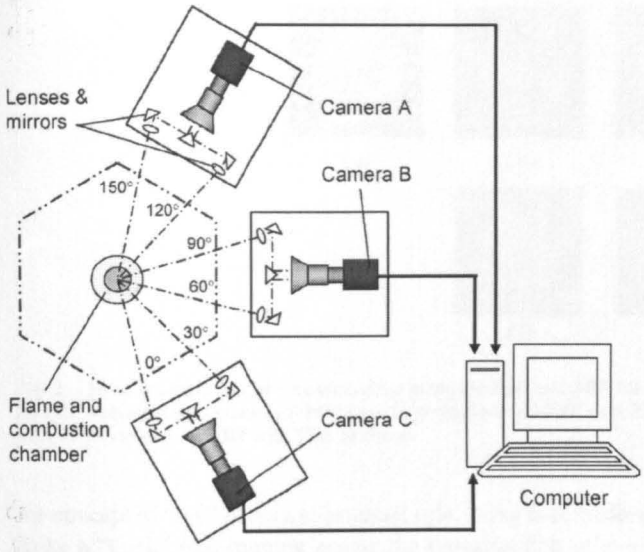

Fig. 1. Schematic of the flame imaging system.

software. The camera has a compact RGB color progressive 1/3-in CCD sensor with square pixels and a primary mosaic filter and a frame rate of 25 frames/s. The cameras are arranged on one side of the burner with an angle of 60° between two adjacent cameras. The optical transmission unit comprises a set of lenses and mirrors, forming two optical paths for each camera and enabling the transmission of the flame image from two different directions with an angle of 30° to the same CCD panel. With such an arrangement, the imaging system produces six flame images concurrently from six directions. The three frame grabbers, which are synchronized by the system software, acquire and digitize the image signals and convert them into 2-D matrices.

The optical setup was calibrated using a template with concentric square patterns with an increment of 10 mm between adjacent lines. The template was placed at the center of the burner. A computer program was developed to draw reference lines within the image windows where the images of the template were displayed. The mirrors and lenses were adjusted to ensure that the images of the concentric squares matched the reference lines accurately. The procedure was repeated for each optical path so that the three cameras had the same focus point for the six optical paths. Since RGB cameras are used here, each image can be disintegrated into three principal channels, i.e., red (R), green (G), and blue (B). The 3-D reconstruction of the flame luminosity can then be achieved for each color band. Any pair of the color-banded luminous reconstruction of the flame, i.e., R and G, R and B, or G and B, can thus be used for further analysis, such as the determination of temperature distribution of the flame using two-color techniques [11].

III. Methodology

A. FBP

The process of projecting the light from a combustion flame onto an imaging sensor is physically equivalent to a Radon transformation, where a 2-D flame cross section undergoes transformation to produce a 1-D section projection [11]. Consequently, the reconstruction of a flame cross section from its 1-D projection is essentially the inverse Radon transformation. The general expression of the Radon transformation of a 2-D function $g(\overline{x})$ is given by [12]

$$P_\theta(x') = \int_{-\infty}^{\infty} g(\overline{x})\delta(\overline{x}\cdot\overline{n} - x')d\overline{x} \tag{1}$$

where $P_\theta(x')$ is the projection of $g(\overline{x})$ along a particular angle θ and through the rectilinear path determined by the Dirac delta function $\delta(\overline{x}\cdot\overline{n} - x')$, where $\overline{n} = (\cos\theta, \sin\theta)$ is a unit vector normal to the projection beam, and $\overline{x}$ is a vector on the projection beam.

The *central slice* (also known as *central projection*) theorem [12] states that the Fourier transform of a 2-D function $g(\overline{x})$ yields the same result as the successive execution of Radon and 1-D Fourier transforms in the radial direction. Consequently, we can reconstruct the function $g(\overline{x})$ by back-projecting and adding successively the filtered projections Q_θ, i.e.,

$$g(\overline{x}) = \int_0^{\pi} Q_\theta(\overline{x}\cdot\overline{n})d\theta \tag{2}$$

where

$$Q_\theta(\overline{x}\cdot\overline{n}) = (h * P_\theta)(x') \tag{3}$$

where h is the filter impulse response, and $*$ denotes convolution. In practice, it is more efficient to implement the convolution in the frequency domain by using the Fast Fourier Transform. For a total number of M_p projections, the reconstructed function can be approximated to

$$g(\overline{x}) \approx \frac{\pi}{M_p}\sum_{i=1}^{M_p} Q_{\theta_i}(\overline{x}\cdot\overline{n}_i). \tag{4}$$

LFBP is a modified algorithm of the FBP [13]. It has been proven that the LFBP can effectively restrain the blurring, which is normally encountered in the FBP. The difference between the FBP and the LFBP lies in the transformation of (4) where the additive operation $\sum$ is substituted by the logical operator $\odot$ in such a way that if A, B, and C are square matrices [13], i.e.,

$$C = A \odot B, \qquad c_{ij} = \begin{cases} 0, & \text{if } a_{ij} = 0 \cup b_{ij} = 0 \\ 1, & \text{if } a_{ij} = b_{ij}. \end{cases} \tag{5}$$

B. ART

Unlike the FBP approach, the ART considers the image cross section to be composed of an array of unknowns, each of which is contained in an "imaginary cell," and then establishes a set of algebraic equations for the unknowns in terms of the lateral measured data in such a way that in each cell, the function $g(\overline{x}) = g(x, y)$ is considered to be a constant. In this procedure,

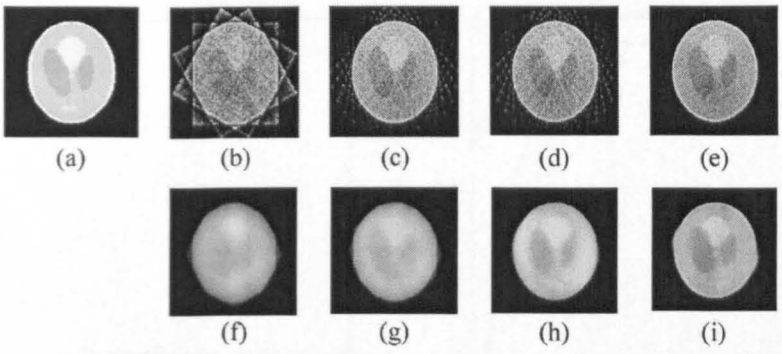

Fig. 2. Head phantom and its reconstructions using the FBP and ART for a different number of projections. (a) Head phantom. (b) FBP with six projections. (c) FBP with eight projections. (d) FBP with 16 projections. (e) FBP with 32 projections. (f) ART with six projections. (g) ART with eight projections. (h) ART with 16 projections. (i) ART with 32 projections.

the concept of "ray" plays a substantial role. A ray is considered to be a "thick" line running across the cross section or $x-y$ plane. With such an approach, the problem is now reduced to solve the following set of simultaneous equations [12]:

$$\begin{aligned}
\omega_{11}g_1 + \omega_{12}g_2 + \cdots + \omega_{1N}g_N &= p_1 \\
\omega_{21}g_1 + \omega_{22}g_2 + \cdots + \omega_{2N}g_N &= p_2 \\
&\vdots \\
\omega_{M1}g_1 + \omega_{M2}g_2 + \cdots + \omega_{MN}g_N &= p_M
\end{aligned} \tag{6}$$

or more concisely

$$\sum_{j=1}^{N} \omega_{ij}g_j = p_i, \qquad i = 1, 2, \ldots, M \tag{7}$$

where ω_{ij} is the weighting factor representing the contribution of the jth cell to the ith ray, g_j denotes the constant value of $g(x, y)$ within the jth cell, p_i is the portion of the projection measured with the ith ray, M is the total number of rays considering all the projections, and N is the total number of cells.

The simplest method of calculating the weighting components ω_{ij} is merely replacing them by 1's or 0's depending upon whether the center of the jth imaginary cell is within the ith ray. To continue the implementation, an initial vector solution $\overline{g}^{(0)} = (g_1^{(0)}, g_2^{(0)}, \ldots, g_N^{(0)})$ is guessed by assigning a value of zero to all its components. Successive values of this vector solution are met according to the following expression:

$$\overline{g}^{(k)} = \overline{g}^{(k-1)} - \frac{\overline{g}^{(k-1)} \cdot \overline{\omega}_k - p_k}{\overline{\omega}_k \cdot \overline{\omega}_k} \overline{\omega}_k \tag{8}$$

where $\overline{\omega}_k$ is the weighting vector, $\overline{\omega}_k = (\omega_{k1}, \omega_{k2}, \ldots, \omega_{kN})$, and $\overline{\omega}_k \cdot \overline{\omega}_k$ is the dot product of $\overline{\omega}_k$ with itself.

C. LFBP–ART

The task of performing the tomographic reconstruction of the luminosity distribution of a flame using the proposed imaging system presents a major challenge in that the number of independent projections is limited, leading to an underdetermined problem. This can, however, be overcome using a suitable LFBP–ART. A major advantage of the LFBP over the FBP is that it provides the information of outer contours of the object being reconstructed. This additional information can be utilized to increase the number of equations used in the ART, which can be expressed as

$$\omega_{ij}g_j = 0, \qquad \text{if} \quad c_{ij} = 0; \quad \{c_{ij} \in C\} \tag{9}$$

where $\omega_{ij}g_j$ are the elements in (6), and C is the matrix in (5). This additional set of equations corrects the hyperplanes represented in (7), resulting in a more accurate solution in performing the iterative operation described in (8).

The external contour obtained using the LFBP is utilized to determine which points have to be calculated using the ART. That is if a particular point lies outside the contour, no unknowns are assigned and no calculations are performed. The value assigned to this point is set to be zero, indicating that there is no any possible luminosity at this position. It is in this way that no spurious values outside the external contour will be computed. This approach not only reduces significantly the number of required calculations but also improves the accuracy of the reconstruction.

IV. Results and Discussion

A. Simulation

1) Gray-Level Reconstruction for a Limited Number of Projections: As our ultimate aim is to develop a 3-D flame imaging system for a practical application, the feasibility of the arrangement is dependent upon its simplicity, and therefore, a small number of projections are desirable for the 3-D reconstruction. To compare the effectiveness of different reconstruction algorithms using a limited number of 2-D projections, computer simulation was performed using an 8-bit gray-level scale digital image of a head phantom, as shown in Fig. 2(a) [14]. Both the FBP and the ART were implemented using Microsoft Visual C++.NET for the reconstruction of the head phantom. Fig. 2(b)–(i) depicts the reconstructed results for a different number of 1-D projections by using the FBP and the ART,

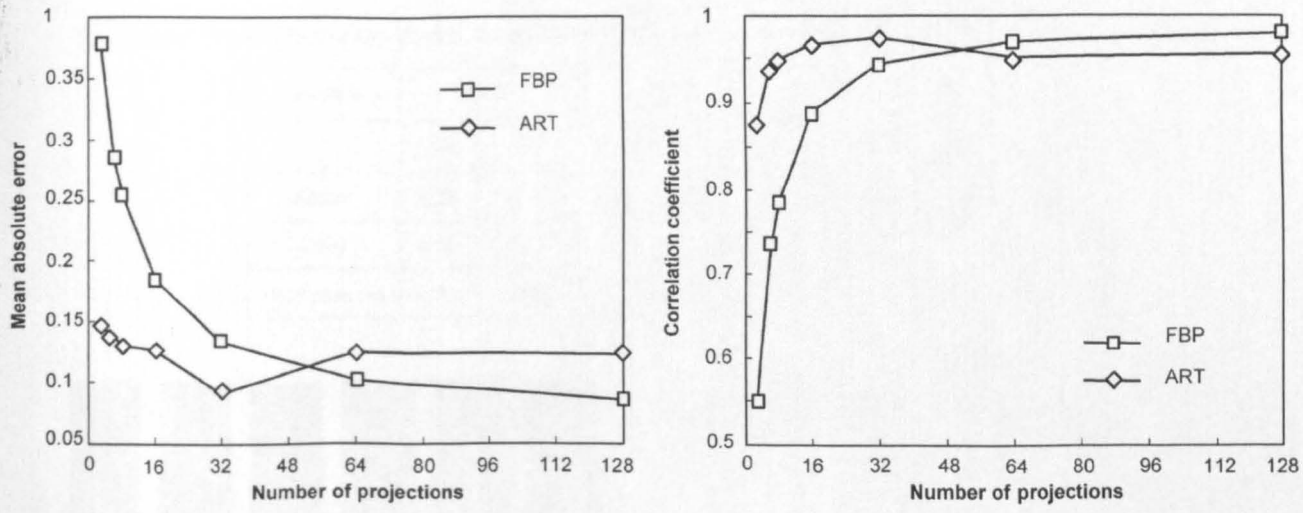

Fig. 3. Mean absolute error and correlation coefficient against number of projections.

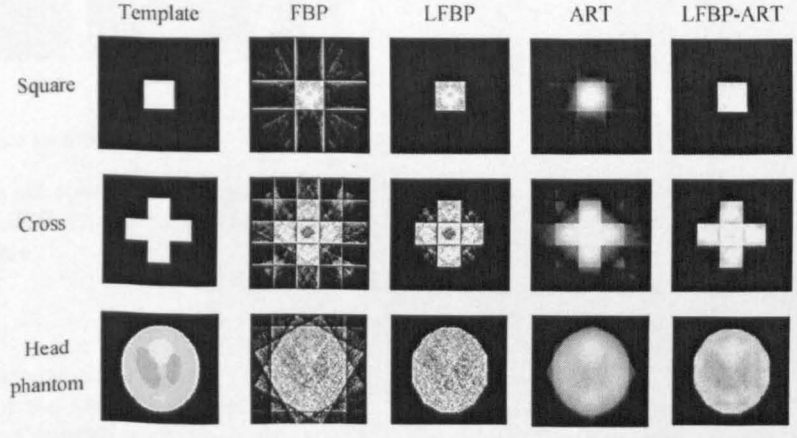

Fig. 4. Comparison of the four tomographic algorithms.

respectively. The projections were taken on an equiangular basis and, in both cases, were confined to a semicircle. For instance, as the angle between the first and the last projections has to be 180° at maximum, the case of using six projections gives the equiangular distance of 30° between two consecutive projections. It can be seen that the reconstruction using the ART with six projections gives definitive contours and main internal features of the phantom head [Fig. 2(f)]. In contrast, the FBP proves itself to be unable to establish the shape and presents a highly fuzzy inner structure of the object for such a limited number of projections [Fig. 2(b)].

To further analyze the accuracy of the reconstructions using the two algorithms, two evaluation criteria were applied. One is the mean absolute error and another is the correlation coefficient between the original image of the head phantom and the reconstructed results. Because the head phantom and its reconstructions are stored in the computer memory as 256 × 256 matrices, which can easily be converted into 65 536 pixel-long vectors, a pixel-by-pixel treatment was utilized to calculate the absolute errors and the correlation coefficients, as shown in Fig. 3. It is clear that the ART provides consistently better reconstruction results for a small number of projections. However, as the FBP is not sensitive to small angles between projections, it commences to produce better results as the number of projections reaches 64.

2) Gray-Level Reconstruction Using Different Tomographic Algorithms: Simulation was also carried out to examine the effectiveness of the four different tomographic algorithms described in Section III for the reconstruction of the given number of 2-D projections. Fig. 4 depicts the reconstructed results for different test templates (i.e., a square, a cross, and the head phantom) using the four algorithms. For each test template, six different 1-D projections that were taken on an equiangular basis and separated by 30° were used in the reconstruction. It can be seen that, with only six projections, the LFBP gives the very similar reconstruction results as the FBP does but reduces considerably the background noise in the reconstruction. The simulation results have suggested that the LFBP–ART would yield the best reconstruction in all the three cases.

The mean absolute error and the correlation coefficient between the original test templates and the reconstructed results were also computed for a further comparison, and the results are summarized in Table I. It is evident that the LFBP–ART gives the smallest mean absolute error and highest

TABLE I
MEAN ABSOLUTE ERROR AND CORRELATION COEFFICIENT (CC) OF RECONSTRUCTIONS FOR FOUR DIFFERENT ALGORITHMS

Template	FBP		LFBP		ART		LFBP-ART	
	Error	CC	Error	CC	Error	CC	Error	CC
Square	0.38	0.75	0.09	0.99	0.19	0.93	0.02	0.99
Cross	0.56	0.74	0.30	0.93	0.29	0.94	0.11	0.99
Head phantom	0.53	0.76	0.35	0.90	0.28	0.94	0.15	0.98

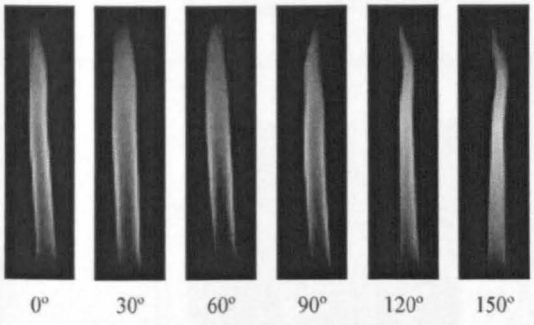

Fig. 5. Typical 2-D images of a gaseous flame.

correlation coefficient in all cases. This investigation has led to the conclusion that an LFBP–ART offers the best approach to the reconstruction problem.

B. Experimental Results

1) Gray-Level Reconstruction of a Gaseous Flame: To evaluate the performance of the imaging system and the effectiveness of the developed algorithms, a series of experiments was conducted on a laboratory-scale gas-fired combustion rig. The system was used to capture multiple 2-D images of a butane flame concurrently from six different directions under steady combustion conditions. The LFBP–ART algorithm as an integrated part of the system software was implemented to reconstruct the gray-level sections of the flame using the images obtained. Fig. 5 shows a typical set of the 2-D images of the flame.

Fig. 6(a) shows the reconstructed luminous cross sections of the flame using the LFBP–ART approach. Comparing the reconstructed cross sections with the original images (Fig. 5), one can make several observations. For instance, cross section i is more circular as it is the nearest to the burner outlet. It also shows a sharp difference between the brighter outers and the darker inners. Moving upward, one can observe that the circularity of the cross sections deteriorates. This is also observed in different widths of the corresponding sections of the images captured from different angles (Fig. 5). Additionally, the luminosity distribution of the upper cross sections appears to be more homogeneous than the lower sections, as observed in Fig. 5.

The reconstruction of flame cross sections can be computed repeatedly for every pixel row along the flame axis. Consequently, a large number of cross sections are obtained that are combined to form a complete 3-D reconstructed model of the flame. When this is accomplished, an exhaustive internal examination can be performed by viewing the longitudinal sections of the flame. Fig. 6(b) shows typical examples of reconstructed longitudinal sections of the flame. It should be noted that the visual representation of the reconstructed longitudinal sections depends on the point of view. The results presented in Fig. 6(b) refer to the sections viewed from the direction of 0° (refer to the reference image in Fig. 5). Section vi depicts the longitudinal section along the burner axis, while v and vii present the sections about ten steps (pixels) back and forward the burner, respectively. Since the three segments are close to the burner axis, they show similar luminous profiles. This result agrees well with the original 2-D images of the flame (Fig. 5).

2) Gray-Level Reconstruction of a Coal Flame: Experimental tests were also conducted on a coal-fired industry-scale combustion test facility. Due to the restriction of onsite installation, only a single camera was used to capture the flame images. In view of fact that the combustion condition is fairly steady during the test runs, the assumption on the rotational symmetry of the flame was applied here [11], and thus, the six projections required in the reconstruction are treated the same in this study. Fig. 7(a) illustrates a typical instantaneous image of the coal-fired flame, whereas Fig. 7(b) shows the luminosity reconstruction of the flame for four cross sections. The pseudo-color technique is used here for a better data presentation, where red presents the highest gray level and black the lowest. Bear in mind that, as the single-camera approach achieves the 3-D reconstruction of the flame from only one image assuming rotational symmetry of the flame, circular outer contours are clearly visible. It is clear, however, that the reconstructed cross sections of the flame appear to give a good indication of the internal structures and variations in luminous properties of the flame along the burner axis and radial directions.

V. CONCLUSION

A prototype instrumentation system based on digital imaging and process tomographic techniques has been developed for 3-D luminous reconstruction of combustion flames. Three RGB CCD cameras, together with optical transmission devices, capture the 2-D images of a flame concurrently from six different directions. A new approach of combining the LFBP and ART (i.e., LFBP–ART) for the reconstruction of flame sections has been proposed and evaluated. Simulation results

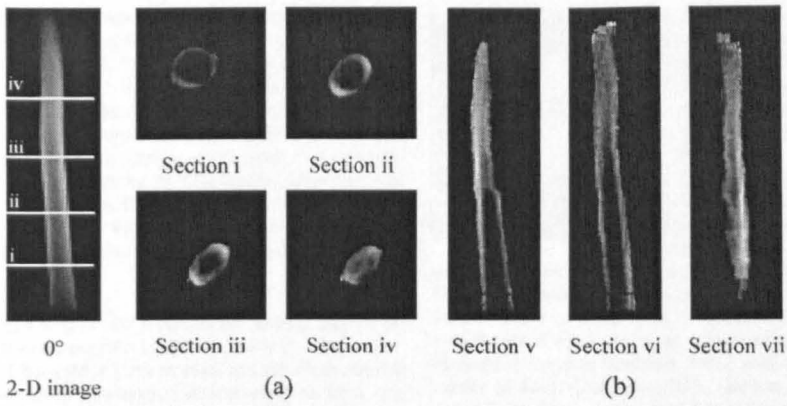

Fig. 6. Luminosity reconstruction of a gaseous flame for the six 2-D projections shown in Fig. 5. (a) Reconstructed cross sections. (b) Reconstructed longitudinal sections.

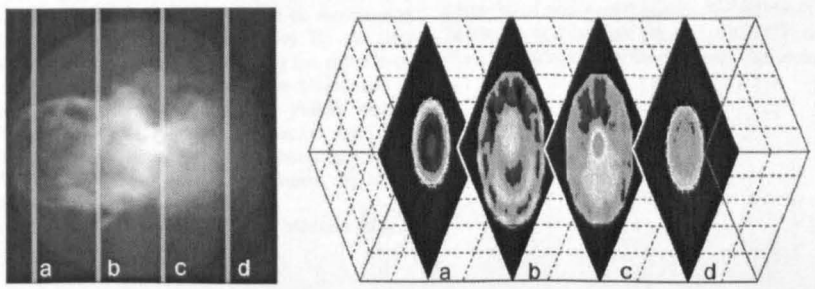

Fig. 7. Image of a coal-fired flame and the reconstructed cross sections. (a) Image of a coal-fired flame. (b) Reconstructed cross sections of the flame.

have demonstrated that, for a limited number of projections (up to six), the proposed LFBP–ART approach gives consistently the smallest mean absolute error and highest correlation coefficient for the given test templates. Experimental results obtained using both gas- and coal-fired flames have shown that the imaging system and the algorithms developed are capable of reconstructing the luminosity distribution of flame sections from the six projections and, hence, a complete 3-D luminous model of the flame. The information obtained can be directly used for quantifying the 3-D geometrical, luminous, and fluid-dynamic characteristics of a combustion flame.

ACKNOWLEDGMENT

The authors would like to thank Dr. G. Riley, S. Cornwell, and G. Cornish of RWE npower plc (U.K.), who offered engineering support for the practical work carried out on their Combustion Test Facility in Didcot, Oxfordshire, U.K. The views expressed are those of the authors and not necessarily those of the British Coal Utilisation Research Association or the Department of Trade and Industry.

REFERENCES

[1] G. Lu, Y. Yan, and M. J. F. Colechin, "A digital imaging based multi-functional flame monitoring system," *IEEE Trans. Instrum. Meas.*, vol. 53, no. 4, pp. 1520–1158, 2004.

[2] Y. Yan, G. Lu, and M. J. F. Colechin, "Advanced monitoring and characterisation of pulverised coal flames," *Fuel*, vol. 81, pp. 647–656, 2002.

[3] G. Lu and Y. Yan, "Temperature profiling of pulverised coal flames using multi-colour pyrometric and digital imaging techniques," *IEEE Trans. Instrum. Meas.*, vol. 55, no. 4, pp. 1303–1308, 2006.

[4] R. C. Waterfall, R. He, and C. M. Beck, "Visualizing combustion using electrical impedance tomography," *Chem. Eng. Sci.*, vol. 52, no. 13, pp. 2129–2138, Jul. 1997.

[5] A. Schwarz, "Multi-tomographic flame analysis with a Schlieren apparatus," *Meas. Sci. Technol.*, vol. 7, no. 3, pp. 406–413, Mar. 1996.

[6] F. Moratti, M. Annunzotia, and S. Giammartini, *An Artificial Vision System for the 3D Reconstruction and the Dynamical Characterisation of Industrial Flames*. Rome, Italy: ENEA-C.R.E. Casaccia, 1997.

[7] H. C. Zhou, S. D. Han, F. Sheng, and C. G. Zheng, "Visualization of three-dimensional temperature distributions in a large-scale furnace via regularized reconstruction from radiative energy images: Numerical studies," *J. Quant. Spectrosc. Radiat. Transf.*, vol. 72, no. 4, pp. 361–383, Feb. 2002.

[8] H. C. Zhou, C. Lou, Q. Cheng, Z. Jiang, J. He, B. Huang, Z. Pei, and C. Lu, "Experimental investigations on visualization of three-dimensional temperature distributions in a large-scale pulverized-coal-fired boiler furnace," vol. 30, pp. 1699–1706, 2005.

[9] H. C. Bheemul, G. Lu, and Y. Yan, "Three-dimensional visualization and quantitative characterization of gaseous flames," *Meas. Sci. Technol.*, vol. 13, no. 10, pp. 1643–1650, 2002.

[10] W. Fisher and H. Burkhardt, "Three-dimensional temperature measurement in flames by multispectral tomographic image analysis," *Proc. SPIE*, vol. 1349, pp. 96–105, Nov. 1990.

[11] P. B. Brisley, G. Lu, Y. Yan, and S. Cornwell, "Three dimensional temperature measurement of combustion flames using a single monochromatic CCD camera," *IEEE Trans. Instrum. Meas.*, vol. 54, no. 4, pp. 1417–1421, Aug. 2005.

[12] A. C. Kak and M. Slaney, *Principles of Computerized Tomgraphic Imaging*. Piscataway, NJ: IEEE Press, 1988.

[13] L. J. Xu and L. A. Xu, "Ultrasound tomography system used for monitoring bubbly gas/liquid two-phase flow," *IEEE Trans. Ultrason., Ferroelectr., Freq. Control*, vol. 44, no. 1, pp. 67–76, Jan. 1997.

[14] G. Gilabert, G. Lu, J. Shao, and Y. Yan, "Tomographic reconstruction of the luminosity distribution of a combustion flame," in *Proc. IEEE Instrum. Meas. Technol. Conf.*, Sorrento, Italy, Apr. 24–27, 2006, pp. 147–150.

Guillermo Gilabert was born in Barcelona, Spain, in 1974. He received the B.Sc. (Hons.) degree in applied physics with computing from Napier University, Edinburgh, U.K., in 2002 and the M.Sc. degree in electronics and electrical engineering from the University of Glasgow, Glasgow, U.K., in 2003.

He is currently working toward the Ph.D. degree with the Department of Electronics, University of Kent, Canterbury, U.K., where he is working on the 3-D monitoring and characterization of fossil fuel flames using digital imaging techniques.

Gang Lu (SM'05) received the B.Eng. degree in mechanical engineering from Central South University, Changsha, China, in 1982 and the Ph.D. degree in advanced combustion instrumentation from the University of Greenwich, London, U.K., in 2000.

He is currently a Lecturer of electronic instrumentation with the Department of Electronics, University of Kent, Canterbury, U.K. He started his career as a Research Engineer and had worked on mechanical design and engineering development for the iron and steel making industry in China for more than ten years. He entered U.K. as a Research Assistant with the University of Greenwich in 1996 and then as a Postdoctoral Research Fellow during 2000–2004. He was with the University of Kent as a Research Associate between June 2004 and March 2006. He has been involved in a range of projects on advanced monitoring and characterization of fossil fuel flames. His main area of research is combustion instrumentation.

Dr. Lu is a Chartered Engineer and a member of the Energy Institute (U.K.).

Yong Yan (M'04–SM'04) received the B.Eng. and M.Sc. degrees in instrumentation and control engineering from Tsinghua University, Beijing, China, in 1985 and 1988, respectively, and the Ph.D. degree in solids flow measurement and instrumentation from the University of Teesside, Middlesbrough, U.K., in 1992.

He started his academic career in 1988 as an Assistant Lecturer at Tsinghua University. In 1989, he joined the University of Teesside as a Research Assistant. After a short period of postdoctoral research, he worked initially as a Lecturer at the University of Teesside during 1993–1996 and then as a Senior Lecturer, Reader, and Professor, respectively, at the University of Greenwich, London, U.K., during 1996–2004. He is currently a Professor of electronic instrumentation and the Head of Instrumentation and Embedded Systems Research Group with the Department of Electronics, University of Kent, Canterbury, U.K. He has published ten research monographs and 170 research papers and has supervised more than ten Ph.D. research students to successful completion.

Dr. Yan is a Fellow of the Institute of Physics, U.K. and Institute of Measurement and Control, U.K. He is a member of five U.K. national technical committees and expert panels. He received the Achievement Medal from the Institution of Electrical Engineers in 2003 and the Engineering Innovation Prize from the Institution of Engineering Technology in 2006.